AD-A088 511 KAMAN AVIDYNE BURLINGTON MA F/G 21/5
FURTHER EVALUATION OF BLAST TESTS OF AN ENGINE INLET.(U)
MAR 79 J R RUETENIK, R F SMILEY, M A TOMAYKO DNA001-78-C-0239
UNCLASSIFIED KA-TR-165 DNA-4994F NL

1 OF 3
AD A088511

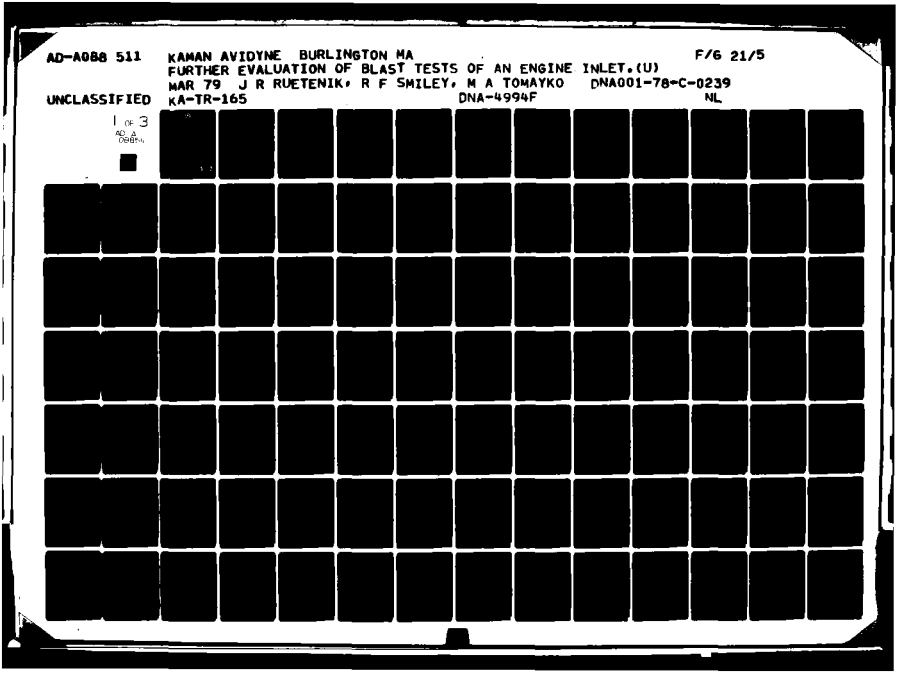

(12) LEVEL II

DNA 4994F

FURTHER EVALUATION OF BLAST TESTS OF AN ENGINE INLET

Kaman AviDyne
83 Second Avenue
Burlington, Massachusetts 01803

31 March 1979

Final Report for Period 1 April 1978—31 March 1979

CONTRACT No. DNA 001-78-C-0239

APPROVED FOR PUBLIC RELEASE;
DISTRIBUTION UNLIMITED.

THIS WORK SPONSORED BY THE DEFENSE NUCLEAR AGENCY
UNDER RDT&E RMSS CODE B342078464 N99QAXAJ50401 H2590D.

Prepared for
Director
DEFENSE NUCLEAR AGENCY
Washington, D. C. 20305

Destroy this report when it is no longer needed. Do not return to sender.

PLEASE NOTIFY THE DEFENSE NUCLEAR AGENCY, ATTN: TISI, WASHINGTON, D.C. 20305, IF YOUR ADDRESS IS INCORRECT, IF YOU WISH TO BE DELETED FROM THE DISTRIBUTION LIST, OR IF THE ADDRESSEE IS NO LONGER EMPLOYED BY YOUR ORGANIZATION.

(18) DNA, SBIE

UNCLASSIFIED

SECURITY CLASSIFICATION OF THIS PAGE (When Data Entered)

(19) **REPORT DOCUMENTATION PAGE**

READ INSTRUCTIONS BEFORE COMPLETING FORM

1. REPORT NUMBER: DNA 4994F, HD-E300 882
2. GOVT ACCESSION NO.: AD-A088 511
3. RECIPIENT'S CATALOG NUMBER:

(6) 4. TITLE (and Subtitle): FURTHER EVALUATION OF BLAST TESTS OF AN ENGINE INLET.

(9) 5. TYPE OF REPORT & PERIOD COVERED: Final Report for Period 1 Apr 78—31 Mar 79.

(14) 6. PERFORMING ORG. REPORT NUMBER: KA-TR-165

(10) 7. AUTHOR(s): J. Ray Ruetenik, Robert F. Smiley, Michael A. Tomayko

(15) 8. CONTRACT OR GRANT NUMBER(s): DNA 001-78-C-0239 new

9. PERFORMING ORGANIZATION NAME AND ADDRESS:
Kaman AviDyne
83 Second Avenue
Burlington, Massachusetts 01803

10. PROGRAM ELEMENT, PROJECT, TASK AREA & WORK UNIT NUMBERS:
Subtask N99QAXAJ504-01
(16)

11. CONTROLLING OFFICE NAME AND ADDRESS:
Director
Defense Nuclear Agency
Washington, D.C. 20305

(11) 12. REPORT DATE: 31 March 1979

13. NUMBER OF PAGES: 260 (12) 262

14. MONITORING AGENCY NAME & ADDRESS (if different from Controlling Office):
(17) J504

15. SECURITY CLASS (of this report): UNCLASSIFIED

15a. DECLASSIFICATION DOWNGRADING SCHEDULE:

16. DISTRIBUTION STATEMENT (of this Report)

Approved for public release; distribution unlimited.

17. DISTRIBUTION STATEMENT (of the abstract entered in Block 20, if different from Report)

18. SUPPLEMENTARY NOTES

This work sponsored by the Defense Nuclear Agency under RDT&E RMSS Code B342078464 N99QAXAJ50401 H2590D.

19. KEY WORDS (Continue on reverse side if necessary and identify by block number)

Aircraft	Engine	Shock
Blast	Experimental Test	Shock Tube
B-1	Inlet	Subsonic
Computer Studies	Pressure	Wind Tunnel

20. ABSTRACT (Continue on reverse side if necessary and identify by block number)

A test program was conducted to simulate blast wave intercepts with a scaled aircraft engine in subsonic flight. Initial results were reported in DNA 4590F. This report presents additional test data and evaluated results.

Jumps in total pressure at the engine face produced by blast interaction with the blastward and leeward inlets are evaluated with respect to effects of four test variables: inlet weight flow, Mach number, shock overpressure and

DD FORM 1 JAN 73 1473 EDITION OF 1 NOV 65 IS OBSOLETE

UNCLASSIFIED

SECURITY CLASSIFICATION OF THIS PAGE (When Data Entered)

19497Ø

20. ABSTRACT (Continued)

intercept angle. The total pressure rose more rapidly in the blast inlet than the leeward inlet, following blast intercept, and by a larger amount. In many tests the rise in the leeward inlet was followed by a rapid fall-off, indicating possible flow separation in the inlet walls.

The two-dimensional Blast Induced Distortion (BID) code provides good representation of effects essentially two-dimensional and inviscid, such as ramp, cowl and engine-face pressures of the blastward inlet.

Blast wave reflection from the engine is expected to be a potential cause of distortion through boundary-layer retardation. The effect on engine-face total pressure is examined with respect to the four test variables. Improved calculations of the effect of the engine-reflected blast wave on the boundary layers in the inlets, made using the generalized NASA-Lewis BLAYER code, indicate that boundary-layer separation would result.

Conversion factors for U.S. customary to metric (SI) units of measurement.

To Convert From	To	Multiply By
angstrom	meters (m)	1.000 000 X E -10
atmosphere (normal)	kilo pascal (kPa)	1.013 25 X E +2
bar	kilo pascal (kPa)	1.000 000 X E +2
barn	meter^2 (m^2)	1.000 000 X E -28
British thermal unit (thermochemical)	joule (J)	1.054 350 X E +3
calorie (thermochemical)	joule (J)	4.184 000
cal (thermochemical)/cm^2	mega joule/m^2 (MJ/m^2)	4.184 000 X E -2
curie	giga becquerel (GBq)*	3.700 000 X E +1
degree (angle)	radian (rad)	1.745 329 X E -2
degree Fahrenheit	degree kelvin (K)	t_K = (t° f + 459.67)/1.8
electron volt	joule (J)	1.602 19 X E -19
erg	joule (J)	1.000 000 X E -7
erg/second	watt (W)	1.000 000 X E -7
foot	meter (m)	3.048 000 X E -1
foot-pound-force	joule (J)	1.355 818
gallon (U.S. liquid)	meter^3 (m^3)	3.785 412 X E -3
inch	meter (m)	2.540 000 X E -2
jerk	joule (J)	1.000 000 X E +9
joule/kilogram (J/kg) (radiation dose absorbed)	Gray (Gy)**	1.000 000
kilotons	terajoules	4.183
kip (1000 lbf)	newton (N)	4.448 222 X E +3
kip/$inch^2$ (ksi)	kilo pascal (kPa)	6.894 757 X E +3
ktap	newton-second/m^2 ($N-s/m^2$)	1.000 000 X E +2
micron	meter (m)	1.000 000 X E -6
mil	meter (m)	2.540 000 X E -5
mile (international)	meter (m)	1.609 344 X E +3
ounce	kilogram (kg)	2.834 952 X E -2
pound-force (lbf avoirdupois)	newton (N)	4.448 222
pound-force inch	newton-meter (N·m)	1.129 848 X E -1
pound-force/inch	newton/meter (N/m)	1.751 268 X E +2
pound-force/$foot^2$	kilo pascal (kPa)	4.788 026 X E -2
pound-force/$inch^2$ (psi)	kilo pascal (kPa)	6.894 757
pound-mass (lbm avoirdupois)	kilogram (kg)	4.535 924 X E -1
pound-mass-$foot^2$ (moment of inertia)	kilogram-$meter^2$ ($kg·m^2$)	4.214 011 X E -2
pound-mass/$foot^3$	kilogram/$meter^3$ (kg/m^3)	1.601 846 X E +1
rad (radiation dose absorbed)	Gray (Gy)**	1.000 000 X E -2
roentgen	coulomb/kilogram (C/kg)	2.579 760 X E -4
shake	second (s)	1.000 000 X E -8
slug	kilogram (kg)	1.459 390 X E +1
torr (mm Hg, 0° C)	kilo pascal (kPa)	1.333 22 X E -1

*The becquerel (Bq) is the SI unit of radioactivity; 1 Bq = 1 event/s.
**The Gray (Gy) is the SI unit of absorbed radiation.

A more complete listing of conversions may be found in "Metric Practice Guide E 380-74," American Society for Testing and Materials.

PREFACE

This work was performed by the AviDyne Division of the Kaman Sciences Corporation for the Defense Nuclear Agency under Contract DNA-001-78-C-0239. CAPT J. Michael Rafferty of the DNA Shock Physics Directorate served as technical monitor.

Dr. J. Ray Ruetenik of Kaman AviDyne was the project leader under Dr. Norman P. Hobbs, Technical Director of KA. Mr. Robert F. Smiley performed engineering functions.

Appreciation is expressed to CAPT Rafferty for his continuing interest and support of this program.

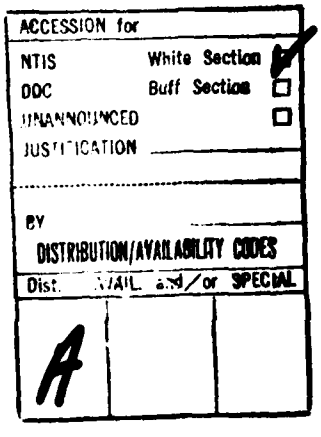

TABLE OF CONTENTS

TABLE OF CONTENTS (CONCLUDED)

LIST OF ILLUSTRATIONS

LIST OF ILLUSTRATIONS (CONTINUED)

LIST OF ILLUSTRATIONS (CONTINUED)

LIST OF ILLUSTRATIONS (CONTINUED)

LIST OF ILLUSTRATIONS (CONTINUED)

LIST OF ILLUSTRATIONS (CONTINUED)

LIST OF ILLUSTRATIONS (CONTINUED)

LIST OF ILLUSTRATIONS (CONTINUED)

LIST OF ILLUSTRATIONS (CONCLUDED)

LIST OF TABLES

SECTION 1
INTRODUCTION

The problem of the interaction of a blast wave from a nuclear explosion with an aircraft engine-inlet system is of importance for military survivability/vulnerability evaluations.

An experimental study regarding this problem was recently conducted at the Arnold Engineering Development Center (AEDC) (References 1 and 2). In this study blast waves produced by shock tubes impinged on a 0.1-scale B-1 inlet pair mounted in the AEDC 16T transonic wind tunnel. Tests were performed at tunnel (pre-blast) Mach numbers of 0, 0.55, 0.70, 0.85 and 0.90 for blast overpressures (scaled to 1 atm. ambient pressure) from 2 to 6 psi for inlet flow rates representative of cruise and maximum power conditions. These tests are described in detail in Reference 1, which also presents a preliminary analysis of the test data and a preliminary correlation of the test results with predictions of the Blast Induced Distortion BID-2 computer code (Reference 3).

The present report is a continuation of the studies of Reference 1 covering the following topics. Section 2 discusses the blast response of the mean total pressure at the engine face. Section 3 discusses general features of blast and operational effects on engine-face mean total pressure signature. Section 4 discusses specific effects of blast and operational variables on engine-face mean total pressure. Section 5 presents detailed comparisons of theoretical and experimental inlet pressures and distortion parameters. Section 6 presents an evaluation of some large late-time inlet distortion data discussed in Reference 1. Section 7 discusses engine reflected shock-boundary layer interaction. Conclusions are presented in Section 8.

Since this report is closely related to Reference 1, it is assumed herein, to limit repetition of material from that reference, that the reader is familiar with Reference 1, particularly regarding test geometry and test instrumentation. However, for the reader's

convenience, Table 1.1 and Figures 1.1 and 1.2 indicating test conditions and pressure transducer locations in the engine inlets and at the engine face are repeated here from Reference 1. (See Reference 1 for an explanation of the table and figures.)

TABLE 1.1

16T WIND TUNNEL TEST CONDITIONS

Run	Part Point No.	Mach No.	Flow Rate (lb/sec)		Tube No.	Tube Pressure (psia)	Nominal Shock Overpressure (psi)	Intercept Angle (deg)	Yaw Ang. (deg)
			OB Inlet	IB Inlet					
1	501.01	0	0	0	2	69	2.7	79	0
2	615.03	.552	235	235	3	186	4.7	91	
3	591.03	.550	351	348	1	157	3.7	76	
4	589.03	.551	351	348	2	115	3.8	97	
5	590.02	.549	351	349	3	124	4.0	94	
6	602.02	.700	302	300	1	72	2.6	86	
7	600.04	.701	302	302	2	58	2.6	106	
8	573.04	.700	304	302	↓	112	5.0	98	
9	601.03	.701	302	300	3	69	3.0	104	
10	574.03	.701	303	300	↓	132	4.4	97	
11	621.03	.700	351	351	1	73	3.0	84	
12	519.02	.699	348	344	↓	103	3.8	88	
13	527.02	.700	349	344	↓	135	4.8	78	
14	626.02	.701	352	352	↓	142	4.8	79	
15	512.03	.700	351	344	2	59	2.8	103	
16	517.02	.700	349	344	↓	85	3.8	103	
17	525.02	.701	348	344	↓	113	5.0	100	
18	624.02	.700	350	350	↓	139	5.2	99	
19	513.03	.700	351	344	3	70	3.0	102	
20	518.02	.700	348	343	↓	102	4.2	99	
21	526.02	.700	349	344	↓	133	4.8	98	
22	625.02	.701	350	350	↓	155	5.6	92	↓
23	570.03	.699	351	350	1	144	3.6	87	+5.0
24	568.04	.700	350	349	2	132	5.8	103	+5.0
25	569.03	.703	350	349	3	143	4.2	105	-5.0
26	559.02	.850	300	298	1	61	2.2	89	0
27	598.03	.848	299	299	↓	90	3.0	85	
28	584.03	.847	294	293	↓	122	5.0	82	
29	608.04	.850	299	299	↓	142	4.4	82	
30	557.04	.850	300	298	2	55	-	-	
31	596.05	.848	300	300	↓	73	3.8	108	
32	582.03	.847	300	297	↓	94	4.4	105	
33	606.03	.849	300	299	↓	120	-	-	
34	558.03	.850	303	301	3	60	>2	-	
35	597.03	.848	300	300	↓	85	4.0	104	
36	583.03	.847	298	296	↓	114	4.4	102	
37	607.03	.850	299	298	↓	140	4.8	108	
38	546.02	.847	348	347	1	121	3.6	84	
39	544.04	.847	348	347	2	94	4.0	107	
40	619.02	.850	352	351	↓	120	5.8	110	
41	545.03	.847	348	347	3	113	4.4	105	
42	620.02	.850	351	350	↓	139	5.6	100	
43	553.03	.900	327	329	1	117	3.0	86	
44	550.02	.899	349	354	2	86	4.0	107	↓
45	551.01	.900	349	354	3	104	4.2	105	

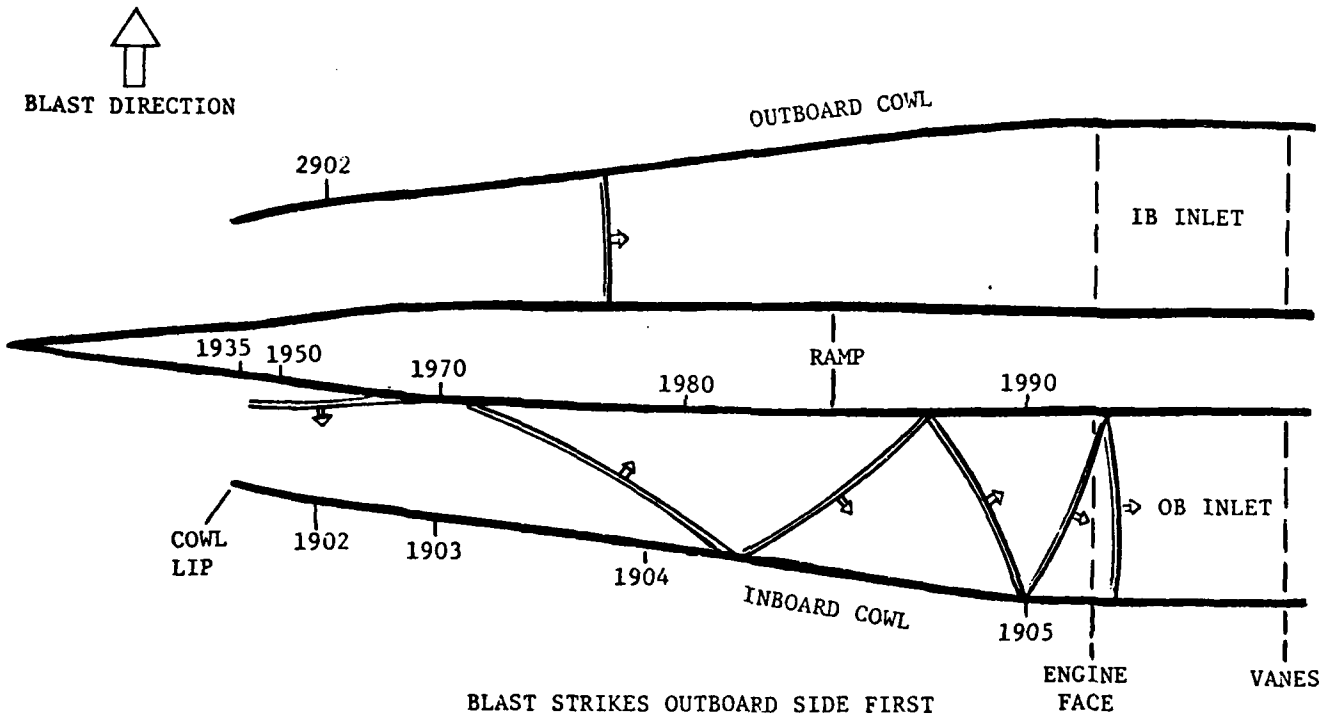

Figure 1.1. Sketch showing typical shock wave pattern and transducer locations in the inlets.

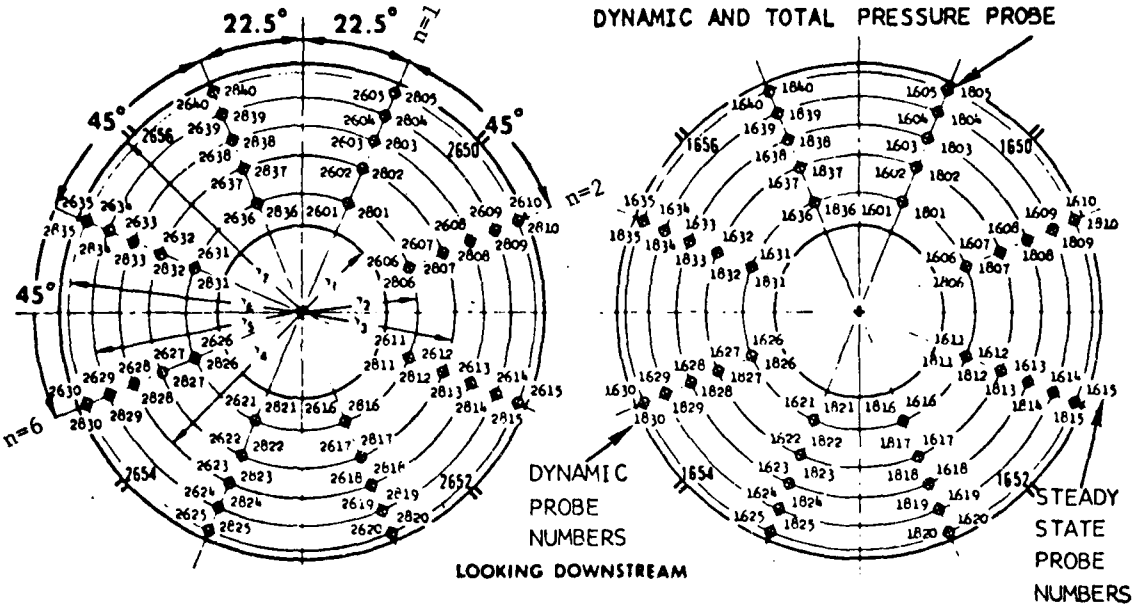

Figure 1.2. Engine face transducer locations. (Rockwell drawing)

SECTION 2
RESPONSE OF MEAN TOTAL PRESSURE AT ENGINE FACE

The effect of the blast wave interaction upon the mean total pressure at the engine face as measured in the tests is examined in this section and the following two sections. In this section the test records of the mean total pressures at the two engine faces are examined qualitatively for each run on a run-by-run basis. In Section 3 the records are grouped so as to show the effect of each test variable, one at a time - shock overpressure, intercept angle, inlet flow rate and free-stream Mach number - and the general effects of the variables are examined qualitatively. In Section 4 the effect of these test variables upon specific features of the records are examined on a quantitative basis.

2-1 GENERAL FEATURES OF EFFECT ON MEAN TOTAL PRESSURE.

The blast wave first intercepts the cowl of the blastward inlet, then diffracts around the cowl and into the inlet. It then reflects from the splitter between the two inlets and diffracts around the splitter and into the leeward inlet. At each engine face of the two inlets a series of shock waves arrives as a result of the diffractions and multiple reflections from the duct walls.

Typical records of the reduced mean total pressures at the engine faces of the two inlets are shown in Figure 2.1. The quantities R20 and R2I are the ratios of the instantaneous mean total pressures at the engine faces of the outboard and inboard inlets, respectively, to the preblast total pressure in the wind tunnel. The mean total pressures for each inlet were obtained from averages of the 40 pitot probe measurements at each engine face. Tube 2 was fired in this run, so R20 is the record for the blastward inlet and R2I the record for the leeward inlet; the same would be true for a Tube 1 firing and the opposite for a Tube 3 firing.

R20 in Figure 2.1 is constant at 0.99 until about 8.83 milliseconds (ms). It then jumps up to about 1.1 on shock arrival at the engine face, followed by a steep ramp-up of about 0.33 ms duration to a

peak of about 1.4. The ramp is believed to consist generally of a staircase of weak shocks produced by the multiple reflections of the initial blast shock from the splitter and the walls of the inlet. R20 then drops off from 1.4 down to about 1.3 due to the weakening of the upstream reflection by diffraction of the incident shock around the splitter and other outside surfaces of the inlets.

At 9.7 ms R20 increases abruptly again due to reflection of the shock wave from the downstream throttle formed by the control vanes. This wave is an upstream facing shock followed by a compression wave. The rate of rise of the engine-face total pressure varies with test conditions and the particular characteristics of the initial shock and compression wave within the inlet.

The strength of the upstream-facing shock/compression wave in terms of pressure would be greater than might appear from records of total pressure. This reflected wave slows down the flow passing through it. The velocity reduction across the shock itself decreases the total pressure, offsetting partially the increase in total pressure due to pressure rise.

The reflection from a fan stage would be expected to produce a stronger wave than occurs from the reflection from the throttle (choked orifice). This is demonstrated by calculations for the upstream reflection of a shock wave from a typical high-performance fan in Reference 1, Section 8.5.

The concern regarding the upstream-facing shock/compression wave is that it tends to distort the flow within the inlet passing through it to an extent that stalling of the fan stages within the engine might result. Calculations presented in Reference 1, Section 9, demonstrated that the boundary layers on the ramp and cowl surfaces of the blastward inlet, and possibly the cowl surface of the leeward inlet, would separate for full-scale inlets (10x model size) due to a representative reflected wave (5-psi blast intercept at 90 degrees for Mach 0.85 and 350 lb/s full-scale reduced weight flow).

Following the arrival at the engine face of the reflected wave from the control-vane throttle, R20 at the engine face then decreases slowly in this run until about 12 ms, at which time it falls off rapidly because of the fall off of pressure within the portion of the blast wave in the area of the inlet mouth. For firings from Tube 1, R20 often increased at about 3 ms or so after shock arrival, due to arrival of the cold driver gas from the shock tube.

At the engine face of the leeward inlet Figure 2.1 shows that the inboard total pressure R2I was constant at 0.99 in the test until 9.4 ms. It then jumped to about 1.10 upon arrival of the blast shock that had diffracted around the splitter. RTI then continued to rise due to further blast flow around the splitter, then level off and abruptly rose again at 10.1 ms due to the shock reflected from the control vanes of the inboard inlet.

Beginning at about 10.4 ms R2I then fell off rapidly. This is attributed to the large sideslip angle produced by the blast-induced flow at the inlets, which will be discussed further. A large sideslip angle would produce separation of the flow from the leeward surface of the splitter or retard the flow sufficiently that it would be vulnerable to separation by the interaction with the reflected shock from the control vanes.

The R20 and R2I records are discussed below relative to the effects of the tunnel Mach number, M, the inlet full-scale weight flow at the engine face, W2R; the particular shock tube fired; and the (nominal) overpressure of the incident blast shock, Δp_s.

One difference between firings from Tube 1 and those from Tubes 2 and 3 is the blast intercept angle, ϕ. Intercept angles from Tube 1 ranged from 76 to 89 degrees from head-on; intercept angles from Tubes 2 and 3 were greater, ranging from 91 to 110 degrees. The second difference between the firings was that Tubes 1 and 2 fired from the outboard side of the inlets and Tube 3 from the opposite side, over the fuselage, so the blast wave from Tube 3 traveled over more of the fuselage model.

2-2 MACH 0, 0 LB/S FULL-SCALE WEIGHT-FLOW.

The R20 and R2I records for Run 1 with the tunnel off and a zero weight flow through the two inlets are shown in Figure 2.2. The record for the blastward inlet R20 indicates that after the shock arrived at the engine face (9.7 ms) R20 increased to about 1.26 and then fell off with very little indication of any reflection from the control vanes. RTO finally leveled off about 1 ms after shock arrival at about one-half of the peak value. The abrupt rise in RTO, beginning 3.9 ms after shock arrive (13.6 ms), is attributed to the arrival of the cold driver gas from the shock tube, which ends the test.

The record for the leeward inlet indicates that R2I rose stepwise at shock arrival (11.7 ms) to a level of about 1.08, continued to climb to a maximum of about 1.14 and then decayed slowly. It is speculated that the decay may be due to a gradual separation of the flow from the leeward side of the splitter and ramp of the inboard inlet. The dynamic pressure is small at Mach zero relative to the static overpressure so that separation would not produce as large an effect on R2I as in the example shown in Figure 2.1, where the Mach number is 0.70.

2-3 MACH 0.55, 235 LB/S FULL-SCALE WEIGHT FLOW.

Figure 2.3 shows the records for Run 2, which had the lowest non-zero weight flow for the two inlets, 235 lb/s (full scale) each. The tunnel Mach number was also the lowest non-zero value, 0.55, and the incident shock overpressure was high, 4.7 psi (nominal). Tube 3 was fired, so the inboard inlet (R2I) was on the blastward side.

The record for R2I in Figure 2.3 has a high first peak, which is attributed to the relatively high shock overpressure. The reflected shock from the throttle control vanes, which arrived about 0.7 ms after the first shock, appears to have been the strongest here of all of the tests, in terms of the increment in R2I. The weight flow was also low in this test, and comparisons between tests indicated that low weight flow increased the second rise.

The R20 record in Figure 2.3 shows the effect of a strong initial shock for the leeward inlet, by the abrupt rise to a value of 1.13. It then continues to rise more slowly to 1.16, fall off, then rise again. The latter rise is attributed to a weak reflection from the control vanes that reaches the engine face about one millisecond after shock arrival. The R20 record then exhibits a rapid decay which is attributed to a large sideslip angle, produced by the blast wave, that degrades the flow uniformity entering the leeward inlet. The combination of a low Mach number, low mass flow and strong blast wave results in a large sideslip angle.

This is an example where the RTO fall-off for the leeward inlet commenced slightly after the arrival of the reflected shock at the engine face. This would be expected to be the sequence of events if the reflected shock caused shock-boundary layer separation within the inlet. Further information would be needed to verify that separation actually occurred, however it does appear clear from the record that significant flow deterioration did take place within the leeward inlet.

This strong throttle-reflected shock in the blastward inlet and the combination of a throttle-reflected shock in the leeward inlet followed by a rapid decay could be detrimental to the operation of engines attached to such an inlet. The throttle-reflected shocks, simulating engine reflected shocks, would tend to separate the flow within the inlets, resulting in a rapid decrease in total pressure and possible stall of a gas turbine engine.

2-4 MACH 0.55, 350 LB/S FULL-SCALE WEIGHT FLOW.

The results of firings at Mach 0.55 and a full-scale reduced weight flow of 350 lb/s, (Runs 3, 4 and 5) are shown in Figure 2.4.

The results for Run 5, Figure 4c, at 350 lb/s can be compared with those for Run 2, Figure 2.3, at 235 lb/s. Both firings were from Tube 3 with comparable shock overpressures, 4.0 and 4.7 psi, respectively. The first peak for the blastward inlet is similar for the two weight

flows, but the second peak, from the throttle reflection, is much smaller for the higher weight flow and it also is spread out more timewise. This characteristic of weak throttle reflections is true also for the other two firings at Mach 0.55 and 350 lb/s, Figures 2.4a and 2.4b.

For the leeward inlet at Mach 0.55, the first peak of Run 5, Figure 2.4c, is similar to the first peak of the 300 lb/s firing, Run 2, Figure 2.3. The throttle reflection for the higher weight flow, Figure 2.4c, is weaker than for the lower weight flow, Figure 2.3, as it was for the blastward inlet. The decay rate is not as steep either, as at the lower weight flow. It is speculated that these effects may be due to a lower blast-induced sideslip angle for Run 5 than for Run 2 because of the higher weight flow and slightly lower shock overpressure.

2-5 MACH 0.70, 300 LB/S FULL-SCALE WEIGHT FLOW.

The records of the reduced total pressures RTO and RTI at the engine face for tests at Mach 0.70 and a full-scale reduced weight flow of 300 lb/s, Runs 6 to 10, are presented in Figure 2.5. For the firing from Tube 1 (Run 6, Figure 2.5a) the shapes of the records are generally similar to those for the example discussed in Figure 2.1. Again, the second jump, due to the reflected shock from the throttle, which simulates the engine, is substantial for both the blastward and leeward inlets. The total pressures both remain high for about 3-1/2 ms after shock arrival until cold gas appears to have arrived from the shock tube (R20) or blast decay sets in (R2I).

The weaker blast firings (2.6, 3.0 psi) from Tube 2 (Run 7) and Tube 3 (Run 9) show a marked falloff in the blastward total pressures after the throttle reflection arrives. This fall off is believed to be due to decay in the blast wave arriving at the inlet. Therefore the falloff for the leeward inlet is not attributed to sideslip angle in this case. For the strong shocks (5.0 and 4.4 psi) from Tube 2, Run 8, and Tube 3, Run 10, however, the blastward ratios held up well for 3 to 4 ms after shock arrival, so the falloff of the leeward ratios beginning at about 1 ms after shock arrival is attributed to the large sideslip angle produced by the blast wave (and not to decay in the blast properties arriving at the inlet).

2-6 MACH 0.70, 350 LB/S FULL-SCALE WEIGHT FLOW.

The results for Mach 0.70, and a full-scale weight flow of 350 lb/s, Runs 11 to 22, are shown in Figure 2.6. For Tube 1 firings, Figure 2.6a-d, the effect of weight flow on the interaction is found by comparison with Run 6, Figure 2.5a, for the same Mach number but only 302 lb/s. For the blastward inlet the first peak in RTO for Run 11, Figure 2.6a, which has a nearly equal shock overpressure (3.0 psi) to Run 6 (2.6 psi), is similar to the peak for Run 6. The second peak in comparison to the first, is much smaller for Run 11, than at the lower weight flow of Run 6.

The total pressures for Tube 1 at 350 lb/s hold up in both the blastward and leeward inlets for the full 3-ms nominal test period for the higher overpressures of 3.8 to 4.8 psi (Runs 12-14). This means that sideslip is not causing a problem to the leeward inlet. There is a small falloff for 3.0 psi (Run 11).

There is a feature of the blast wave that should be noted, for later discussion, from the results shown in Figure 2.6. It will be discussed with respect to Run 12, Figure 2.6b. The blast shock front arrives at the blastward inlet first, of course, which is why R20 rises about 1/2 ms before R2I for Tube 1. The interior flow of the blast wave would also arrive first at the blastward inlet. However, the rapid falloff in the total pressure for the blastward inlet (RTO) at about 12-1/2 ms is preceded by the falloff for the leeward inlet (RTI) by a time of about 1/2 to 1 ms. It also decays earlier at the leeward inlet for the firings at higher shock overpressures, as is evident in Figures 2.6c-d. Examination of measurements of the blast waves produced by this method has shown that this earlier decay at the leeward inlet is a result of the three-dimensional (vs. one-dimensional) character of the blast wave. In this case a decaying portion of the blast wave reaches the leeward inlet before a decaying portion reaches the blastward inlet.

The question then arises whether the decay in total pressure observed sometimes for the leeward inlet, which is attributed in some cases to blast-induced sideslip, might in fact be due to this decay in the blast pressure instead. The question cannot be resolved with certainty at this time. But, from an examination of trends with varying blast strengths and from measurements with external claw probes, it appears at present that the blast decay results in a definite signature, such as appears in Run 12, Figure 2.6b.

Another feature of the blast signature is shown in Figure 2.6c for Run 13. At about 13 ms, R20 rises at an increasing rate. This rise is associated with the arrival of the cold driver gas from the shock tube. It is also observed for the leeward inlet by the rise in R2I beginning at about the same time. This rise is followed by the pressure decay of the blast wave cited above for the leeward inlet (R2I), starting at about 14-1/2 ms, and for the blastward inlet (R20), starting somewhere between about 15 to 17 ms. The results for Run 14, Figure 2.6d, are similar.

These records all indicate that there is a usually good 3 ms or more of good test flow within the blast wave before these blast anomalies affect the results for this model. The anomalies appear to produce characteristic signatures in the records that make them rather well defined.

Tube 2 firings at Mach 0.70 and 350 lb/s, Figures 2.6e-h, and Tube 3 firings, Figures 2.6i-l, produce weak throttle reflections for the blastward inlet until the blast shock overpressure approaches about 5 psi, Figures 2.6h and 2.6k-l. For the leeward inlet there is essentially no throttle reflection. There is however a decay for the leeward inlet, beginning about 1-2 ms after blast shock arrival, that is attributed to blast-induced sideslip angle. The rate of the decay increases with blast strength which follows the trend expected for an increasing angle of sideslip, associated with a stronger blast wave.

2-7 MACH 0.70, 350 LB/S, ±5° YAW.

The results with yaw angles of ±5 degrees are presented in Figure 2.7. In each test the model was yawed with the nose away from the particular shock tube that was fired. This means that the sideslip angle is increased by the blast wave.

The test conditions of Run 23, Figure 2.7a, compare otherwise most nearly with those of Run 12, Figure 2.6b. The results for the blastward inlet are rather similar. The leeward inlet shows a noticeably greater falloff beginning about 1 ms after blast arrival (or at 10.5 ms). This means that the 3.6-psi blast wave with the 5-deg yaw angle evidently produces too much sideslip for the flow within the leeward inlet to maintain total pressure.

The test conditions for Run 24 with Tube 2, Figure 2.7b, compare most nearly to those for Run 18, Figure 2.7h, except for the initial yaw angle. For the blastward inlet the throttle reflection is weaker, but otherwise the results are similar. For the leeward inlet the falloff due to yaw is much more marked than for Tube 1, Figure 2.7a, beginning very shortly after shock arrival.

The results for Run 25 with a firing from Tube 3, Figure 2.7c, are similar to those for Tube 2, Run 24. The test conditions are the same as for Run 20, Figure 2.6j, except for the -5-deg yaw. The blastward inlet results are about the same as for Tubes 1 and 2, Figures 2.7a and b. The leeward inlet has a rapid pressure falloff, as for Tube 2.

2-8 MACH 0.85, 300 LB/S FULL-SCALE WEIGHT FLOW.

The total pressure results at the engine face for Mach 0.85 and a weight flow of 300 lb/s are shown in Figure 2.8. Firings with Tube 1 are presented in Figures 2.8a-d. The jumps due to throttle reflections (engine simulation) for the blastward inlet are stretched out much more in time for the weaker shocks, below about 4 psi, than they were at the lower Mach numbers. The reflected wave steepens up as the blast strength is increased, so that at 4.4 psi for Run 29 (Figure 2.8d) it is quite steep. The jump to the second peak is also large.

The total pressures in Figures 2.8a-d for the leeward inlet with Tube 1 firings build up well and generally hold up for the blast period of about 3 ms. The only particular falloff occurs with the weaker shocks of 2.2 and 3.0 psi (Figures 2.8a and b) beginning about 1.5 ms after shock arrival, which is attributed to decay in the blast wave, since it roughly follows the fall-off of the blastward total pressure.

For Tube 2 and 3 firings at Mach 0.85, Figures 2.8e-j, the results are also similar to the Mach-0.7 results, Figure 2.5, for the same tubes. The rapid falloff in the total-pressure ratios beginning about 1-1/2 ms after shock arrival is again attributed to the decay in the blast wave at the inlet. There is a strong effect of the throttle reflection for the blastward inlet, also, appearing in the steepening of the second rise and increase in level of the second peak as the blast strength is increased. The leeward records have typical first peaks, but again only very weak effects of throttle reflections which are masked by a rapid decay in total pressure. There is no clear indication of separation occurring in the leeward inlet at Mach 0.85 as there was for the higher shock overpressures at Mach 0.70 (Figures 2.5c and e).

2-9 MACH 0.85, 350 LB/S FULL-SCALE WEIGHT FLOW.

The results for Mach 0.85 and a full-scale reduced weight flow of 350 lb/s are shown in Figure 2.9. For Tube 1, Figure 2.9a, the blastward inlet for a 3.6-psi shock, Run 38, has a sharp initial peak and a strong throttle reflection, similar to the results for Run 29, Figure 2.8d, at 300 lb/s and a 4.4-psi shock overpressure. The results for the leeward inlet are also similar to those with 300 lb/s.

For Tubes 2 and 3 at Mach 0.85, Figures 2.9b-e, the results are similar to those for 300 lb/s, Figures 2.8e-l, including the rapid decay attributed to the blast wave decay (not to sideslip).

2-10 MACH 0.90, 350 LB/S FULL-SCALE WEIGHT FLOW.

The results for Mach 0.90, Figure 2.10, are similar to the results for Mach 0.85, Figure 2.9, for both the blastward and leeward inlets.

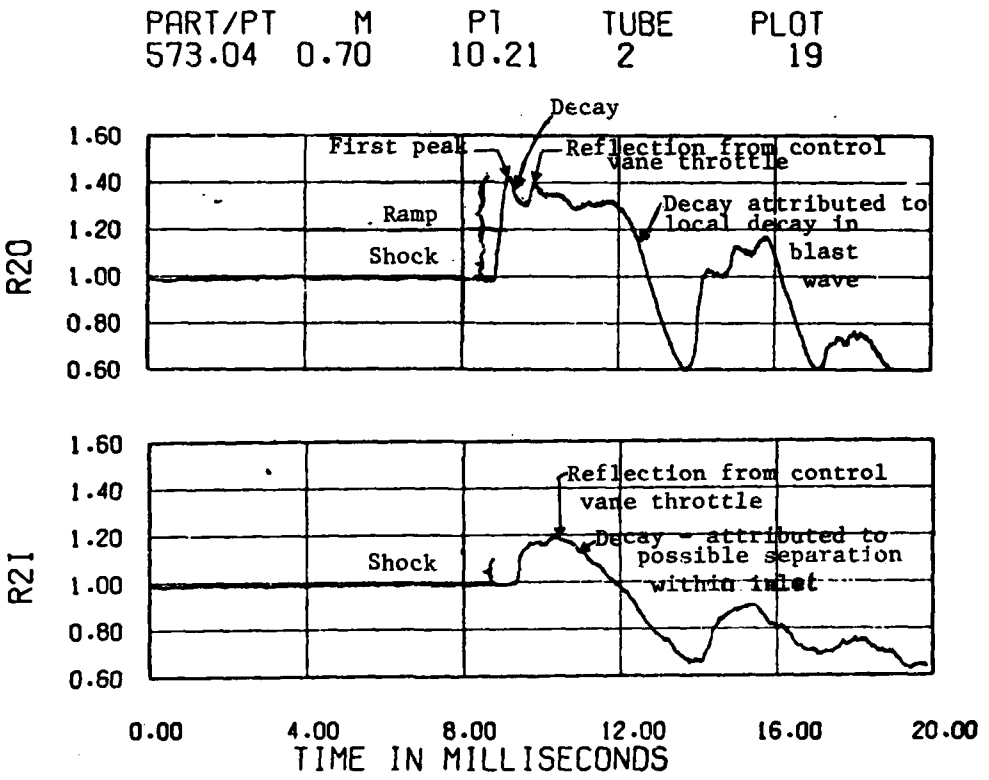

Figure 2.1. Typical engine-face mean total pressures. Run 8. Mach 0.70, W2R=300 lb/s (nom), Δp_s=5.0 psi, ϕ=98 deg.

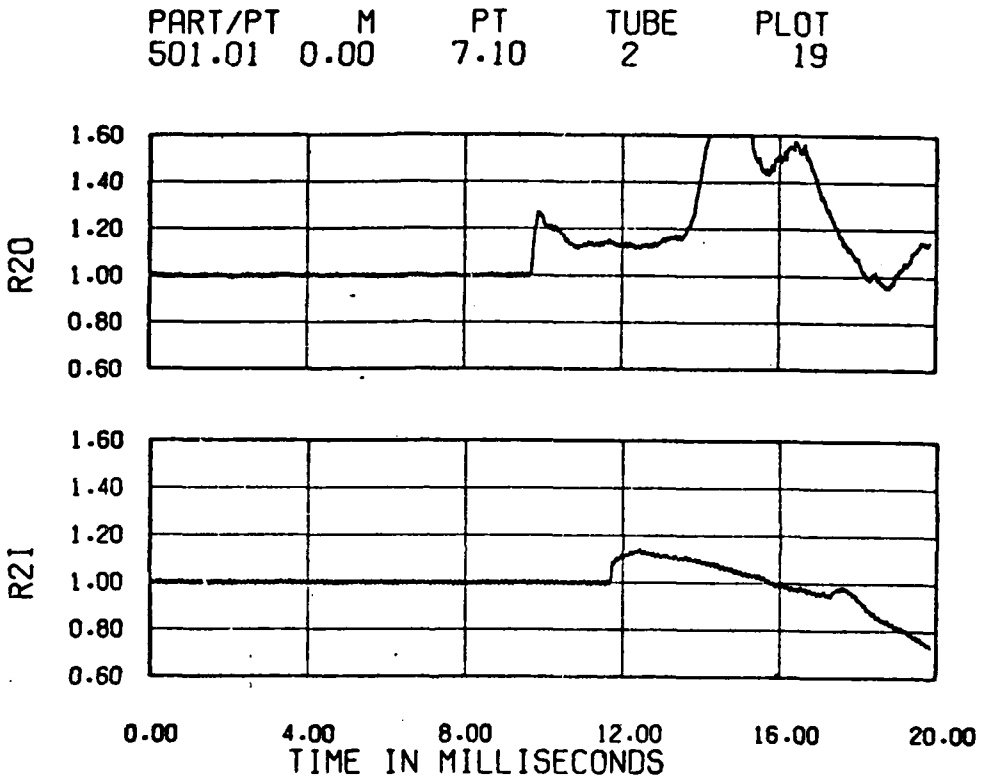

Figure 2.2. Engine-face mean total pressures. Run 1.
Mach 0, W2R=0 lb/s (nom), Δp_s=2.7 psi (nom), ϕ=79 deg.

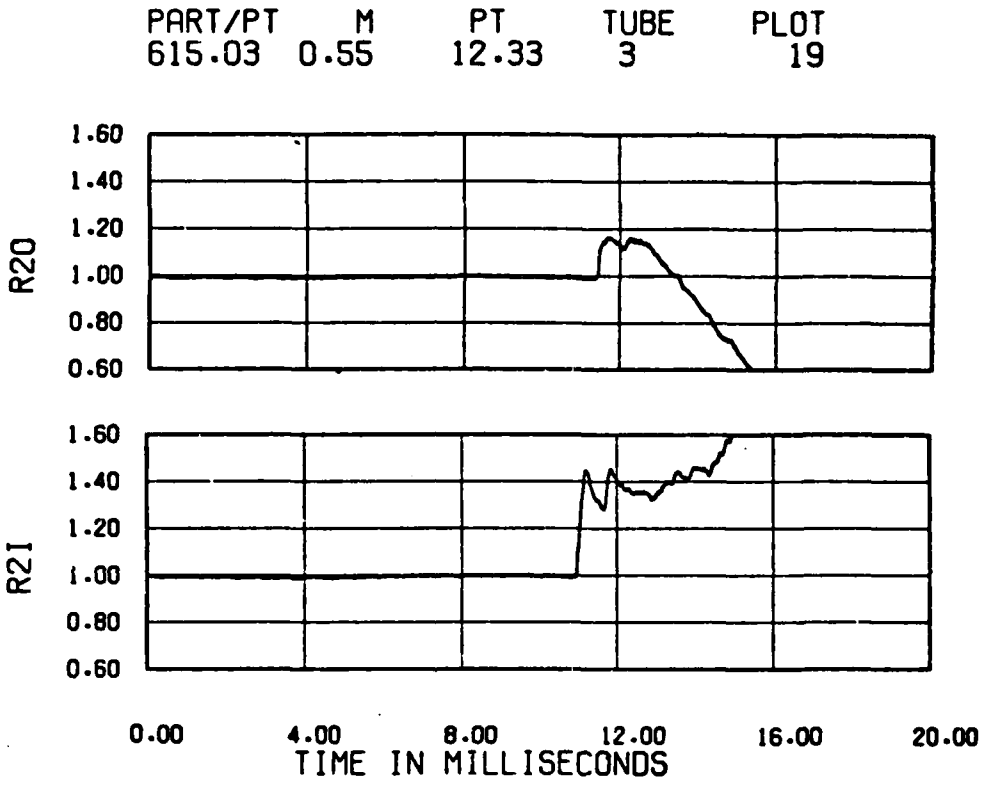

Figure 2.3. Engine-face mean total pressures. Run 2. Mach 0.55, W2R=235 lb/s (nom) Δp_s=4.7 psi (nom), ϕ=91 deg.

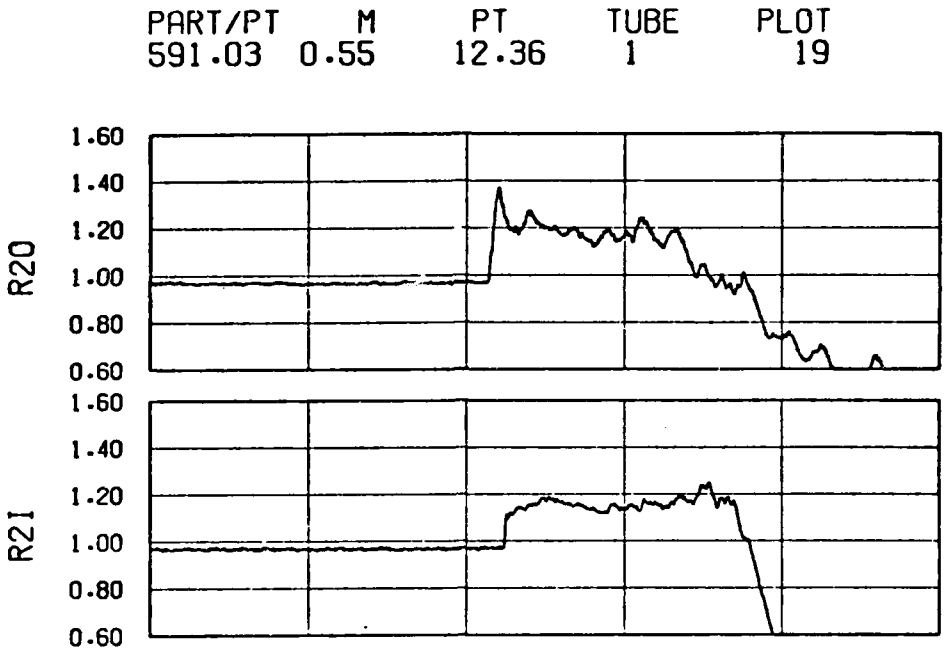

(a) Run 3, Δp_s=3.7 psi (nom), ϕ=76 deg.

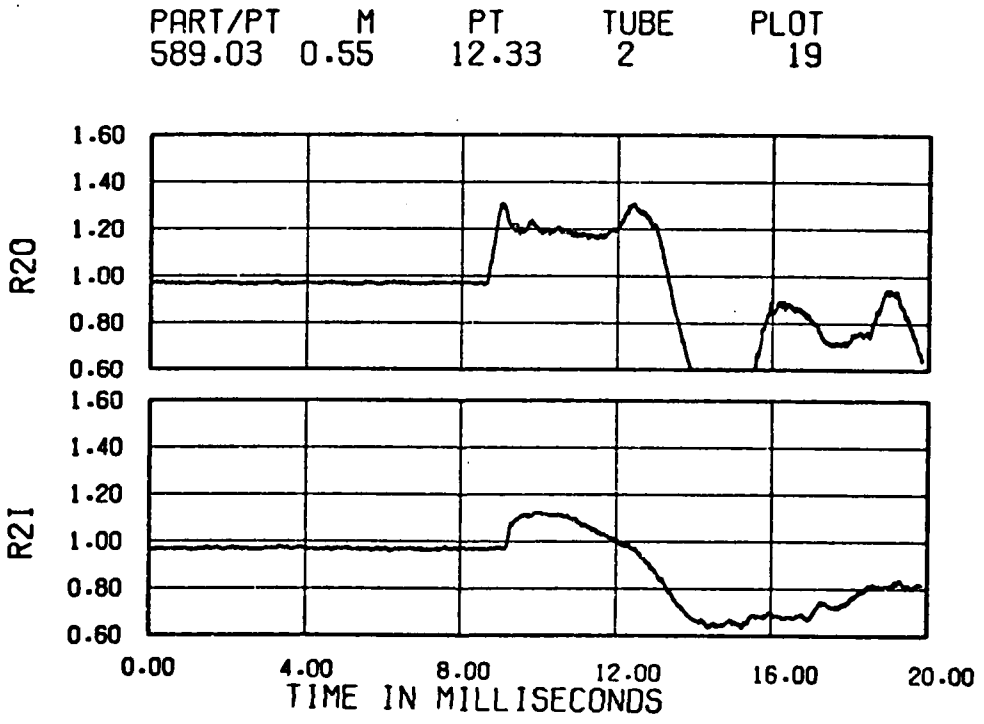

(b) Run 4, Δp_s=3.8 psi (nom), ϕ=97 deg.

Figure 2.4. Engine-face mean total pressures. Mach 0.55, W2R=350 lb/s (nom).

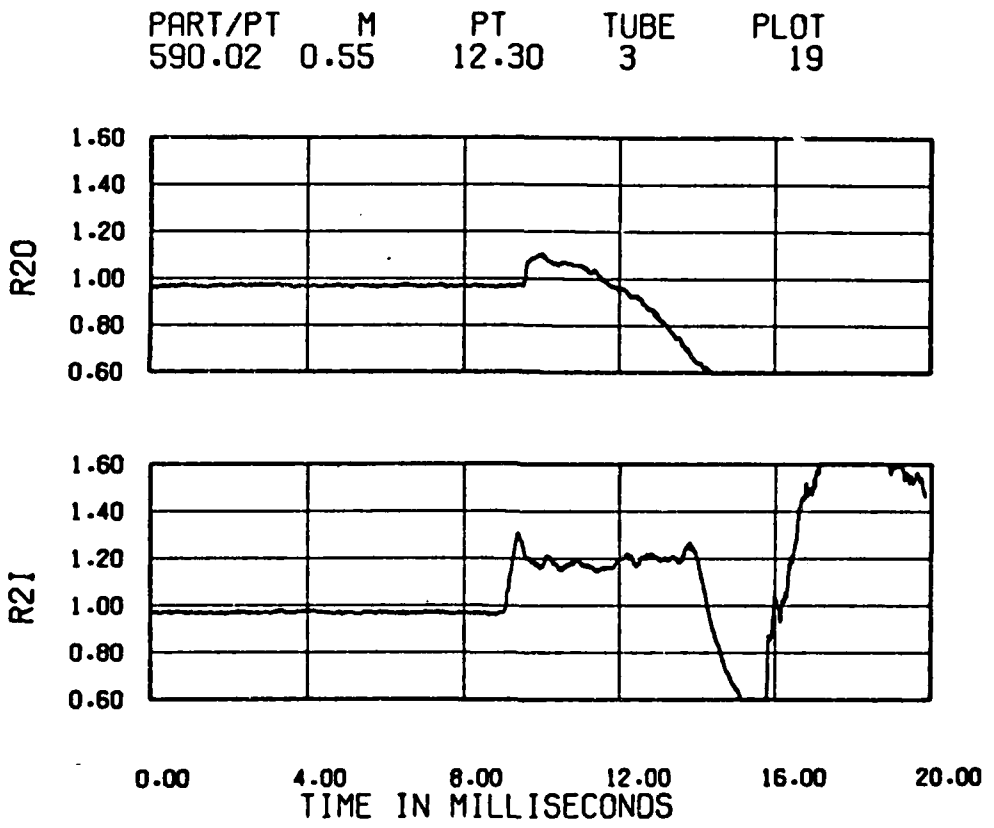

(c) Run 5, Δp_s=4.0 psi (nom), ϕ=94 deg.

Figure 2.4. Concluded.

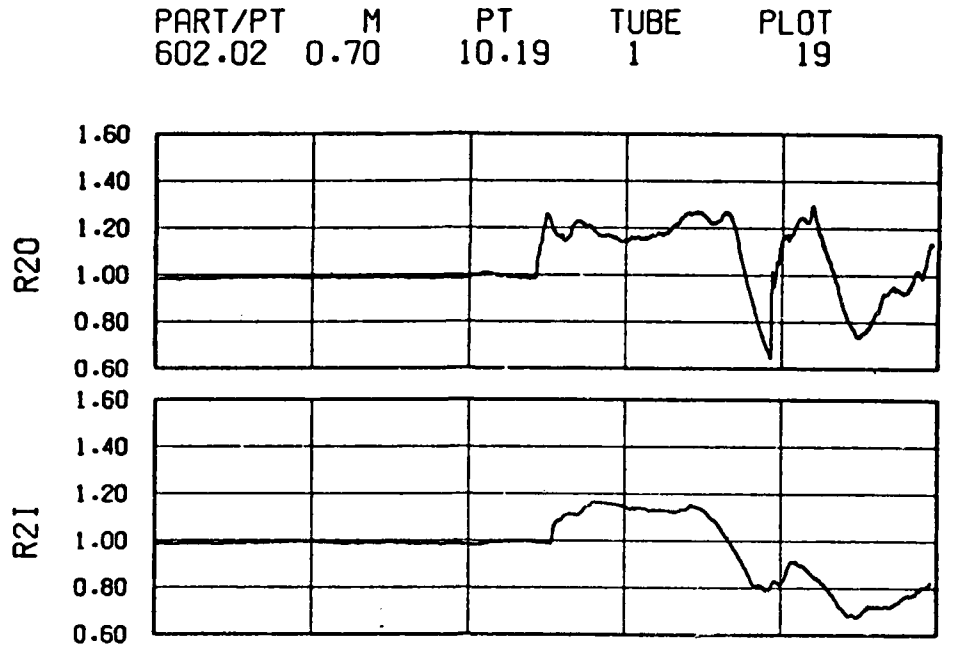

(a) Run 6, Δp_s=2.6 psi (nom), ϕ=86 deg.

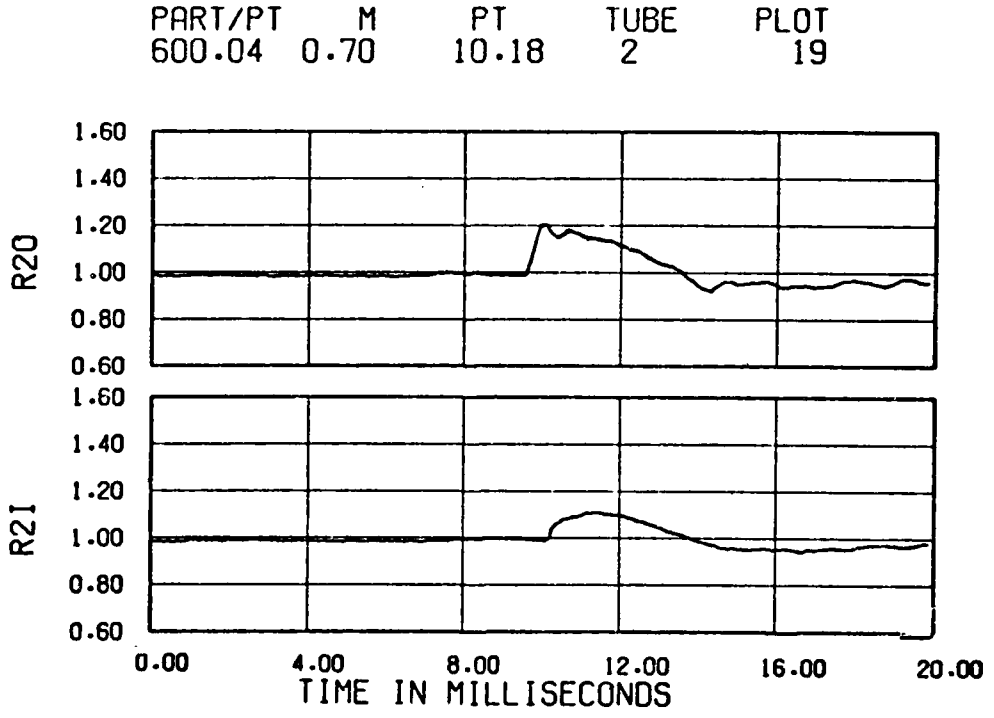

(b) Run 7, Δp_s=2.6 psi (nom), ϕ=106 deg.

Figure 2.5. Engine-face mean total pressures. Mach 0.70, W2R=300 lb/s (nom).

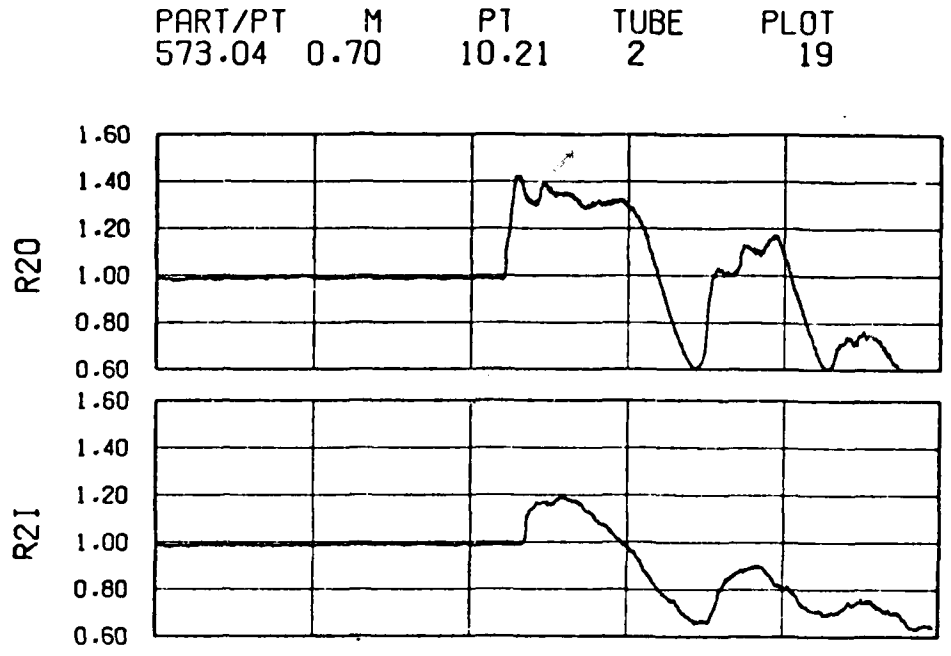

(c) Run 8, Δp_s=5.0 psi (nom), ϕ=98 deg.

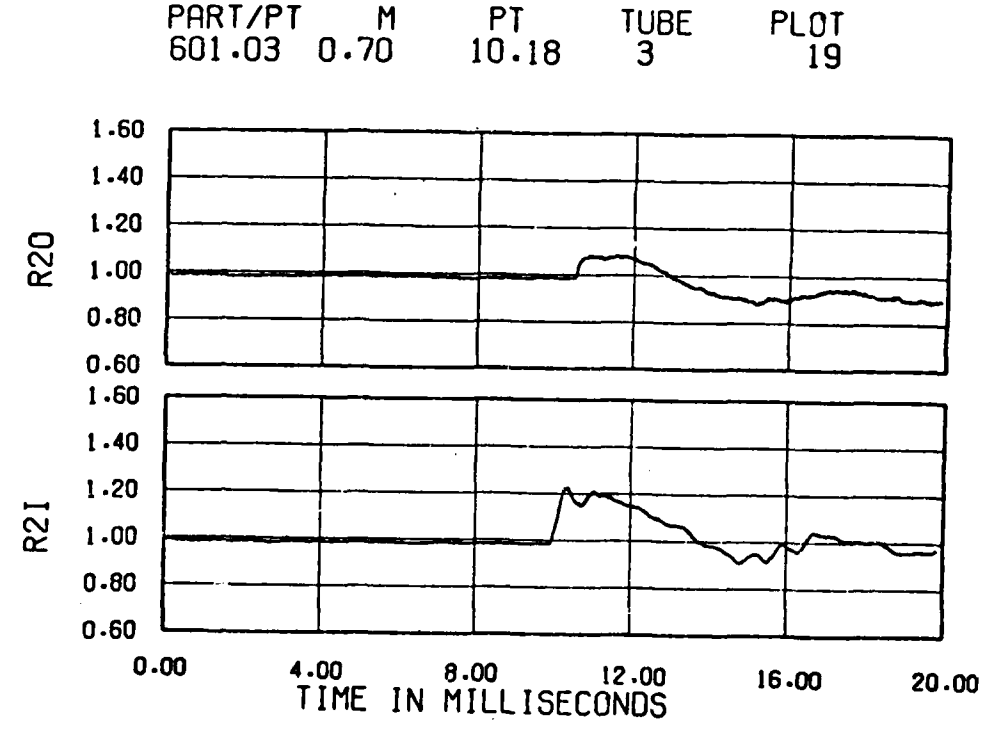

(d) Run 9, Δp_s=3.0 psi (nom), ϕ=104 deg.

Figure 2.5. Continued.

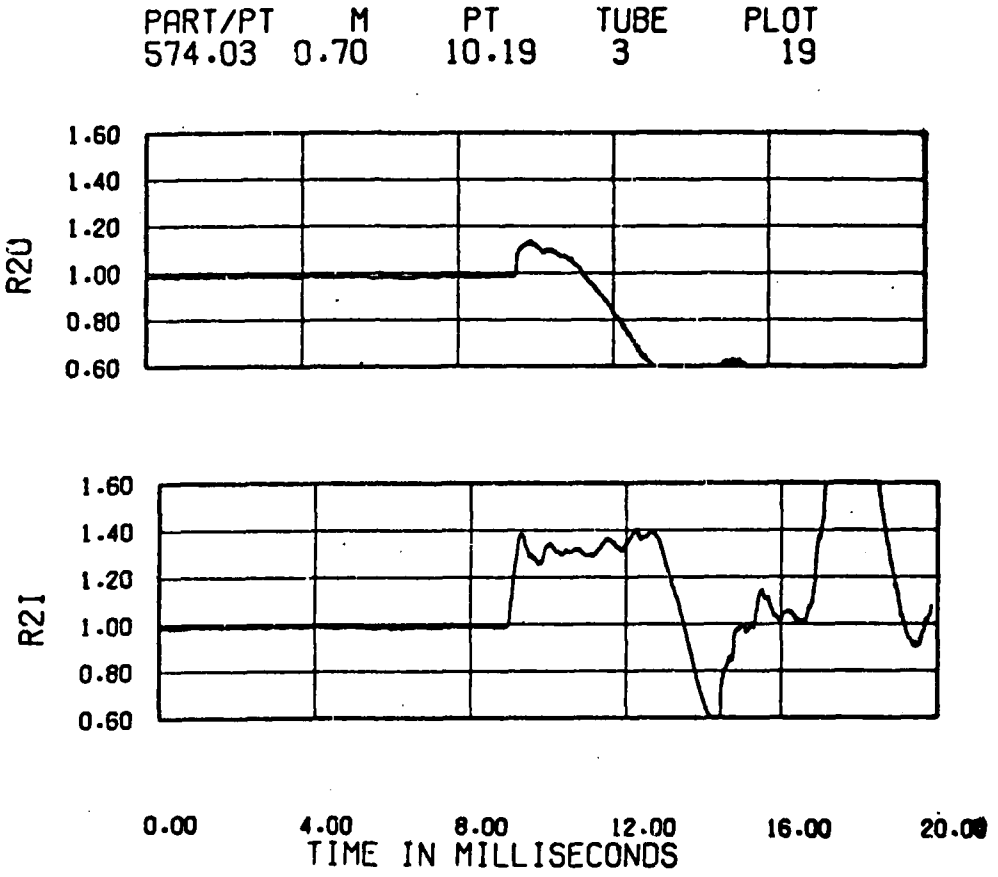

(e) Run 10, Δp_s=4.4 psi (nom), ϕ=97 deg.

Figure.2.5. Concluded.

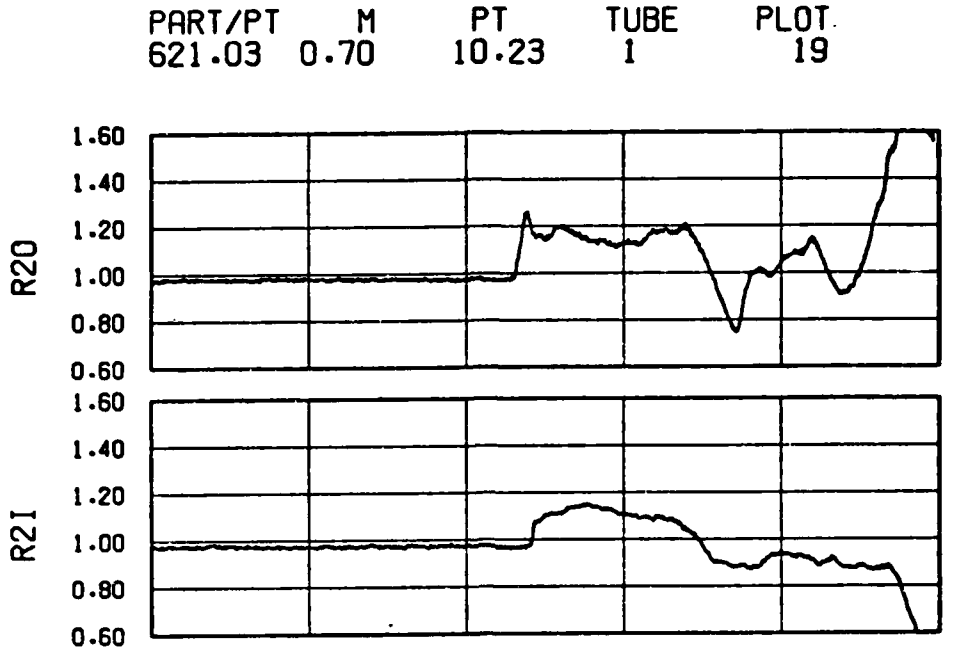

(a) Run 11, Δp_s=3.0 psi (nom), ϕ=84 deg.

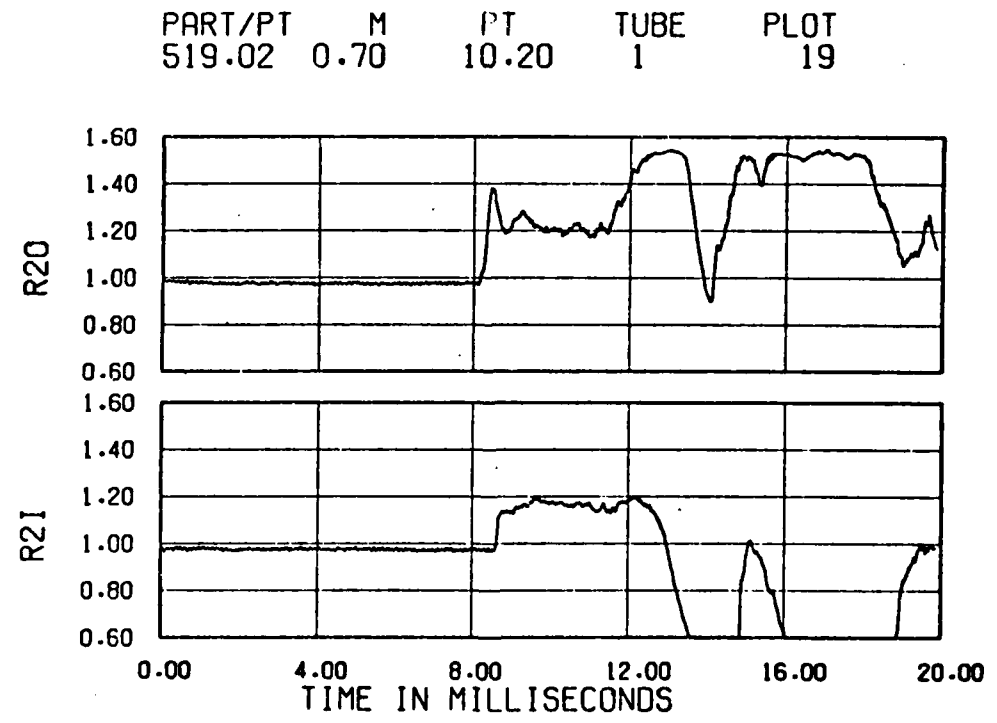

(b) Run 12, Δp_s=3.8 psi (nom), ϕ=88 deg.

Figure 2.6. Engine-face mean total pressures. Mach 0.70, W2R=350 lb/s (nom).

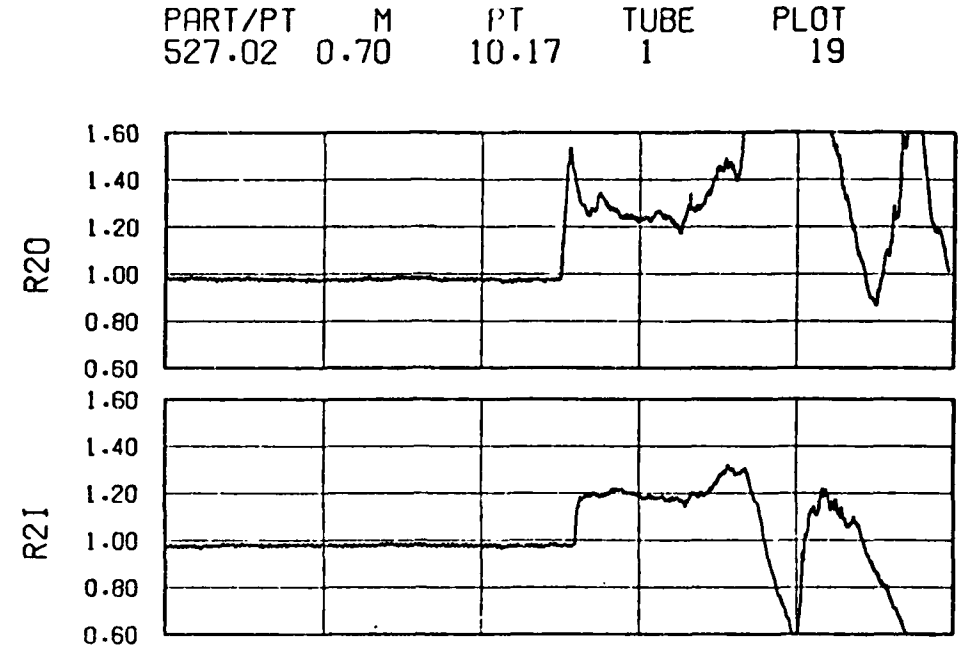

(c) Run 13, Δp_s=4.8 psi (nom), ϕ=78 deg.

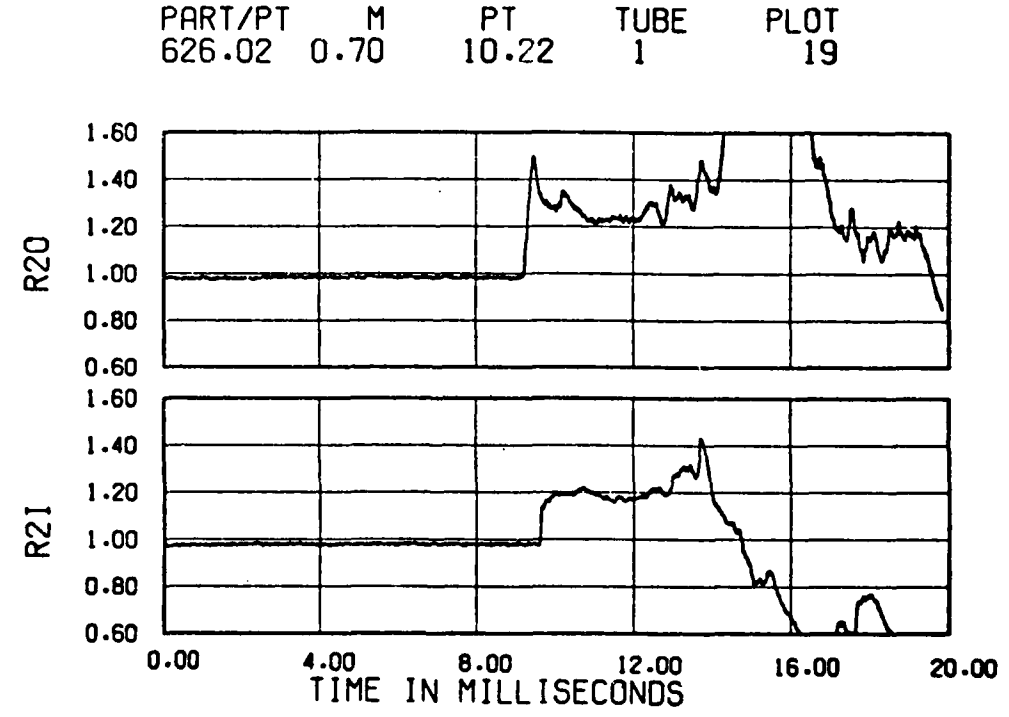

(d) Run 14, Δp_s=4.8 psi (nom), ϕ=78 deg.

Figure 2.6. Continued.

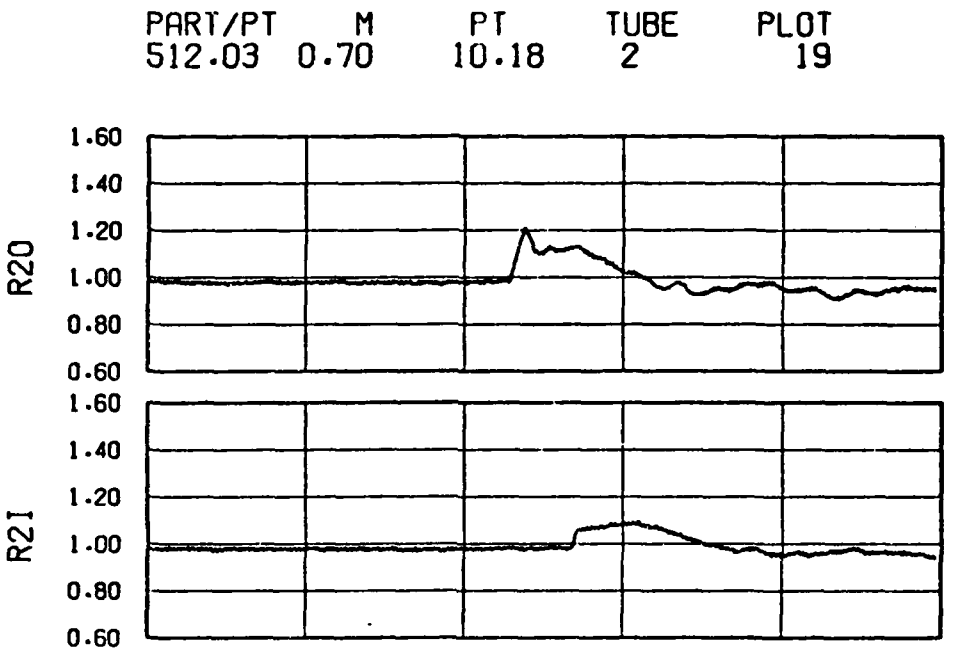

(e) Run 15, Δp_s=2.8 psi (nom), ϕ=103 deg.

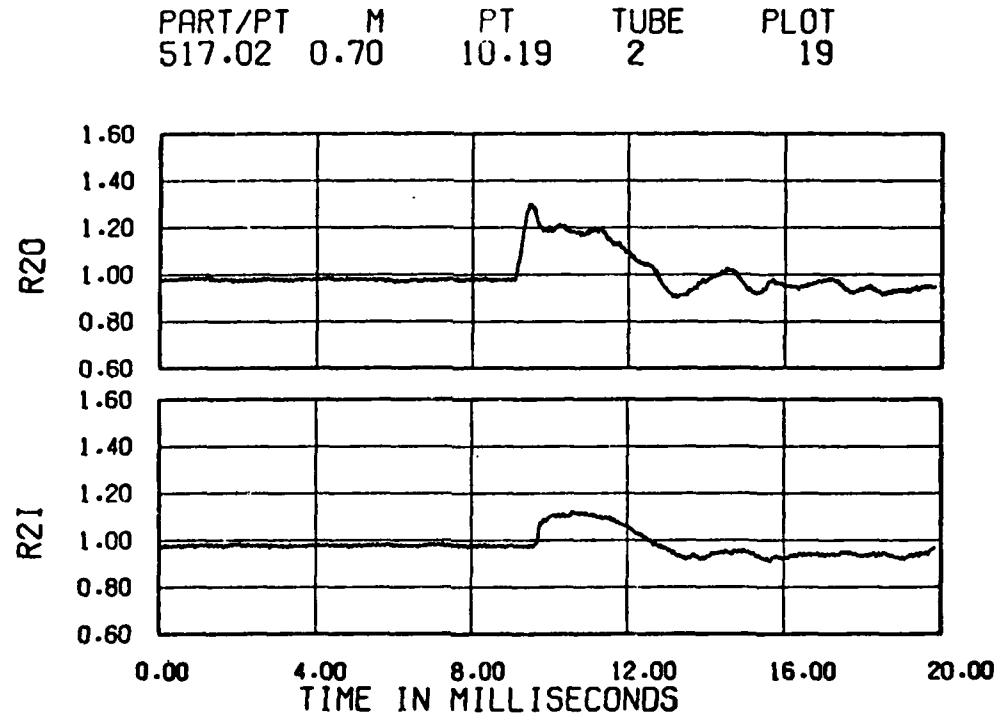

(f) Run 16, Δp_s=3.8 psi (nom), ϕ=103 deg.

Figure 2.6. Continued.

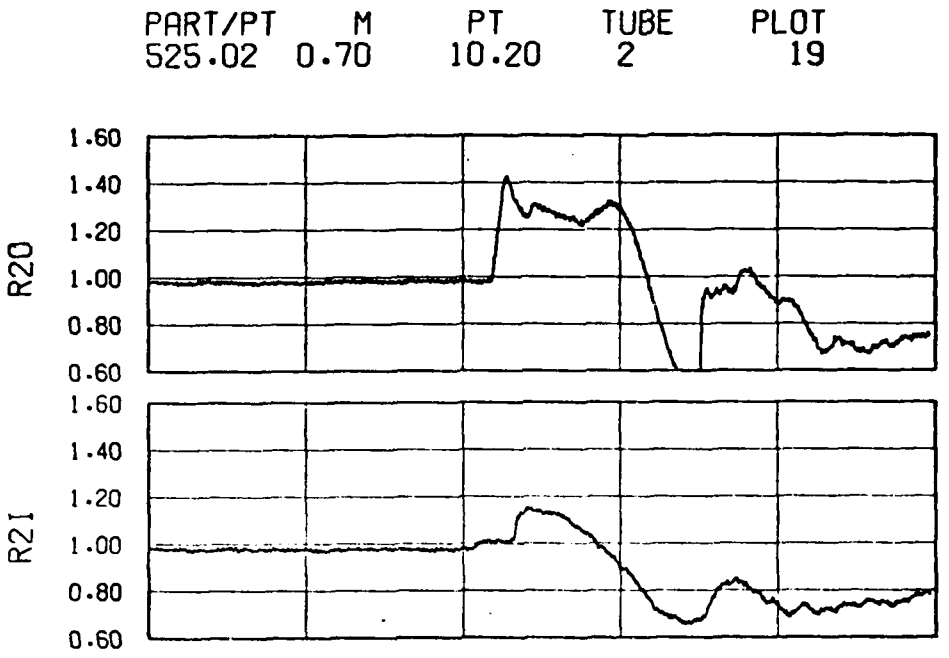

(g) Run 17, Δp_s=5.0 psi (nom), ϕ=100 deg.

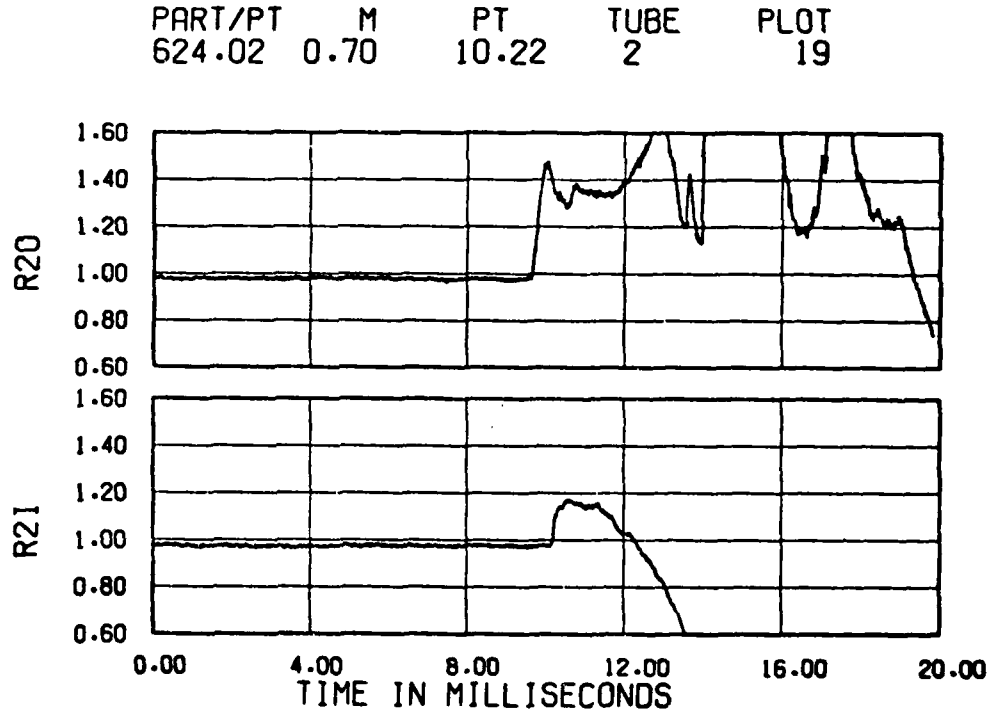

(h) Run 18, Δp_s=5.2 psi (nom), ϕ=99 deg.

Figure 2.6. Continued.

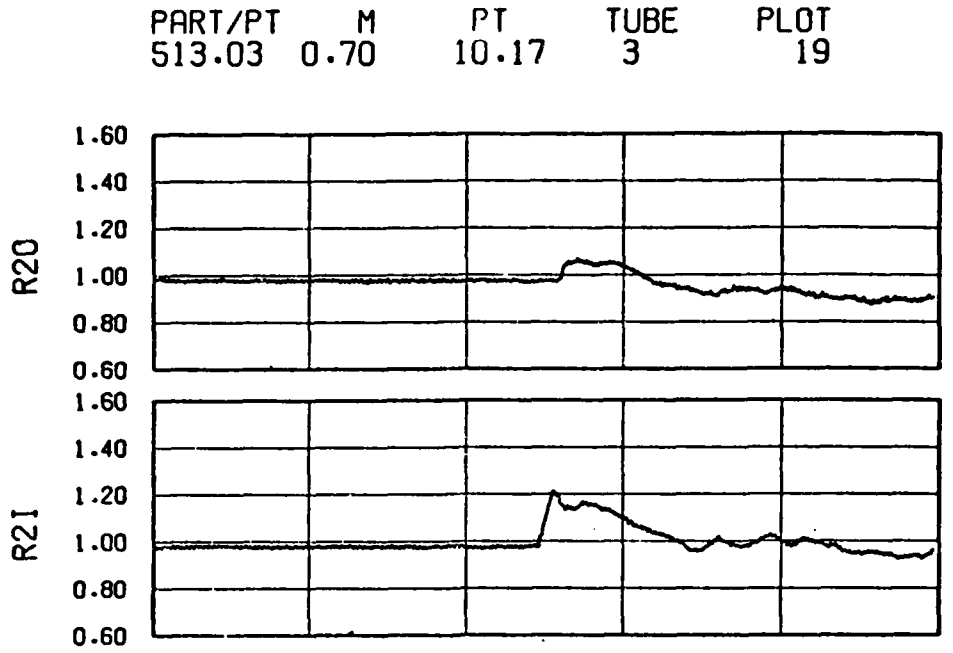

(i) Run 19, Δp_s=3.0 psi (nom), ϕ=102 deg.

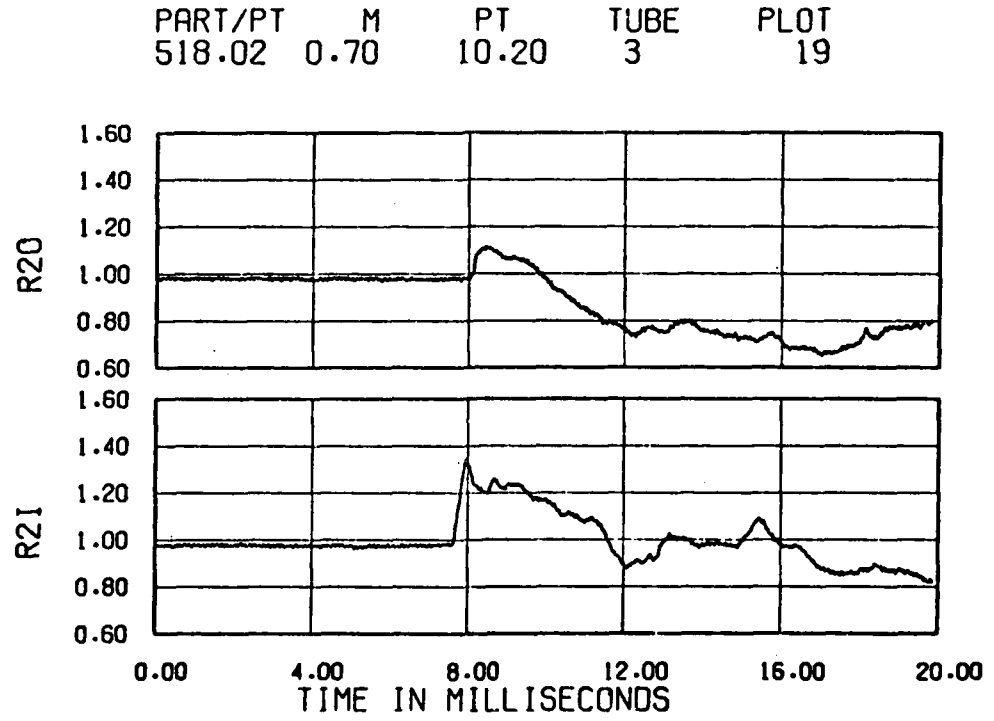

(j) Run 20, Δp_s=4.2 psi (nom), ϕ=99 deg.

Figure 2.6. Continued.

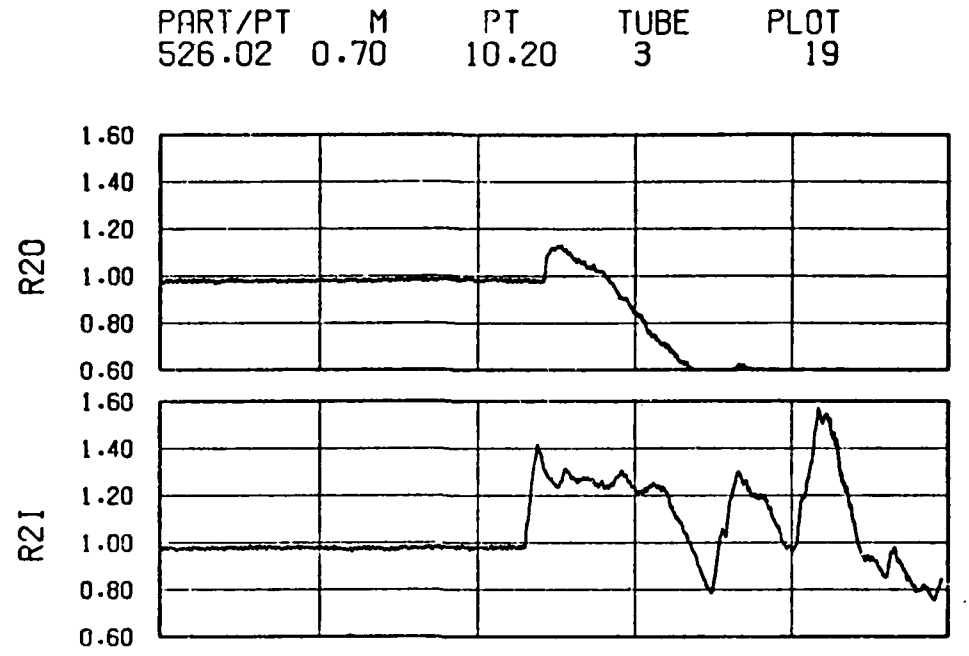

(k) Run 21, Δp_s=4.8 psi (nom), ϕ=98 deg.

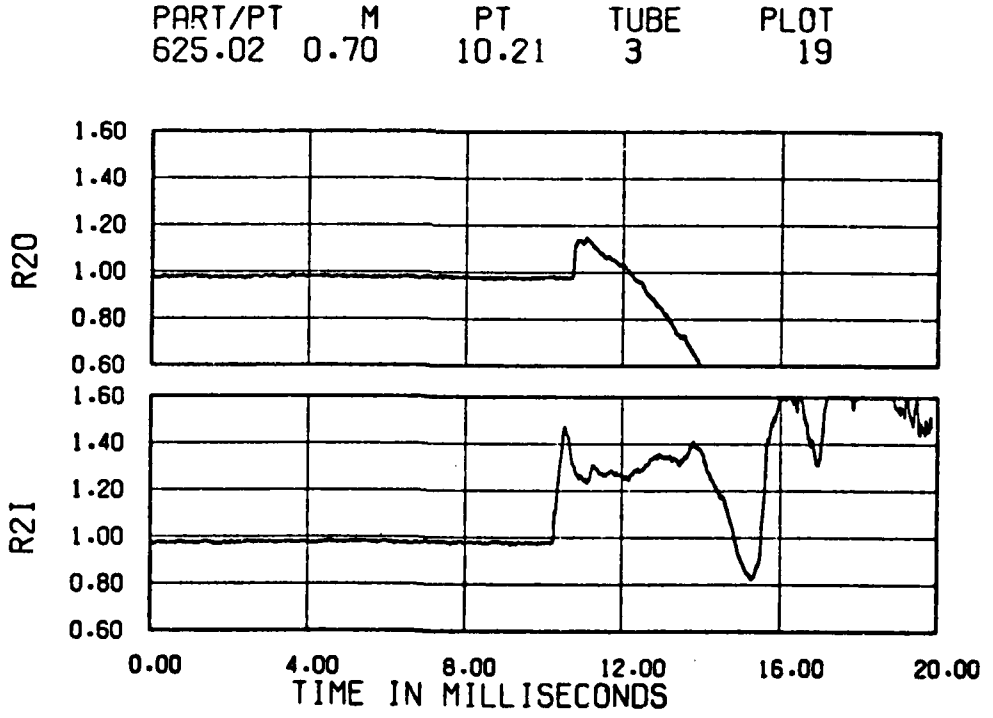

(ℓ) Run 22, Δp_s=5.6 psi (nom), ϕ=92 deg.

Figure 2.6. Concluded.

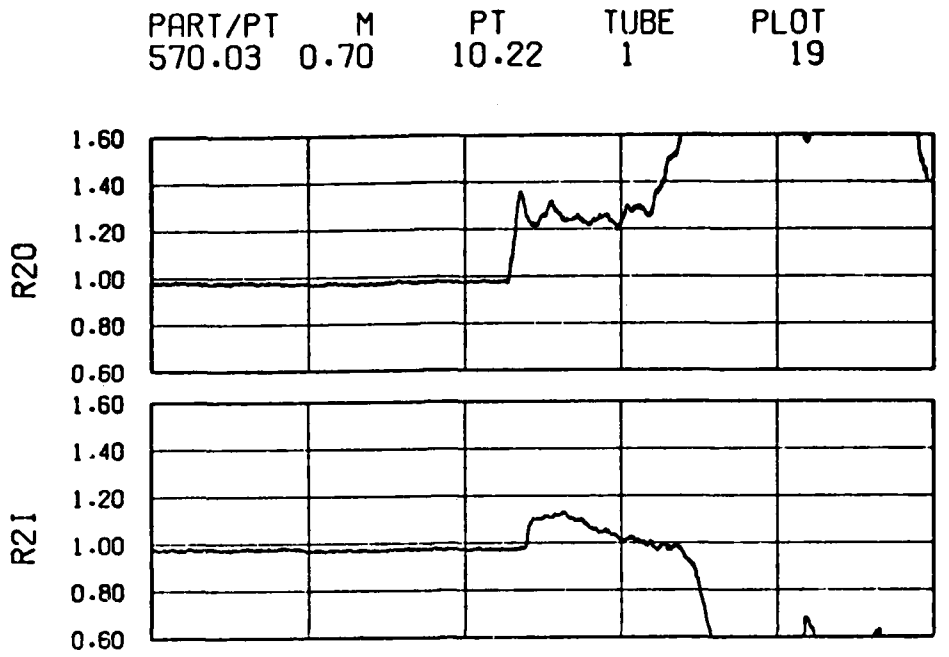

(a) Run 23, yaw angle = +5.0 deg, Δp_s=3.6 psi (nom), ϕ=87 deg.

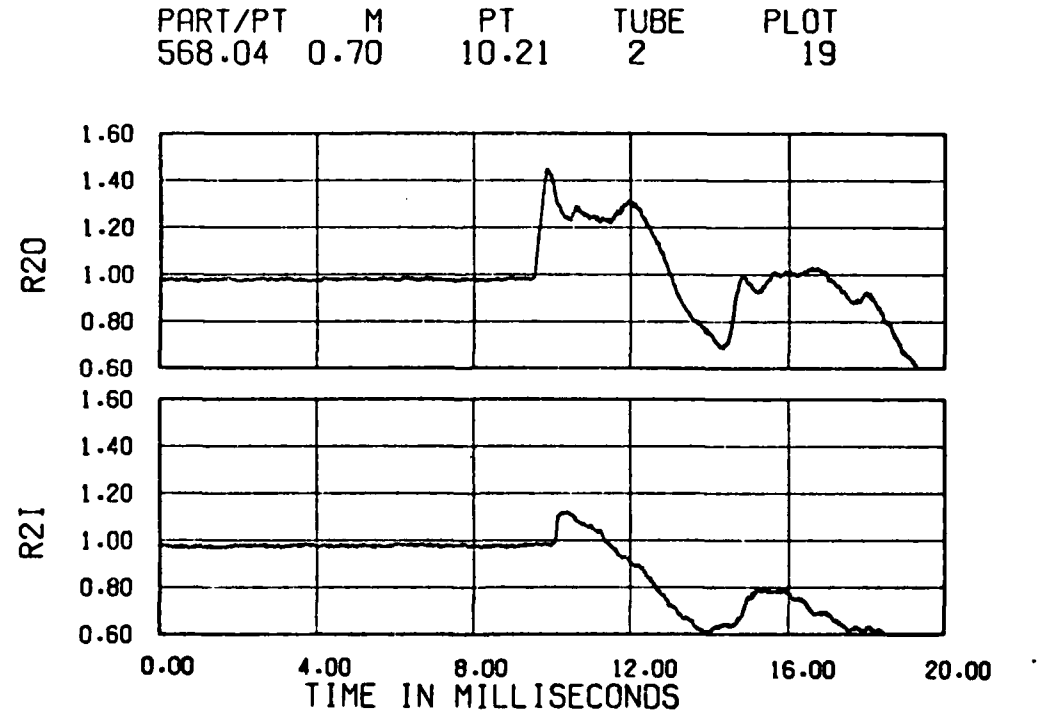

(b) Run 24, yaw angle = +5.0 deg, Δp_s=5.8 psi (nom), ϕ=103 deg.

Figure 2.7. Engine-face mean total pressures.
Mach 0.70, W2R=350 lb/s (nom).

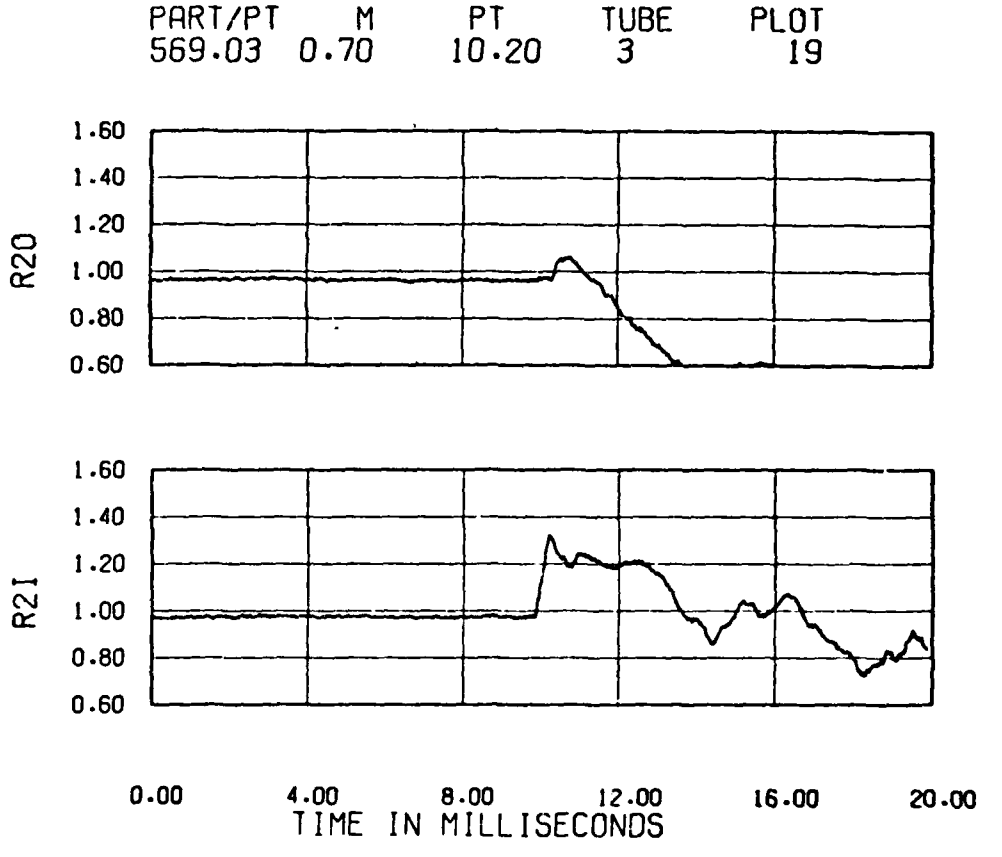

(c) Run 25, yaw angle = -5.0 deg, Δp_s=4.2 psi (nom), ϕ=105 deg.

Figure 2.7. Concluded.

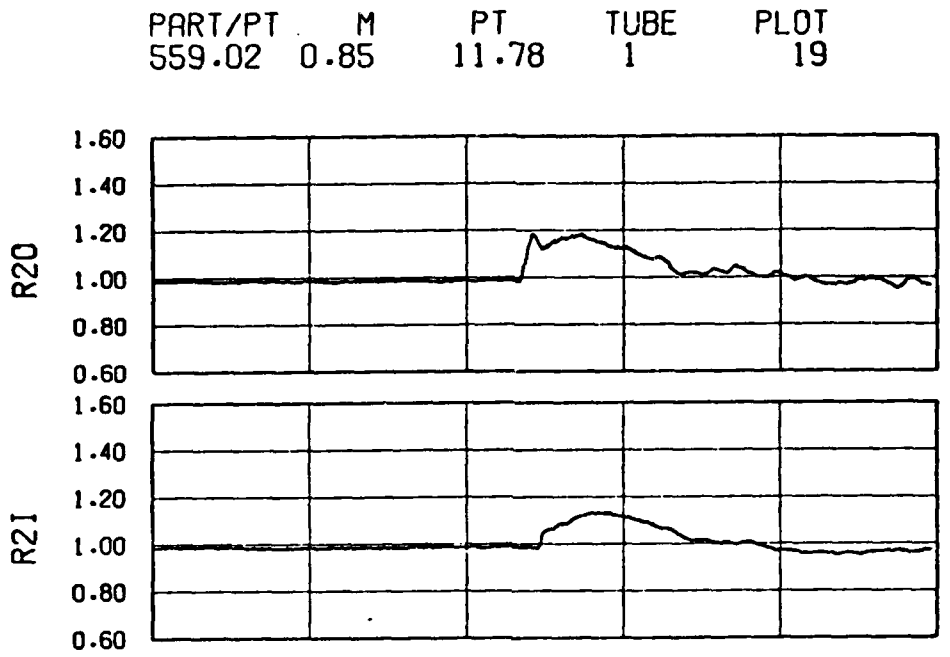

(a) Run 26, Δp_s=2.2 psi (nom), ϕ=89 deg.

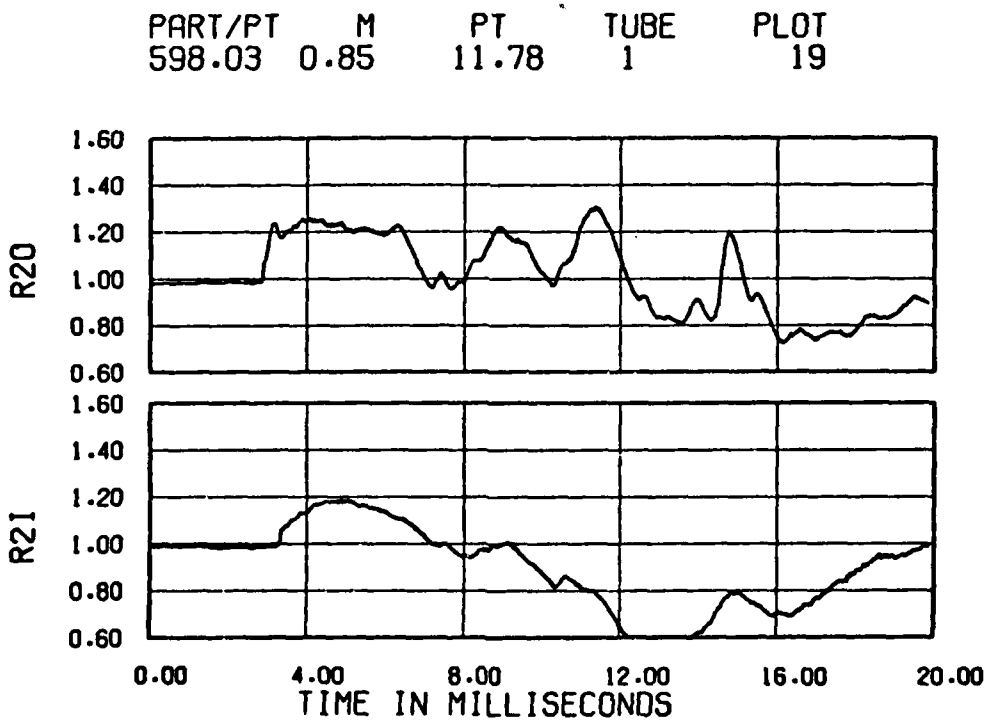

(b) Run 27, Δp_s=3.0 psi (nom), ϕ=85 deg.

Figure 2.8. Engine-face mean total pressures. Mach 0.85, W2R=300 lb/s (nom).

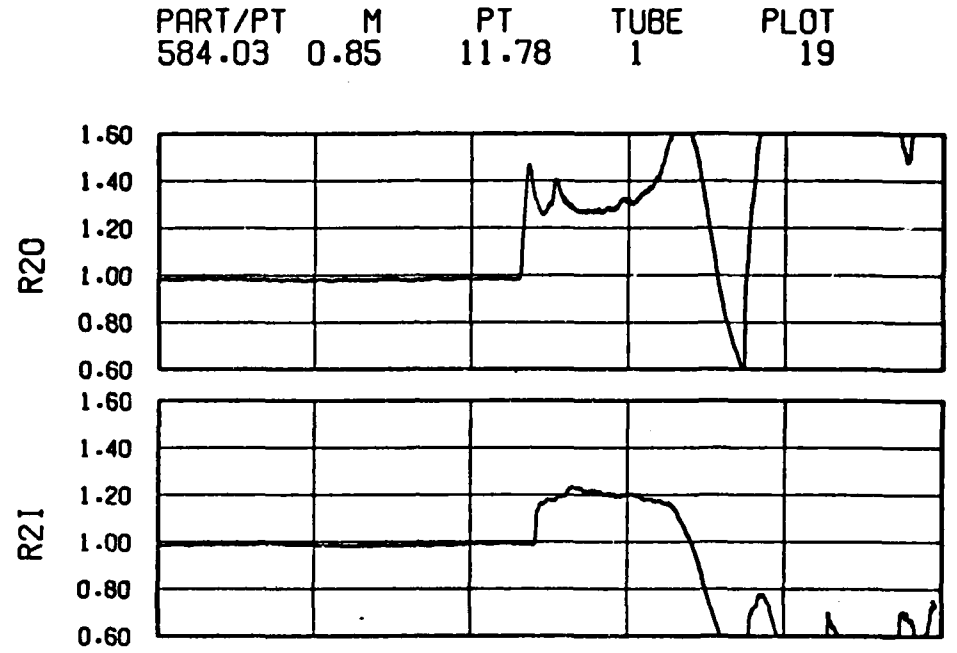

(c) Run 28, Δp_s=5.0 psi (nom), ϕ=82 deg.

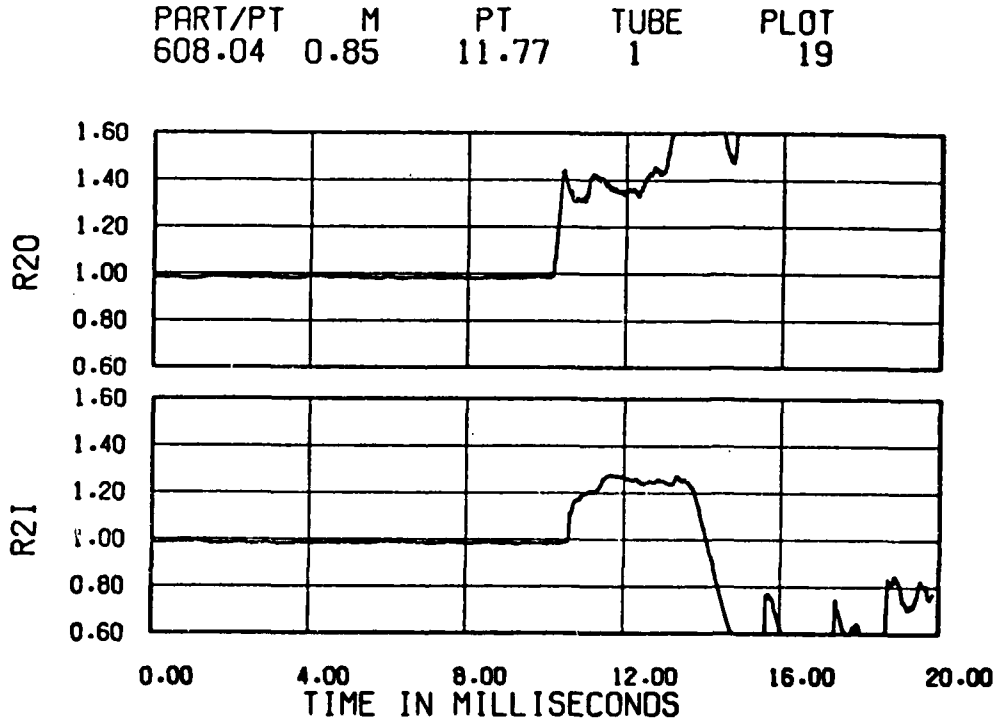

(d) Run 29, Δp_s=4.4 psi (nom), ϕ=82 deg.

Figure 2.8.(Continued.)

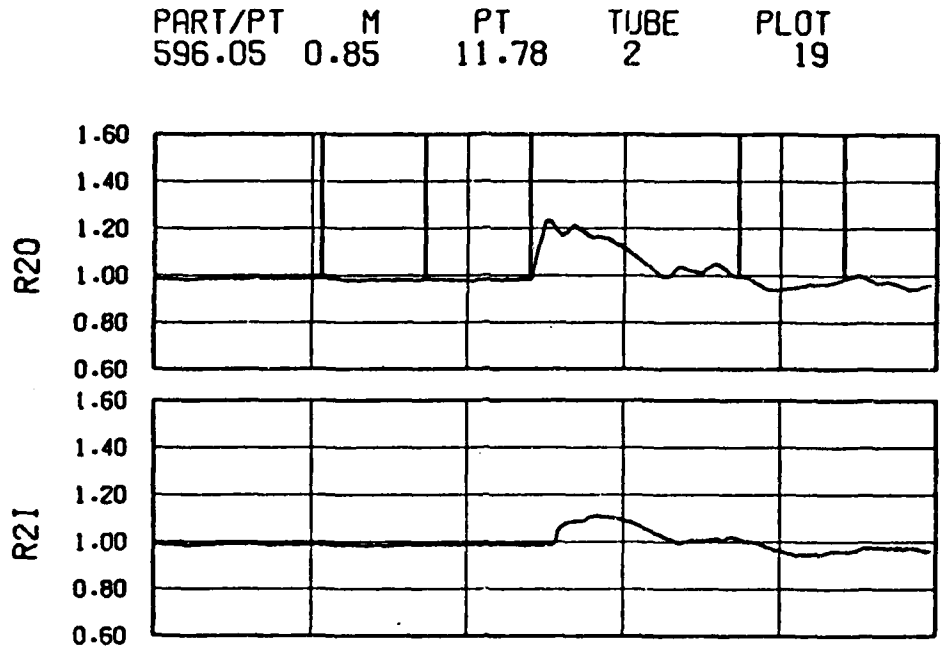

(e) Run 31, Δp_s=3.8 psi (nom), ϕ=108 deg.

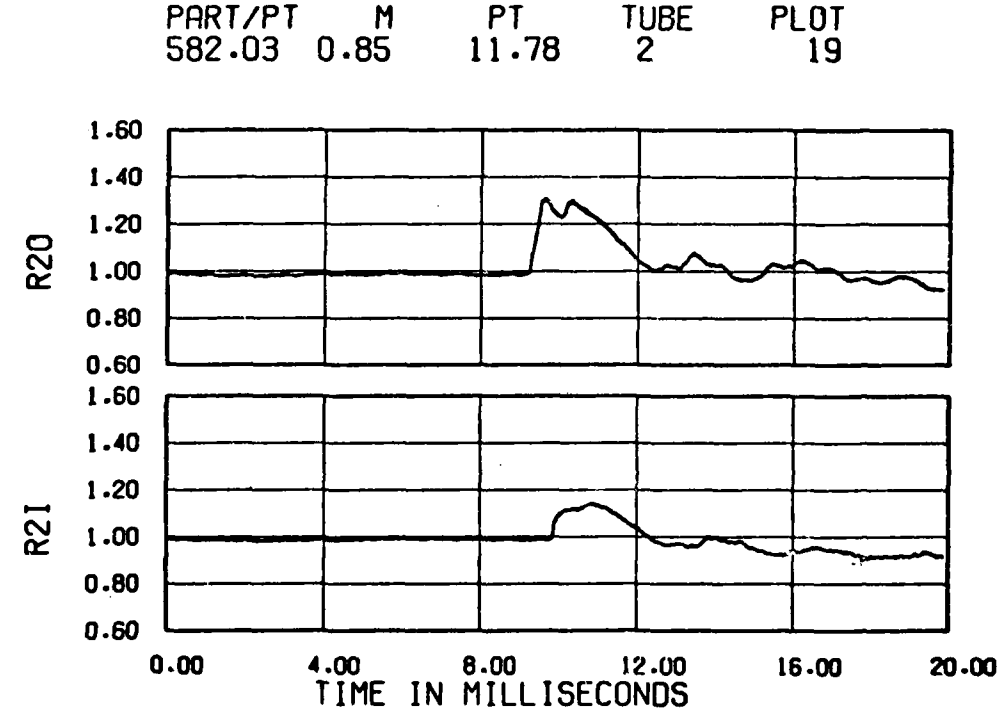

(f) Run 32, Δp_s=4.4 psi (nom), ϕ=105 deg.

Figure 2.8. Continued.

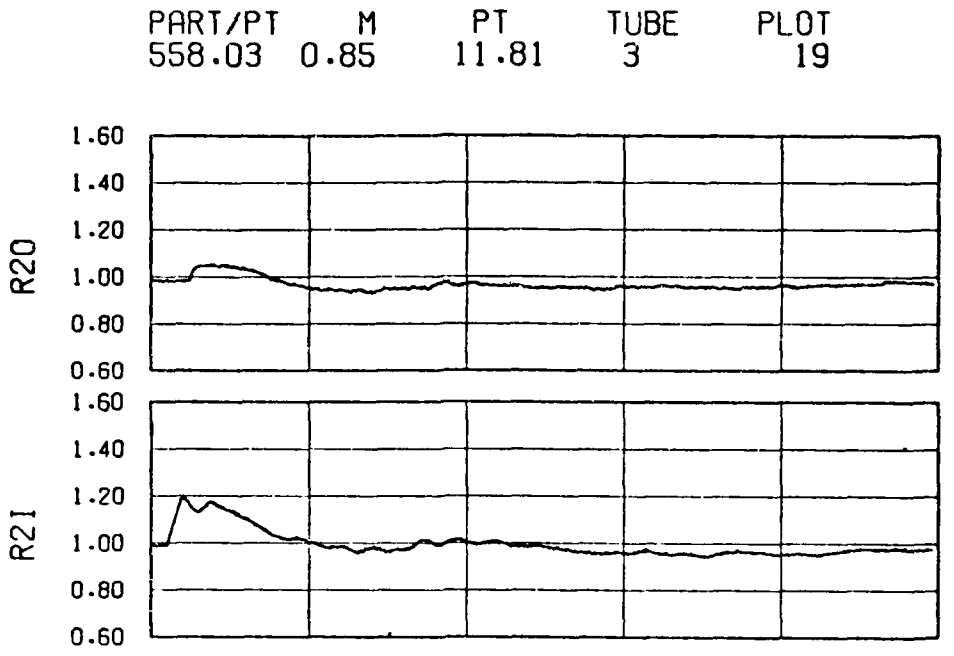

(g) Run 34, Δp_s=2 + psi (nom).

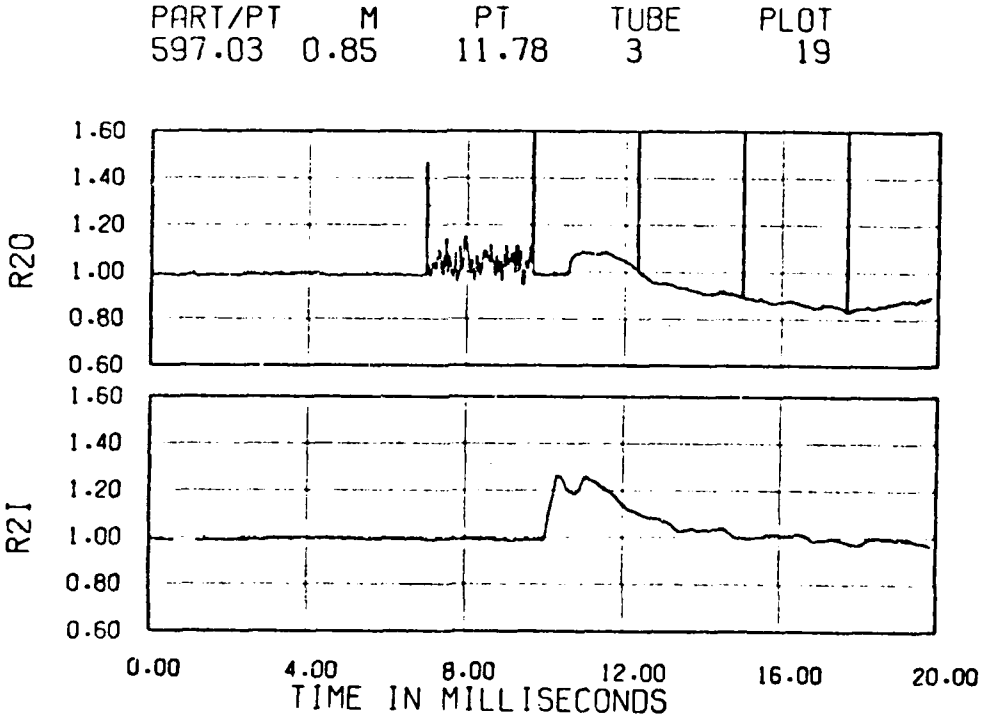

(h) Run 35, Δp_s=4.0 psi (nom), ϕ=104 deg.

Figure 2.8. Continued.

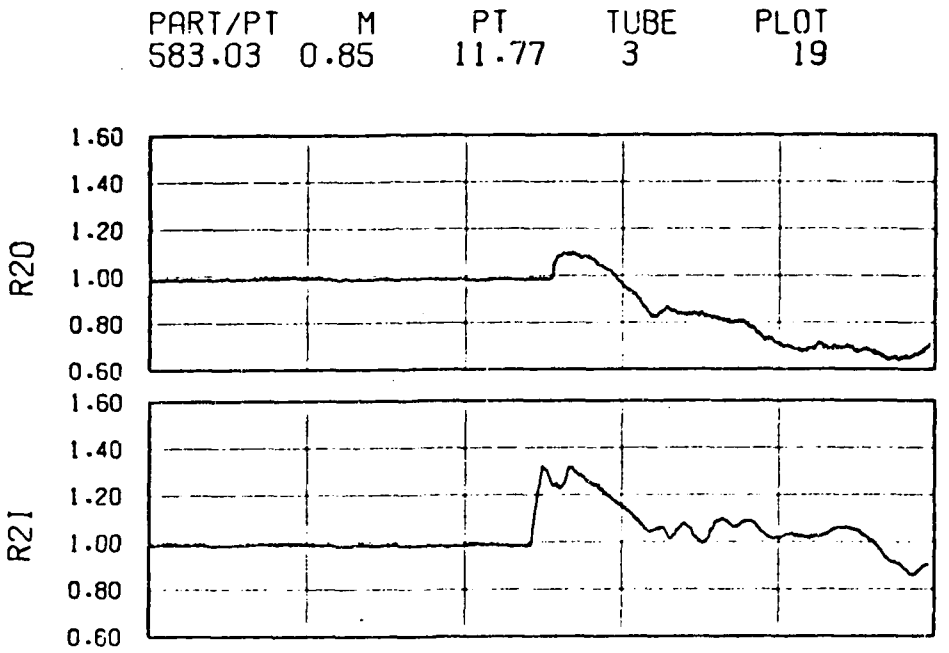

(i) Run 36, Δp_s=4.4 psi (nom), ϕ=102 deg.

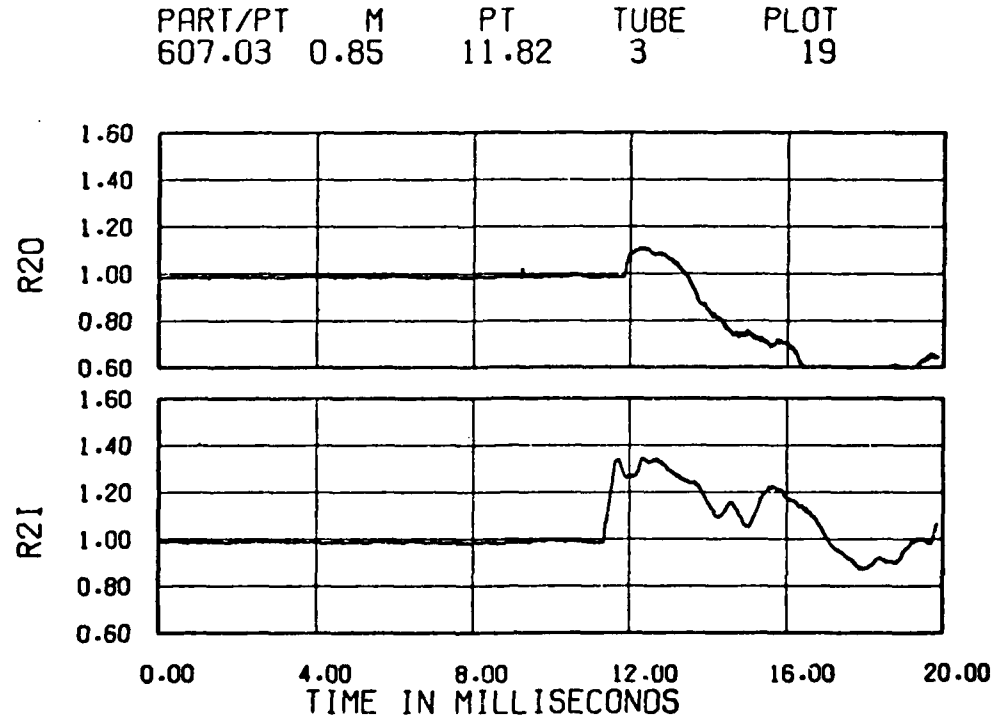

(j) Run 37, Δp_s=4.8 psi (nom), ϕ=103 deg.

Figure 2.8. Concluded.

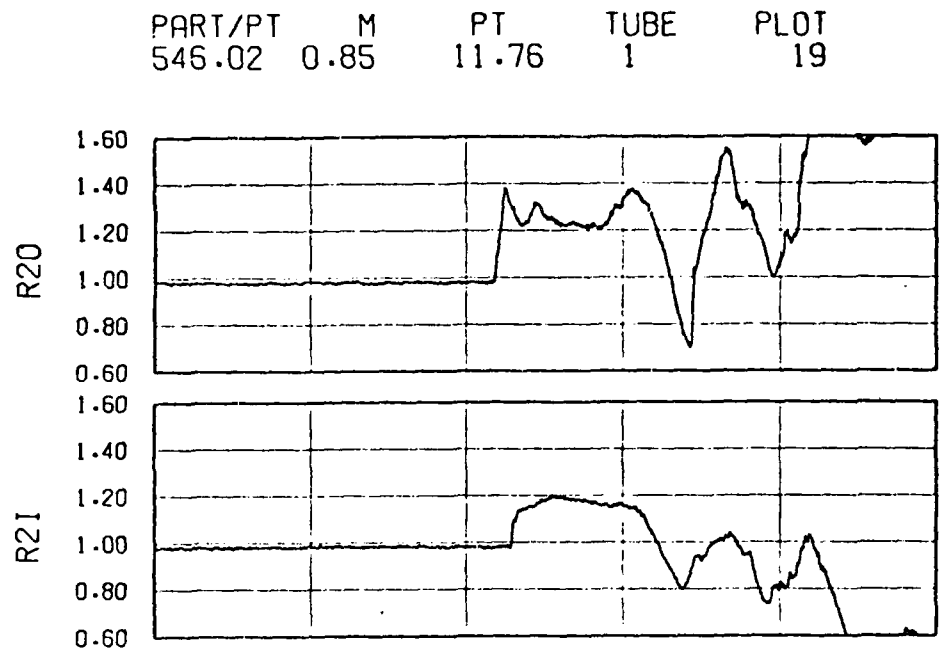

(a) Run 38, Δp_s=3.6 psi (nom), ϕ=84 deg.

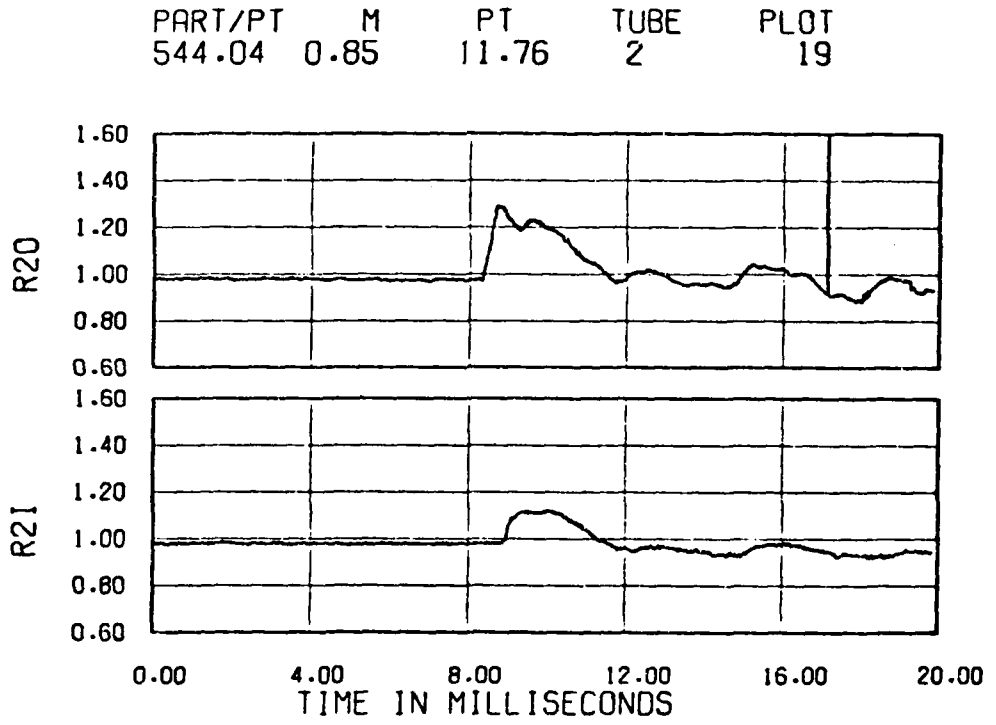

(b) Run 39, Δp_s=4.0 psi (nom), ϕ=107 deg.

Figure 2.9. Engine-face mean total pressures. Mach 0.85, W2R=350 lb/s (nom).

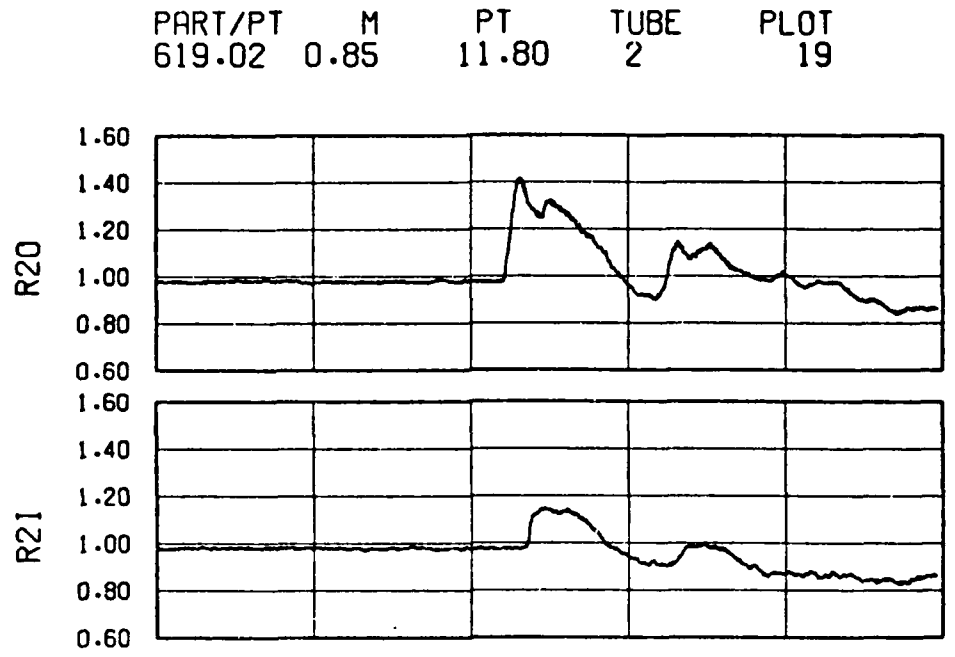

(c) Run 40, Δp_s=5.8 psi (nom), ϕ=110 deg.

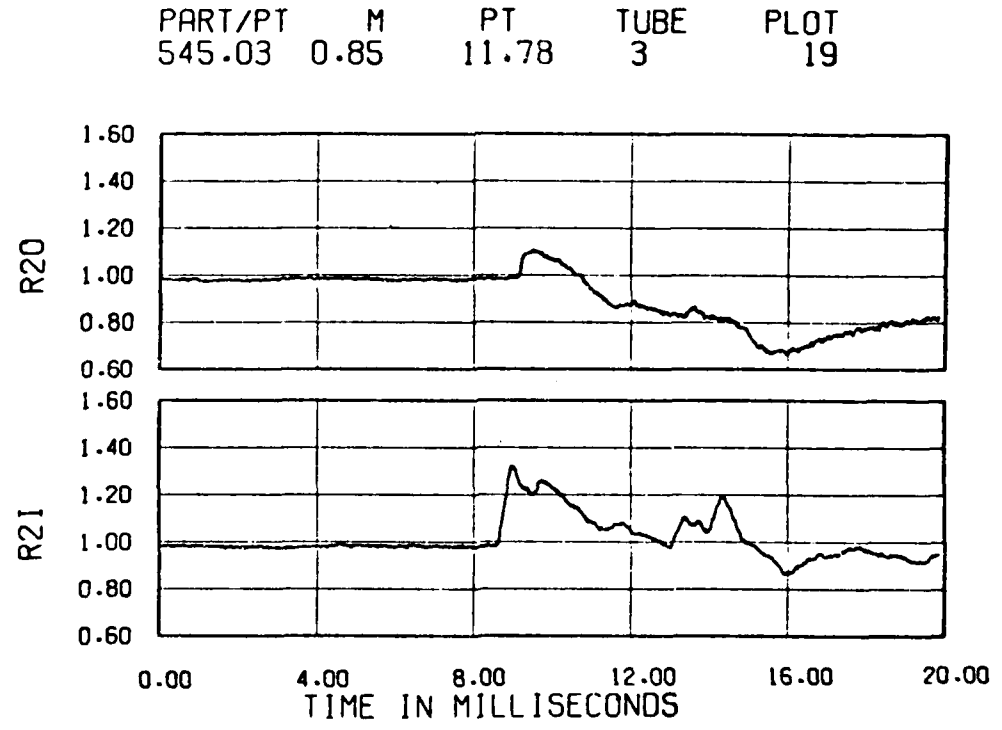

(d) Run 41, Δp_s=4.4 psi (nom), ϕ=105 deg.

Figure 2.9. Continued.

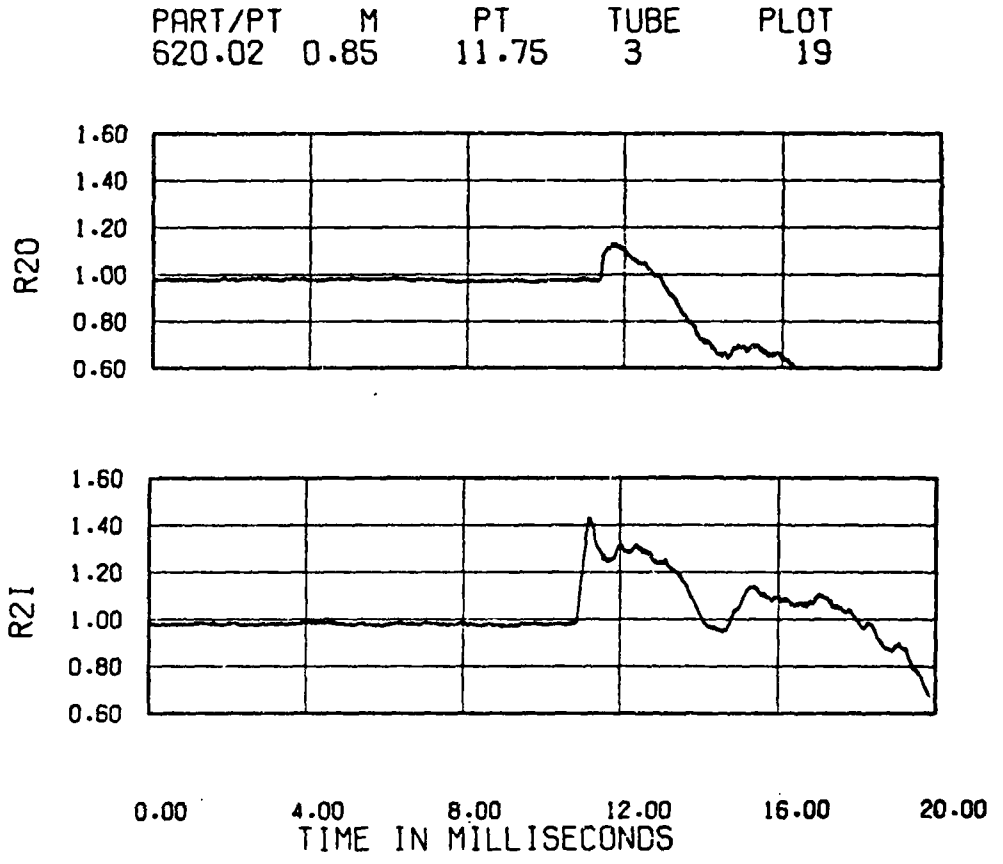

(e) Run 42, Δp_s=5.6 psi (nom), ϕ=100 deg.

Figure 2.9. Concluded.

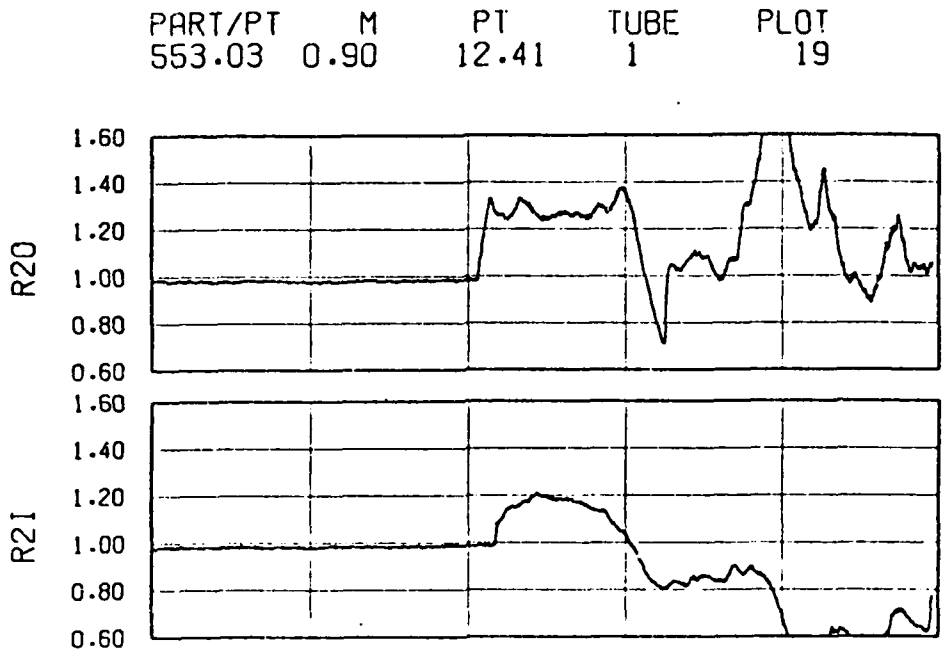

(a) Run 43, Δp_s=3.0 psi (nom), ϕ=86 deg.

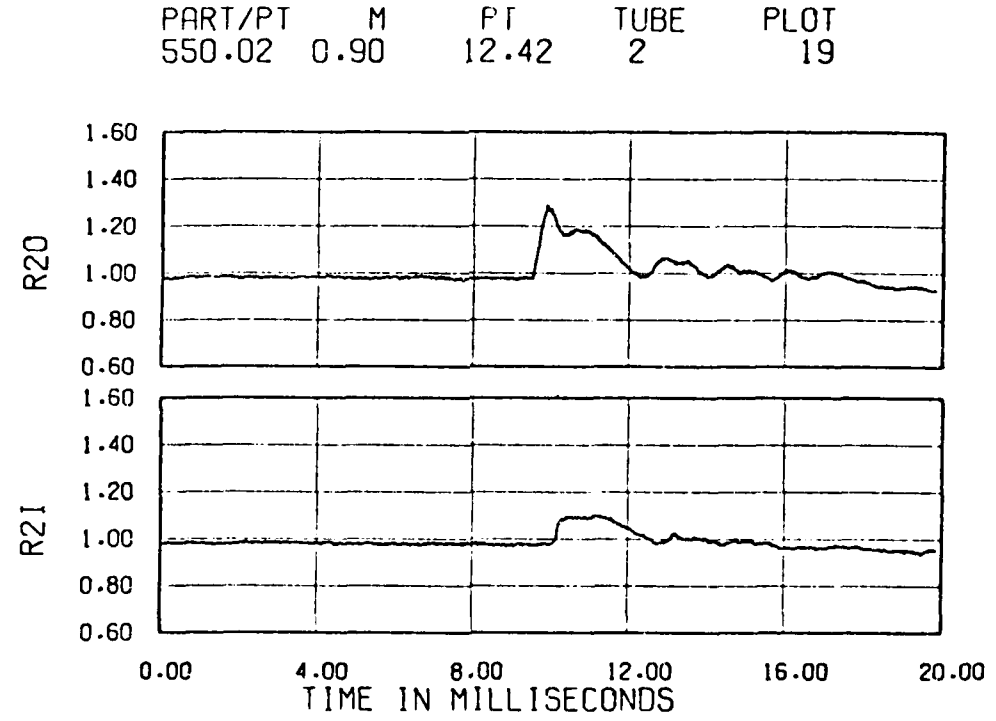

(b) Run 44, Δp_s=4.0 psi (nom), ϕ=107 deg.

Figure 2.10. Engine-face mean total pressures. Mach 0.90, W2R=350 lb/s (nom).

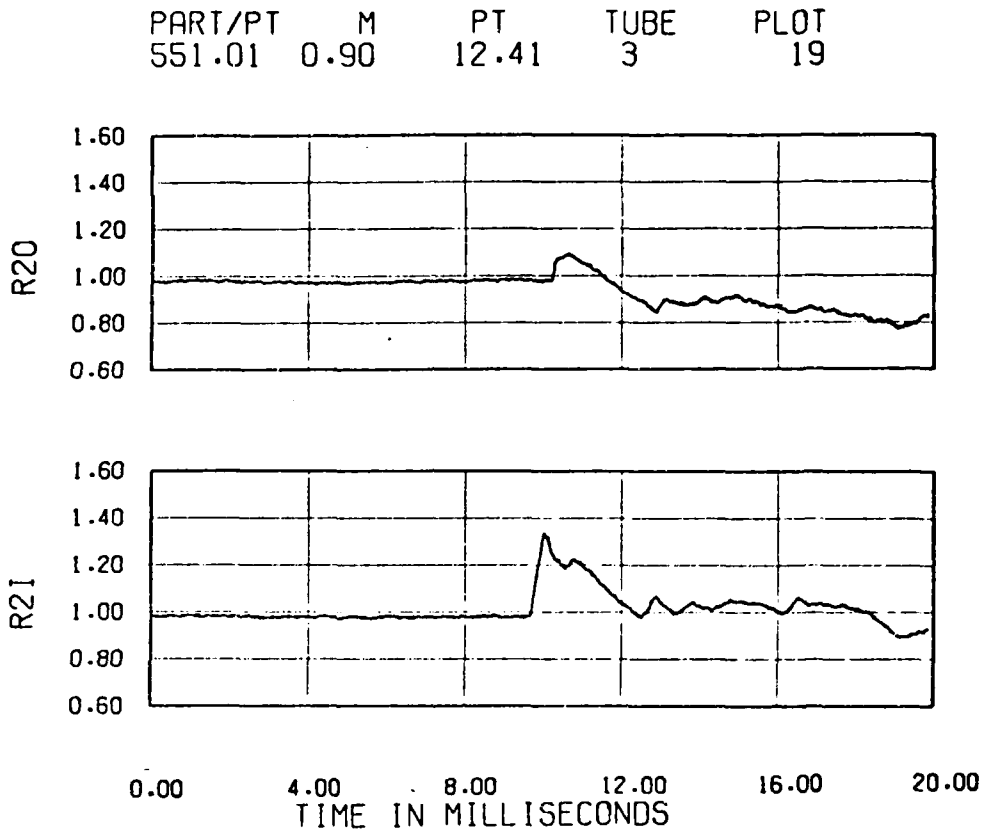

(c) Run 45, Δp_s=4.2 psi (nom), ϕ=105 deg.

Figure 2.10. Concluded.

SECTION 3
GENERAL FEATURES OF BLAST AND OPERATIONAL EFFECTS ON ENGINE-FACE MEAN TOTAL-PRESSURE SIGNATURE

The effect of the blast parameters and operational parameters on the mean total pressure at the engine face is examined in this section. The blast parameters are the shock overpressure of the incident shock, Δp_s, and its intercept angle, ϕ, to the inlet. The operational parameters are the inlet full-scale reduced weight flow, W2R, and wind tunnel Mach number, M.

The records of the reduced mean total pressure at the engine face are grouped in Figures 3.1 to 3.56 according to test conditions (Δp_s, ϕ, W2R, M) to show the effect of each variable separately. The results are presented separately for the blastward and leeward inlets.

3-1 EFFECT OF BLAST SHOCK OVERPRESSURE.

The effect of the blast shock overpressure, Δp_s, on the RTI and RTO records is shown in Figures 3.1 to 3.7 for the blastward inlet and Figures 3.8 to 3.14 for the leeward inlet.

For the blastward inlet, the effect of increasing the shock overpressure is to increase the magnitude of the first peak and to make the shape of the peak a sharper spike as for example Figure 3.1. The magnitude of the first peak will be examined quantitatively in Section 4. The second peak, which is produced by the reflection from the control vane throttle simulating the engine, steepens up in rise rate with greater shock overpressure. The height of the second peak, referenced to its initial point of rise, essentially does not vary with shock overpressure.

The variation of the engine-face total pressure following the second peak is generally independent of the shock overpressure until the test is terminated by the arrival of the cold driver gas from the shock tube. The cold gas appears to arrive in Figure 3.1b at about

11.7 ms (3.4 ms after shock arrival) and in Figure 3.1c at about 13.2 ms (3.2 ms after shock arrival). The most obvious exception to this independence of shock overpressure is shown in Figure 3.5 at Mach 0.70, 350 lb/s full-scale weight flow for firings from Shock Tube 3. This decay in RTI following the second peak for the two lowest overpressure tests, Runs 19 and 20, is attributed to a decay in the blast overpressure.

The mean engine-face total pressure records for the leeward inlet, Figures 3.8 to 3.14, have a characteristically different signature from those for the blastward inlet. These records for the leeward inlet show that the initial shock jump is followed generally by a continuing rise. For example, in Figure 3.8a the total pressure following shock arrival rises to a peak in about 1 1/2 ms. The first part of the rise, which reaches a plateau in about 1/4 ms, is attributed to post diffraction effects of the blast wave around the splitter. The climb from the plateau to the peak is attributed to reflection effects from the choked throttle, that simulates the engine.

The magnitude of the initial (shock) jump in reduced total pressure for the leeward inlet, Figures 3.8-3.14 increases with increasing shock overpressure. For the seven firings from Shock Tube 1, Figures 3.8-3.9, the shape of the pressure records for the 3-ms test period is pretty much the same. The wave reflected from the throttle always has the relatively slow rise characteristic for the leeward inlet.

The leeward inlet records for firings from Shock Tube 2, Figures 3.10-3.11, are similar to those for Shock Tube 1 except that the mean total pressure falls off significantly after about a millisecond, depending upon the shock overpressure. This fall off is attributed to the development of large flow nonuniformity and possible separation within the inlet due to the large blast-induced sideslip angles. For Shock Tube 3, Figures 3.12-3.14, the mean total pressure also falls off rapidly for shock overpressures of 4 psi or more, but in these cases the blast overpressure at the inlet exhibits a similar decay, so the possibility of separation being present cannot be assessed.

3-2 EFFECT OF BLAST INTERCEPT ANGLE.

The effect of the blast shock intercept angle, ϕ, on the RTI and RTO records is presented in Figures 3.15-3.29. Firings from Shock Tube 1 had the smallest intercept angles (most head-on). Firings from Shock Tubes 2 and 3 produced intercepts with about the same angles (from head-on), except that Shock Tube 3 fired from the opposite side of the aircraft model from the other two.

For the blastward inlet, Figures 3.15-3.22, the first peak in the reduced mean total pressure has a sharper spike for the more head-on firings (Shock Tube 1). The second peak, from the reflection from the throttle (simulated engine), in all cases appears to be larger for more head-on interception. From firings from Shock Tubes 2 and 3, a significant fall-off in mean total pressure is sometimes evident after about one millisecond (Figures 3.16, 3.17, 3.19, 3.21, 3.22), but in all cases the blast overpressure also decays similarly, so the decay cannot be attributed simply to the intercept angle.

For the leeward inlet, Figures 3.23-3.29, the initial shock jump (the first vertical rise) is generally greater for the smaller intercept angle (Tube 1). Not much can be said about the effect of the intercept angle for later times here because of blast decay at the inlet for Tubes 2 and 3 in these runs, with the exception of Runs 17 and 21, Figure 3.25. In the latter cases (Mach 0.70, 350 lb/s, 4.8-5.0 psi) there is a very marked effect of the intercept angle on the mean total pressure, which is attributed to separation at the large blast-induced angle of sideslip that results.

3-3 EFFECT OF WEIGHT FLOW.

The effect of the full-scale weight flow, W2R, on the RTI and RTO records is shown in Figures 3.30 to 3.37 for the blastward inlet and in Figures 3.38 to 3.45 for the leeward inlet.

For the blastward inlet the higher weight flow results sometimes in a sharper spiked first peak and nearly always in a weaker second rise, from the throttle reflection. The magnitude of the first

peak does not appear to correlate well with flow rate, but it generally decays further before the apparent arrival of the throttle-reflected wave.

For the leeward inlet, Figures 3.38-3.45, the initial shock jump is frequently somewhat greater for the higher weight flow. The peak of the reflected wave, in the few cases where it can be observed, because of the absence of the effect of rapid blast decay at the inlet, Figures 3.38, 3.39, it is essentially independent of the flow rate. For one case, Figure 3.41 (Mach 0.70, Shock Tube 2, Δp_s=5.0 psi), the flow rather clearly appears to show the effects of separation within the inlet. The case with the greater flow rate (Run 17) has a less evident and weaker throttle reflection and a fall off that starts sooner.

3-4 EFFECT OF MACH NUMBER.

The effect of Mach number, M, on the RTI and RTO records is presented in Figures 3.46 to 3.51 for the blastward inlet and Figures 3.52 to 3.56 for the leeward inlet.

For the blastward inlet, there is no significant effect of Mach number on the first peak, either during the rise or decay portion. Regarding the later period, there were only two conditions where there were enough runs not having a large decay in the external blast wave, Figures 3.46 and 3.47. There is no clear effect of Mach number on the record after the first peak. In particular, there is no regular effect on the second peak, from the throttle reflection.

For the leeward inlet, there is no apparent effect of Mach number on the first peak either. Again, only two conditions had non-decaying blast waves, enabling examination of the later record, Figures 3.52 and 3.53, and neither of these show any discernable effect of Mach number.

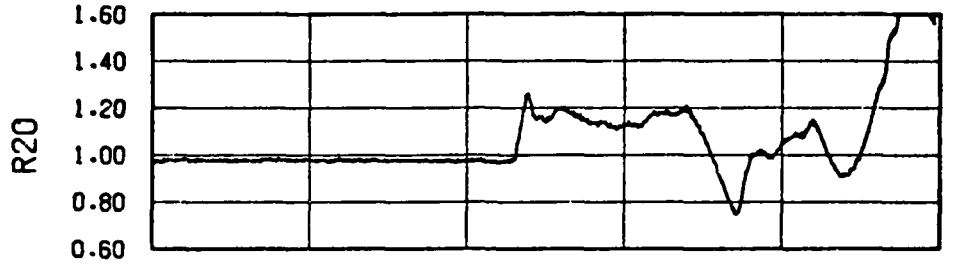

a. Run 11, Δp_s = 3.0 psi

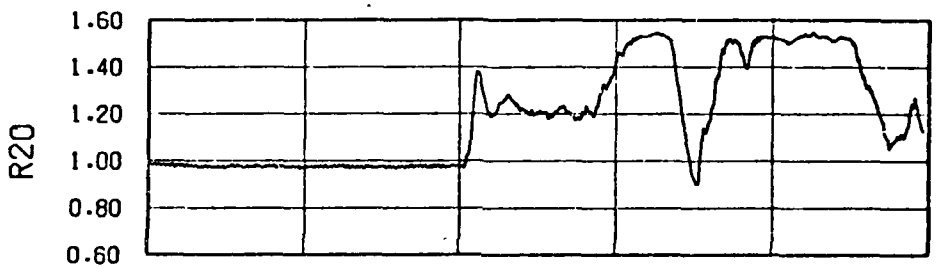

b. Run 12, Δp_s = 3.8 psi

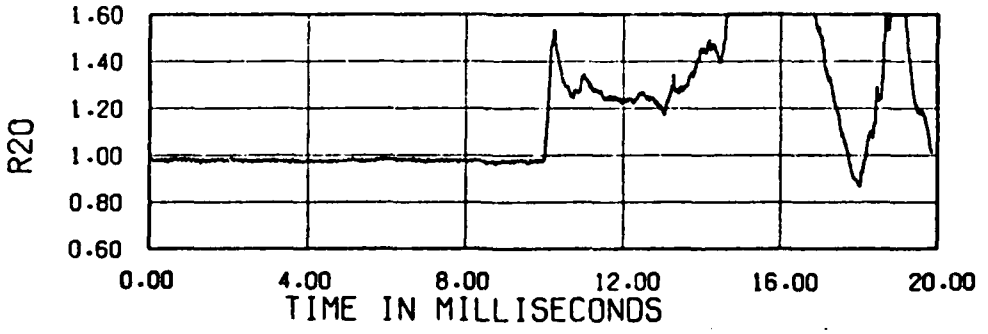

c. Run 13, Δp_s = 4.8 psi

Figure 3.1. Effect of blast shock overpressure on engine-face mean total pressure in blastward inlet at Mach 0.70. Weight flow 350 lb/s (nom). Shock Tube 1.

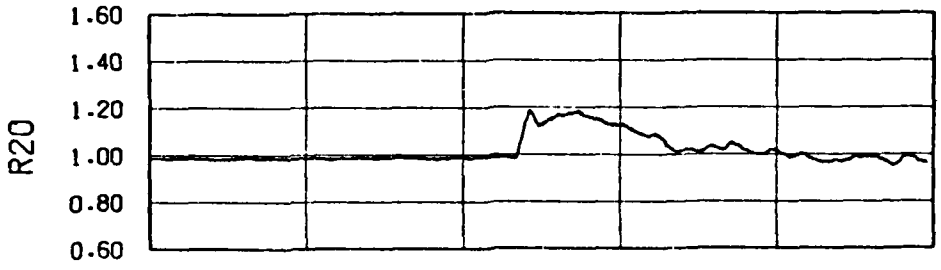

a. Run 26, Δp_s = 2.2 psi

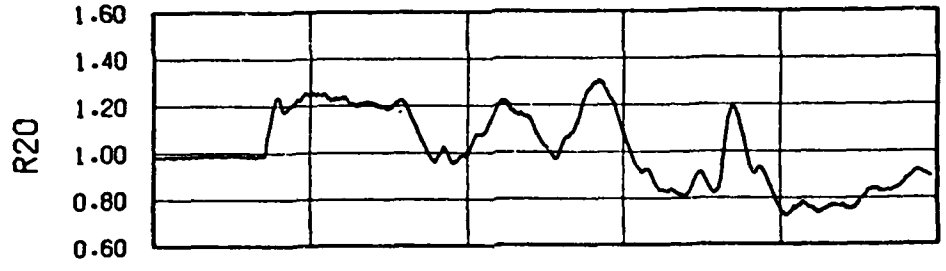

b. Run 27, Δp_s = 3.0 psi

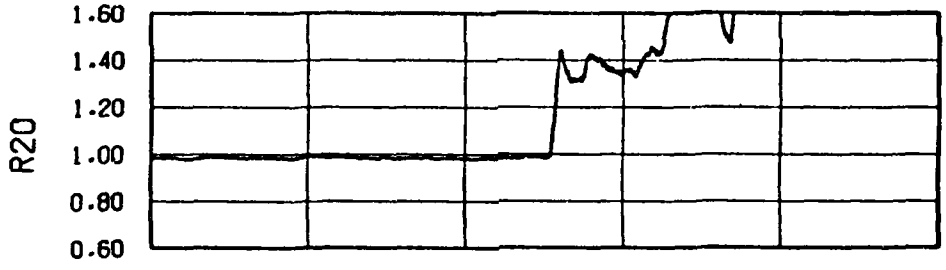

c. Run 29, Δp_s = 4.4 psi

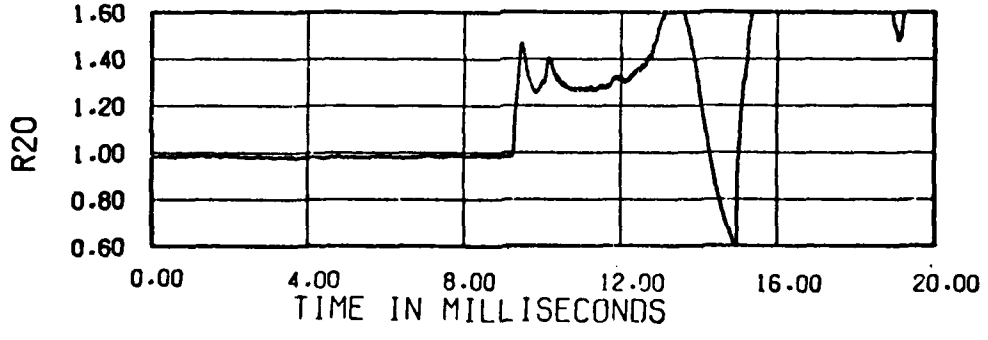

d. Run 28, Δp_s = 5.0 psi

Figure 3.2. Effect of blast shock overpressure on engine-face mean total pressure in blastward inlet at Mach 0.85. Weight flow 300 lb/s (nom). Shock Tube 1.

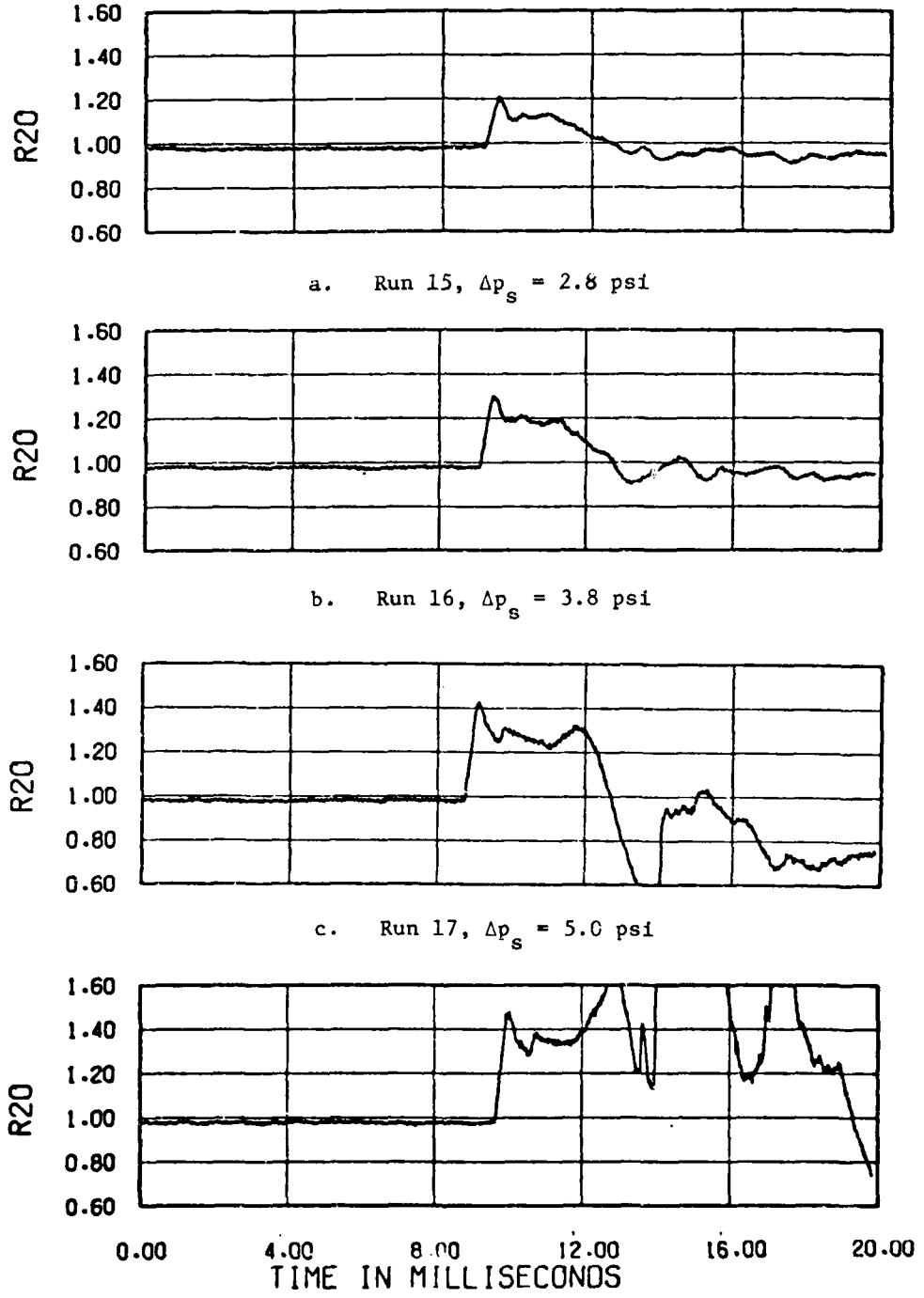

a. Run 15, Δp_s = 2.8 psi

b. Run 16, Δp_s = 3.8 psi

c. Run 17, Δp_s = 5.0 psi

d. Run 18, Δp_s = 5.2 psi

Figure 3.3. Effect of blast shock overpressure on engine-face mean total pressure in blastward inlet at Mach 0.70. Weight flow 350 lb/s (nom). Shock Tube 2.

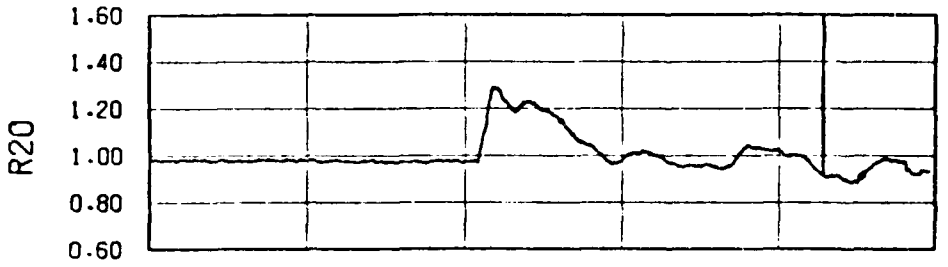

a. Run 39, Δp_s = 4.0 psi

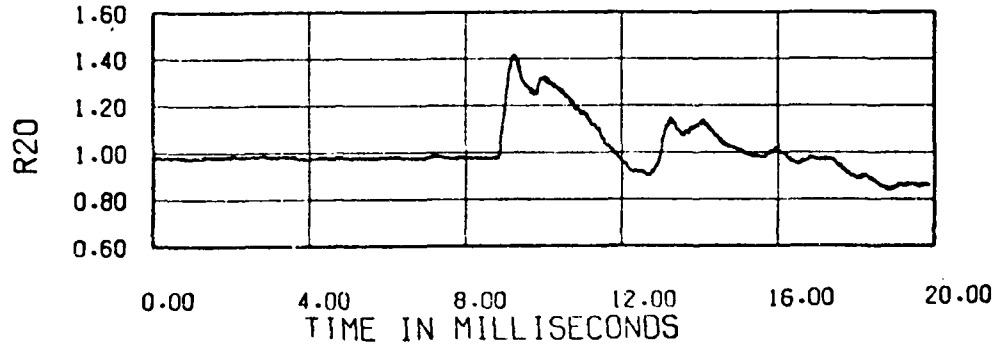

b. Run 40, Δp_s = 5.8 psi

Figure 3.4. Effect of blast shock overpressure on engine-face mean total pressure in blastward inlet at Mach 0.85. Weight flow 350 lb/s (nom). Shock Tube 2.

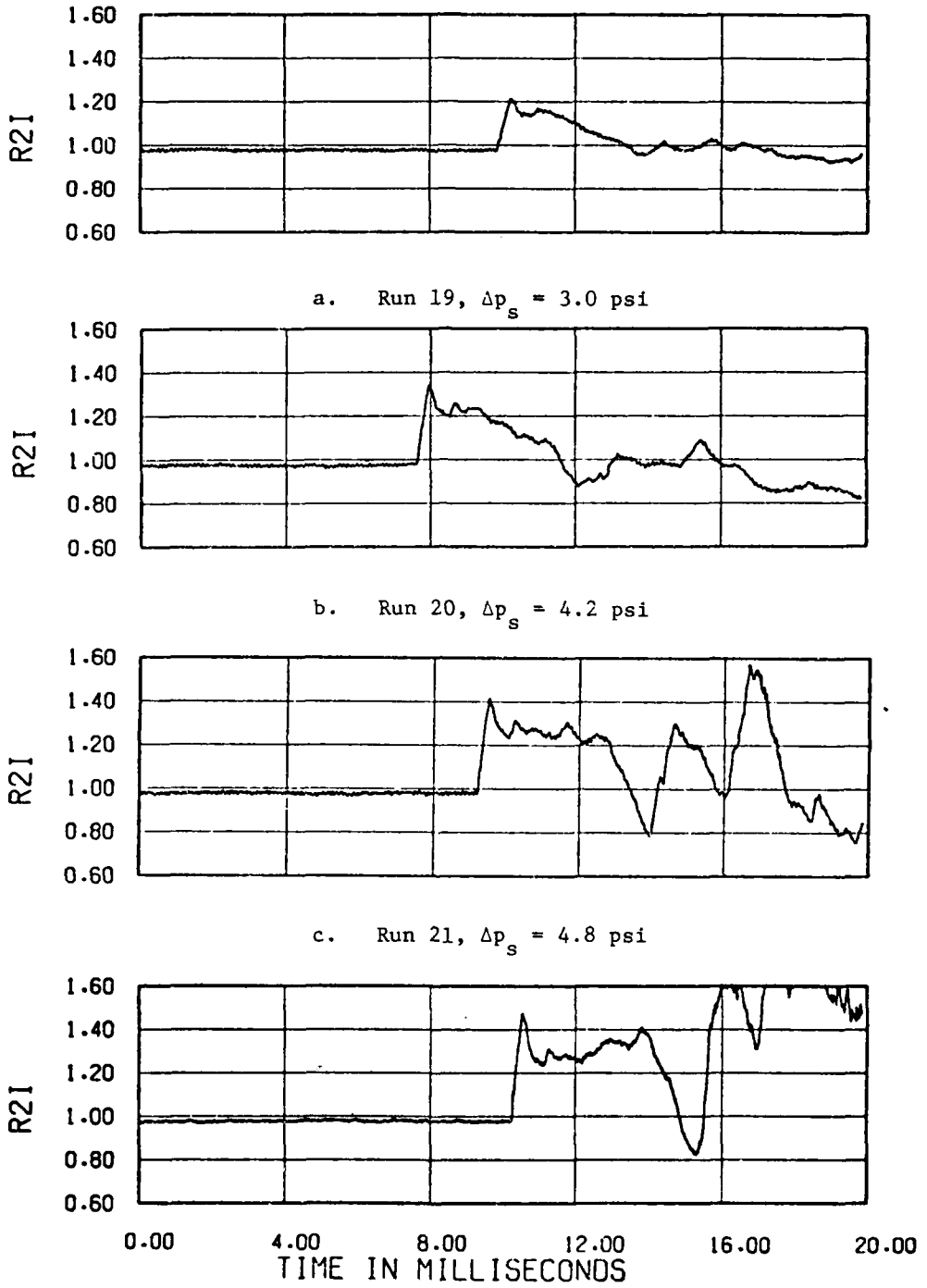

a. Run 19, Δp_s = 3.0 psi

b. Run 20, Δp_s = 4.2 psi

c. Run 21, Δp_s = 4.8 psi

d. Run 22, Δp_s = 5.6 psi

Figure 3.5. Effect of blast shock overpressure on engine-face mean total pressure in blastward inlet at Mach 0.70. Weight flow 350 lb/s (nom). Shock Tube 3.

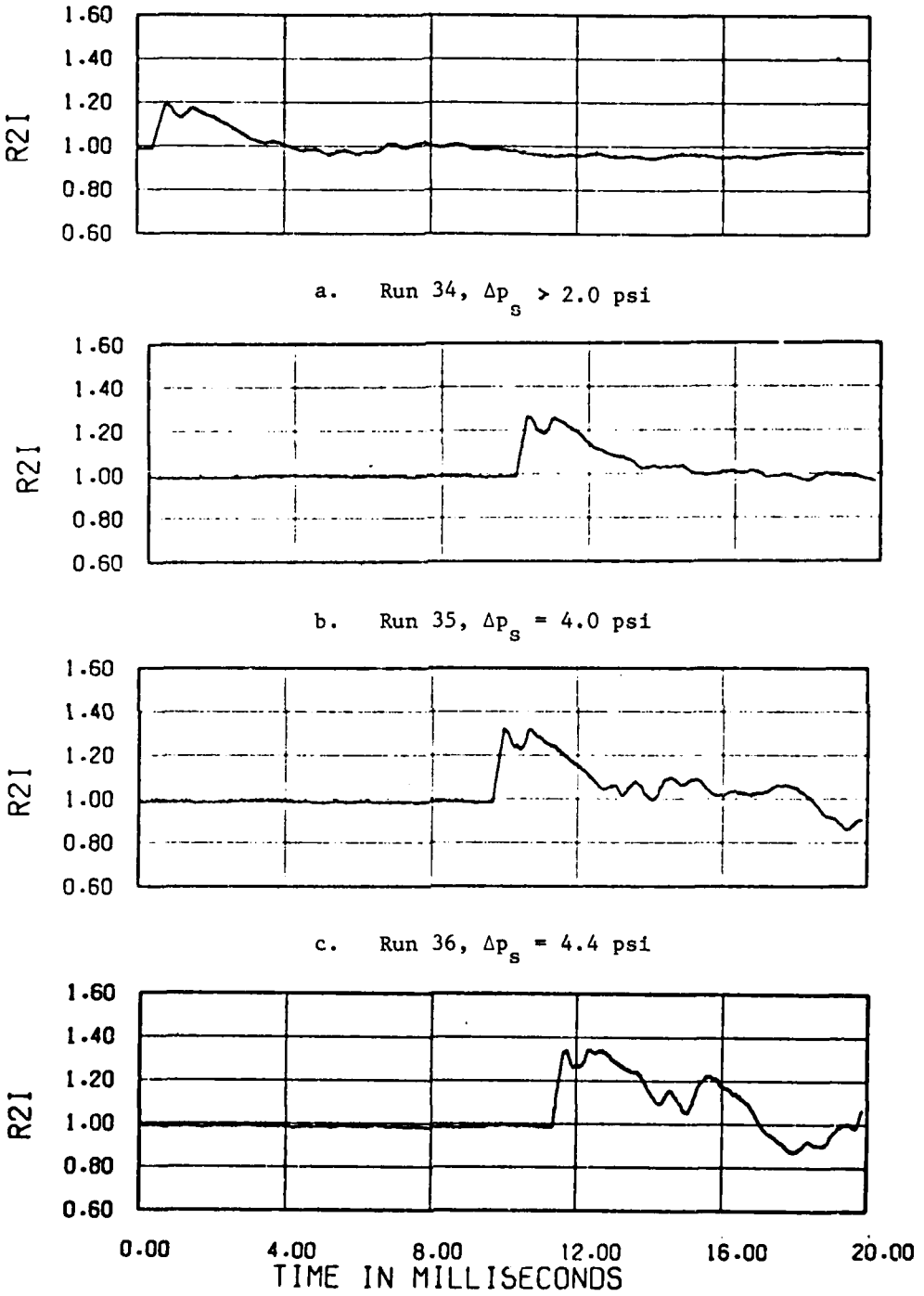

a. Run 34, Δp_s > 2.0 psi

b. Run 35, Δp_s = 4.0 psi

c. Run 36, Δp_s = 4.4 psi

d. Run 37, Δp_s = 4.8 psi

Figure 3.6. Effect of blast shock overpressure on engine-face mean total pressure in blastward inlet at Mach 0.85. Weight flow 300 lb/s (nom). Shock Tube 3.

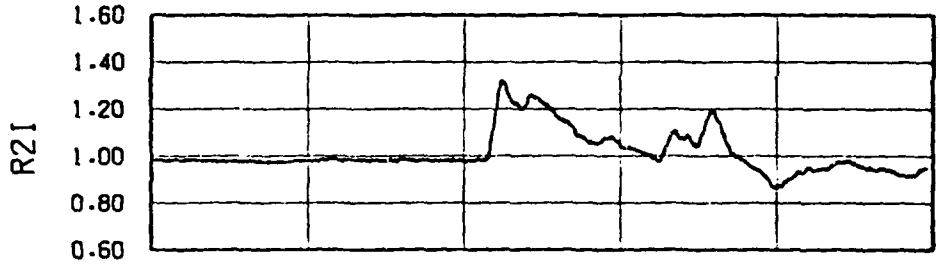

a. Run 41, Δp_s = 4.4 psi

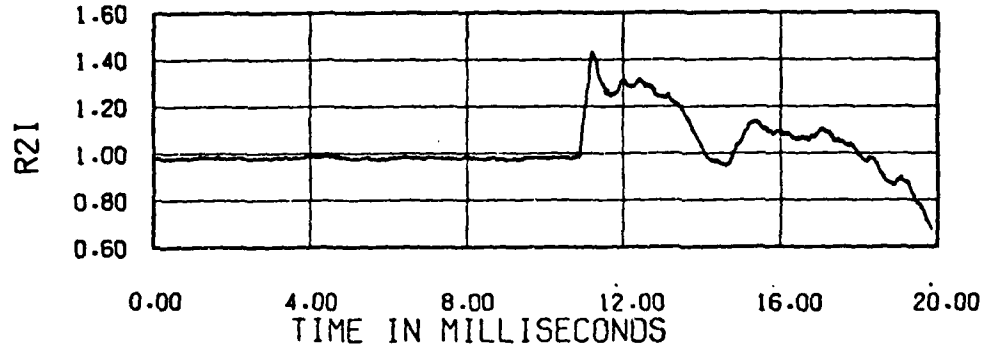

b. Run 42, Δp_s = 5.6 psi

Figure 3.7. Effect of blast shock overpressure on engine-face mean total pressure in blastward inlet at Mach 0.85. Weight flow 350 lb/s (nom). Shock Tube 3.

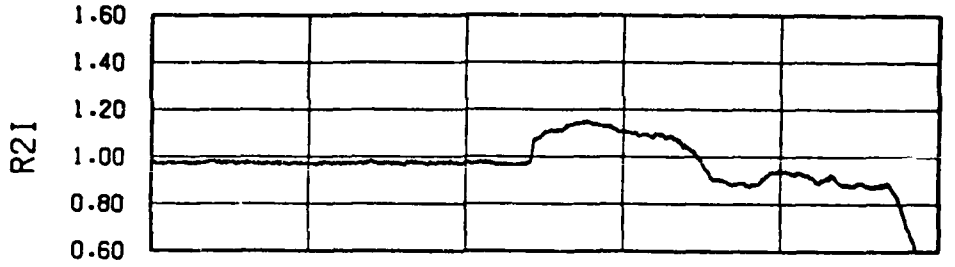

a. Run 11, Δp_s = 3.0 psi

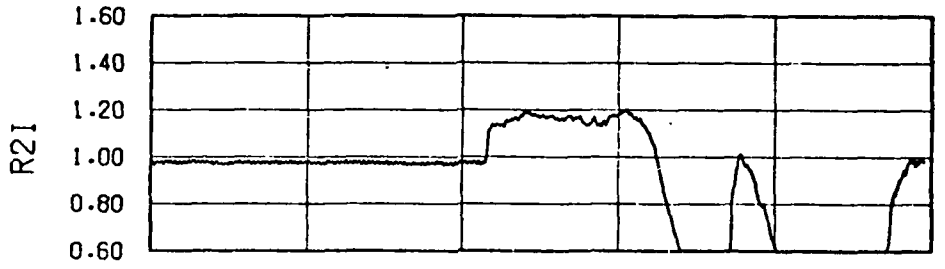

b. Run 12, Δp_s = 3.8 psi

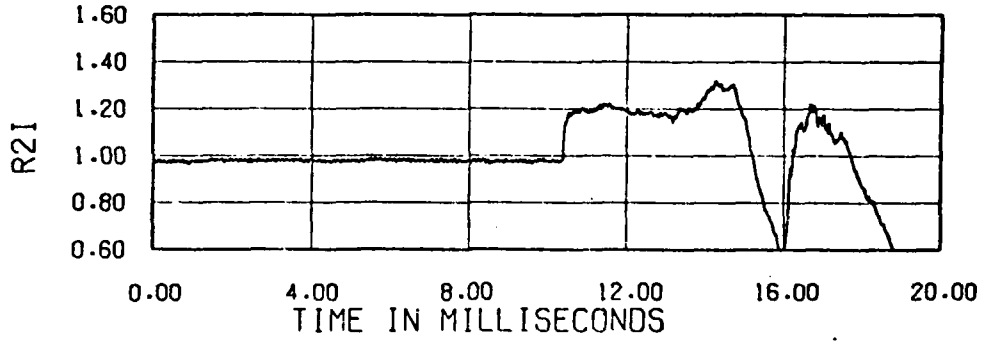

c. Run 13, Δp_s = 4.8 psi

Figure 3.8. Effect of blast shock overpressure on engine-face mean total pressure in leeward inlet at Mach 0.70. Weight flow 350 lb/s (nom). Shock Tube 1.

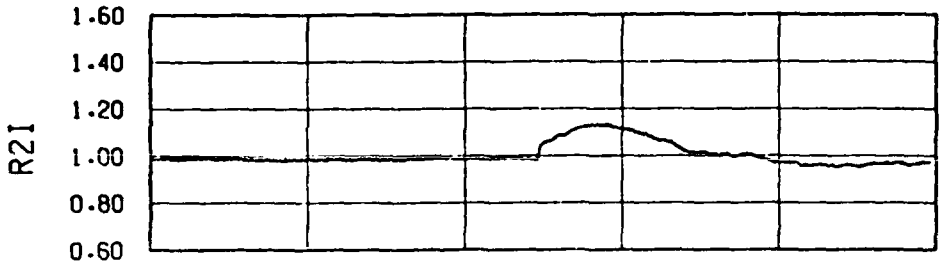

a. Run 26, Δp_s = 2.2 psi

b. Run 27, Δp_s = 3.0 psi

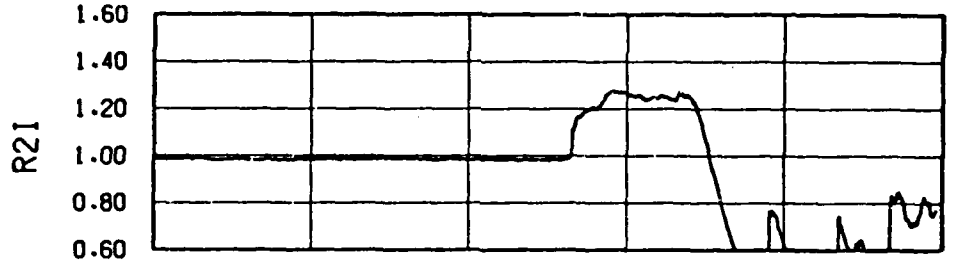

c. Run 29, Δp_s = 4.4 psi

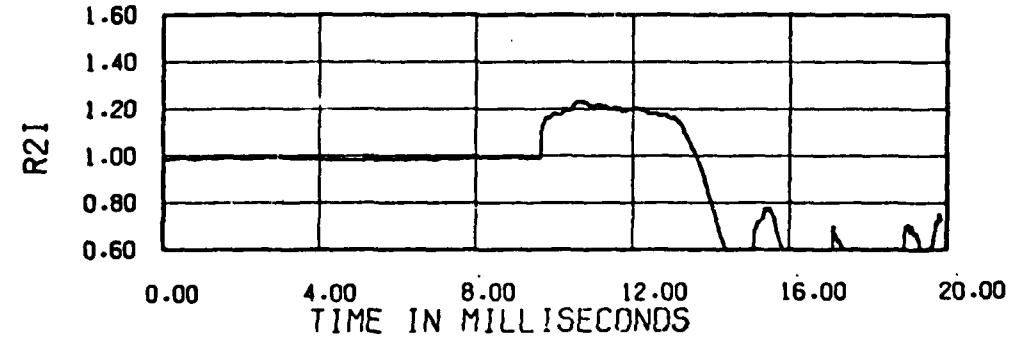

d. Run 28, Δp_s = 5.0 psi

Figure 3.9. Effect of blast shock overpressure on engine-face mean total pressure in leeward inlet at Mach 0.85. Weight flow 300 lb/s (nom). Shock Tube 1.

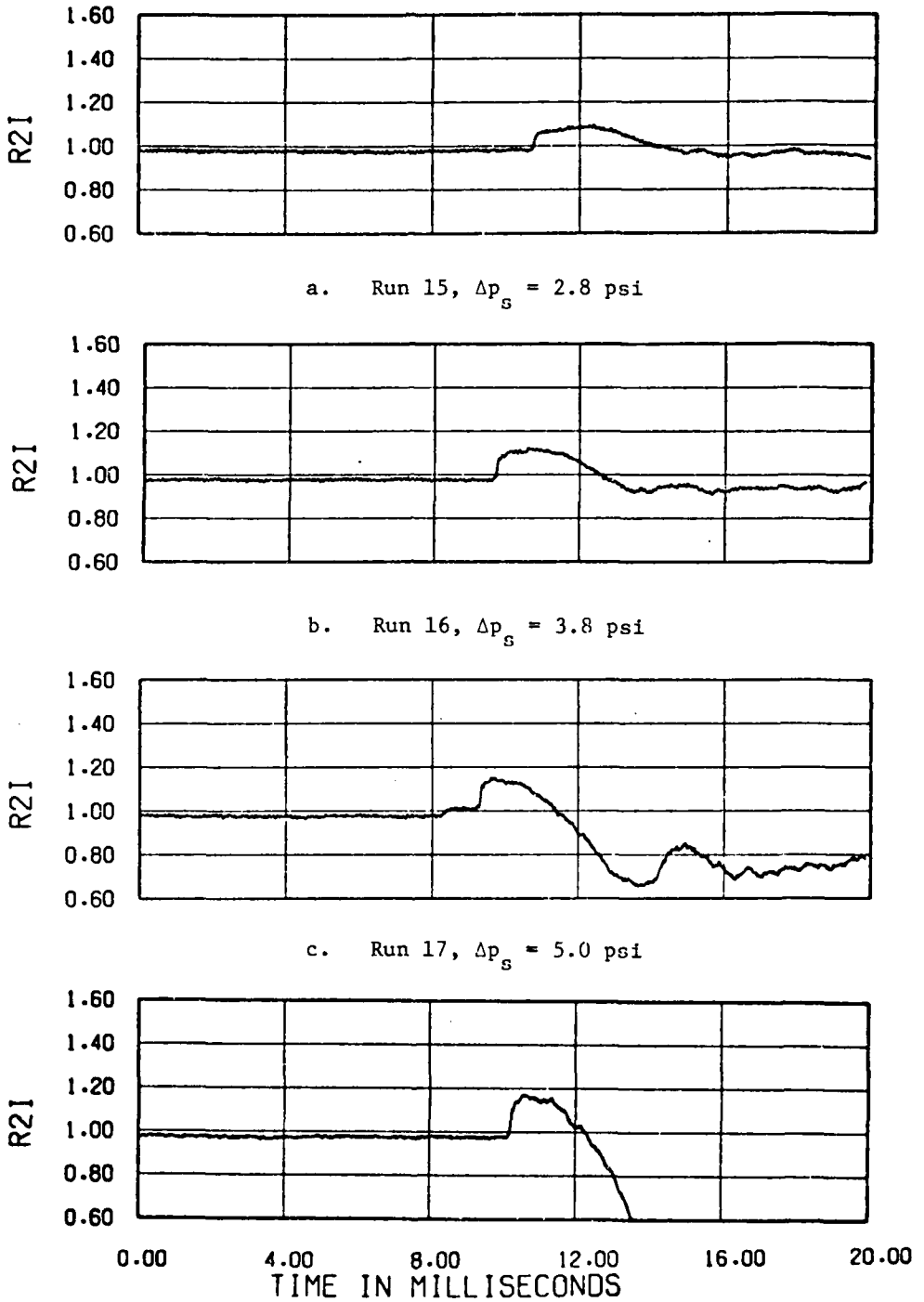

a. Run 15, Δp_s = 2.8 psi

b. Run 16, Δp_s = 3.8 psi

c. Run 17, Δp_s = 5.0 psi

d. Run 18, Δp_s = 5.2 psi

Figure 3.10. Effect of blast shock overpressure on engine-face mean total pressure in leeward inlet at Mach 0.70. Weight flow 350 lb/s (nom). Shock Tube 2.

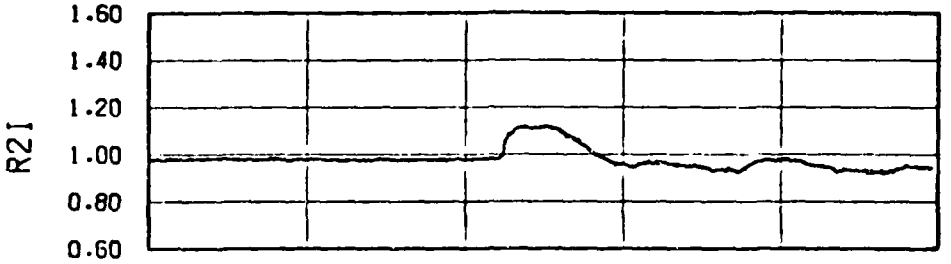

a. Run 39, Δp_s = 4.0 psi

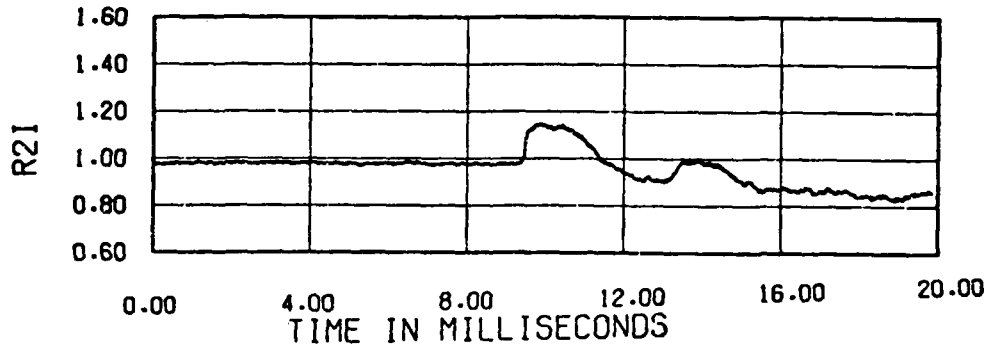

b. Run 40, Δp_s = 5.8 psi

Figure 3.11. Effect of blast shock overpressure on engine-face mean total pressure in leeward inlet at Mach 0.85. Weight flow 350 lb/s (nom). Shock Tube 2.

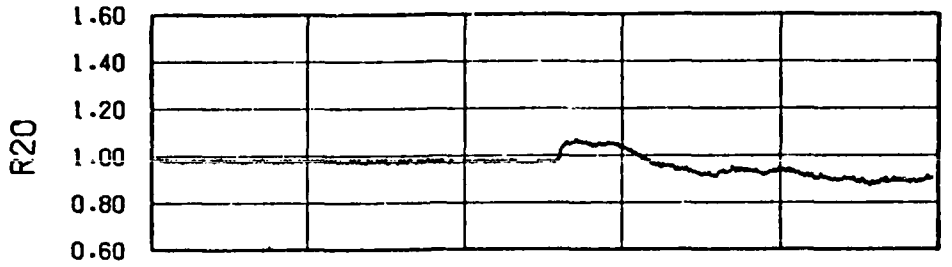

a. Run 19, Δp_s = 3.0 psi

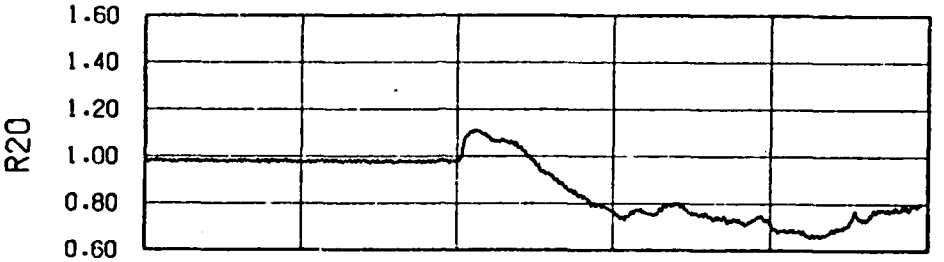

b. Run 20, Δp_s = 4.2 psi

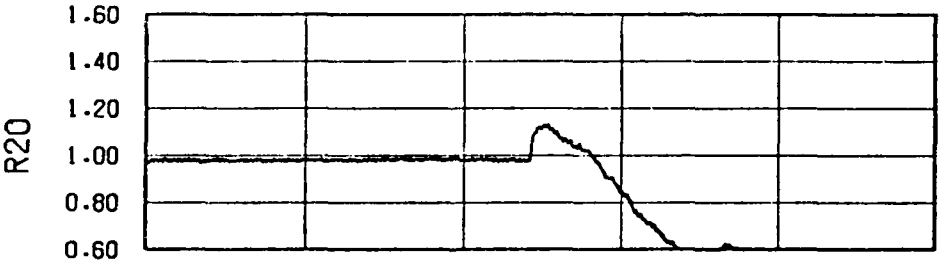

c. Run 21, Δp_s = 4.8 psi

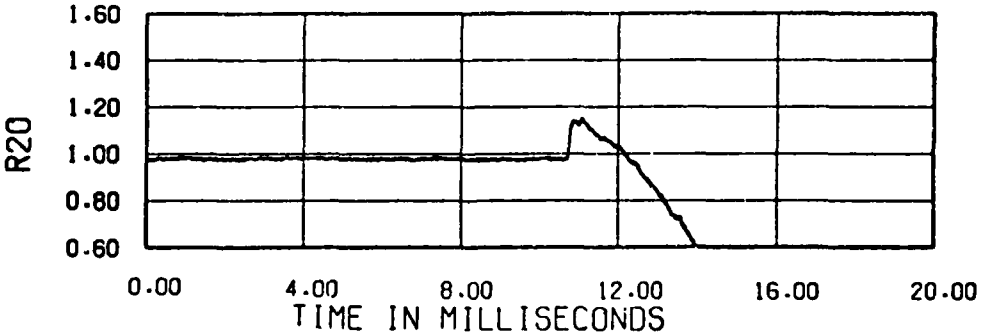

d. Run 22, Δp_s = 5.6 psi

Figure 3.12. Effect of blast shock overpressure on engine-face mean total pressure in leeward inlet at Mach 0.70. Weight flow 350 lb/s (nom). Shock Tube 3.

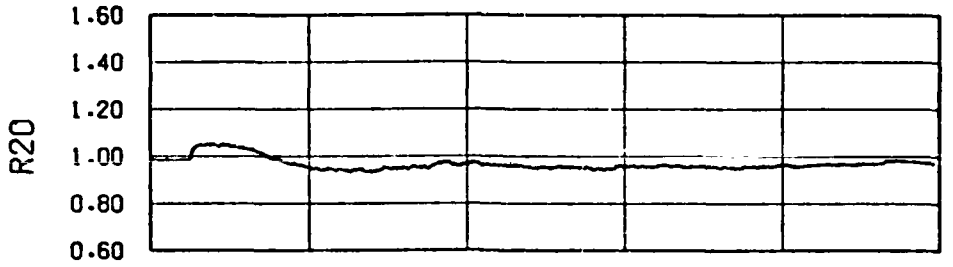

a. Run 34, Δp_s > 2.0 psi

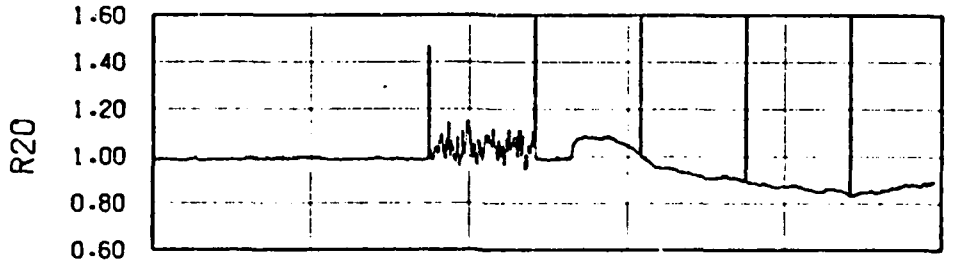

b. Run 35, Δp_s = 4.0 psi

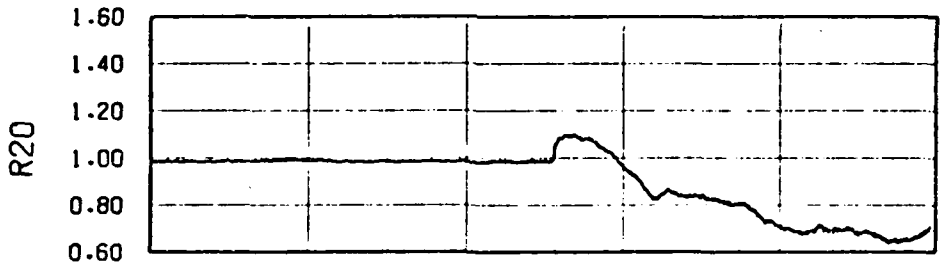

c. Run 36, Δp_s = 4.4 psi

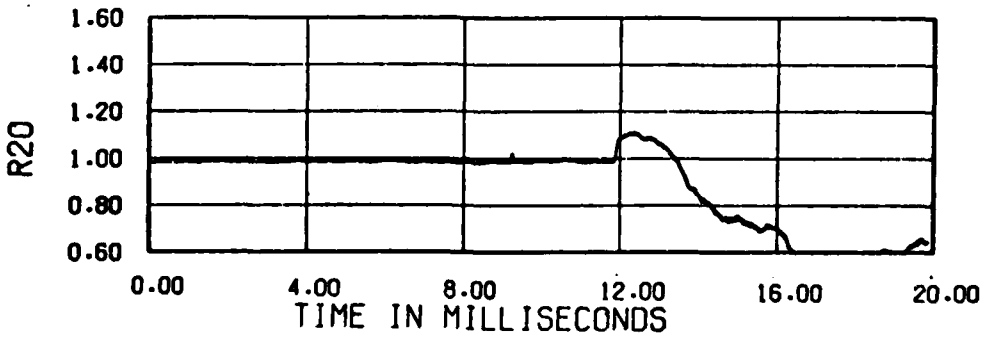

d. Run 37, Δp_s = 4.8 psi

Figure 3.13. Effect of blast shock overpressure on engine-face mean total pressure in leeward inlet at Mach 0.85. Weight flow 300 lb/s (nom). Shock Tube 3.

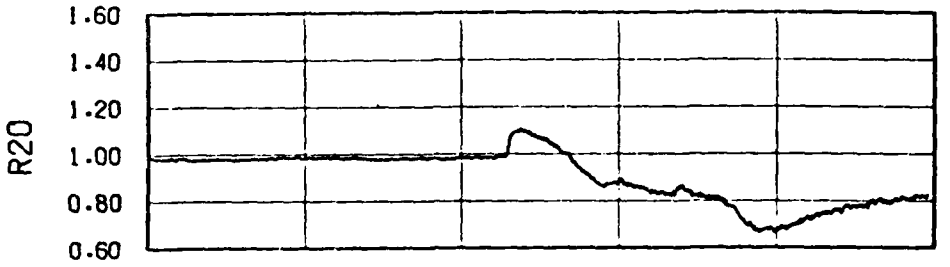

a. Run 41, Δp_s = 4.4 psi

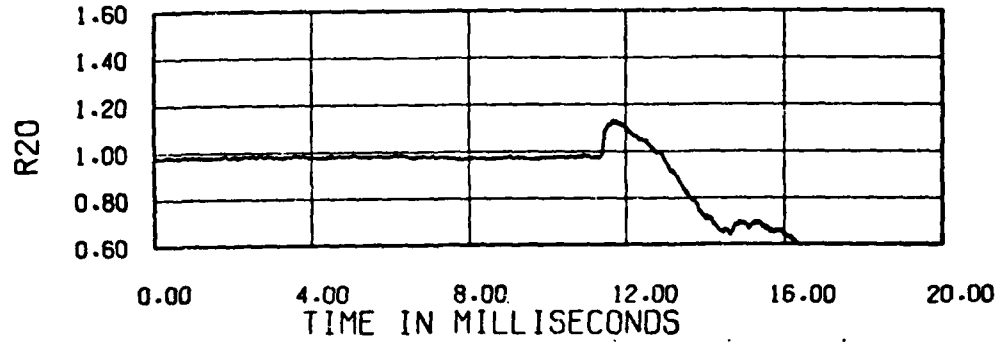

b. Run 42, Δp_s = 5.6 psi

Figure 3.14. Effect of blast shock overpressure on engine-face mean total pressure in leeward inlet at Mach 0.85. Weight flow 350 lb/s (nom). Shock Tube 3.

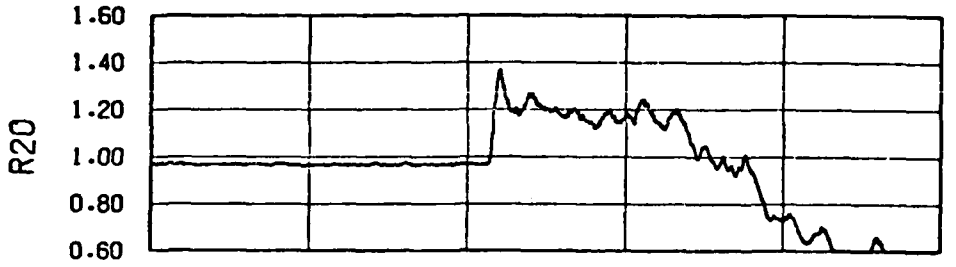

a. Run 3, Shock Tube 1, ϕ = 76 deg., Δp_s = 3.7 psi.

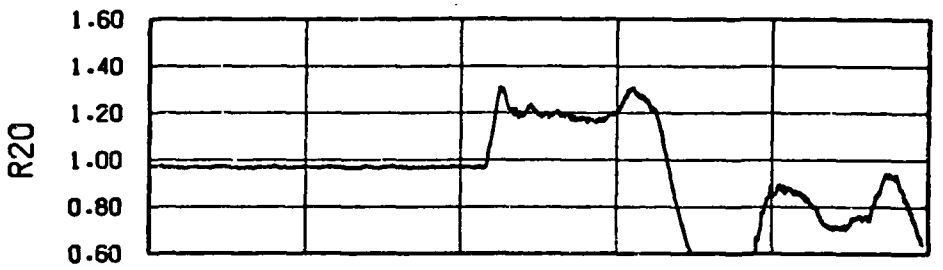

b. Run 4, Shock Tube 2, ϕ = 97 deg., Δp_s = 3.8 psi.

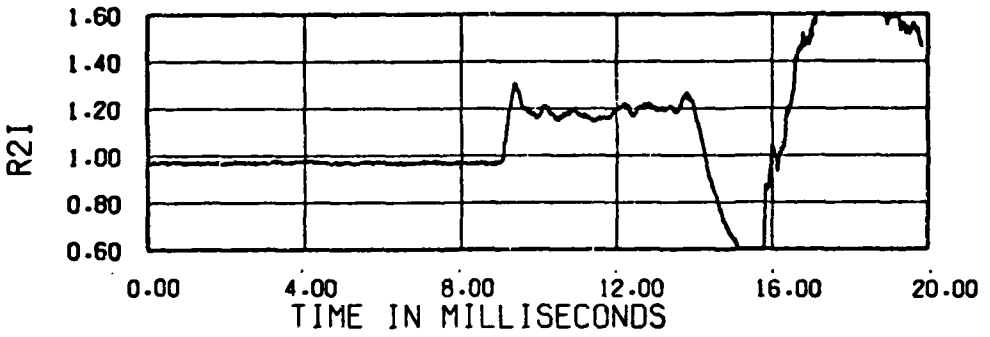

c. Run 5, Shock Tube 3, ϕ = -94 deg., Δp_s = 4.0 psi.

Figure 3.15. Effect of blast intercept angle on engine-face mean total pressure in blastward inlet at Mach 0.55. Weight flow 350 lb/s (nom). Blast shock overpressure 3.8 psi (nom).

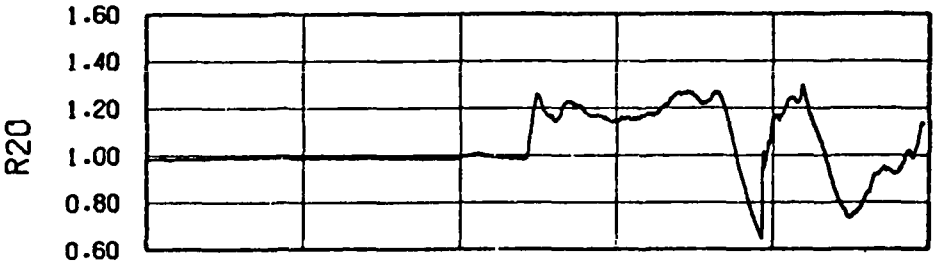

a. Run 6, Shock Tube 1, ϕ = 86 deg., Δp_s = 2.6 psi.

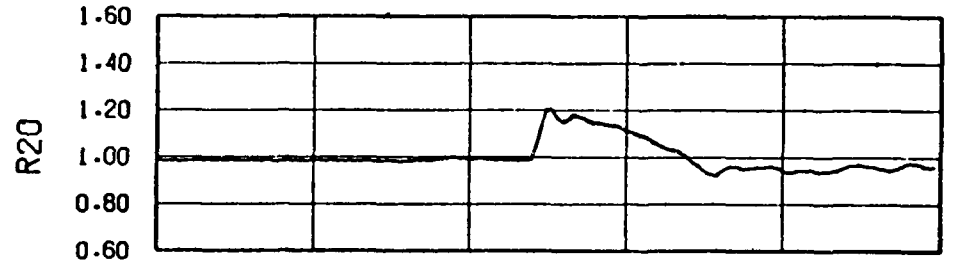

b. Run 7, Shock Tube 2, ϕ = 106 deg., Δp_s = 2.6 psi.

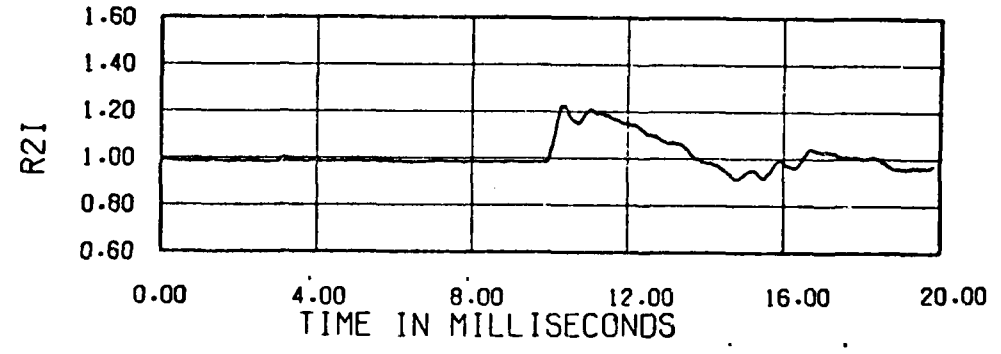

c. Run 9, Shock Tube 3, ϕ = -104 deg., Δp_s = 3.0 psi.

Figure 3.16. Effect of blast intercept angle on engine-face mean total pressure in blastward inlet at Mach 0.70. Weight flow 300 lb/s (nom). Blast shock overpressure 2.7 psi (nom).

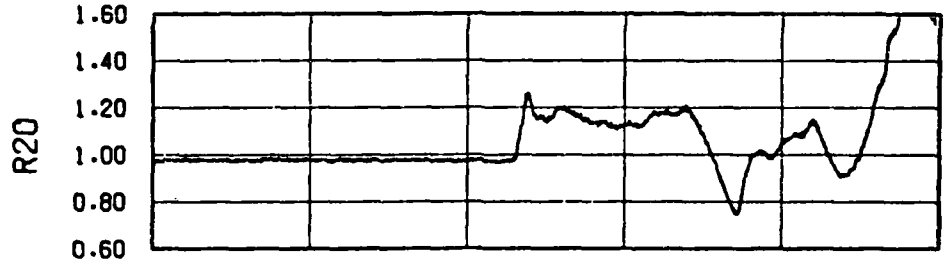

a. Run 11, Shock Tube 1, ϕ = 84 deg., Δp_s = 3.0 psi.

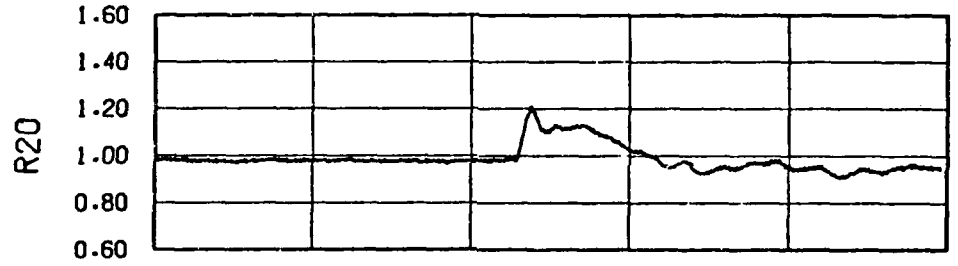

b. Run 15, Shock Tube 2, ϕ = 103 deg., Δp_s = 2.8 psi.

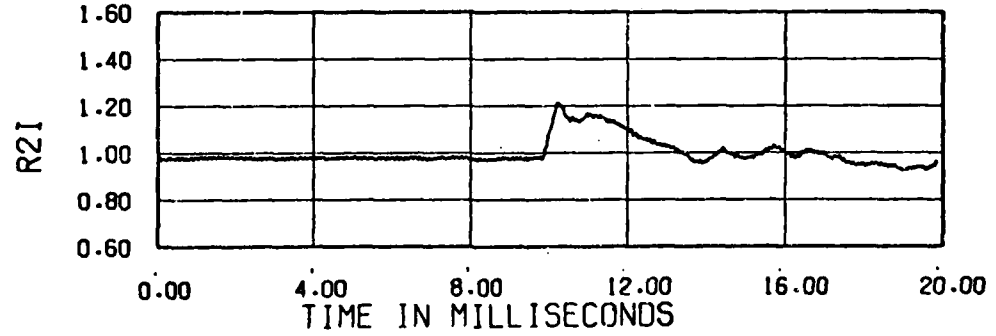

c. Run 19, Shock Tube 3, ϕ = -102 deg., Δp_s = 3.0 psi.

Figure 3.17. Effect of blast intercept angle on engine-face mean total pressure in blastward inlet at Mach 0.70. Weight flow 350 lb/s (nom). Blast shock overpressure 2.9 psi (nom).

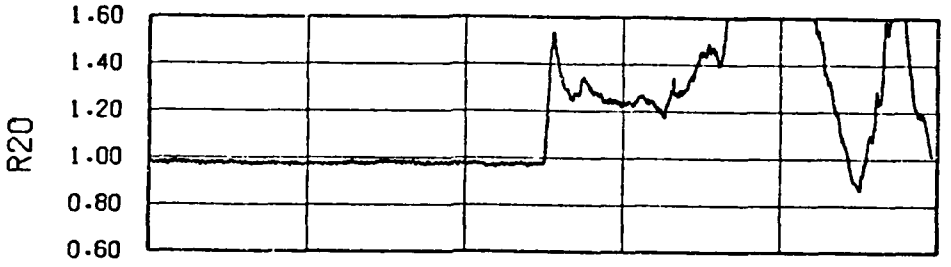

a. Run 13, Shock Tube 1, ϕ = 78 deg., Δp_s = 4.8 psi.

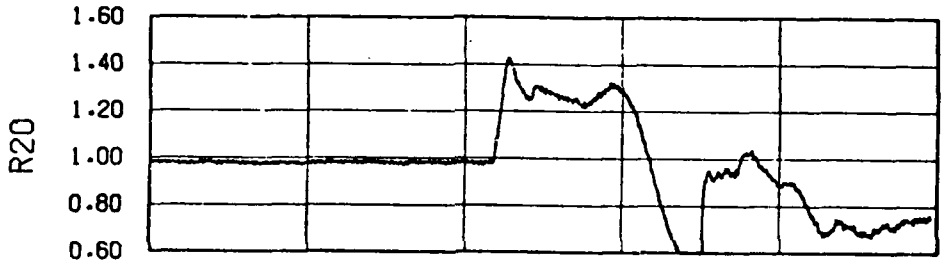

b. Run 17, Shock Tube 2, ϕ = 100 deg., Δp_s = 5.0 psi.

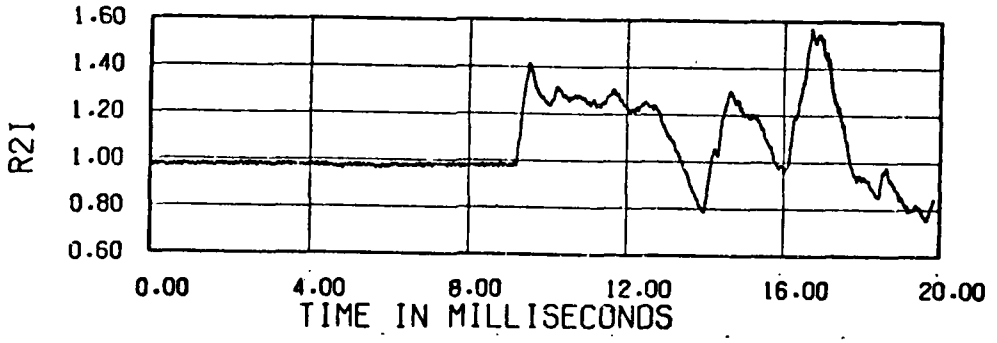

c. Run 21, Shock Tube 3, ϕ = -98 deg., Δp_s = 4.8 psi.

Figure 3.18. Effect of blast intercept angle on engine-face mean total pressure in blastward inlet at Mach 0.70. Weight flow 350 lb/s (nom). Blast shock overpressure 4.9 psi (nom).

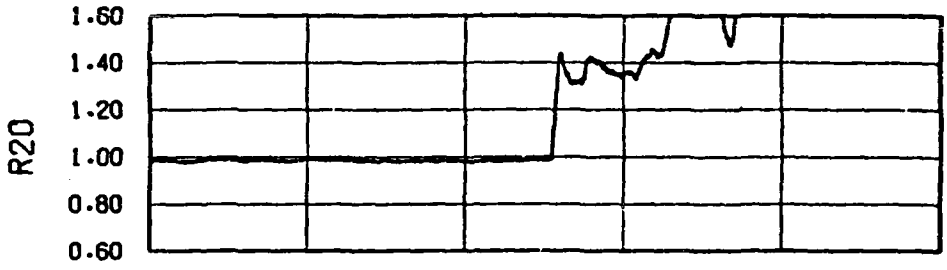

a. Run 29, Shock Tube 1, ϕ = 82 deg., Δp_s = 4.4 psi.

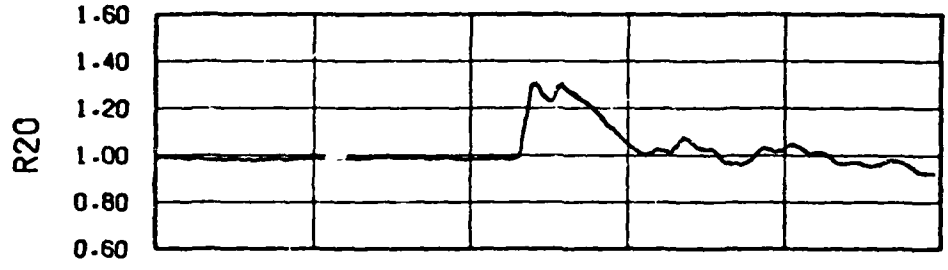

b. Run 32, Shock Tube 2, ϕ = 105 deg., Δp_s = 4.4 psi.

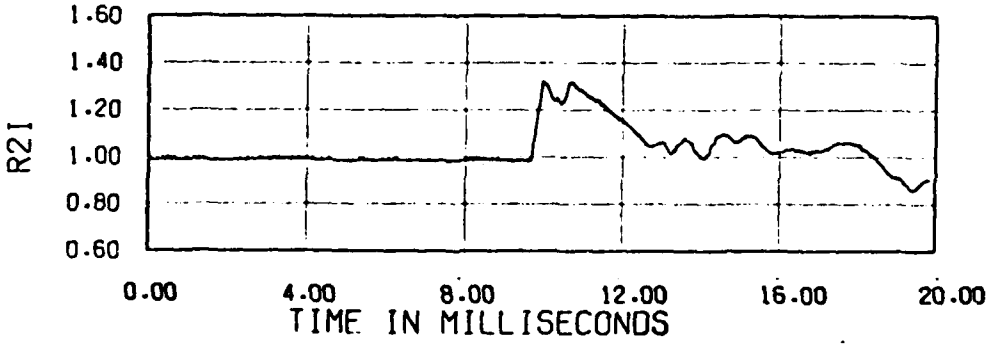

c. Run 36, Shock Tube 3, ϕ = -102 deg., Δp_s = 4.4 psi.

Figure 3.19. Effect of blast intercept angle on engine-face mean total pressure in blastward inlet at Mach 0.85. Weight flow 300 lb/s (nom). Blast shock overpressure 4.4 psi (nom).

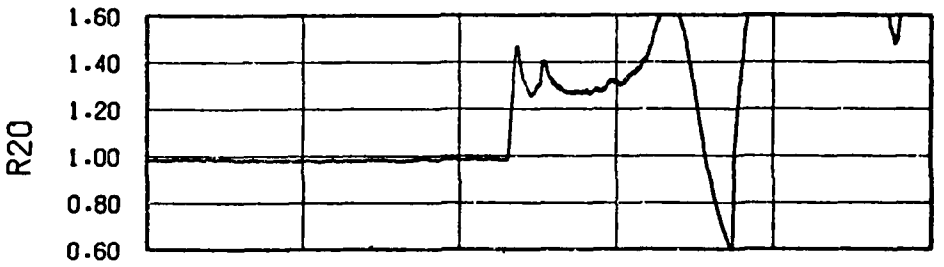

a. Run 28, Shock Tube 1, ϕ = 82 deg., Δp_s = 5.0 psi.

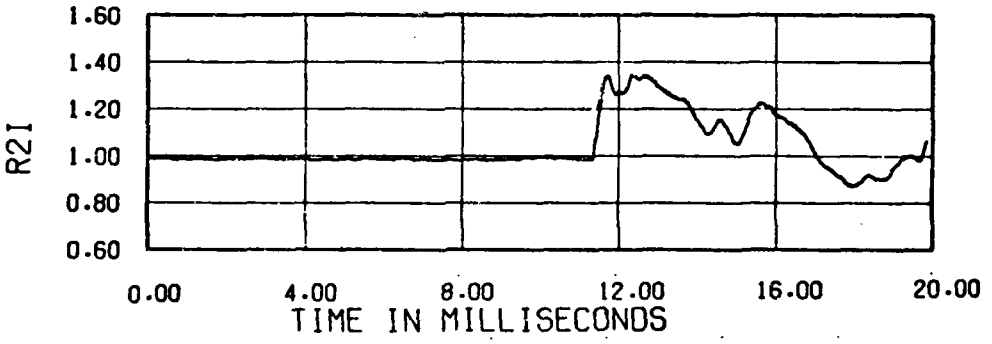

b. Run 37, Shock Tube 3, ϕ = -108 deg., Δp_s = 4.8 psi.

Figure 3.20. Effect of blast intercept angle on engine-face mean total pressure in blastward inlet at Mach 0.85. Weight flow 300 lb/s (nom). Blast shock overpressure 4.9 psi (nom).

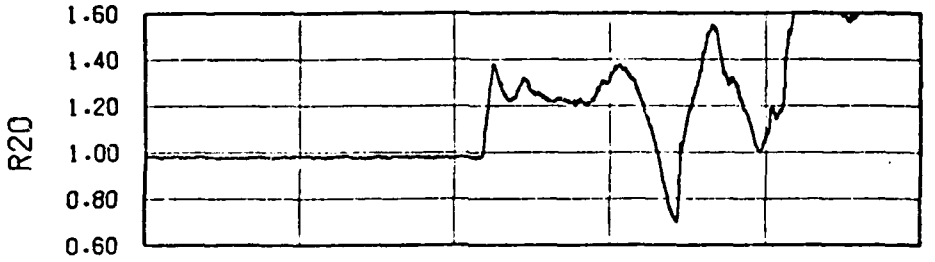

a. Run 38, Shock Tube 1, ϕ = 84 deg., Δp_s = 3.6 psi.

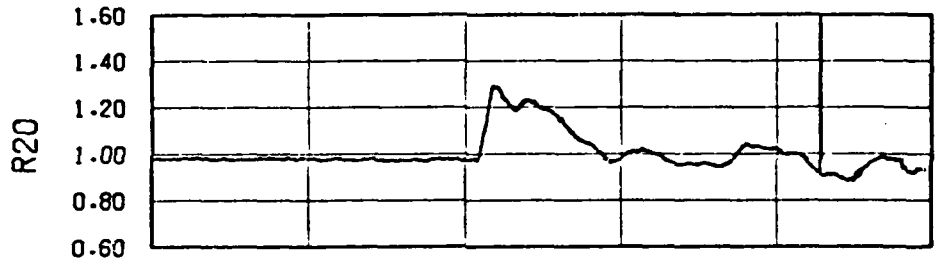

b. Run 39, Shock Tube 2, ϕ = 107 deg., Δp_s = 4.0 psi.

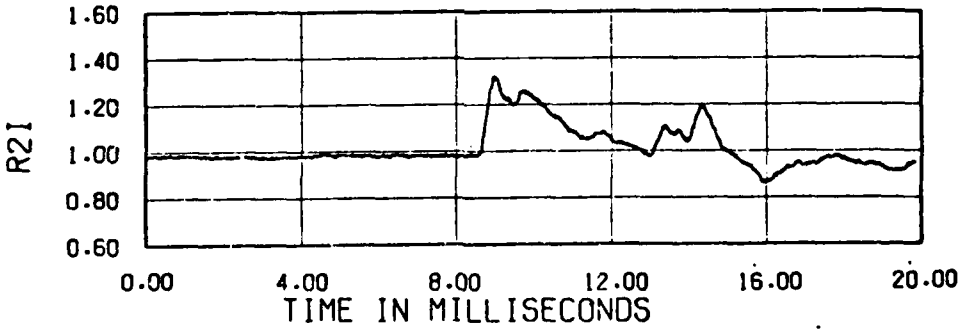

c. Run 41, Shock Tube 3, ϕ = -105 deg., Δp_s = 4.4 psi.

Figure 3.21. Effect of blast intercept angle on engine-face mean total pressure in blastward inlet at Mach 0.85. Weight flow 350 lb/s (nom). Blast shock overpressure 4.0 psi (nom).

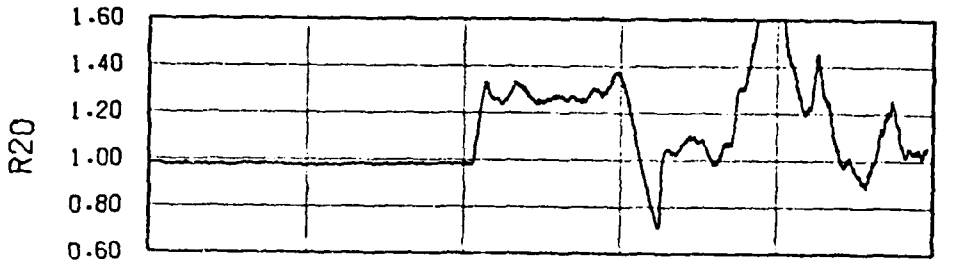

a. Run 43, Shock Tube 1, ϕ = 86 deg., Δp_s = 3.0 psi.

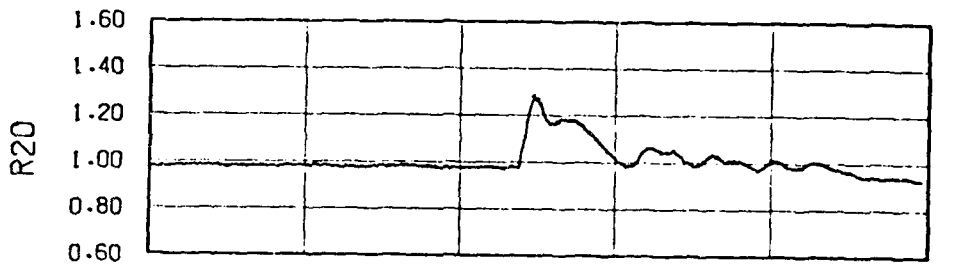

b. Run 44, Shock Tube 2, ϕ = 107 deg., $\Delta p_s \approx$ 4.0 psi.

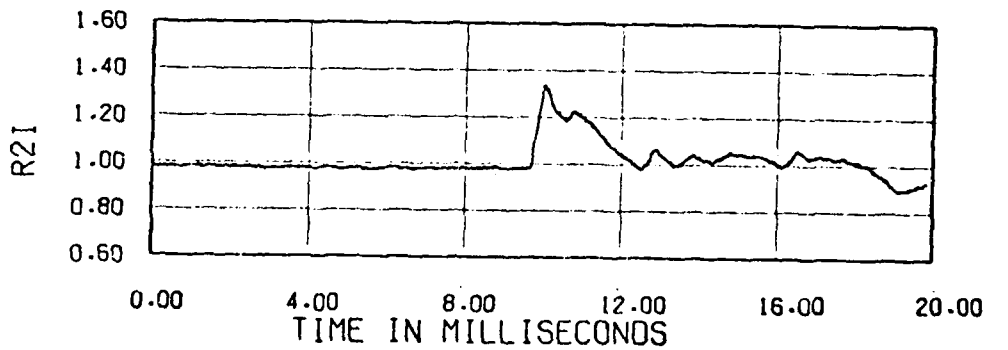

c. Run 45, Shock Tube 3, ϕ = -104 deg., Δp_s = 4.2 psi.

Figure 3.22. Effect of blast intercept angle on engine-face mean total pressure in blastward inlet at Mach 0.90. Weight flow 350 lb/s (nom). Blast shock over-pressure 3.7 psi (nom).

a. Run 6, Shock Tube 1, ϕ = 86 deg., Δp_s = 2.6 psi.

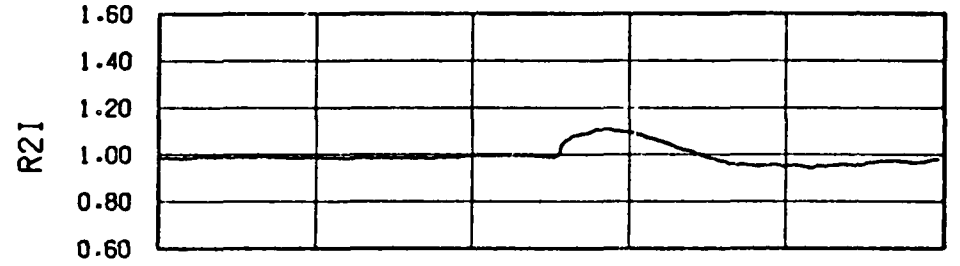

b. Run 7, Shock Tube 2, ϕ = 106 deg., Δp_s = 2.6 psi.

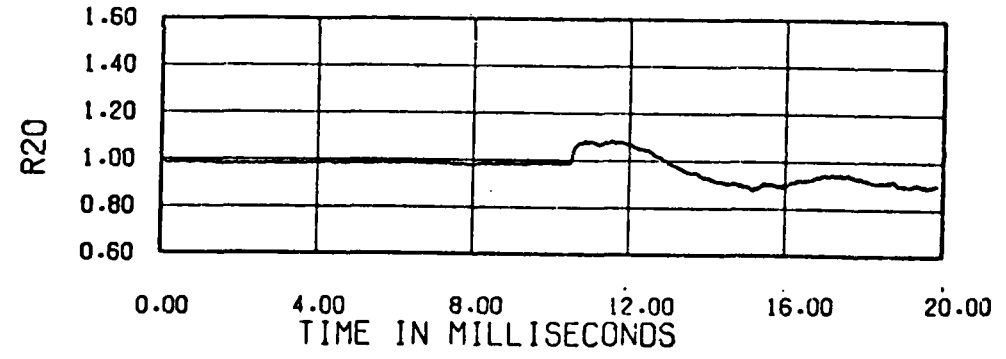

c. Run 9, Shock Tube 3, ϕ = 104 deg., Δp_s = 3.0 psi.

Figure 3.23. Effect of blast intercept angle on engine-face mean total pressure in leeward inlet at Mach 0.70. Weight flow 300 lb/s (nom). Blast shock overpressure 2.7 psi (nom).

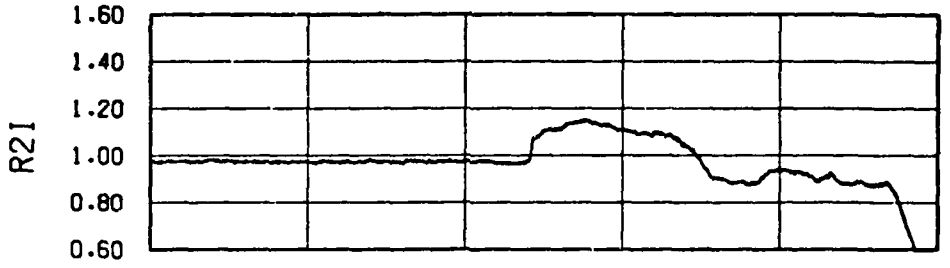

a. Run 11, Shock Tube 1, ϕ = 84 deg., Δp_s = 3.0 psi.

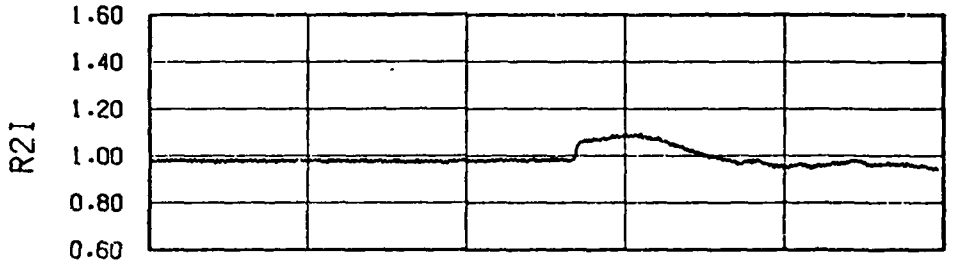

b. Run 15, Shock Tube 2, ϕ = 103 deg., Δp_s = 2.8 psi.

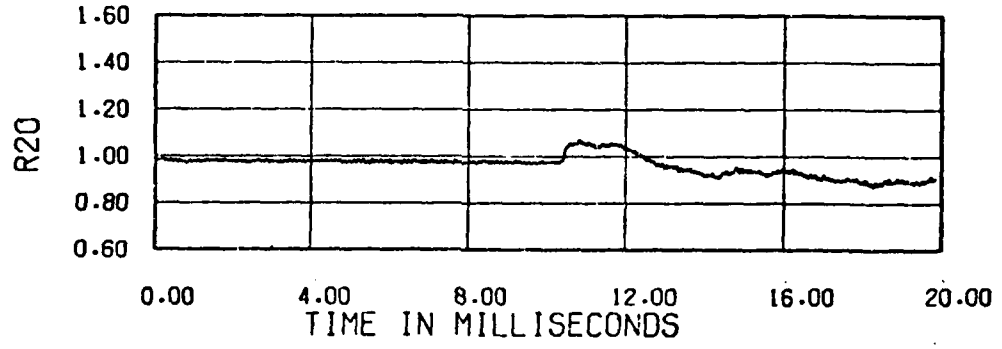

c. Run 19, Shock Tube 3, ϕ = -102 deg., Δp_s = 3.0 psi.

Figure 3.24. Effect of blast intercept angle on engine-face mean total pressure in leeward inlet at Mach 0.70. Weight flow 350 lb/s (nom). Blast shock overpressure 2.9 psi (nom).

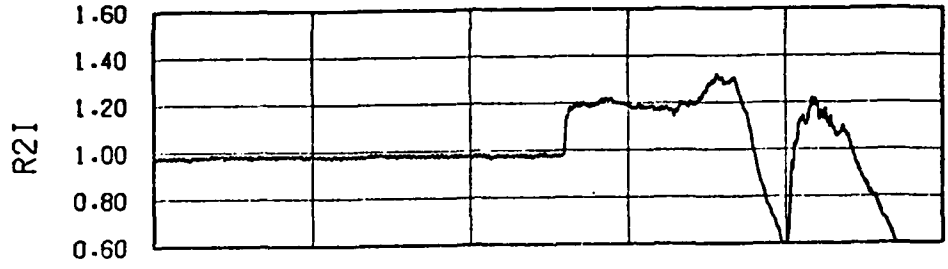

a. Run 13, Shock Tube 1, ϕ = 78 deg., Δp_s = 4.8 psi.

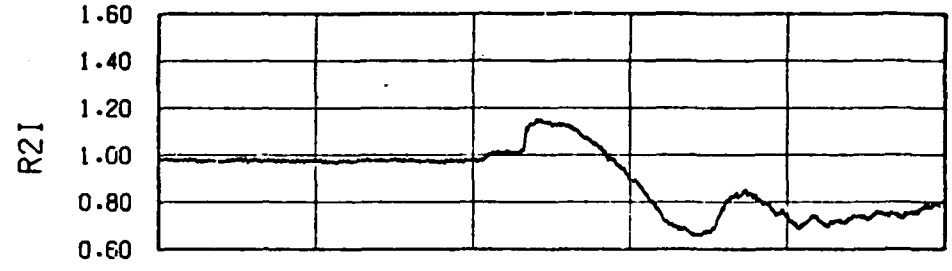

b. Run 17, Shock Tube 2, ϕ = 100 deg., Δp_s = 5.0 psi.

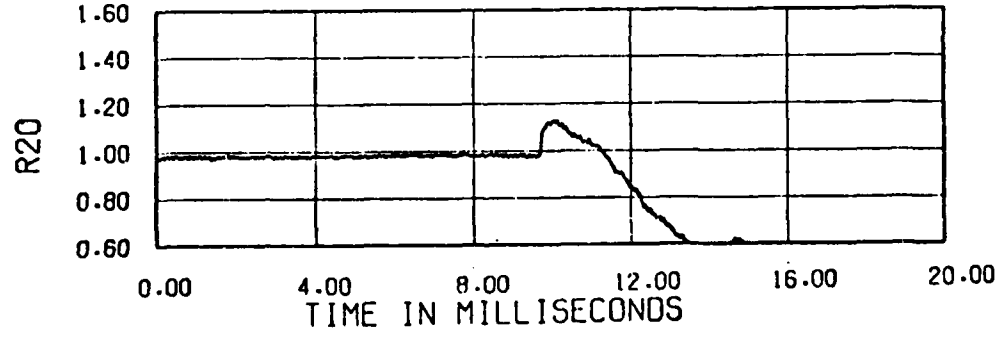

c. Run 21, Shock Tube 3, ϕ = -98 deg., Δp_s = 4.8 psi.

Figure 3.25. Effect of blast intercept angle on engine-face mean total pressure in leeward inlet at Mach 0.70. Weight flow 350 lb/s (nom). Blast shock overpressure 4.9 psi (nom).

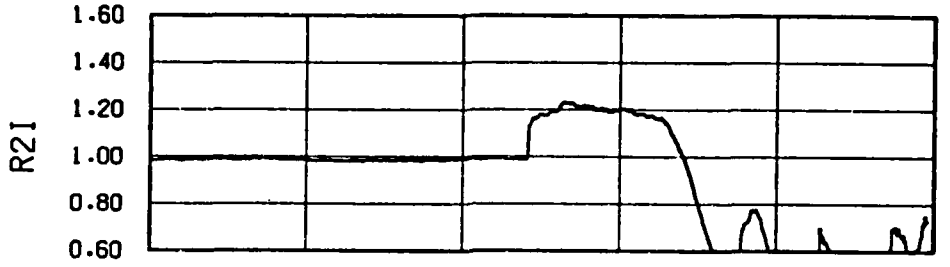

a. Run 28, Shock Tube 1, ϕ = 82 deg., Δp_s = 5.0 psi.

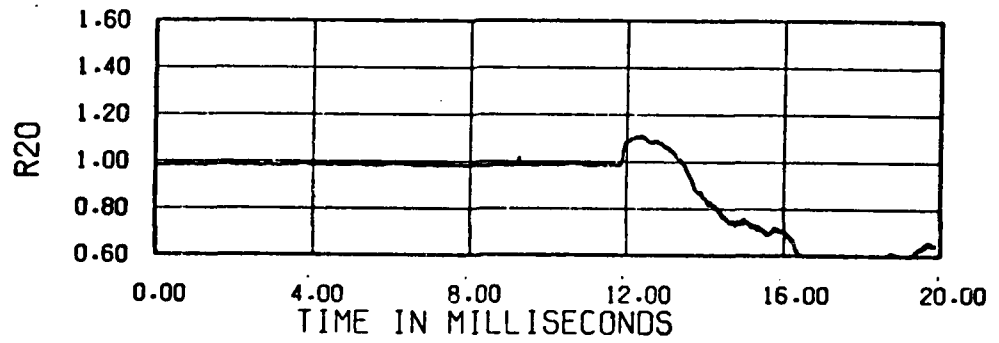

b. Run 37, Shock Tube 3, ϕ = -108 deg., Δp_s = 4.8 psi.

Figure 3.26. Effect of blast intercept angle on engine-face mean total pressure in leeward inlet at Mach 0.85. Weight flow 300 lb/s (nom). Blast shock overpressure 4.9 psi (nom).

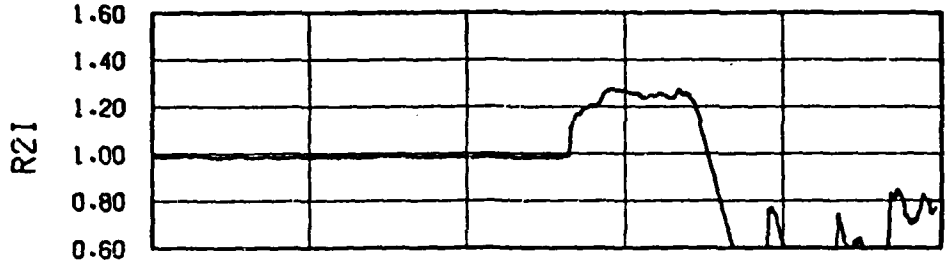

a. Run 29, Shock Tube 1, ϕ = 82 deg., Δp_s = 4.4 psi.

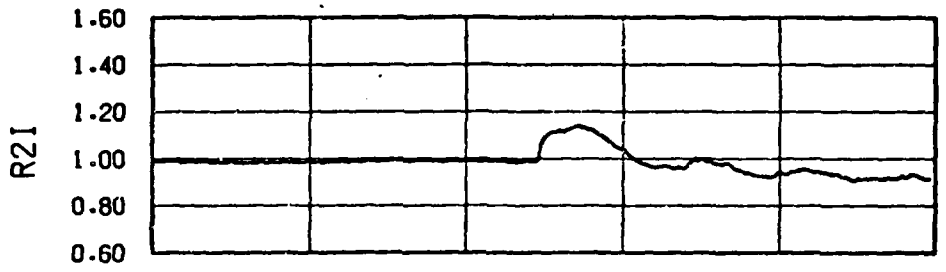

b. Run 32, Shock Tube 2, ϕ = 105 deg., Δp_s = 4.4 psi.

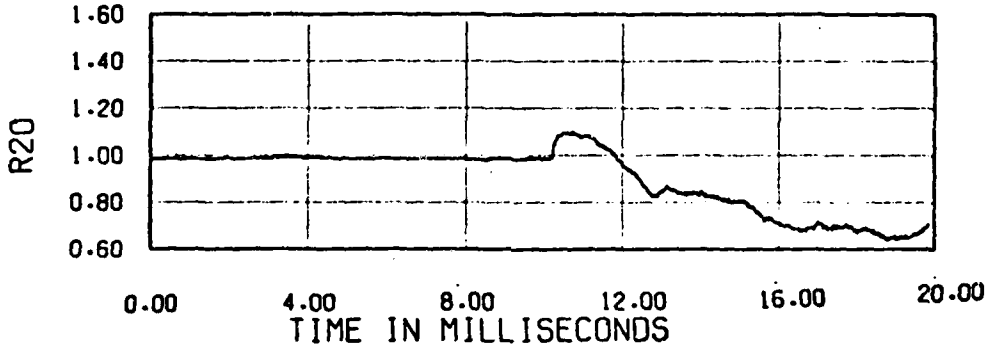

c. Run 36, Shock Tube 3, ϕ = -102 deg., Δp_s = 4.4 psi.

Figure 3.27. Effect of blast intercept angle on engine-face mean total pressure in leeward inlet at Mach 0.85. Weight flow 300 lb/s (nom). Blast shock overpressure 4.4 psi (nom).

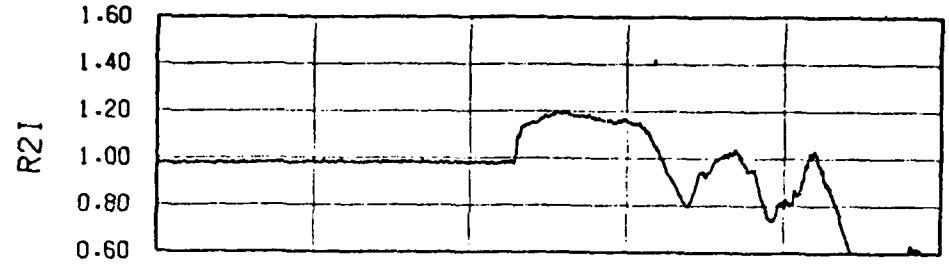

a. Run 38, Shock Tube 1, ϕ = 84 deg., Δp_s = 3.6 psi.

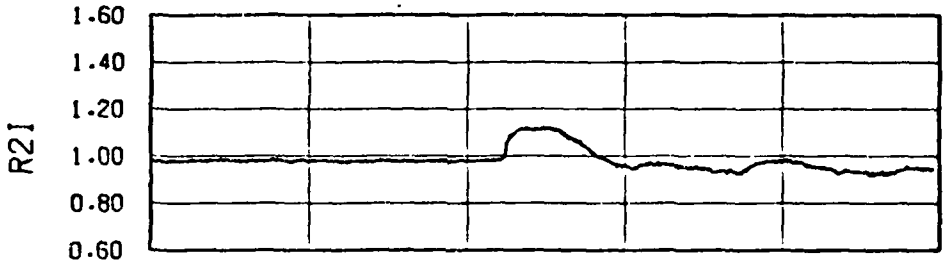

b. Run 39, Shock Tube 2, ϕ = 107 deg., Δp_s = 4.0 psi.

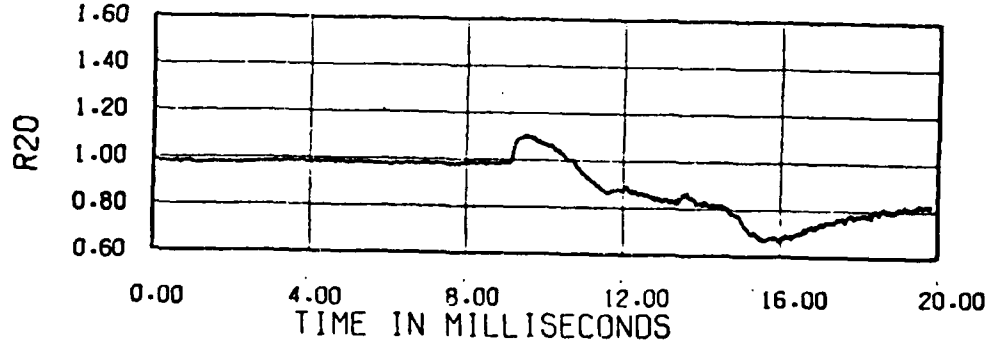

c. Run 41, Shock Tube 3, ϕ = -105 deg., Δp_s = 4.4 psi.

Figure 3.28. Effect of blast intercept angle on engine-face mean total pressure in leeward inlet at Mach 0.85. Weight flow 350 lb/s (nom). Blast shock overpressure 4.0 psi (nom).

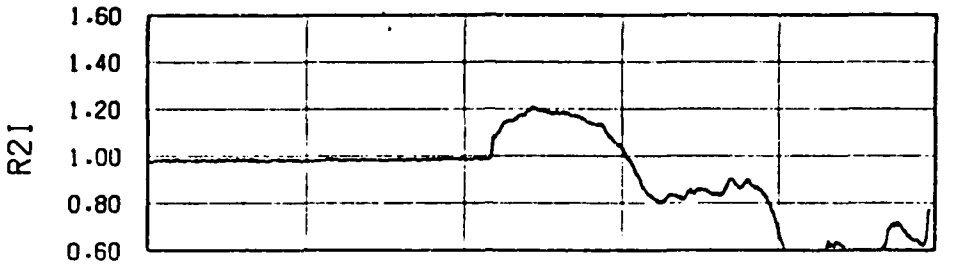

a. Run 43, Shock Tube 1, ϕ = 86 deg., Δp_s = 3.0 psi.

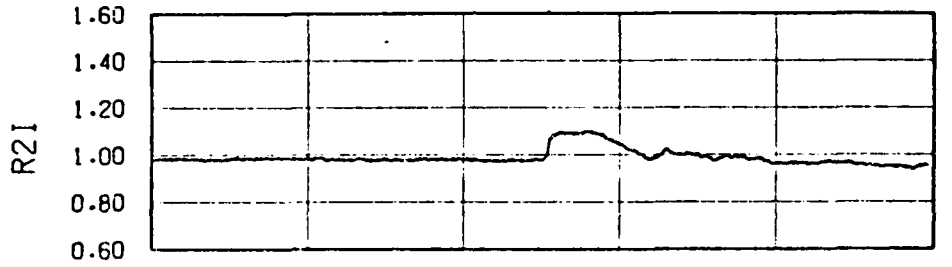

b. Run 44, Shock Tube 2, ϕ = 107 deg., Δp_s = 4.0 psi.

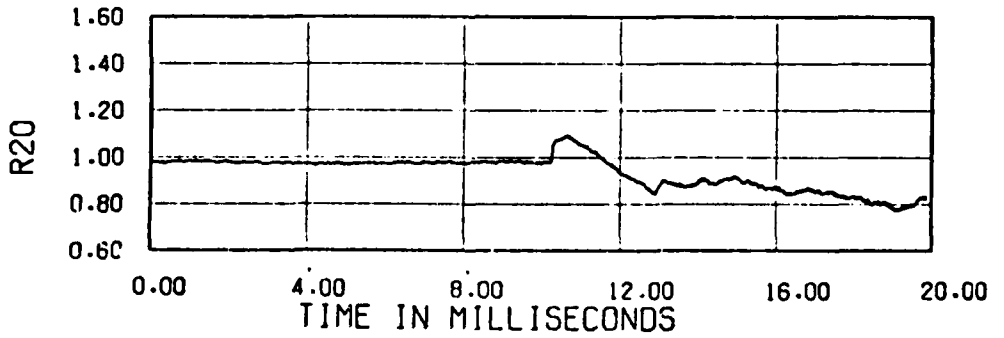

c. Run 45, Shock Tube 3, ϕ = -105 deg., Δp_s = 4.2 psi.

Figure 3.29. Effect of blast intercept angle on engine-face mean total pressure in leeward inlet at Mach 0.90. Weight flow 350 lb/s (nom). Blast shock overpressure 3.7 psi (nom).

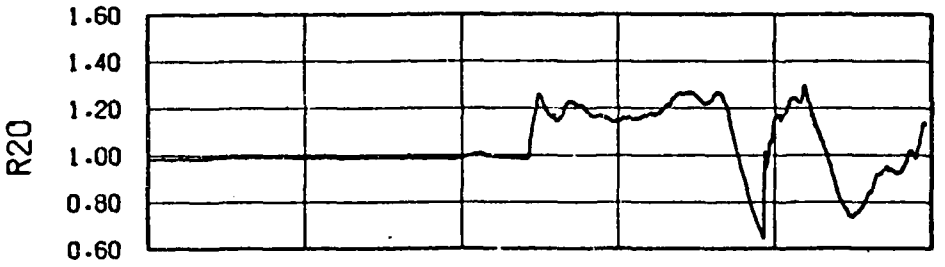

a. Run 6, W2R-FS = 302 lb/s, Δp_s = 2.6 psi.

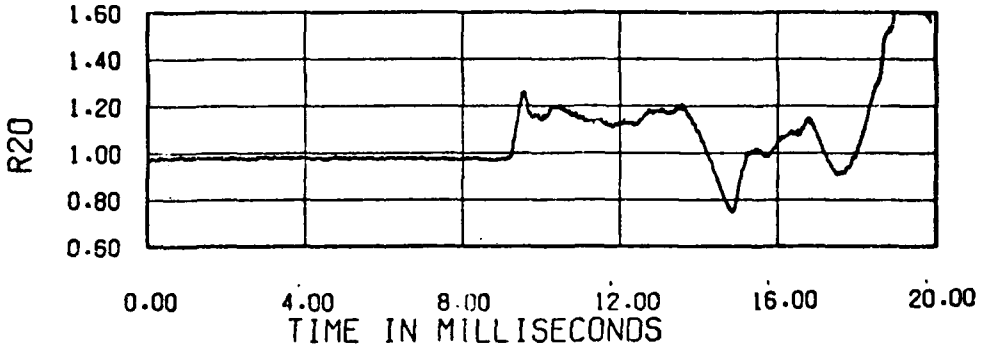

b. Run 11, W2R-FS = 351 lb/s, Δp_s = 3.0 psi.

Figure 3.30. Effect of weight flow on engine-face mean total pressure in blastward inlet at Mach 0.70. Shock Tube 1. Shock overpressure 2.8 psi (nom).

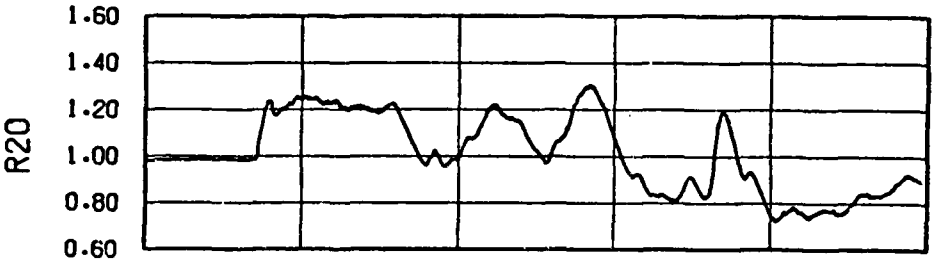

a. Run 27, W2R-FS = 299 lb/s, Δp_s = 3.0 psi.

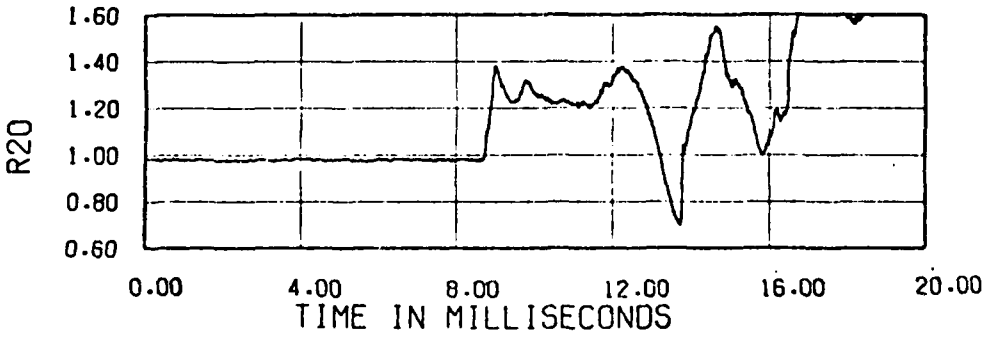

b. Run 38, W2R-FS = 348 lb/s, Δp_s = 3.6 psi.

Figure 3.31. Effect of weight flow on engine-face mean total pressure in blastward inlet at Mach 0.85. Shock Tube 1. Shock overpressure 3.3 psi (nom).

a. Run 7, W2R-FS = 302 lb/s, Δp_s = 2.6 psi.

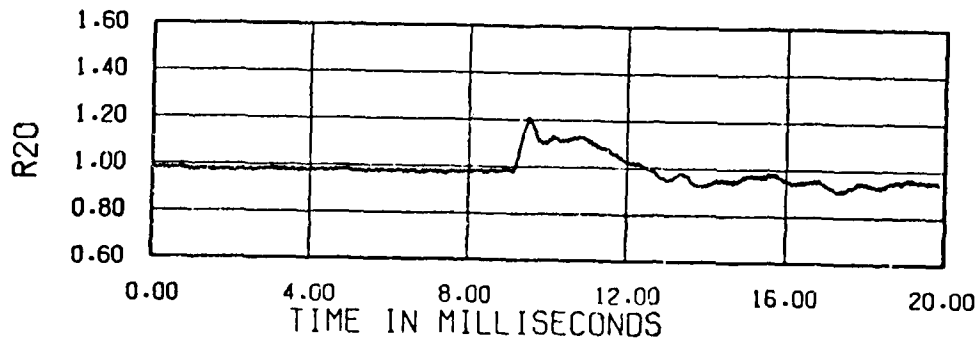

b. Run 15, W2R-FS = 351 lb/s, Δp_s = 2.8 psi.

Figure 3.32. Effect of weight flow on engine-face mean total pressure in blastward inlet at Mach 0.70. Shock Tube 2. Shock overpressure 2.7 psi (nom).

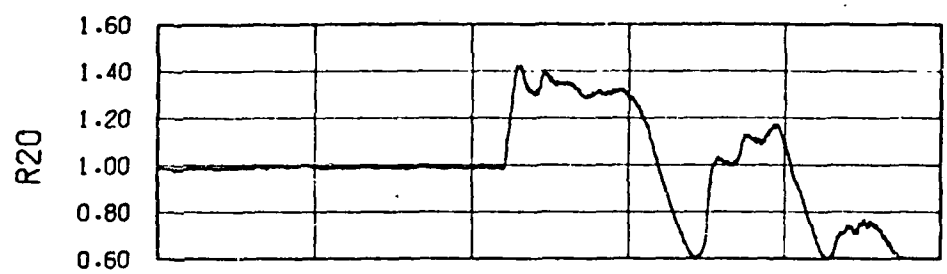

a. Run 8, W2R-FS = 304 lb/s, Δp_s = 5.0 psi.

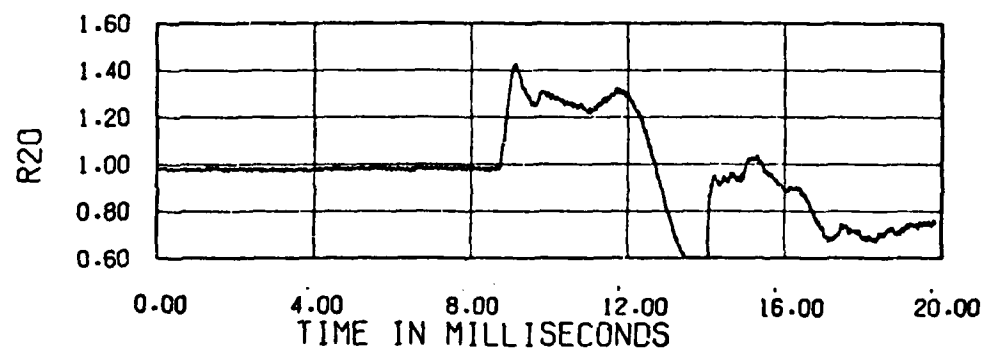

b. Run 17, W2R-FS = 348 lb/s, Δp_s = 5.0 psi.

Figure 3.33. Effect of weight flow on engine-face mean total pressure in blastward inlet at Mach 0.70. Shock Tube 2. Shock overpressure 5.0 psi (nom).

AD-A088 511 KAMAN AVIDYNE BURLINGTON MA F/G 21/5
FURTHER EVALUATION OF BLAST TESTS OF AN ENGINE INLET.(U)
MAR 79 J R RUETENIK, R F SMILEY, M A TOMAYKO DNA001-78-C-0239
UNCLASSIFIED KA-TR-165 DNA-4994F NL

2 of 3
AD A088511

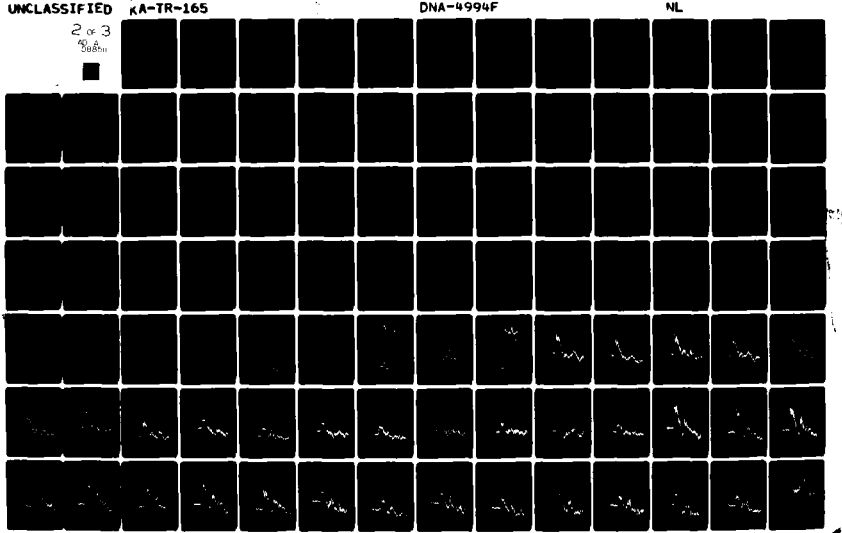

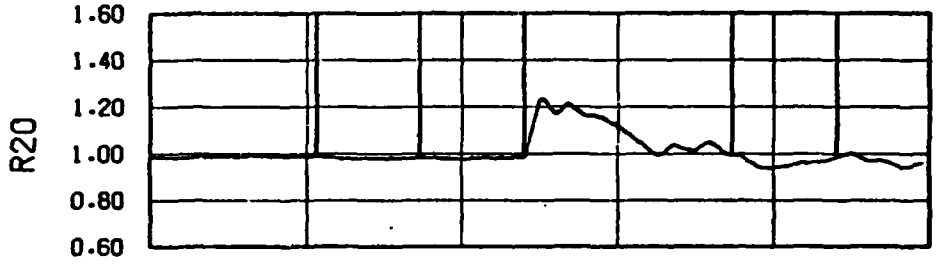

a. Run 31, W2R-FS = 300 lb/s, Δp_s = 3.8 psi.

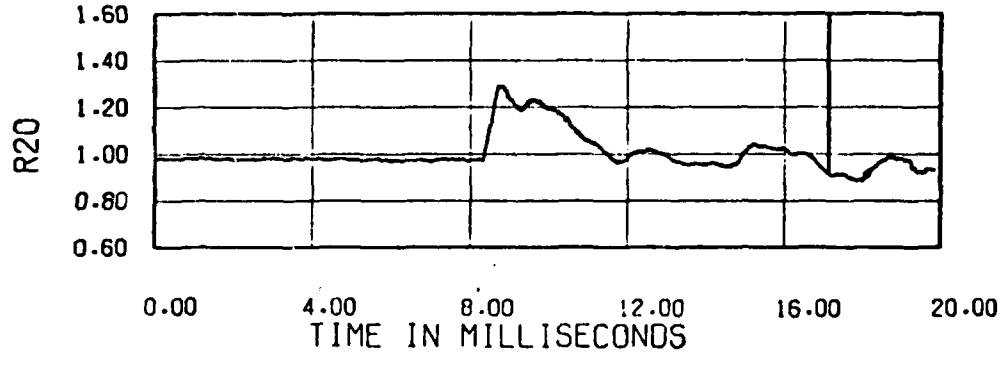

b. Run 39, W2R-FS = 348 lb/s, Δp_s = 4.0 psi.

Figure 3.34. Effect of weight flow on engine-face mean total pressure in blastward inlet at Mach 0.85. Shock Tube 2. Shock overpressure 3.9 psi (nom).

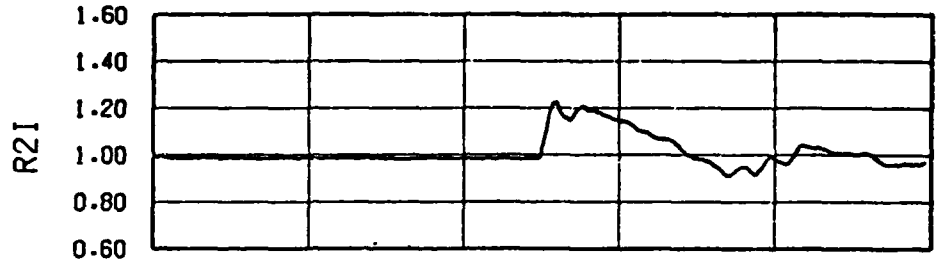

a. Run 9, W2R-FS = 300 lb/s, Δp_s = 3.0 psi.

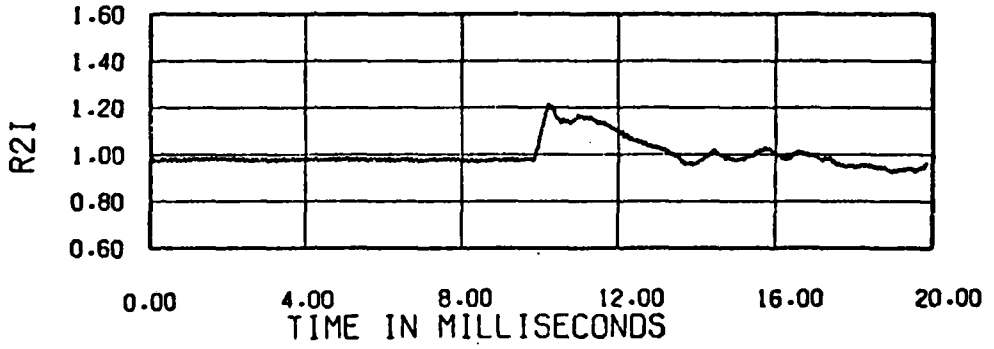

b. Run 19, W2R-FS = 344 lb/s, Δp_s = 3.0 psi.

Figure 3.35. Effect of weight flow on engine-face mean total pressure in blastward inlet at Mach 0.70. Shock Tube 3. Shock overpressure 3.0 psi (nom).

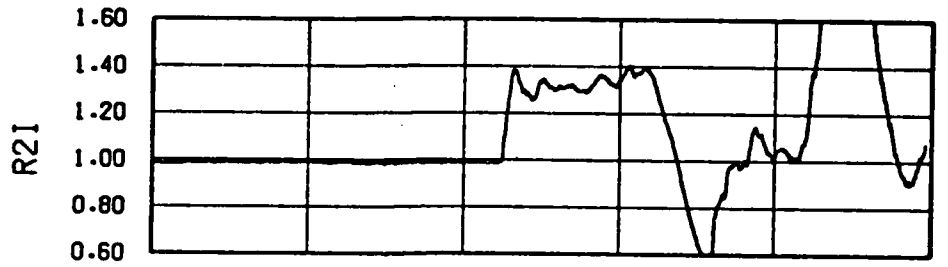

a. Run 10, W2R-FS = 300 lb/s, Δp_s = 4.4 psi.

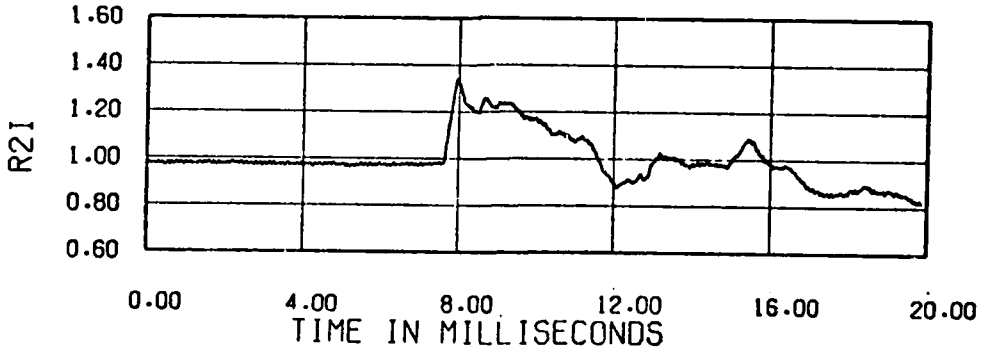

b. Run 20, W2R-FS = 343 lb/s, Δp_s = 4.2 psi.

Figure 3.36. Effect of weight flow on engine-face mean total pressure in blastward inlet at Mach 0.70. Shock Tube 3. Shock overpressure 4.3 psi (nom).

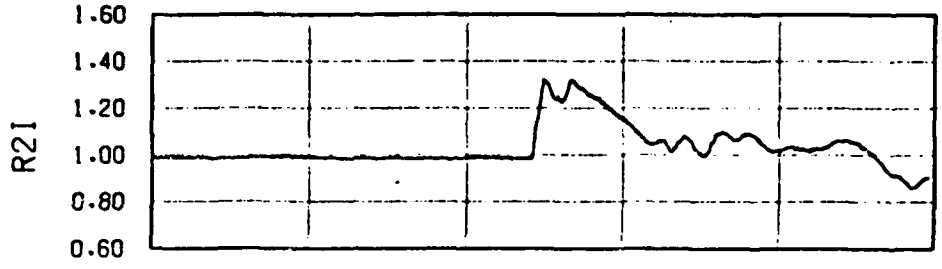

a. Run 36, W2R-FS = 296 lb/s, Δp_s = 4.4 psi.

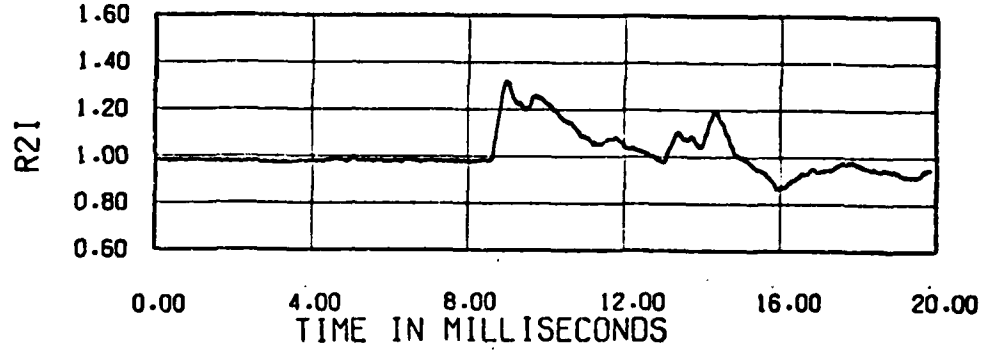

b. Run 41, W2R-FS = 347 lb/s, Δp_s = 4.4 psi.

Figure 3.37. Effect of weight flow on engine-face mean total pressure in blastward inlet at Mach 0.85. Shock Tube 3. Shock overpressure 4.4 psi (nom).

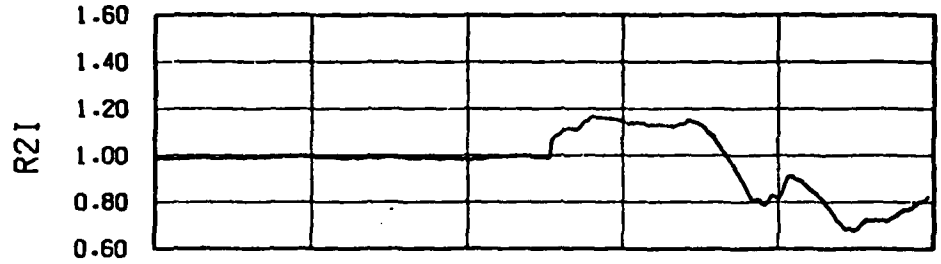

a. Run 6, W2R-FS = 300 lb/s, Δp_s = 2.6 psi.

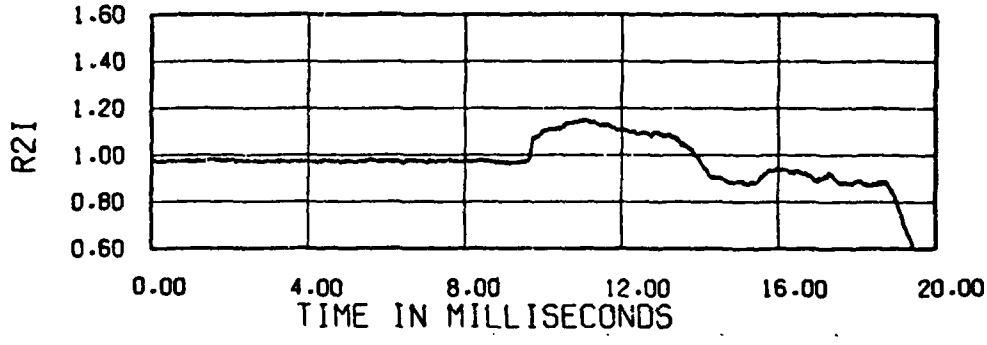

b. Run 11, W2R-FS = 351 lb/s, Δp_s = 3.0 psi.

Figure 3.38. Effect of weight flow on engine-face mean total pressure in leeward inlet at Mach 0.70. Shock Tube 1. Shock overpressure 2.8 psi (nom).

a. Run 27, W2R-FS = 299 lb/s, Δp_s = 3.0 psi.

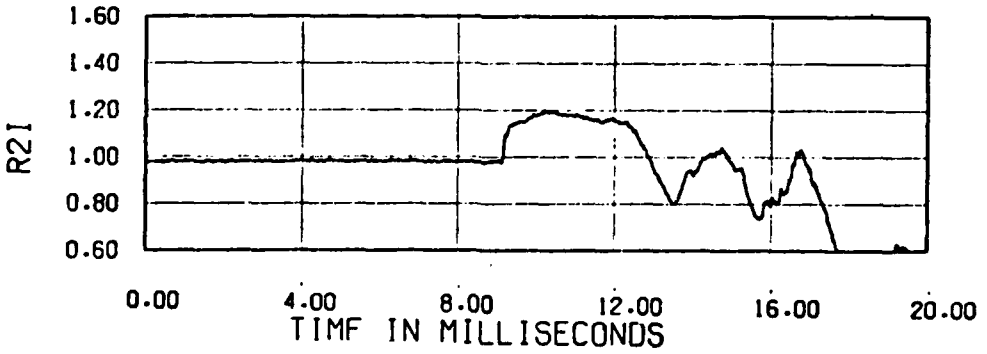

b. Run 38, W2R-FS = 347 lb/s, Δp_s = 3.6 psi.

Figure 3.39. Effect of weight flow on engine-face mean total pressure in leeward inlet at Mach 0.85. Shock Tube 1. Shock overpressure 3.3 psi (nom).

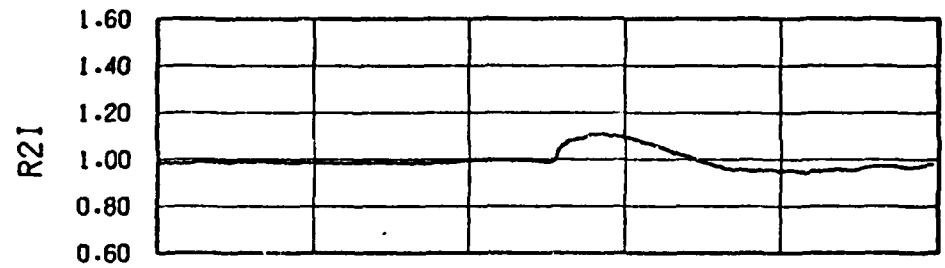

a. Run 7, W2R-FS = 302 lb/s, Δp_s = 2.6 psi.

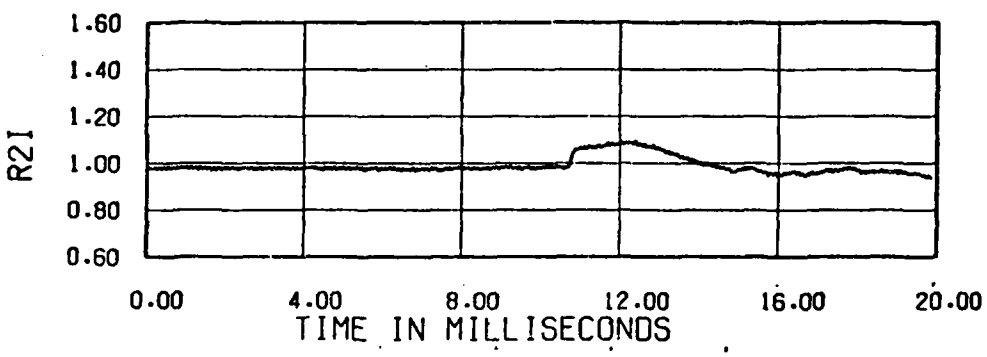

b. Run 15, W2R-FS = 344 lb/s, Δp_s = 2.8 psi.

Figure 3.40. Effect of weight flow on engine-face mean total pressure in leeward inlet at Mach 0.70. Shock Tube 2. Shock overpressure 2.7 psi (nom).

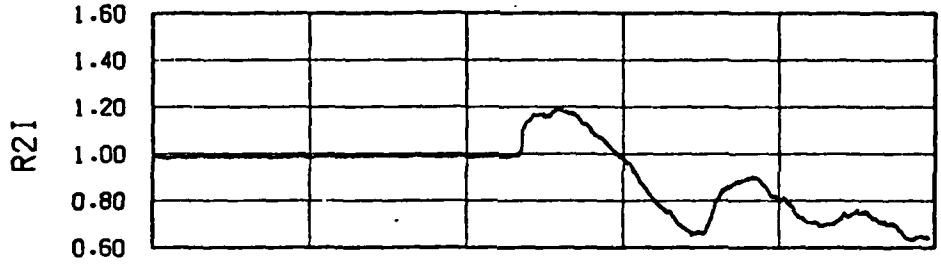

a. Run 8, W2R-FS = 302 lb/s, Δp_s = 5.0 psi.

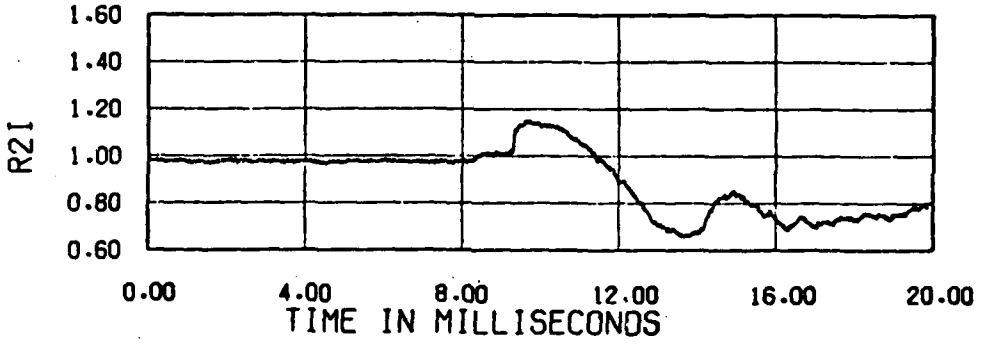

b. Run 17, W2R-FS = 344 lb/s, Δp_s = 5.0 psi.

Figure 3.41. Effect of weight flow on engine-face mean total pressure in leeward inlet at Mach 0.70. Shock Tube 2. Shock overpressure 5.0 psi (nom).

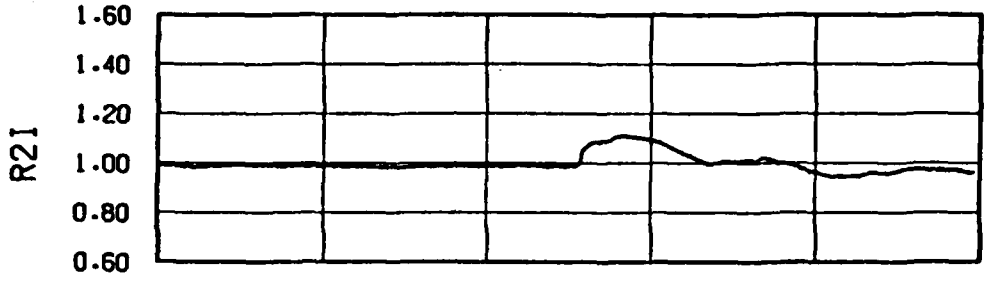

a. Run 31, W2R-FS = 300 lb/s, Δp_s = 3.8 psi.

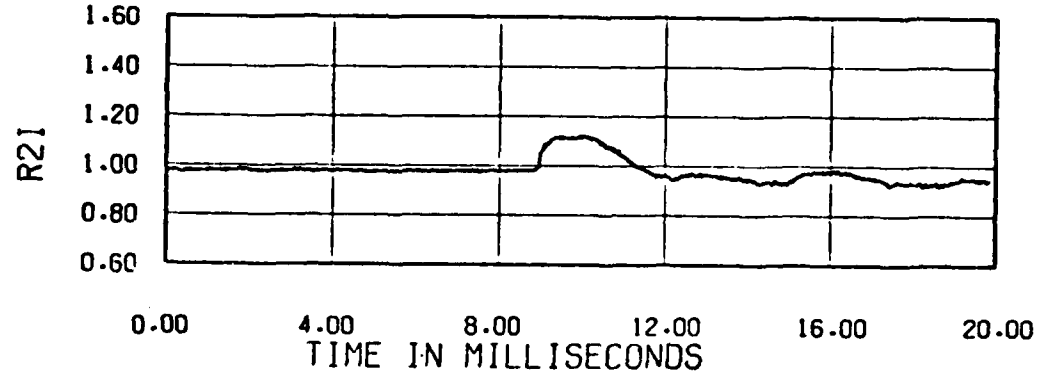

b. Run 39, W2R-FS = 347 lb/s, Δp_s = 4.0 psi.

Figure 3.42. Effect of weight flow on engine-face mean total pressure in leeward inlet at Mach 0.85. Shock Tube 2. Shock overpressure 3.9 psi (nom).

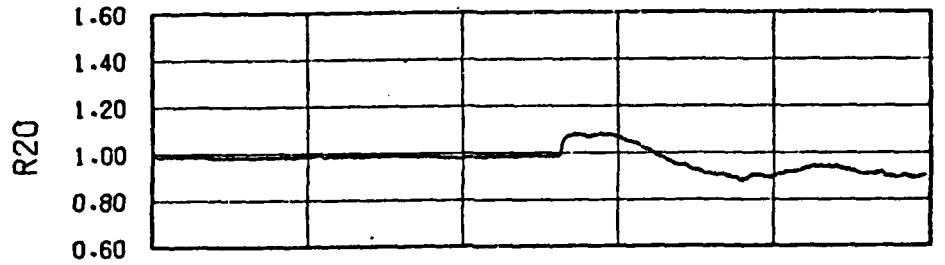

a. Run 9, W2R-FS = 302 lb/s, Δp_s = 3.0 psi.

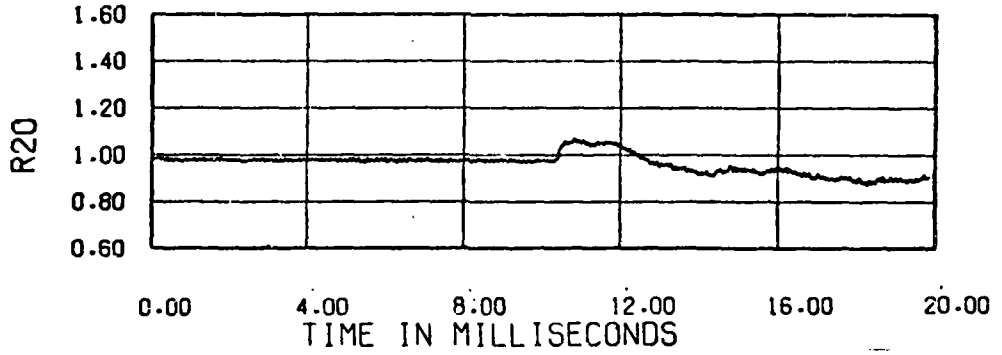

b. Run 19, W2R-FS = 351 lb/s, Δp_s = 3.0 psi.

Figure 3.43. Effect of weight flow on engine-face mean total pressure in leeward inlet at Mach 0.70. Shock Tube 3. Shock overpressure 3.0 psi (nom).

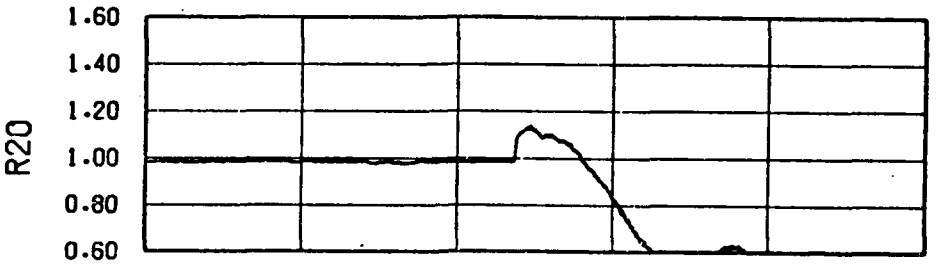

a. Run 10, W2R-FS = 303 lb/s, Δp_s = 4.4 psi.

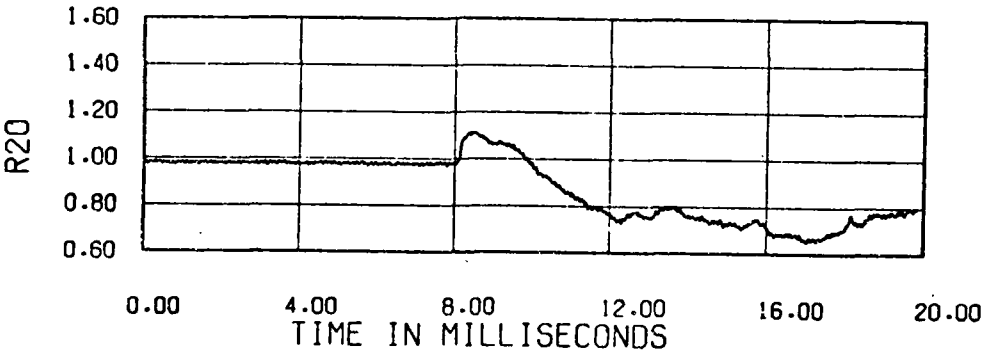

b. Run 20, W2R-FS = 348 lb/s, Δp_s = 4.2 psi.

Figure 3.44. Effect of weight flow on engine-face mean total pressure in leeward inlet at Mach 0.70. Shock Tube 3. Shock overpressure 4.3 psi (nom).

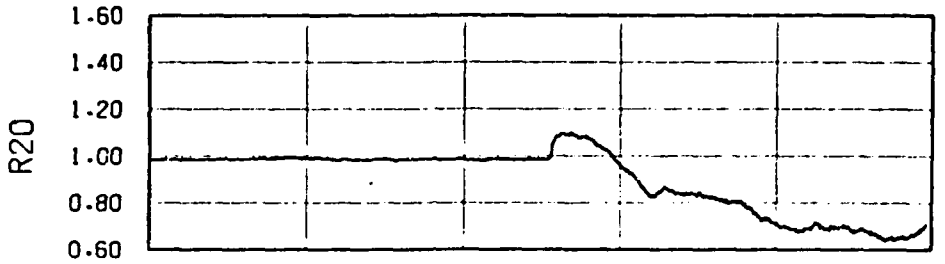

a. Run 36, W2R-FS = 298 lb/s, Δp_s = 4.4 psi.

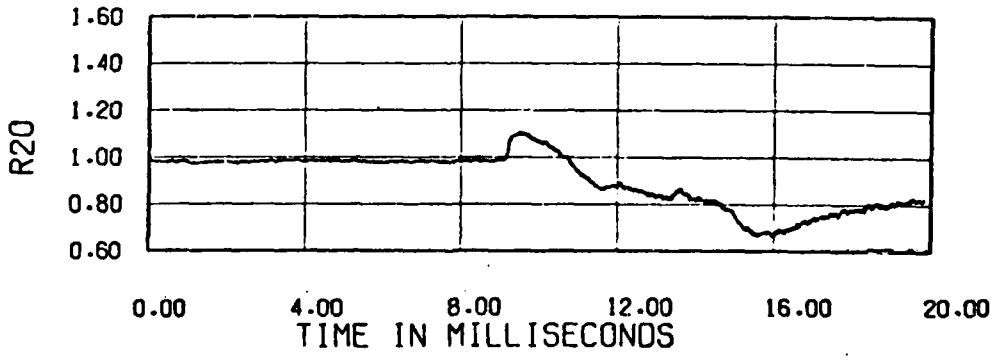

b. Run 41, W2R-FS = 348 lb/s, Δp_s = 4.4 psi.

Figure 3.45. Effect of weight flow on engine-face mean total pressure in leeward inlet at Mach 0.85. Shock Tube 3. Shock overpressure 4.4 psi (nom).

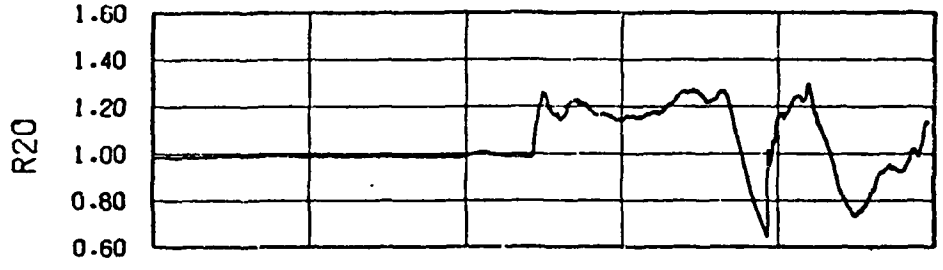

a. Run 6, Mach 0.70, Δp_s = 2.6 psi.

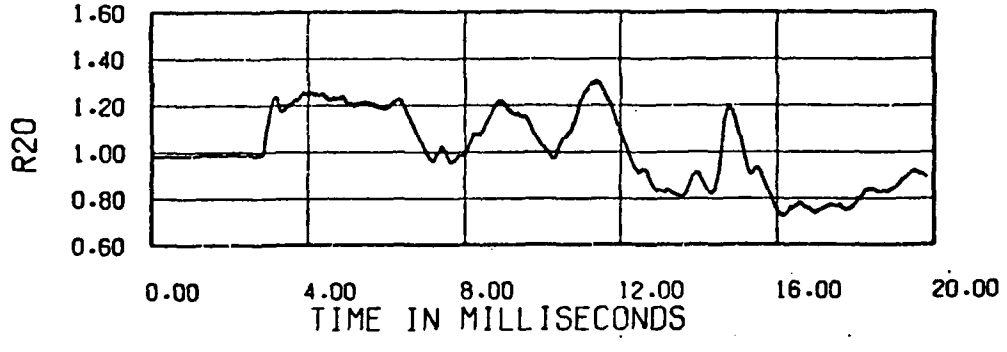

b. Run 27, Mach 0.85, Δp_s = 3.0 psi.

Figure 3.46. Effect of Mach number on engine-face mean total pressure in blastward inlet Weight flow 300 lb/s (nom). Shock Tube 1. Blast shock overpressure 2.8 psi (nom).

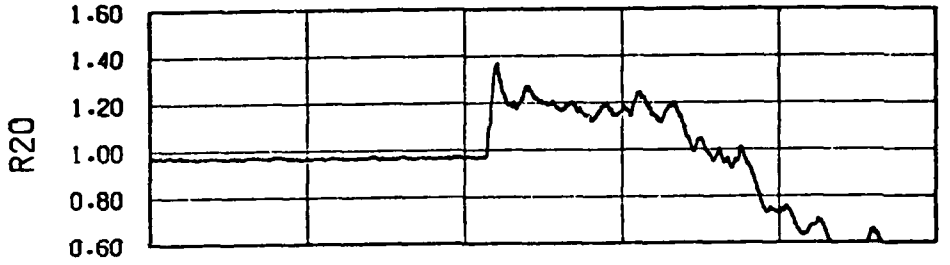

a. Run 3, Mach 0.55, Δp_s = 3.7 psi.

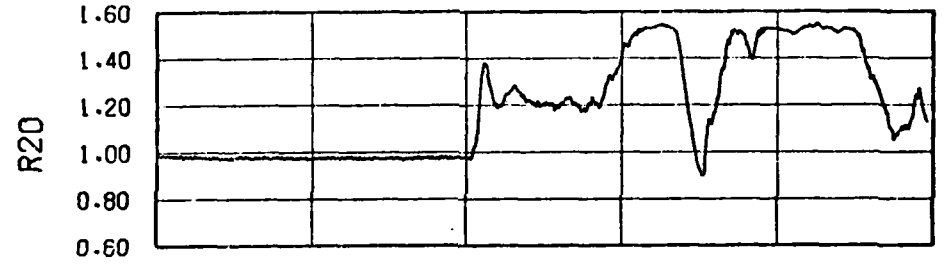

b. Run 12, Mach 0.70, Δp_s = 3.8 psi.

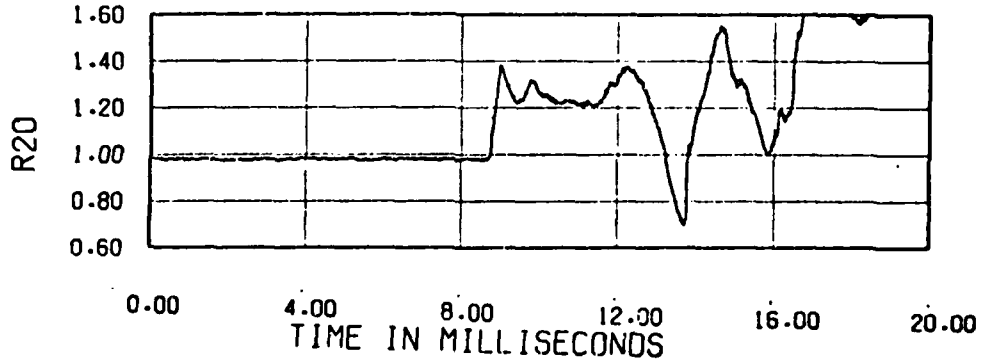

c. Run 38, Mach 0.85, Δp_s = 3.6 psi.

Figure 3.47. Effect of Mach number on engine-face mean total pressure in blastward inlet. Weight flow 350 lb/s (nom). Shock Tube 1. Blast shock overpressure 3.7 psi (nom).

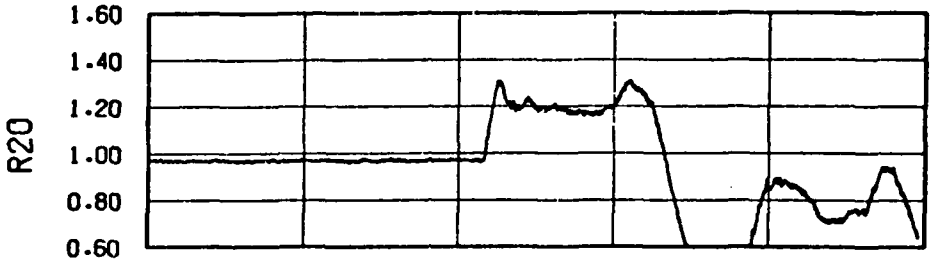

a. Run 4, Mach 0.55, Δp_s = 3.8 psi.

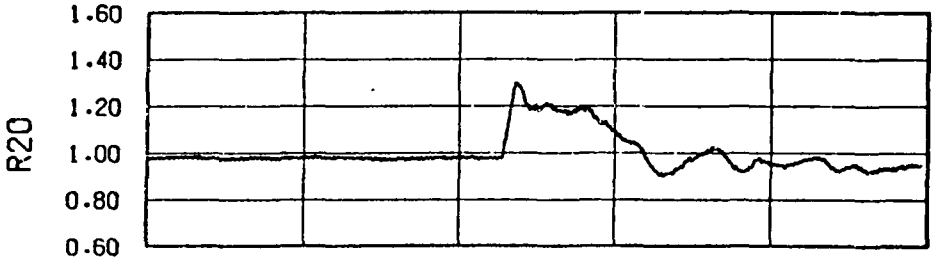

b. Run 16, Mach 0.70, Δp_s = 3.8 psi.

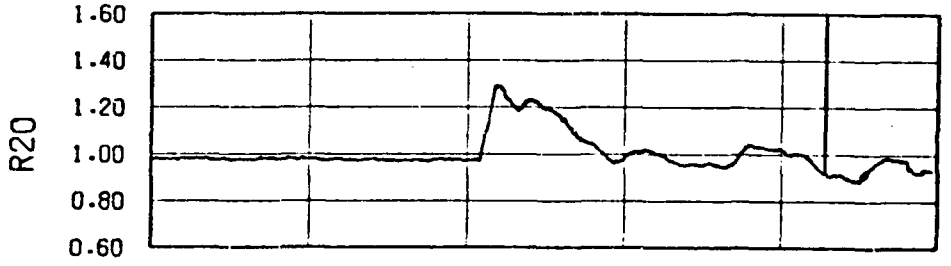

c. Run 39, Mach 0.85, Δp_s = 4.0 psi.

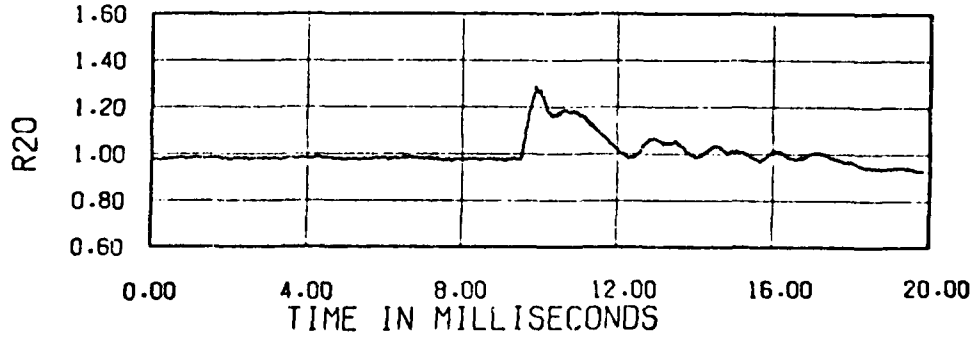

d. Run 44, Mach 0.90, Δp_s = 4.0 psi.

Figure 3.48. Effect of Mach number on engine-face mean total pressure in blastward inlet. Weight flow 350 lb/s (nom). Shock Tube 2. Blast shock overpressure 3.9 psi (nom).

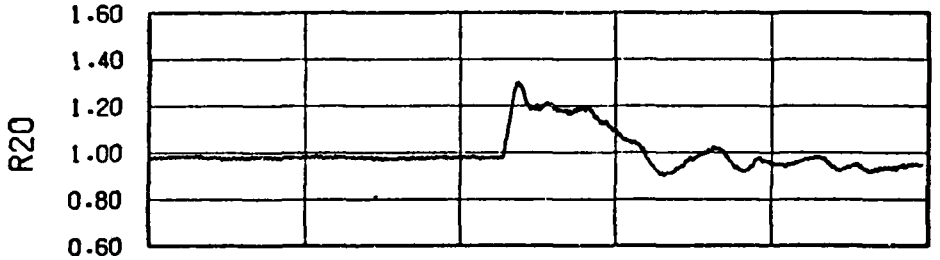

a. Run 16, Mach 0.70, Δp_s = 3.8 psi.

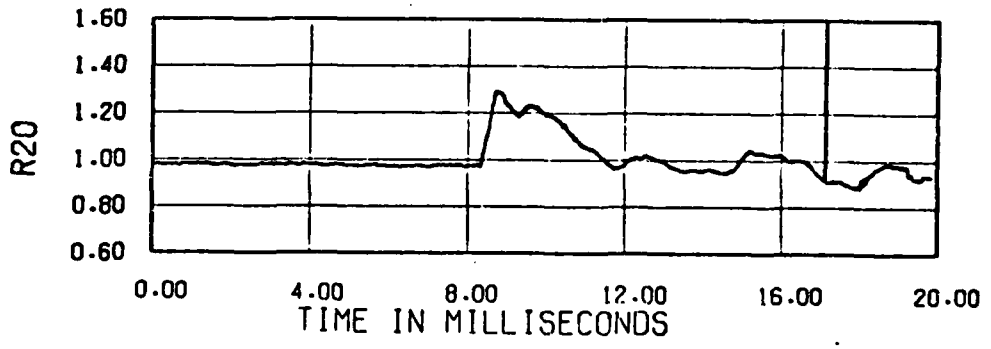

b. Run 39, Mach 0.85, Δp_s = 4.0 psi.

Figure 3.49. Effect of Mach number on engine-face mean total pressure in blastward inlet. Weight flow 350 lb/s (nom). Shock Tube 2. Blast shock overpressure 3.9 psi (nom).

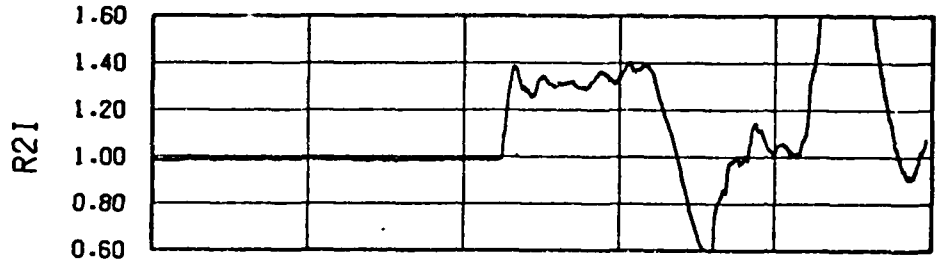

a. Run 10, Mach 0.70, Δp_s = 4.4 psi.

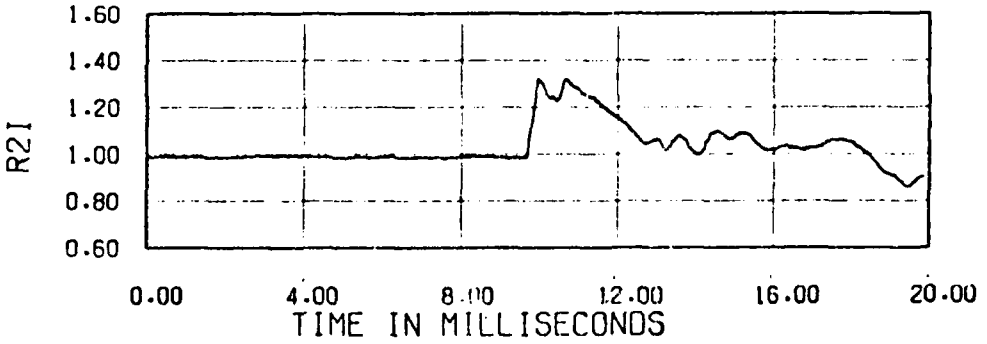

b. Run 36, Mach 0.85, Δp_s = 4.4 psi.

Figure 3.50. Effect of Mach number on engine-face mean total pressure in blastward inlet. Weight flow 300 lb/s (nom). Shock Tube 3. Blast shock overpressure 4.4 psi (nom).

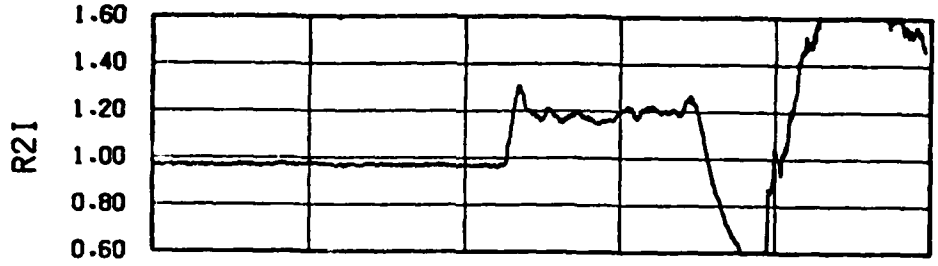

a. Run 5, Mach 0.55, Δp_s = 4.0 psi.

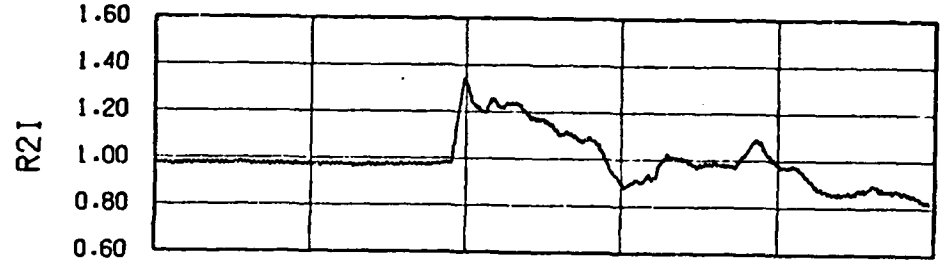

b. Run 20, Mach 0.70, Δp_s = 4.2 psi.

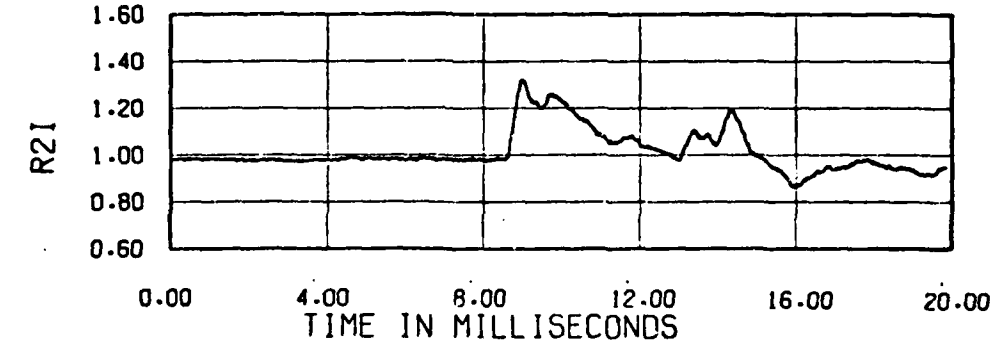

c. Run 41, Mach 0.85, Δp_s = 4.4 psi.

Figure 3.51. Effect of Mach number on engine-face mean total pressure in blastward inlet. Weight flow 350 lb/s (nom). Shock Tube 3. Blast shock overpressure 4.2 psi (nom).

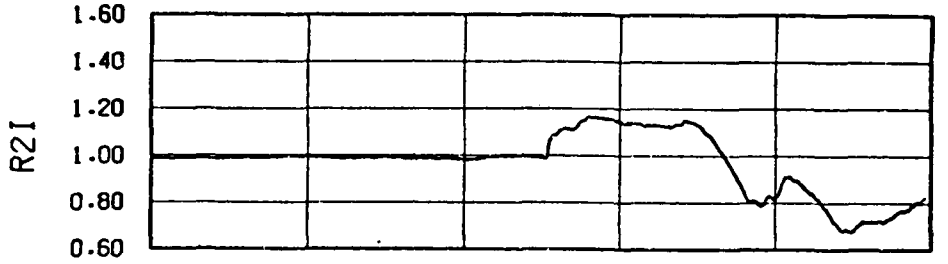

a. Run 6, Mach 0.70, Δp_s = 2.6 psi.

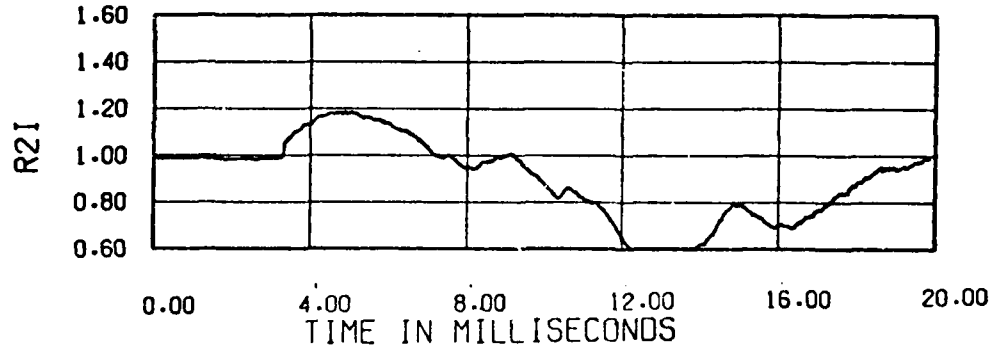

b. Run 27, Mach 0.85, Δp_s = 3.0 psi.

Figure 3.52. Effect of Mach number on engine-face mean total pressure in leeward inlet. Weight flow 300 lb/s (nom). Shock Tube 1. Blast shock overpressure 2.8 psi (nom).

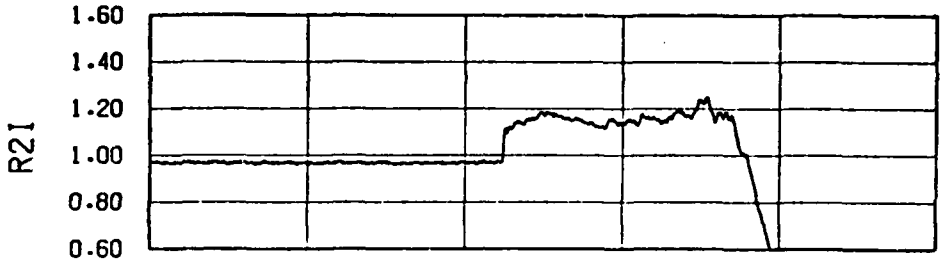

a. Run 3, Mach 0.55, Δp_s = 3.7 psi.

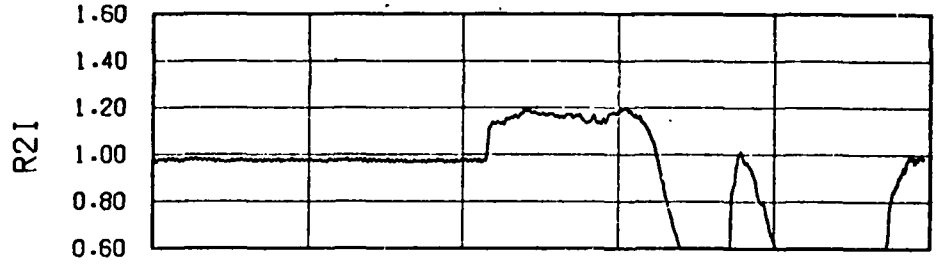

b. Run 12, Mach 0.70, Δp_s = 3.8 psi.

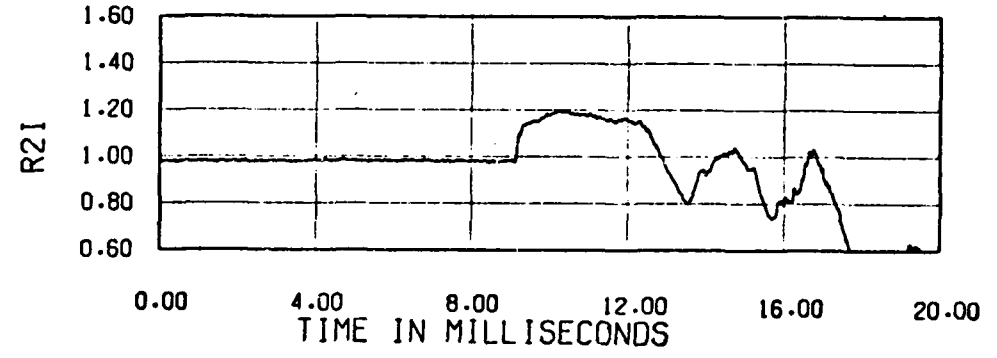

c. Run 38, Mach 0.85, Δp_s = 3.6 psi.

Figure 3.53. Effect of Mach number on engine-face mean total pressure in leeward inlet. Weight flow 350 lb/s (nom). Shock Tube 1. Blast shock overpressure 3.7 psi (nom).

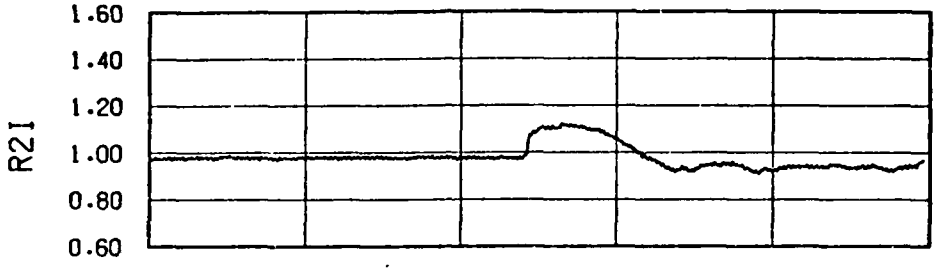

a. Run 16, Mach 0.70, Δp_s = 3.8 psi.

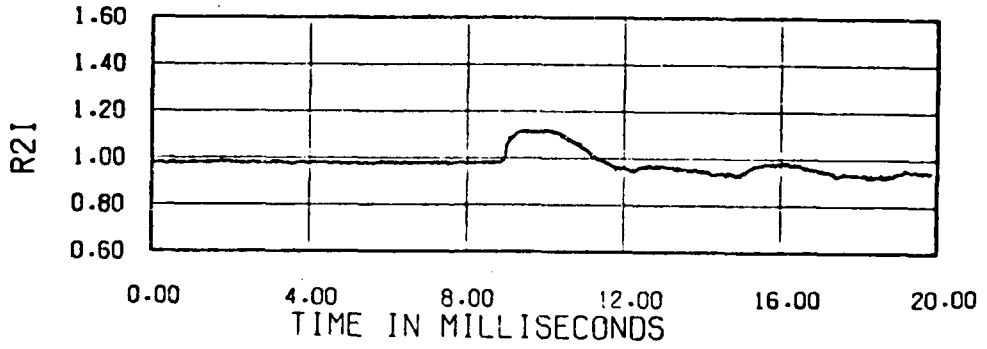

b. Run 39, Mach 0.85, Δp_s = 4.0 psi.

Figure 3.54. Effect of Mach number on engine-face mean total pressure in leeward inlet. Weight flow 350 lb/s (nom). Shock Tube 2. Blast shock overpressure 3.9 psi (nom).

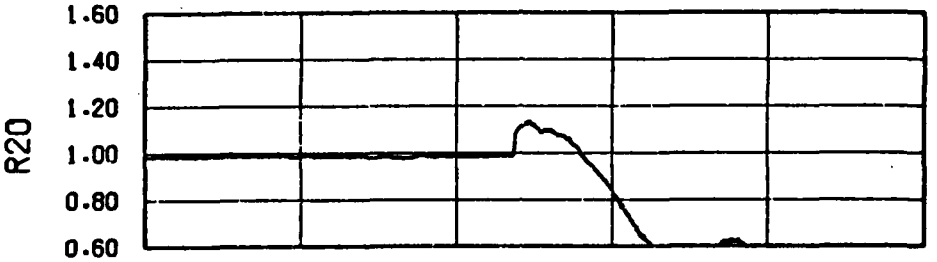

a. Run 10, Mach 0.70, Δp_s = 4.4 psi.

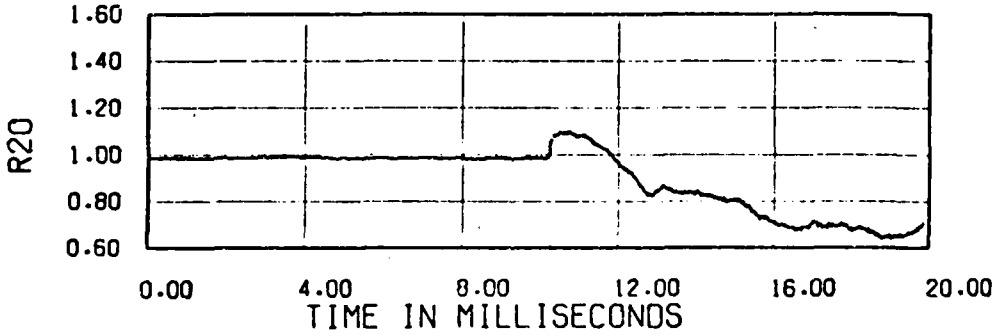

b. Run 36, Mach 0.85, Δp_s = 4.4 psi.

Figure 3.55. Effect of Mach number on engine-face mean total pressure in leeward inlet. Weight flow 300 lb/s (nom). Shock Tube 3. Blast shock overpressure 4.4 psi (nom).

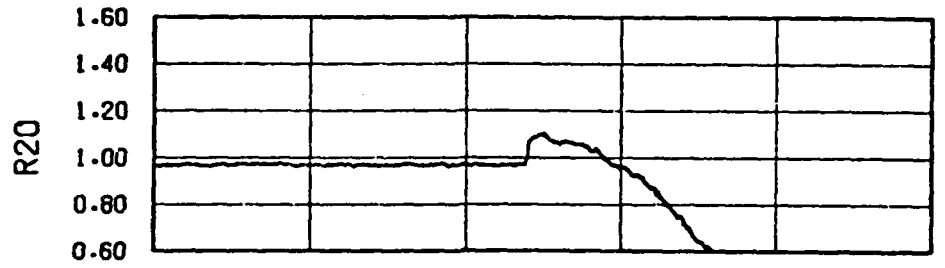

a. Run 5, Mach 0.55, Δp_s = 4.0 psi.

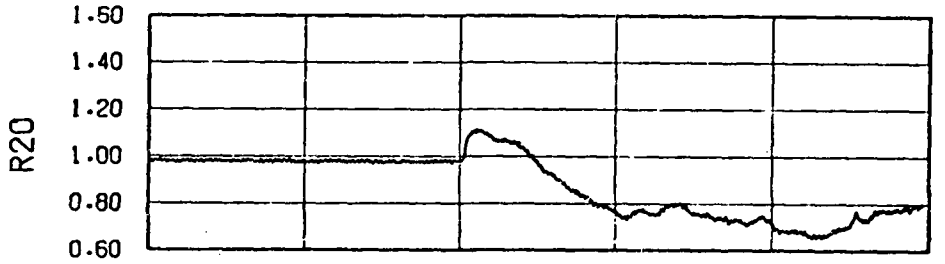

b. Run 20, Mach 0.70, Δp_s = 4.2 psi.

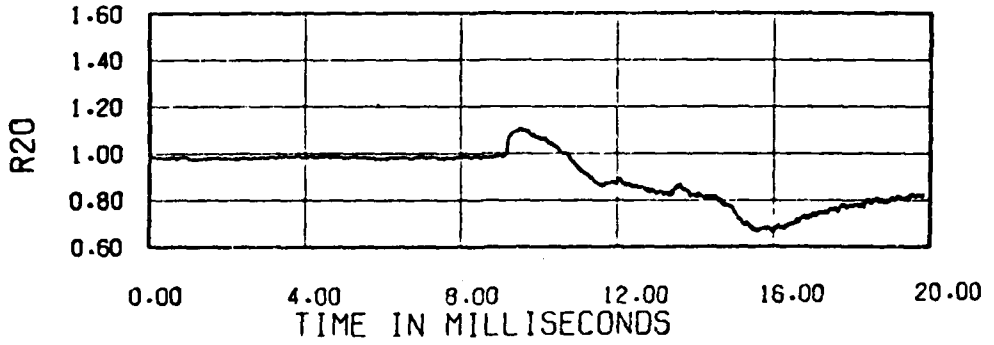

c. Run 41, Mach 0.85, Δp_s = 4.4 psi.

Figure 3.56. Effect of Mach number on engine-face mean total pressure in leeward inlet. Weight flow 350 lb/s (nom). Shock Tube 3. Blast shock overpressure 4.2 psi (nom).

SECTION 4
SPECIFIC EFFECTS OF BLAST AND OPERATIONAL VARIABLES ON ENGINE-FACE MEAN TOTAL PRESSURE

In Section 3, the general features of the reduced mean total pressure at the engine face, RTI and RTO, are examined as a function of the test variables. In this section factors affecting the first and second peaks for the blastward inlet, for which the first peak is the larger, and separation within the leeward inlet are examined.

4-1 VARIATION IN FIRST PEAK OF MEAN TOTAL PRESSURE FOR BLASTWARD INLET.

The first peak in the mean total pressure increment at the engine face is generally during the blast period the highest. Therefore its magnitude is an evident measure of the effect of the wave in the inlet. The factors affecting this magnitude will be analyzed in this section from the test results and BID code calculations.

4-1.1 Effect of Incident Total-Pressure Increment.

In Reference 2.1, Section VII, it is shown that the change in the mean total pressure at the engine face for the blastward inlet has about the same ratio to the incident total-pressure change (i.e., across the blast shock) for intercept angles of 90, 105 and 135 degrees. This comparison was based on results of BID code calculations. In this section the relationship will be examined for the test data.

The jump in mean total pressure at the engine face, from the preintercept value to the first peak after shock arrival, $\Delta p'_{t_2}$ in Figure 4.1, was measured for each run. It is plotted in Figure 4.2 against the jump in total pressure across the blast shock $p_{t_{o_s}}$, in the wind tunnel. The straight line through the median of these data (50 percent on each side of the line) is given by

$$\Delta p'_{t_2} = 1.41\ \Delta p_{t_{o_s}} \tag{4.1}$$

Ninety percent of the data points fall within the $\pm$11 percent of this straight line.

This result means that the jump in the mean total pressure at the engine face to the first peak was roughly 1.41 times as large as the jump in the total pressure across the blast shock in the free stream. Because the spread was essentially only ±11 percent, it is concluded that the jump at the engine face was primarily a function of the jump at the shock.

There are two conclusions from this result. First, the blast-ward inlet acted somewhat as an amplifier of the total pressure increase produced by the blast shock, by a factor of approximately 1.41. Second, the jump in total pressure across the blast shock is the principal factor causing the jump in mean total pressure at the engine face.

Perhaps the 11-percent accuracy of prediction (90 percentile) may be sufficient for most purposes. But an examination will be made in the remainder of this section to identify the factors involved in this remaining spread.

4-1.2 Effect of Test Variables on Engine-Face First-Peak Ratio.

In this subsection, the data will be examined to determine the dependence of $\frac{\Delta p'_{t_2}}{\Delta p_{t_{o_s}}}$, called hereafter "the engine-face peak ratio," upon the test variables.

4-1.2.1 Shock Overpressure Effect.

The engine-face peak ratio is plotted in Figure 4.3 as a function of shock overpressure for Mach 0.70 and 0.85 and full-scale reduced weight flows of 300 and 350 lb/s. There is no apparent consistent trend with shock overpressure.

4-1.2.2 Shock Intercept Angle Effect.

The variation of the engine-face peak ratio, with intercept angle is presented in Figure 4.4 for full-scale reduced weight flows of 300 and 330-350 lb/s. Over the limited range of intercepts tested, there is no clear variation with intercept angle at either mass flow rate.

Results of calculations made with the BID code are plotted for comparison in Figure 4.4b. Results for angles of 135 degrees and greater are not plotted because the reflected wave from the throttle returned to the engine face before the first peak was attained. The BID results indicate the peak ratio is essentially constant over the region of the test data. The BID value is at the low end of the test data, which is attributed to some dissipative effects in the calculations. The BID code results indicate that the peak ratio would be less than the approximate value of 1.41 from these tests.

4-1.2.3 Weight Flow Effect.

The engine-face peak ratio is plotted in Figure 4.5 as a function of the full-scale reduced weight flow, W2R.

The effect of the weight flow on the peak ratio appears to depend upon the strength of the incident shock, based on the data for Mach 0.70, Figure 4.5a. For shocks of 2.2 to 3.0 psi, the peak ratio decreases with weight flow (comparative data are available only for Mach 0.70). For stronger shocks, of 4.0 to 5.0 psi, the ratio at Mach 0.55 decreases with weight flow, at Mach 0.70 it is constant or increases and at Mach 0.85 it increases markedly with weight flow.

4-1.2.4 Mach Number Effect.

The engine-face peak ratio is presented in Figure 4.6 as a function of Mach number.

There appears to be some effect of Mach number on the peak ratio, but it is a weak effect, and the dependence appears to be a function of the weight flow, W2R. At 300 lb/s, the trend is weak, but it slightly decreases with Mach number. At 350 lb/s, the peak ratio increases with Mach number.

4-2 VARIATION IN SECOND PEAK OF MEAN TOTAL PRESSURE AT ENGINE FACE FOR BLASTWARD INLET.

The wave entering the inlet, that produces the first pressure peak in the reduced mean total pressure at the engine face, RTI' and RTO', Figure 4.1, partially reflects from the engine (and also passes

through). A principal concern about the reflected wave is the possibility of its producing separation of the flow within the inlet, by means of the adverse pressure gradient it presents. The separation in turn could produce unacceptable distortion at the engine face, resulting in stall or surge and engine flameout.

The characteristics of the second peak at the engine face are a function of the blast and inlet variables, as shown in Section 3. These characteristics include the steepness of the rise to the second peak, the magnitude of the second peak and the time separation between the first and second peaks. The factors causing separation of the flow under these transient conditions are not well understood. Therefore no attempt will be made here to relate quantitatively the characteristics of the second peak with the blast and inlet variables, as was done for the first peak in Section 4.1. Instead only the qualitative characteristics of the second peak will be reviewed here from the data presented in Section 3.

4-2.1 Effect of Shock Overpressure.

The shape of the rise in RTI and RTO to the second peak is found to be a function of the shock overpressure. As the overpressure is increased, the rise steepens from a compression wave to a quite distinct shock wave (instantaneous pressure rise). This steepening is expected to have a significant effect on the boundary-layer separation.

This steepening of the rise to the second peak is in contrast to the observed rise time to the first peak. The latter was essentially independent of the shock overpressure.

The magnitude of the rise, from the initial point of rise to the second peak, is found to be essentially independent of the shock overpressure.

4-2.2 Effect of Intercept Angle.

The rise to the second peak is steeper to some degree for lower intercept angles (more head-on). In general the magnitude of the jump to the second peak also increases with decreasing intercept angle. This is to be expected from the dependence of the first peak on the

intercept angle: as the angle is decreased, the jump in incident total pressure increment increases, so the magnitude of the first peak is greater. This stronger wave then results in a stronger reflection from the throttle (simulated engine effect).

4-2.3 Effect of Weight Flow.

The magnitude of the rise in RTI and RTO to the second peak is essentially always greater for the lower weight flows. This resulted for most of the Mach numbers tested and for all three shock tubes.

This result may have importance for aircraft in flight under high thrust conditions, such as during base escape, where the weight flow would be high. The weaker reflected wave might result in reducing the possibility for separating the flow within the inlet and distorting the flow at the engine face.

4-2.4 Effect of Mach Number.

There was no observable effect of the Mach number on the strength of the reflected shock wave, as measured by the rise to the second peak of RTI and RTO.

4-3 SUMMARY FOR BLASTWARD INLET.

The magnitude of the jump in mean total pressure at the engine face, $\Delta p'_{t_o}$, in these tests was primarily proportional to the jump in total pressure across the incident shock, $\Delta p_{t_{o_s}}$, within $\pm$11 percent (90 percentile). (The remaining effect was a function principally of the engine-face corrected weight flow and slightly a function of Mach number.) Therefore the jump would increase with increasing shock overpressure and decreasing intercept angle.

The first peak of the mean total pressure at the engine face was more peaked (sharper, spike) for intercepts at smaller angles, more head-on.

The reflected shock from the engine-simulation throttle produced a second peak in the mean total pressure at the engine face. This reflected wave is of concern because of possible separation of the flow within the inlet that might result from its presence.

The pressure rise to the second peak steepened with increasing shock overpressures and, to some degree, with lower intercept angles. The magnitude of the jump at the engine face definitely increased with lower intercept angles. Lower weight flows also produced greater rises to the second peak, but Mach number had no apparent effect.

The BID code correlates with the trend of the variation of the jump to the initial peak in total pressure as a function of shock intercept angle.

4-4 FEATURES OF MEAN TOTAL PRESSURE FOR LEEWARD INLET.

The profile of the engine-face mean total pressure for the leeward inlet varied considerably between runs. However there were definite characteristic features of most of the profiles which are illustrated in Figure 4.7.

The initial shock jump for the leeward inlet, as for the blastward inlet, is one-half or less, generally, of the jump to the peak. This initial jump is produced by the first shock that comes down the inlet. That shock is followed by other shocks, produced by shock reflections and diffractions, which produce the further pressure rise.

The total pressure in the records then generally levels off until reflections of these waves return from the throttle (simulated engine). For the remainder of the test period after the second peak the total pressure either remains essentially steady or it falls off. The fall-off is attributed in some cases to decay of the blast wave at the mouth of the inlet; in other cases it is attributed to possible separation of the flow from the inlet walls. Of all these effects, separation is believed to be the most detrimental to engine operation, so attention is focused here on identifying the test conditions leading to this possible separation.

4-5 FLOW SEPARATION WITHIN LEEWARD INLET.

The assessment of blast-induced separation is tabulated for each run in Table 4.1. The test conditions are tabulated in columns two through five; the assessment of separation is listed in the last three columns.

TABLE 4.1

POST-TEST ASSESSMENT OF POSSIBLE BLAST-INDUCED SEPARATION WITHIN LEEWARD INLET

Run	Nominal Mach No.	Nominal Full-Scale Reduced Weight Flow (lb/s)	Tube No	Nominal Shock Overpressure (psi)	Assessment of Blast-Induced Separation in Inlet		
					None	Likely	Masked By Blast Decay
1	0	0	2	2.7		X	
2	0.55	235	3	4.7		X	
3	0.55	350	1	3.7	X		
4	0.55	350	1	3.8		X	
5	0.55	350	1	4.0		X	
6	0.70	300	1	2.6	X		
7	0.70	300	2	2.6			X
8	0.70	300	2	5.0		?	
9	0.70	300	3	3.0			X
10	0.70	300	3	4.4			X
11	0.70	350	1	3.0	X		
12	0.70	350	1	3.8	X		
13	0.70	350	1	4.8	X		
14	0.70	350	1	4.8	X		
15	0.70	350	2	2.8			X
16	0.70	350	2	3.8			X
17	0.70	350	2	5.0		X	
18	0.70	350	2	5.2		X	
19	0.70	350	3	3.0			X
20	0.70	350	3	4.2			X
21	0.70	350	3	4.8		X	
22	0.70	350	3	5.6		X	
23	0.70	350	1	3.6		?	
24	0.70	350	2	5.8		X	
25	0.70	350	3	4.2		X	
26	0.85	300	1	2.2	X		
27	0.85	300	1	3.0	X		
28	0.85	300	1	5.0	X		
29	0.85	300	1	4.4	X		

TABLE 4.1 (Continued)

Run	Nominal Mach No.	Nominal Full-Scale Reduced Weight Flow (lb/s)	Tube No	Nominal Shock Overpressure (psi)	Assessment of Blast-Induced Separation in Inlet		
					None	Likely	Masked By Blast Decay
30	0.85	300	2	-			
31	0.85	300	2	3.8			X
32	0.85	300	2	4.8			X
33	0.85	300	2	-			
34	0.85	300	3	>2			X
35	0.85	300	3	4.0			X
36	0.85	300	3	4.4			X
37	0.85	300	3	4.8			X
38	0.85	350	1.	3.6	X		
39	0.85	350	2	4.0			X
40	0.85	350	2	5.8			X
41	0.85	350	3	4.4			X
42	0.85	350	3	5.6			X
43	0.90	350	1	3.0		?	
44	0.90	350	2	4.0			X
45	0.90	350	3	4.2			X

Separation is assessed in Table 4.1 as either: (a) none, (b) likely or (c) masked by blast decay. "None" means that there is no apparent sign of separation. "Likely" means that the mean total pressure drops as qualitatively expected if separation were present within the inlet, so it is deduced that separation was a likely cause. (This possibility has been examined in Section 7 for one run by boundary layer calculations.) "Masked by blast decay" indicates that separation is not excluded, but that it cannot be verified by visual examination of the records because of decay that was present in the blast at the inlet mouth.

At Mach 0 and 0.55 separation appears to have occurred for all but one case. That case was for the weakest shock of the tests at 350 lb/s full-scale reduced weight flow.

At Mach 0.70, for the inlet unyawed, separation evidently did not occur for Tube 1 in any test. Separation is believed to have occurred for Tubes 2 and 3. This would indicate that the intercept angle is an important factor. Whether shock overpressure is also an important factor cannot be assessed satisfactorily from these runs because the low overpressure firings from Tubes 2 and 3 also had blast decay present at the inlet. For the remaining runs, Tubes 2 and 3 had higher overpressures, except for one firing which was equal (4.8 psi).

For all firings with the inlet yawed, separation was either likely or, in the case of Run 23, possible.

At Mach 0.85 there was no separation evident for Tube 1, and blast decay masked the results for all firings from Tubes 2 and 3. At Mach 0.90 it is possible that separation occurred for Tube 1, but separation was masked by the present of blast decay for Tubes 2 and 3.

Blast decay at the leeward inlet was a result of the limitations in the size of the blast wave that was produced by the shock tubes. In spite of the large size of the tubes (22.6-in. ID), the fraction of the volume of the blast wave that was satisfactory for blast simulation was relatively small by the time the blast wave reached the inlets. At the higher Mach numbers the wave was masked downstream enough that the wave was unsatisfactory at the leeward inlet after a millisecond or so. Great care was taken to locate the shock tubes to

meet the greatest range of test conditions within the restrictions of the wind tunnel structure, but the blast wave at the leeward inlet could not be maintained without sacrificing blast simulation at the blastward inlet. The limitation in the size of blast waves that can be produced in a wind tunnel does present a restriction to wind tunnel testing of blast effects.

4-6 CONCLUSIONS.

The jump in mean total pressure at the engine face of the blastward inlet following blast intercept is found to be nearly proportional ($\pm$11 percent) to the jump in total pressure across the blast shock for the range of blast conditions tested (Δp_s=2.2-5.8 psi, ϕ=76-110 deg, W2RFS=0-354 lb/s, M=0-0.90). Therefore it primarily increases with increasing shock overpressure and decreasing intercept angle.

The reflection of the blast wave upstream from the engine (simulated by a choked throttle) is expected to be a principal factor to distortion, particularly for the blastward inlet, because of shock-boundary layer interaction, possibly resulting in separation of the flow within the inlet from the walls. The reflection produces a second peak in total pressure at the engine face for the blastward inlet. The rise in total pressure approaching the second peak steepens with increasing shock overpressure, tending to result in formation of an upstream-facing shock within the inlet at a point nearer to the engine end of the inlet, where the reflection enters. The magnitude of the rise to the second peak increases for lower intercept angles (more head-on) and lower weight flows (low engine thrust conditions). It is essentially unaffected by Mach number.

The mean total pressure at the engine face increased more slowly with time for the leeward inlet, following blast intercept, and by a smaller amount.

A rapid fall-off in total pressure from one millisecond or more after shock arrival that was observed in many cases for the leeward inlet is attributed to possible separation within the inlet. It occurred for most of the tests at Mach 0 and 0.55. At Mach 0.70 it occurred essentially only for firings from Shock Tubes 2 and 3, which produced higher angle intercepts. At Mach 0.85 and 0.9 it could not be assessed because of the limited size of the blast wave.

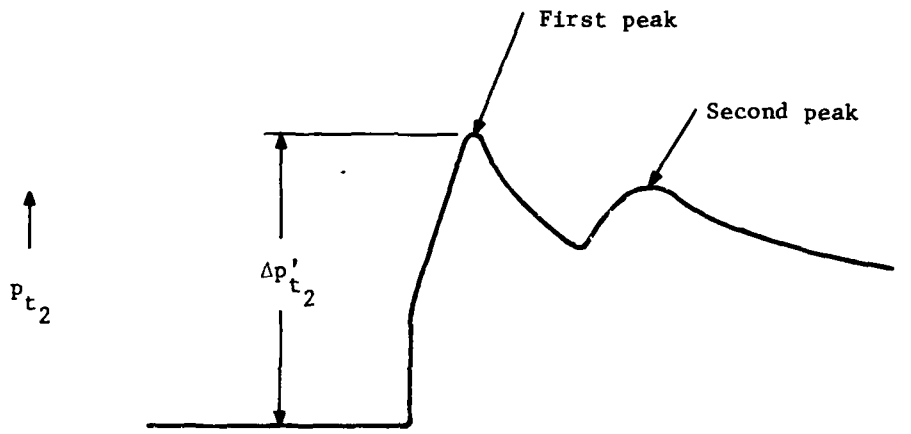

$$RT = \frac{p_{t_2}}{p_{t_0}}$$

$$\Delta RT = \frac{\Delta p_{t_2}}{p_{t_0}}$$

RT = RTI for inboard inlet
= RTO for outboard inlet

Figure 4.1. Sketch illustrating first and second peaks of engine-face mean total pressure for blastward inlet.

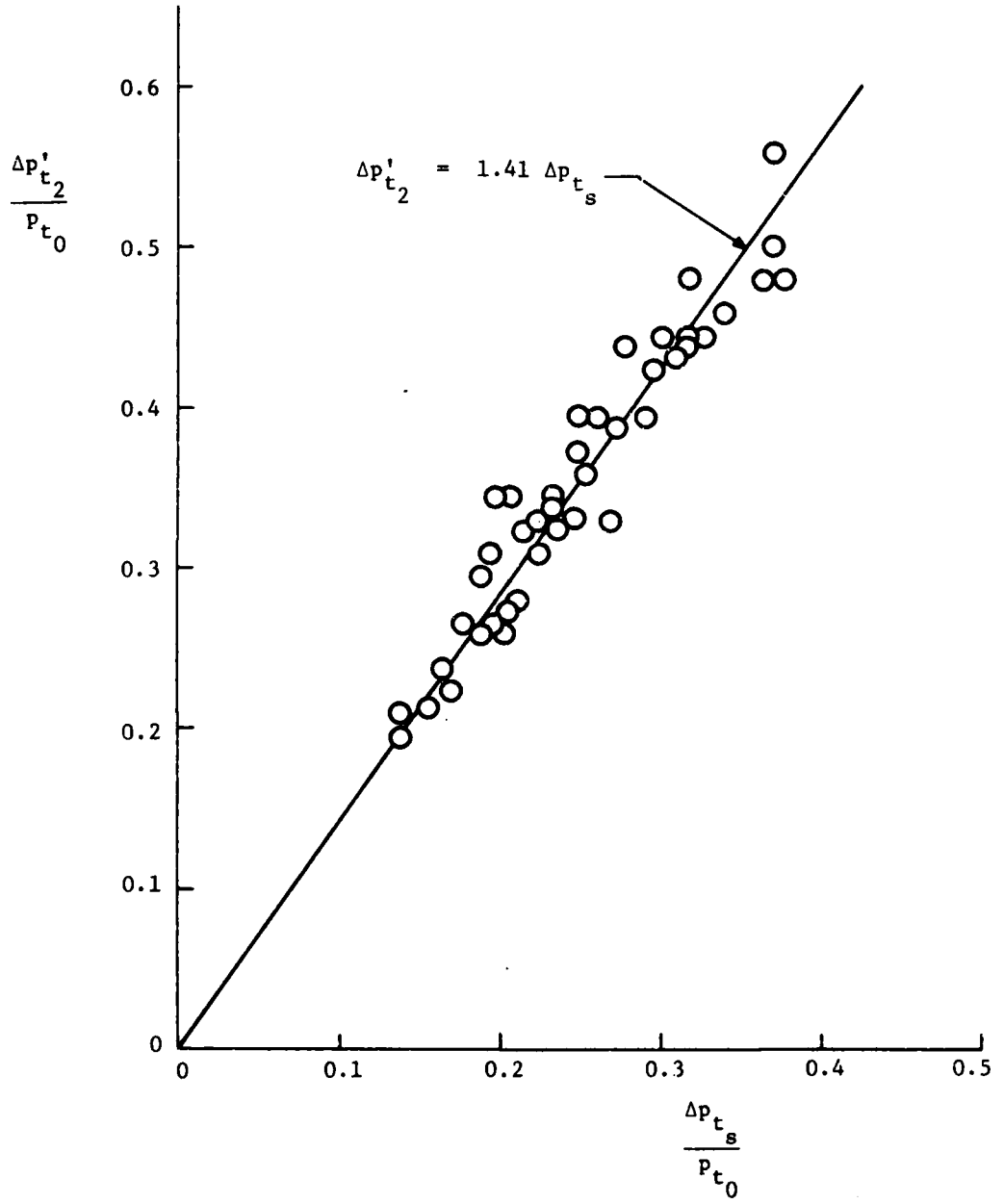

Figure 4.2. Increment in mean total pressure at blastward engine-face versus incident total pressure increment.

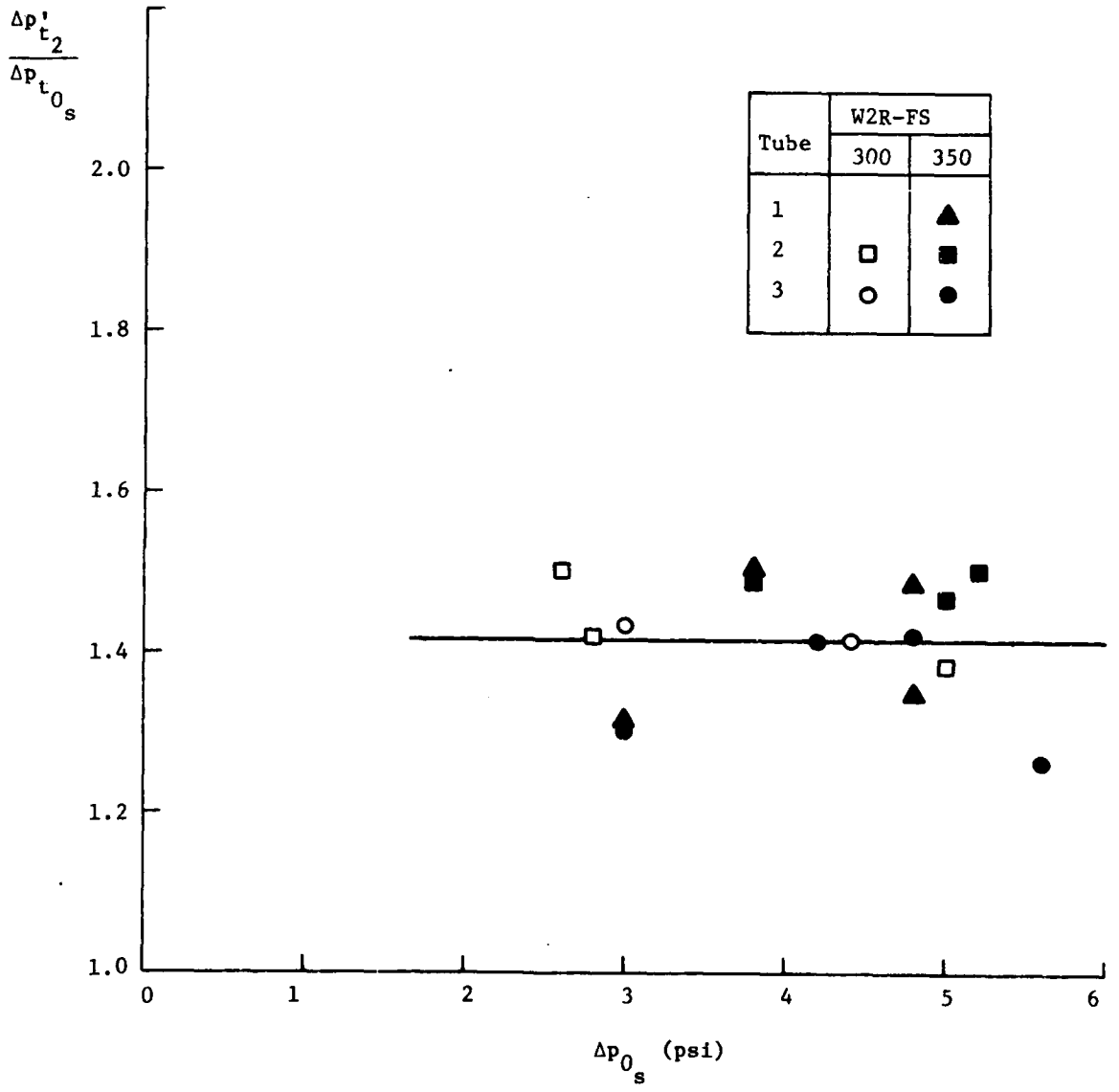

a. Mach No. 0.70

Figure 4.3. Engine-face peak ratio versus incident overpressure.

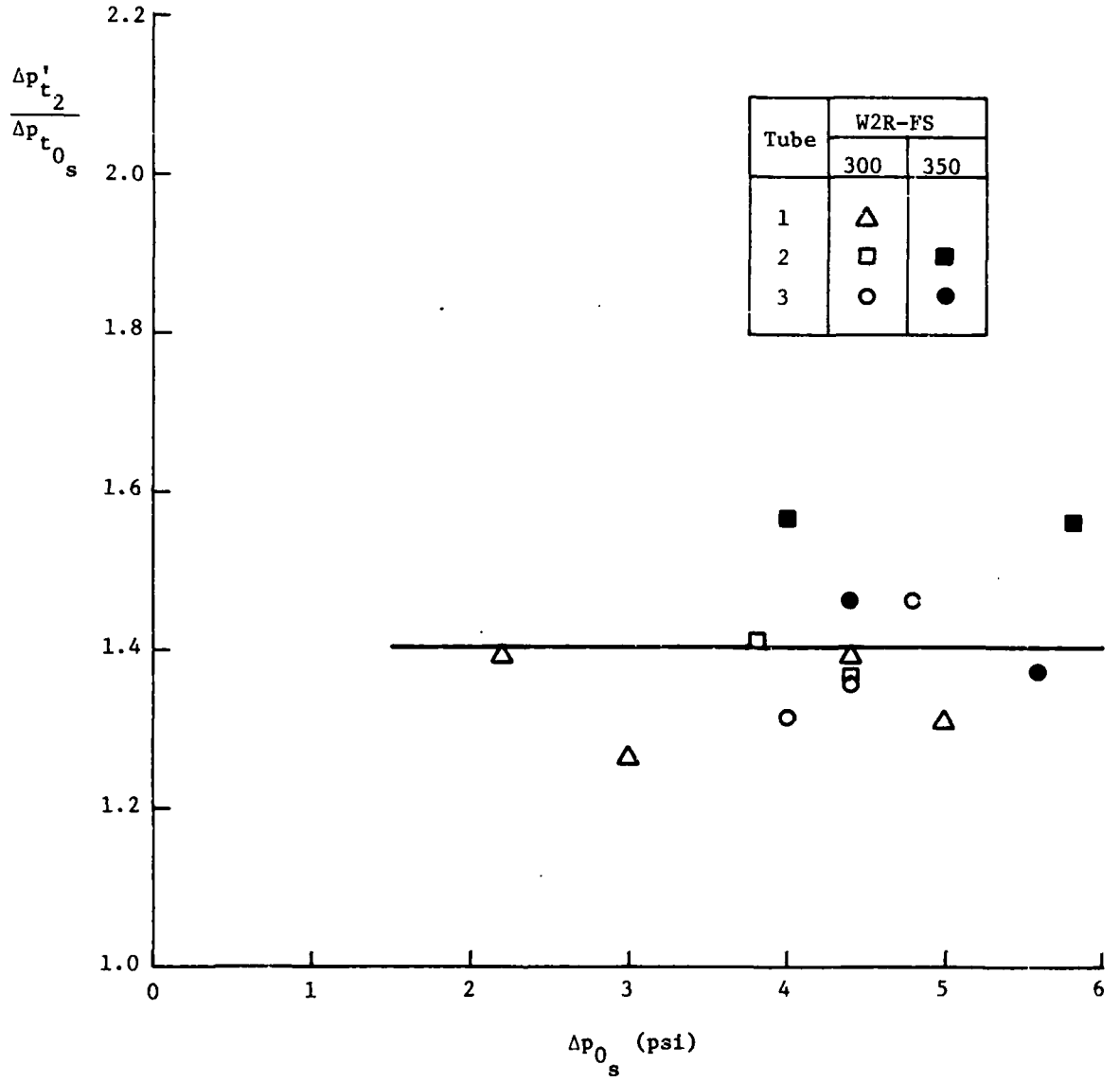

b. Mach No. 0.85

Figure 4.3. Concluded.

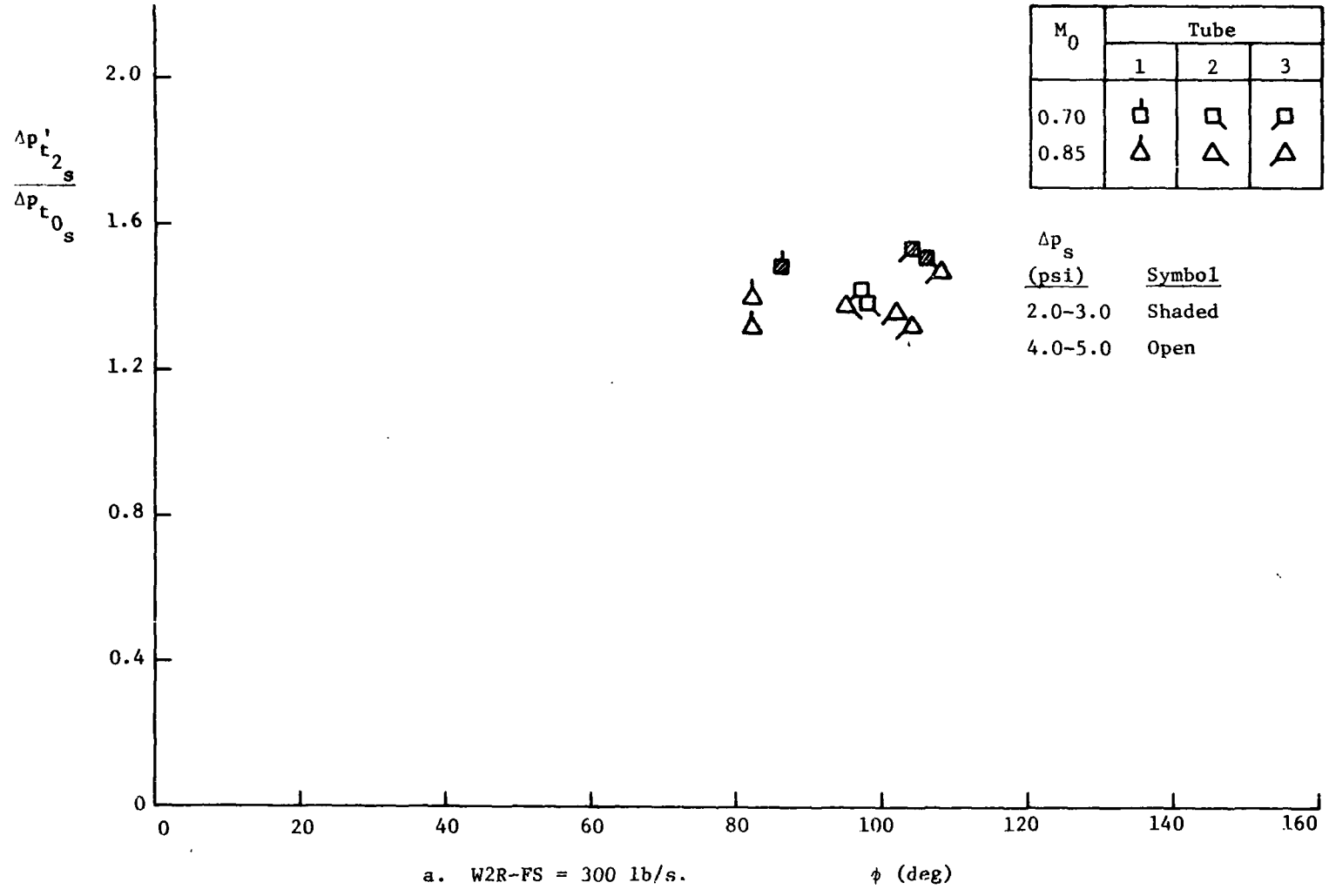

a. W2R-FS = 300 lb/s.

Figure 4.4. Engine-face peak ratio versus blast intercept angle.

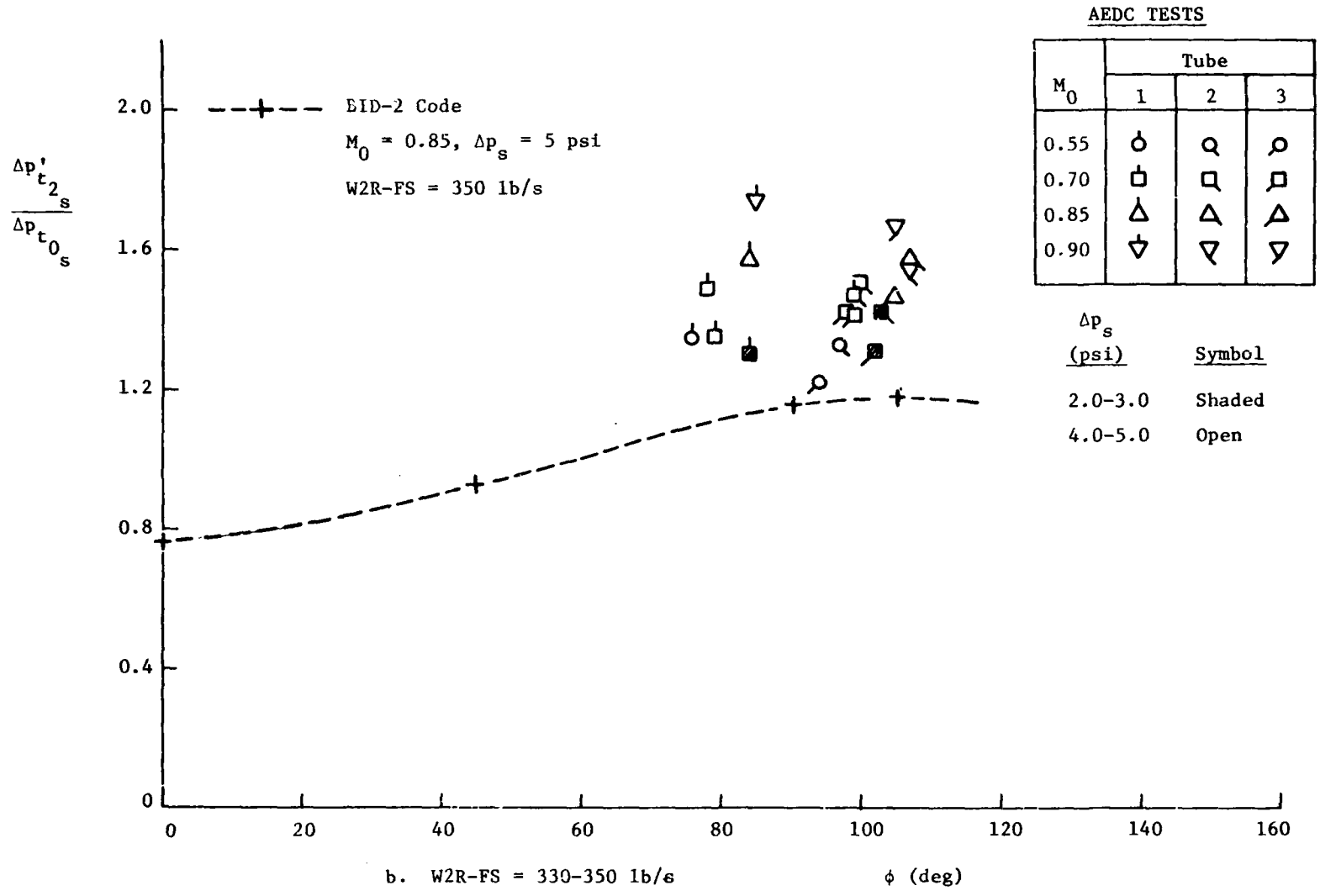

b. W2R-FS = 330-350 lb/s

Figure 4.4. Concluded.

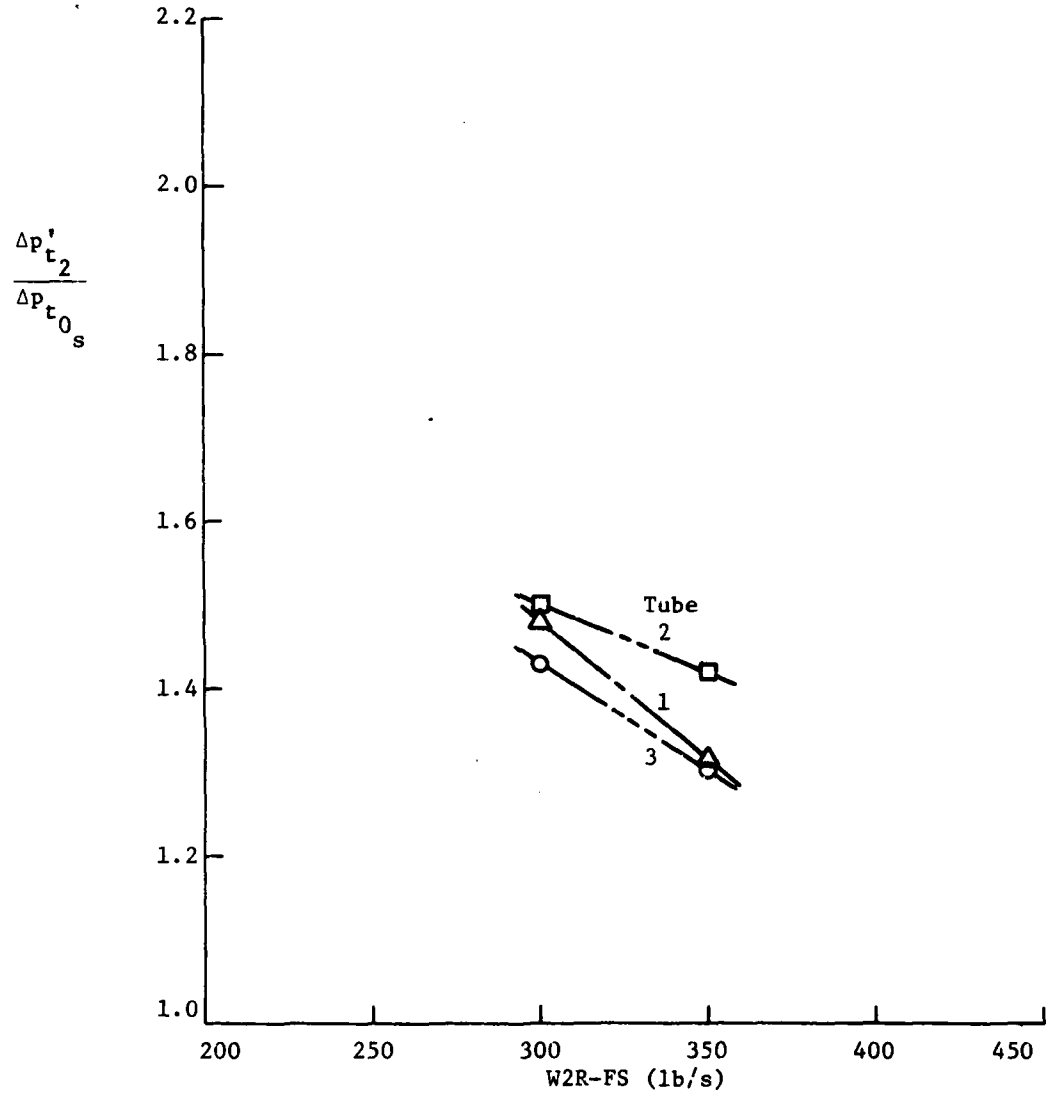

a. $M_0 = 0.70$, $\Delta p_s = 2.2\text{-}3.0$ psi.

Figure 4.5. Engine-face peak ratio versus weight flow.

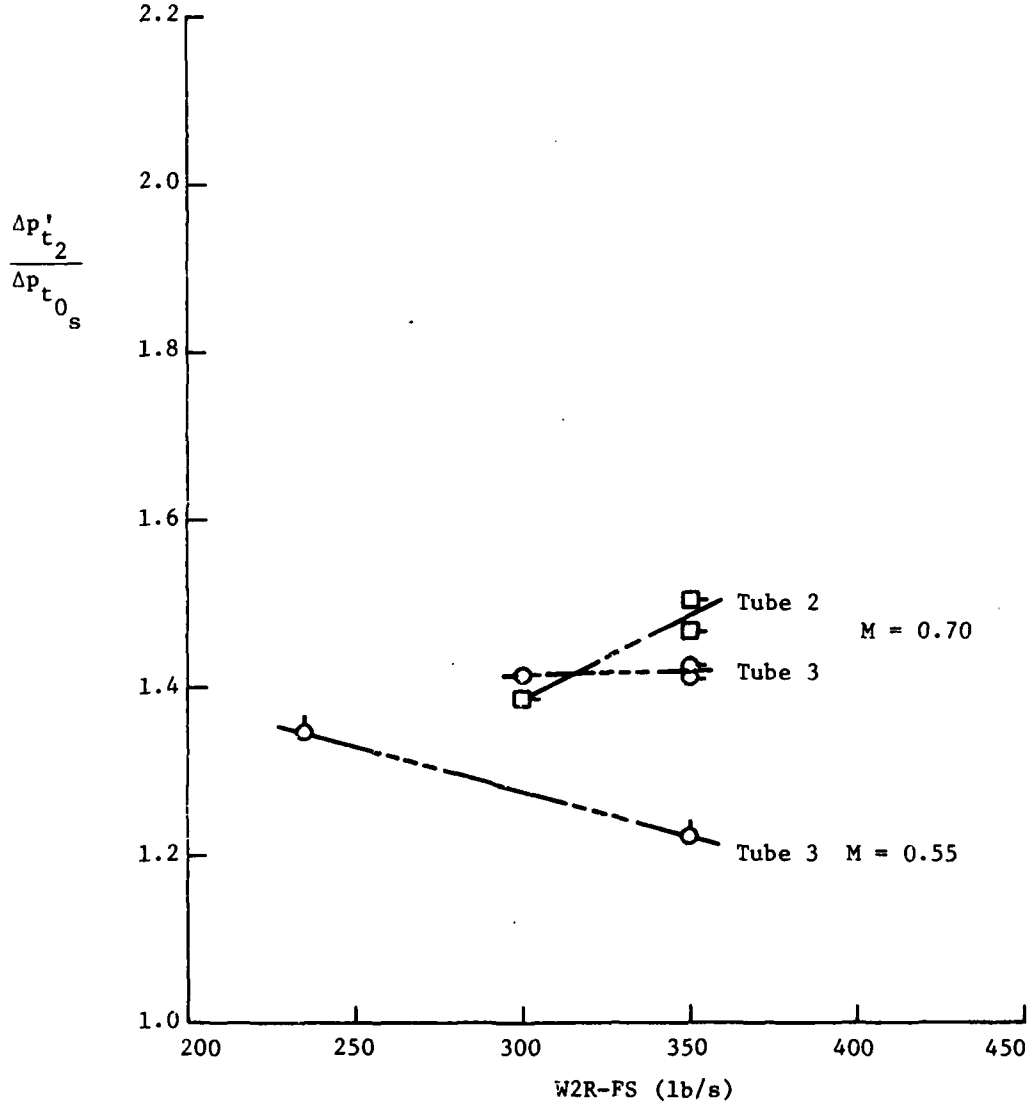

b. M_0 = 0.55-0.70, Δp_s = 0-5.0 psi.

Figure 4.5. Continued.

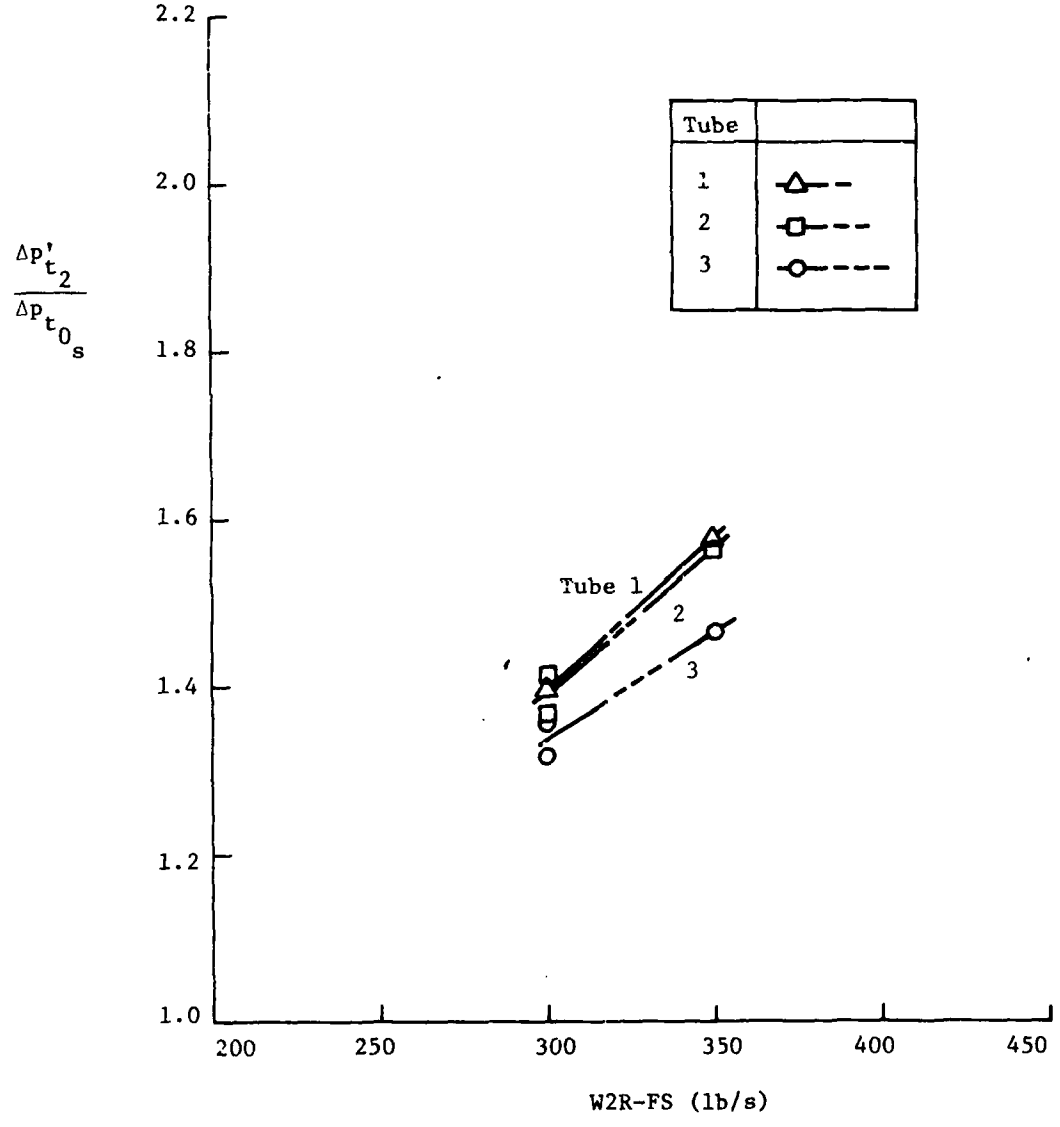

c. $M_0 = 0.85$, $\Delta p_s = 3.8\text{-}4.4$ psi.

Figure 4.5. Concluded.

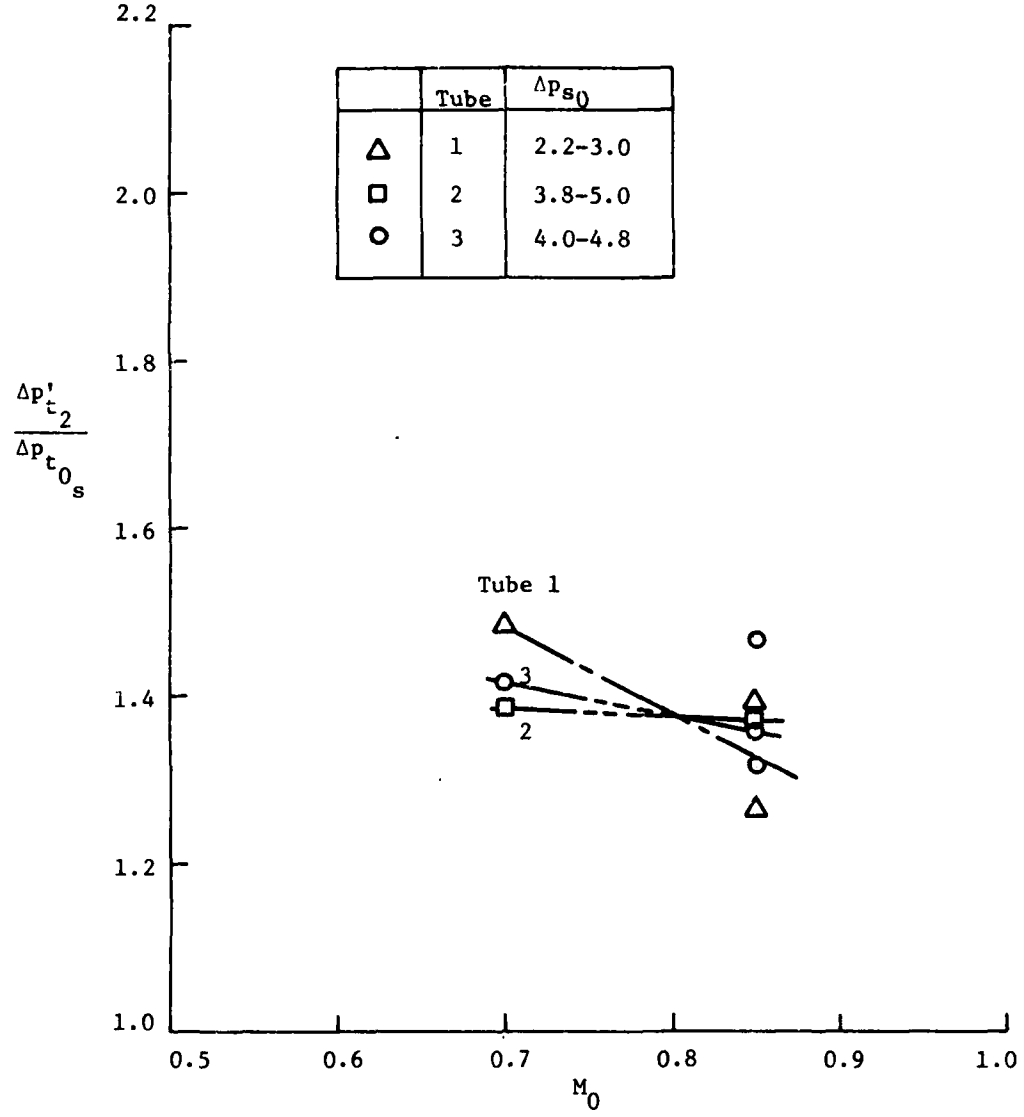

a. W2R-FS = 300 lb/s.

Figure 4.6. Engine-face peak ratio versus Mach number.

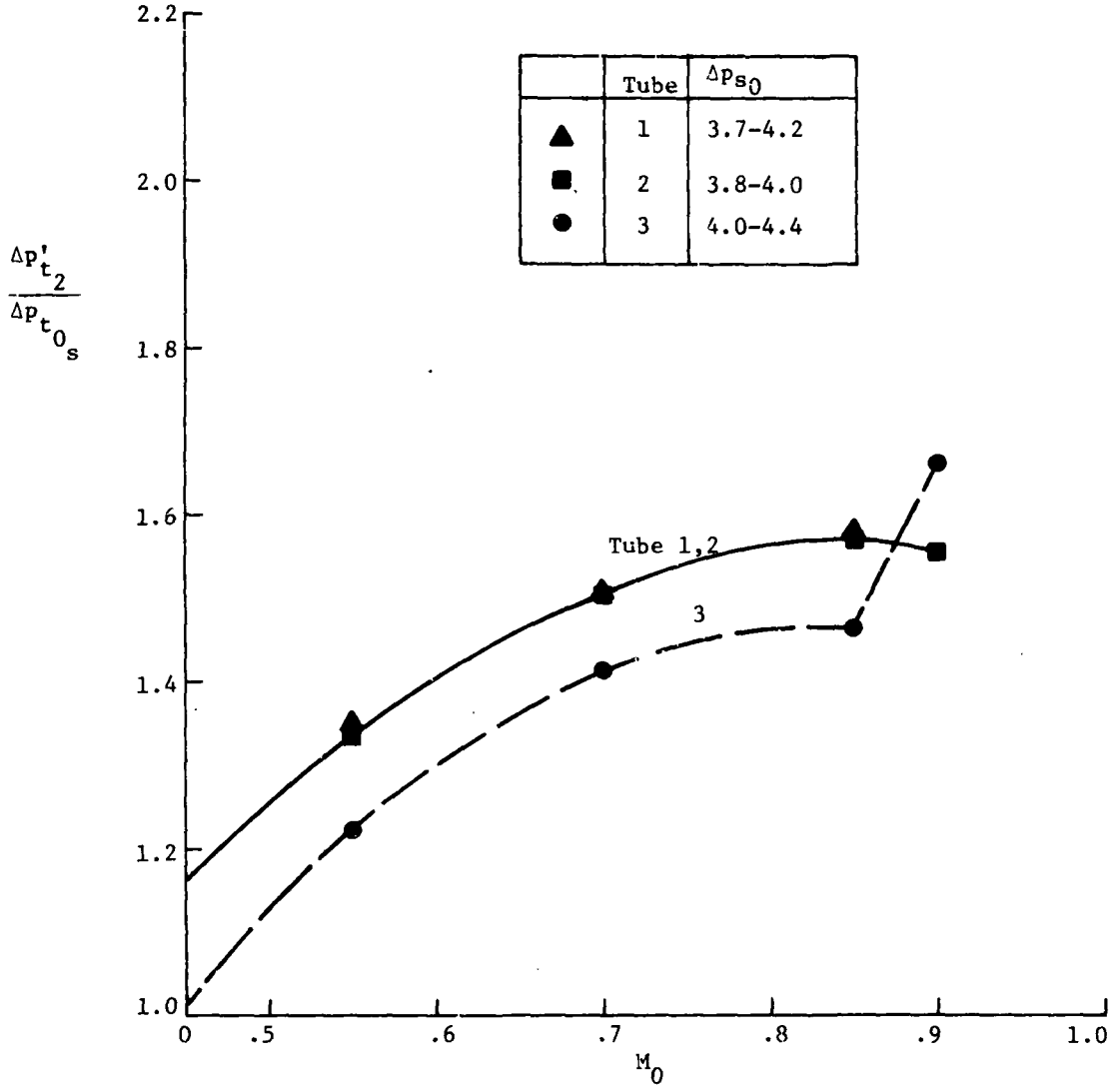

b. W2R-FS = 350 lb/s.

Figure 4.6. Concluded.

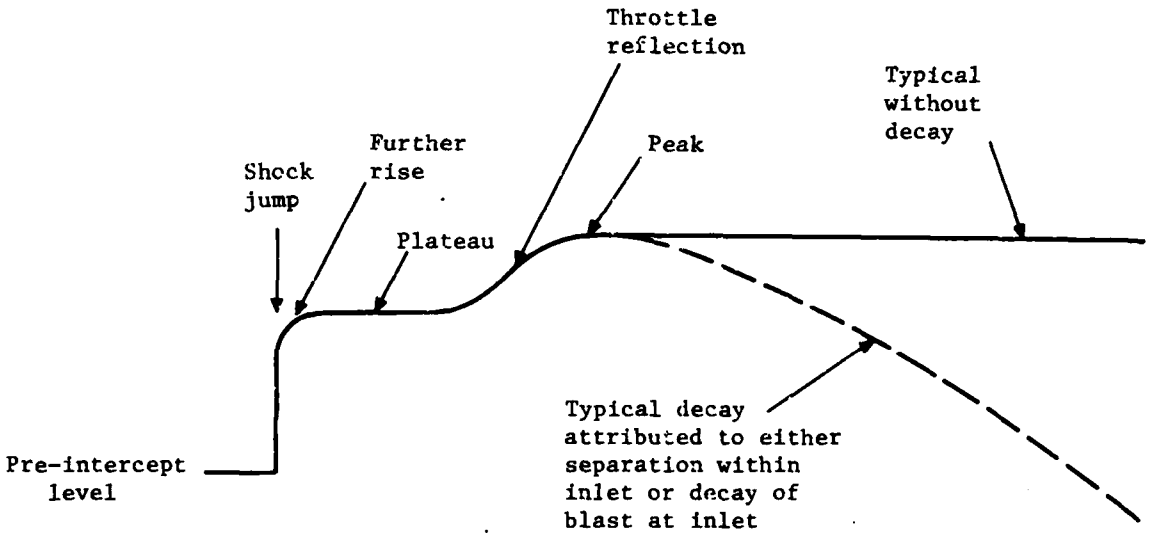

Figure 4.7. Sketch illustrating features of engine-face mean total pressure for leeward inlet.

SECTION 5
COMPARISON OF THEORY AND EXPERIMENT

Concurrent with the performance of the inlet blast tests of Reference 1, Kaman AviDyne developed a theoretical two-dimensional computer code, designated BID (blast-induced-distortion), for predicting the transient flow field produced in a inlet by a blast wave striking the inlet at an arbitrary angle of incidence (Reference 3). Preliminary calculations of inlet pressure time histories were made with this code for four conditions similar to those of the experimental tests and the results of these calculations were compared with the test results in Reference 1. These preliminary calculations were made under the assumption that the blast wave could be represented as having a constant orientation and strength throughout the blast event. The code results based on these simplifications indicated that the major features of the transient pressures observed in the inlet tests are well represented by the BID code results. However, a more extensive comparative study of the test results appeared to be desirable to more definitively establish the limitations of the code predictions. To provide such a correlation, a detailed analysis was made of the time histories of the blast wave strength and orientation after striking the inlet for three blast test runs (see Table 5.1) and BID calculations of inlet response were made using these quantities as inputs. Results of the code runs and data correlations are presented below.

5-1 BLAST INPUT CONDITIONS.

In order to perform calculations of blast response characteristics by the BID code it is necessary to represent the blast pressure, density and velocities incident on the inlets as a time dependent plane wave. These characteristics were determined for the three runs considered here by a detailed synthesis of the data obtained from three claw-static probes located around the inlet (see Reference 1), with first order corrections being made for probe-model interference. The resulting blast input variations for the three runs are presented in Figures 5.1

TABLE 5.1

TEST CONDITIONS FOR CORRELATION RUNS

Run Number	39	40	18
Part Number	544	619	624
Pre-Blast Conditions:			
Mach Number	0.85	0.85	0.70
Mass Flow (lb/s)	348	352	350
Blast Conditions:			
Nom. Shock Overpressure (psi)	4.0	5.8	5.2
Intercept Angle (Deg)	107	110	99

through 5.3. It should be noted that the blast characteristics are defined for a long duration of over 12 ms for the first two cases (Run 39 (Part 544) and Run 40 (Part 619)) but only for less than 4 ms for the third case (Run 18 (Part 624)). In the last case the test geometry resulted in large not-readily-analyzed non-linear flow disturbances at later times, associated with arrival at the inlets of the cold air jet from the shock tube which produced the blast wave.

5-2 INLET PRESSURES.

Theoretical calculations of inlet ramp and cowl pressure time histories from the BID code (Reference 3) are compared with the corresponding AEDC test data (Reference 2) in Figures 5.4 to 5.9 for Runs 39, 40 and 18. Ordinates in these figures are the ratio of inlet static wall pressure to pre-blast wind tunnel total pressure and the numbers to the left of the ordinate scales represent the transducer identification number, transducer locations being indicated in Figure 1.1.*

It is seen that the BID code results are generally in good agreement with all major features of the test data, particularly for Runs 39 and 40. The only apparent conspicuous differences are questions of the relative amplitudes of the calculated and experimental pressures for a few transducers (e.g., transducer 2902 for Run 39 in Figure 5.5) and there is strong evidence that most of these differences can be attributed to errors in calibration factors used to reduce the test data, as is discussed in the Appendix.

5-3 ENGINE FACE PRESSURES.

Considering next total pressures at the engine face location, Figures 5.10 to 5.15 present comparisons of BID code predictions with time histories of experimental total pressures for a variety of positions at the engine face for both the blastward (outboard) and leeward (inboard)

*In order to permit a reasonable quantitative comparison of theory and experiment in this report, it was necessary to take into account the fact that the pre-blast (steady-state) pressures were slightly different for the two cases. This difference was taken into account in pressure-time plots by vertically shifting the theoretical curves so that the pre-blast steady-state values were the same for theory and experiment.

inlets. Ordinate scales are the ratio of total pressure to pre-blast wind tunnel total pressure* and the ordinate label designates the transducer identification number, transducer locations being indicated in Figure 1.2.

5-3.1 Blastward Pressures.

BID predictions of engine face total pressures in the blastward inlet are compared with the corresponding AEDC test data for Runs 39, 40 and 18 in Figures 5.10, 5.12 and 5.14, respectively.

Considering first Run 39, the BID pressure variations are seen to follow well both qualitatively and quantitatively the major features of the test data for all of the transducer locations. To be sure, the code results do somewhat underestimate the initial rate of pressure rise, the first pressure maximum, and some very rapid shock-like changes. Considerably smaller cell sizes would have had to be used in the BID calculations in order to permit resolution of such high frequency variations.

5-3.2 Leeward Pressures.

BID predictions of engine face total pressures in the leeward inlet are also generally in fairly good agreement with the test data with respect to the maximum blast pressure level and the duration of the principal pressure pulse (see Figures 5.11, 5.13, and 5.15). However, it is evident that the BID pressures noticeably lag the experimental pressures with a noticeably slower initial rise of the BID pressures to their peak values. These two related differences may be attributed to the fact that the BID code is a two-dimensional code which assumes that the essentially side-on blast wave for these runs can reach the leeward inlet only by the relatively diffuse process of diffraction around the apex point of the inlet ramp (see Figure 1.1), whereas in actuality the blast wave can also enter the leeward inlet more rapidly by passing directly over or below the outboard inlet. In addition it should be noted that the blast input characteristics used for the BID calculations (Figures 5.1 to 5.3) may not be as applicable to leeward

*See footnote on preceeding page.

inlet calculations as for blastward inlet calculations, since the incident blast wave could be distorted significantly by fuselage interference effects before reaching the inboard inlet.

5-4 DISTORTION AT ENGINE FACE.

Engine face distortion* time histories computed from the BID code runs are compared with the corresponding AEDC test data in Figures 5.16 to 5.21 for the same runs discussed above. Test data and BID calculations are shown on left and right hand sides of facing pages, respectively.

Since the BID code is a two dimensional code and the distortion definitions normally used in B-1 studies (see Reference 1) are three dimensional concepts involving pressures at 40 locations at the engine face location, it was necessary to relate the BID cell pressures to the pressures at the 40 locations. This was done for BID computations simply by taking the BID pressure at each of the 40 engine face locations to be equal to the pressure in the BID cell within which the corresponding engine face transducers is located.

In Figures 5.16 to 5.21 the time of blast arrival at the blastward inlet is indicated approximately by the start of the BID curves on the right hand pages and the time of blast arrival at the engine face is indicated by the start of the first ripples or ramplike rises of the distortion parameters.

5-4.1 IDC.

Consider first the circumferential distortion parameters IDC1 through IDC5 for the individual engine face rings 1 to 5 in parts "a" of Figures 5.16 to 5.21. The pre-blast values of the BID distortion coefficients (before blast arrival at the face) are seen to be qualitatively in good agreement with the corresponding test data for both blastward and leeward inlets to the extent that the distortion increases significantly in going from the inner ring (IDC1) to the outer ring (IDC5). Quantitative agreement is only fair, with the experimental distortions being generally larger than the BID computed distortions.

*See Reference 1 for an explanation of distortion parameters and other terminology used here.

After blast arrival both theory and experiment indicate circumferential distortion increases generally lasting at least several milliseconds. The details of distortion behavior and correlation are somewhat different for the two inlets and for the different runs as discussed below.

For the blastward inlet for all three runs (Figures 5.16a, 5.18a and 5.20a) the computed blast-induced circumferential distortions are seen to be somewhat similar to the experimental distortions for the outer engine rings (IDC4 and IDC5) but the experimental distortions are larger than the computed distortions for the inner rings (IDC1 and IDC2). These larger experimental distortions can probably be attributed partly to the basically three-dimensional effects of the bullet nose hub of the model engine which is not taken into account in the two-dimensional BID code.

For the leeward inlet for Run 39 there is somewhat better correlation between theory and experiment for the inner engine rings (Figure 5.17a). Here, after blast arrival, both calculated and experimental distortions tend to rise to similar levels for the inner rings (IDC1 and IDC2). However, the calculated distortions are too large for the outer rings (IDC4 and IDC5).

For the leeward inlet for Run 40 about the same trends are observed as mentioned above for Run 39 (see Figure 5.19a) except that all the computed BID distortions rise to clearly too large values at late times. This large predicted distortion might be attributed to the fact that the BID code does not contain an adequate simulation of viscosity effects for the circumstances of this run.

For the leeward inlet for Run 18 (Part 624) there appears to be fairly good agreement between the experimental and calculated distortion trends for the relatively short time of the calculations.

Calculated and experimental time histories of the total circumferential distortion parameter IDC may be compared in parts "c" of Figures 5.16 to 5.21. This parameter is a weighted combination of the

individual values of IDC1 through IDC5 discussed above. Generally the calculated pre-blast values of IDC are too low. The calculated blast-induced values are too low for the blastward inlet for Runs 39 and 40 but are too high for the leeward inlet at late times for these runs. For Run 18 calculated and experimental IDC values are similar for both inlets.

5-4.2 IDR.

The engine face radial distortion parameters IDR1 through IDR5 and the total radial distortion parameter IDR are shown in parts "b" and "c", respectively, of Figures 5.16 to 5.21. Generally the experimental distortions are seen to appreciably exceed the BID-computed distortions, particularly for the outer ring (IDC5). Some of the distortion variations are qualitatively similar, e.g., the rising distortion variations for IDR4 and IDR5 in Figure 5.20b, but for other cases, e.g., Figures 5.17b and 5.19b, the experimental distortions indicate substantial blast induced distortion drops which are not predicted by the BID code.

The differences observed here may be attributed primarily to three-dimensional effects and viscosity effects not covered by the BID code.

5-4.3 IDL.

The overall distortion parameter IDL is a weighted combination of the IDC and IDR parameters (see Reference 1). The calculated pre-blast values are generally substantially less than the experimental values (see parts "c" of Figures 5.16 to 5.21). The calculated blast-induced values are generally lower for the blastward inlet (Figures 5.16c, 5.18c and 5.20c) and they appear to become too high for late times for the leeward inlet (Figures 5.17c and 5.19c).

5-4.4 IDA.

The calculated pre-blast average distortion parameter IDA is generally substantially less than the experimental value (see parts "c" of Figures 5.16 to 5.21). The calculated blast-induced distortions

are also lower for the blastward inlet (Figures 5.16c, 5.18c and 5.20c) but reach levels similar to the experimental values for the leeward inlet (Figures 5.17c, 5.19c and 5.21c).

5-4.5 IDT.

The calculated pre-blast total distortion parameter IDT is generally substantially less than the experimental value (see part "c" of Figures 5.16 to 5.21). The calculated blast-induced distortions are also less for most conditions except for the inboard inlet at late times for Runs 39 and 40 (Figures 5.17c and 5.19c) where the late-time calculated and experimental distortions are similar.

5-5 CORRELATION SUMMARY.

In summary, it may be concluded from the preceeding comparisons that the BID code provides a good representation of those features of the blast-induced inlet flow which can be reasonably represented by a two-dimensional inviscid approach, particularly the inlet ramp and cowl pressures and engine face pressures on the blastward inlet. For flow characteristics which may be appreciably affected by three-dimensional effects, such as the leeward inlet and engine face pressures, agreement is not as good but still fair. For flow distortion characteristics, which may be affected both by three-dimensional effects and by viscosity effects (not included in BID), the agreement is less satisfactory. The BID code generally underpredicts the pre-blast experimental distortions. For the blast induced distortions, the code generally substantially underpredicts distortions for the blastward inlet. For the leeward inlet, the code underpredicts IDR, and, for some cases, predicts too high values of IDC and IDL at late times.

The comparisons would be expected to be generally improved by extension of the BID code to three dimensions, particularly in regard to distortion. This extension would require a significant increase in the computer storage and computation time requirements. The rapid strides in improvement of computer capacity and speed makes this extension to three dimensions feasible now.

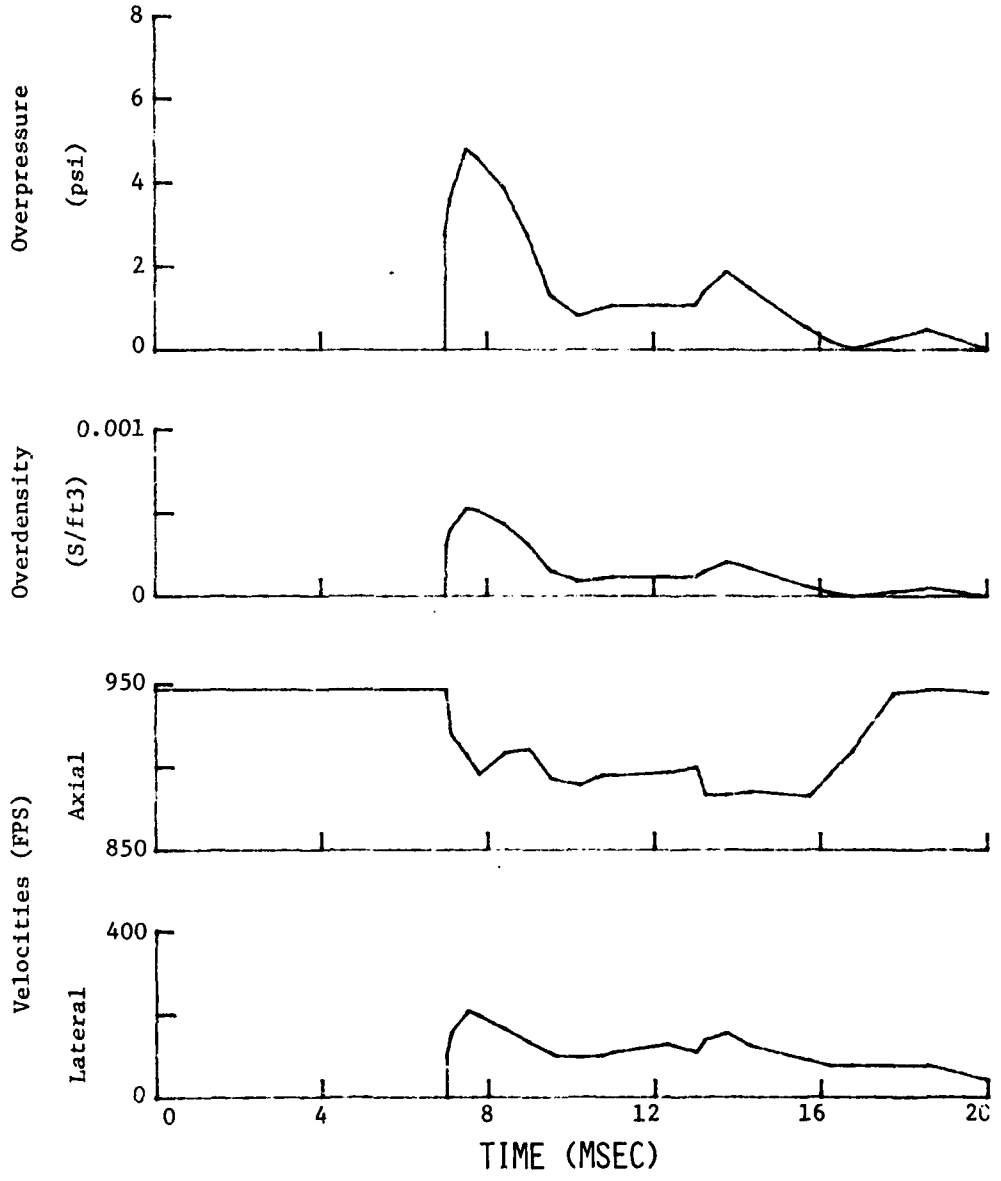

Figure 5.1. Blast input characteristics for Run 39 (Part 544).

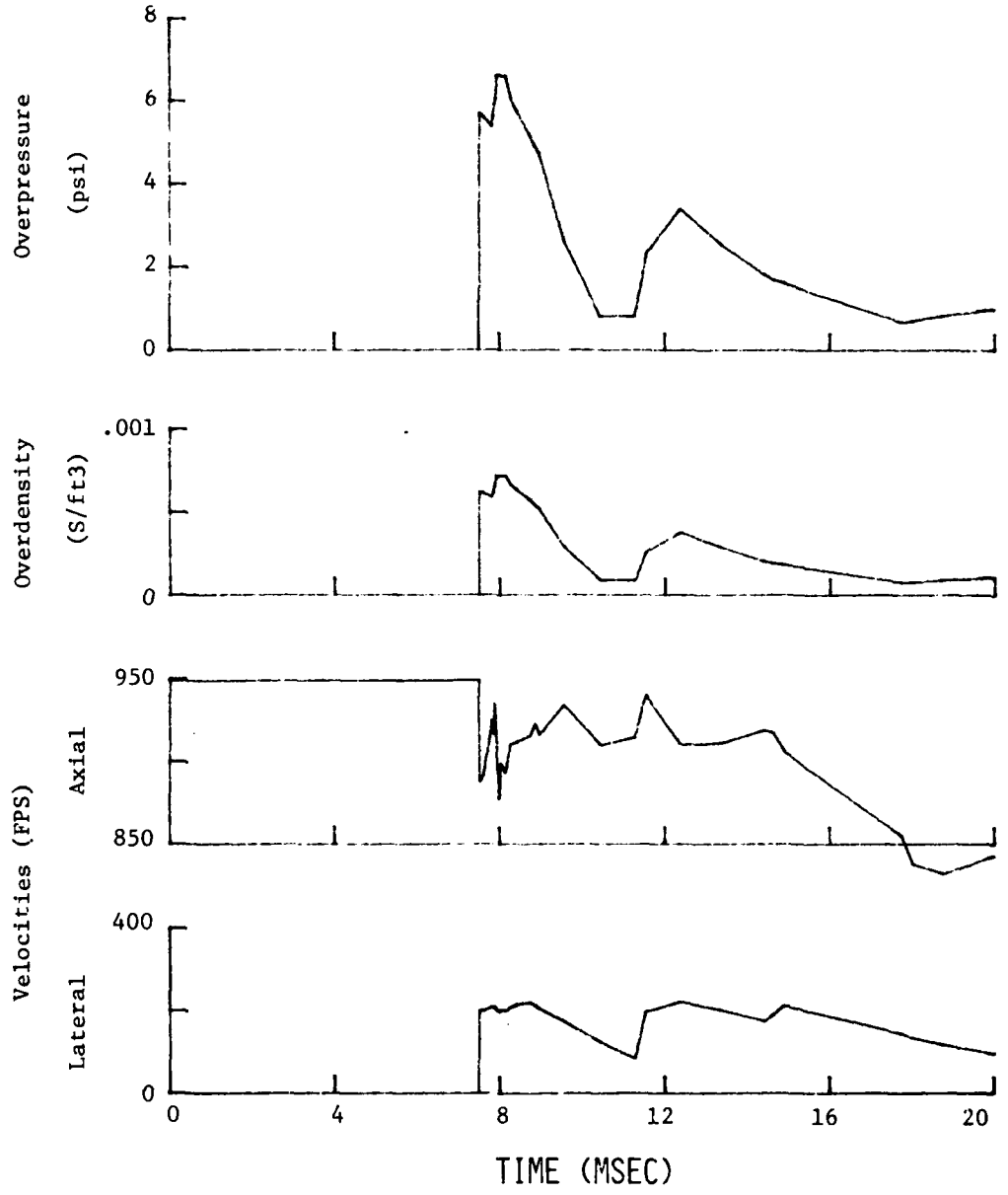

Figure 5.2. Blast input characteristics for Run 40 (Part 619).

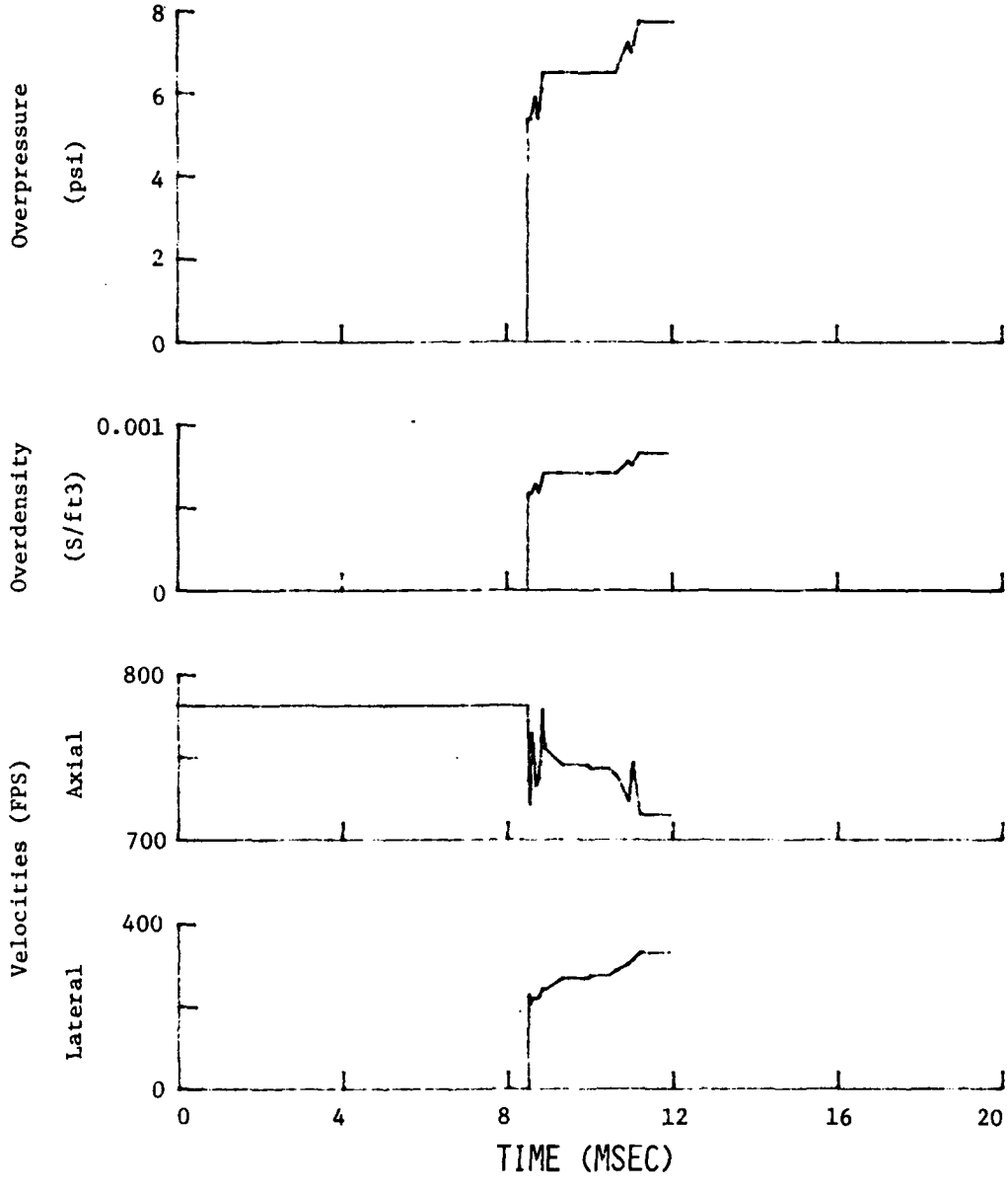

Figure 5.3. Blast input characteristics for Run 18 (Part 624).

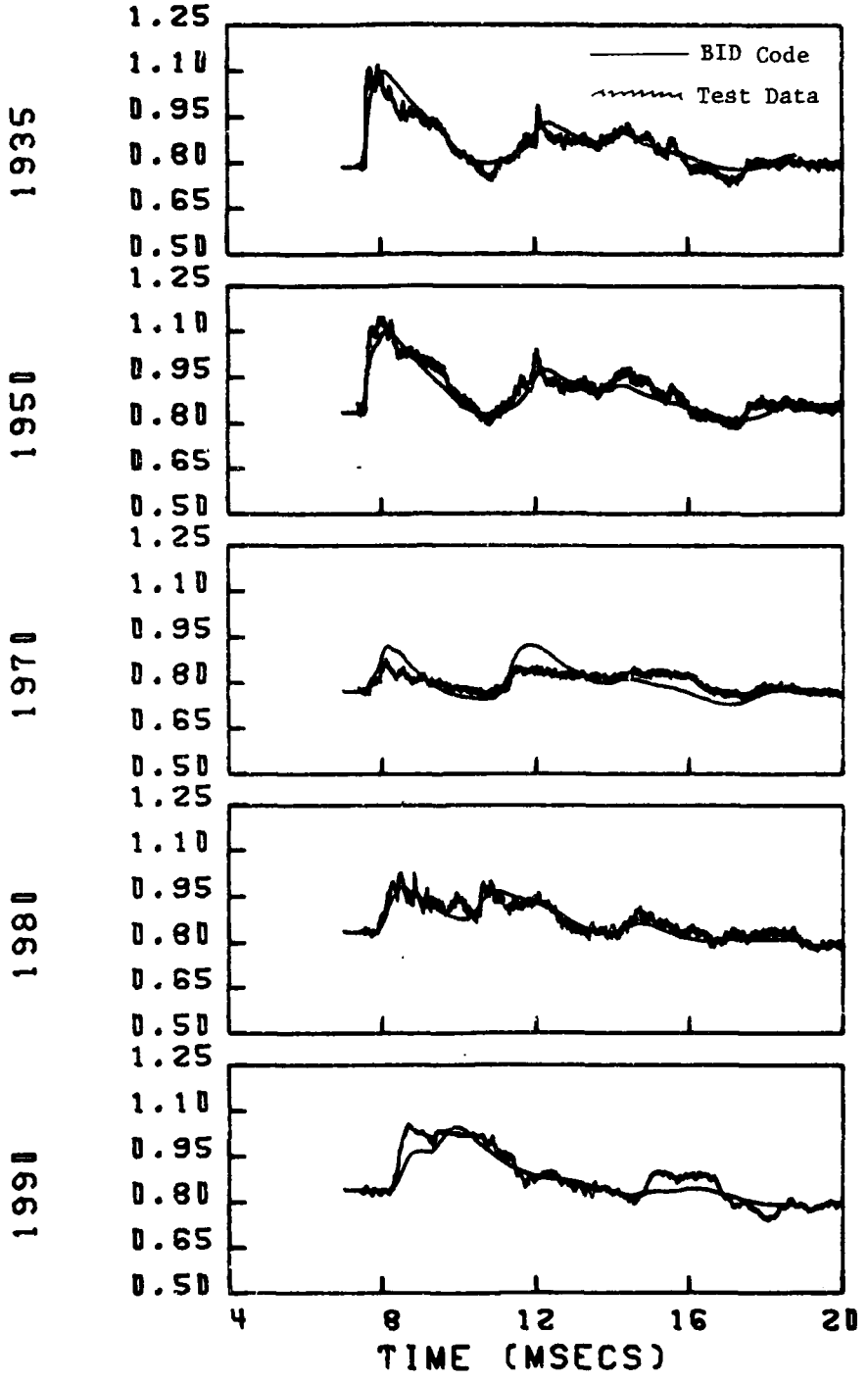

Figure 5.4. Comparison of theoretical and experimental time histories of ramp pressures for Run 39 (Part 544).

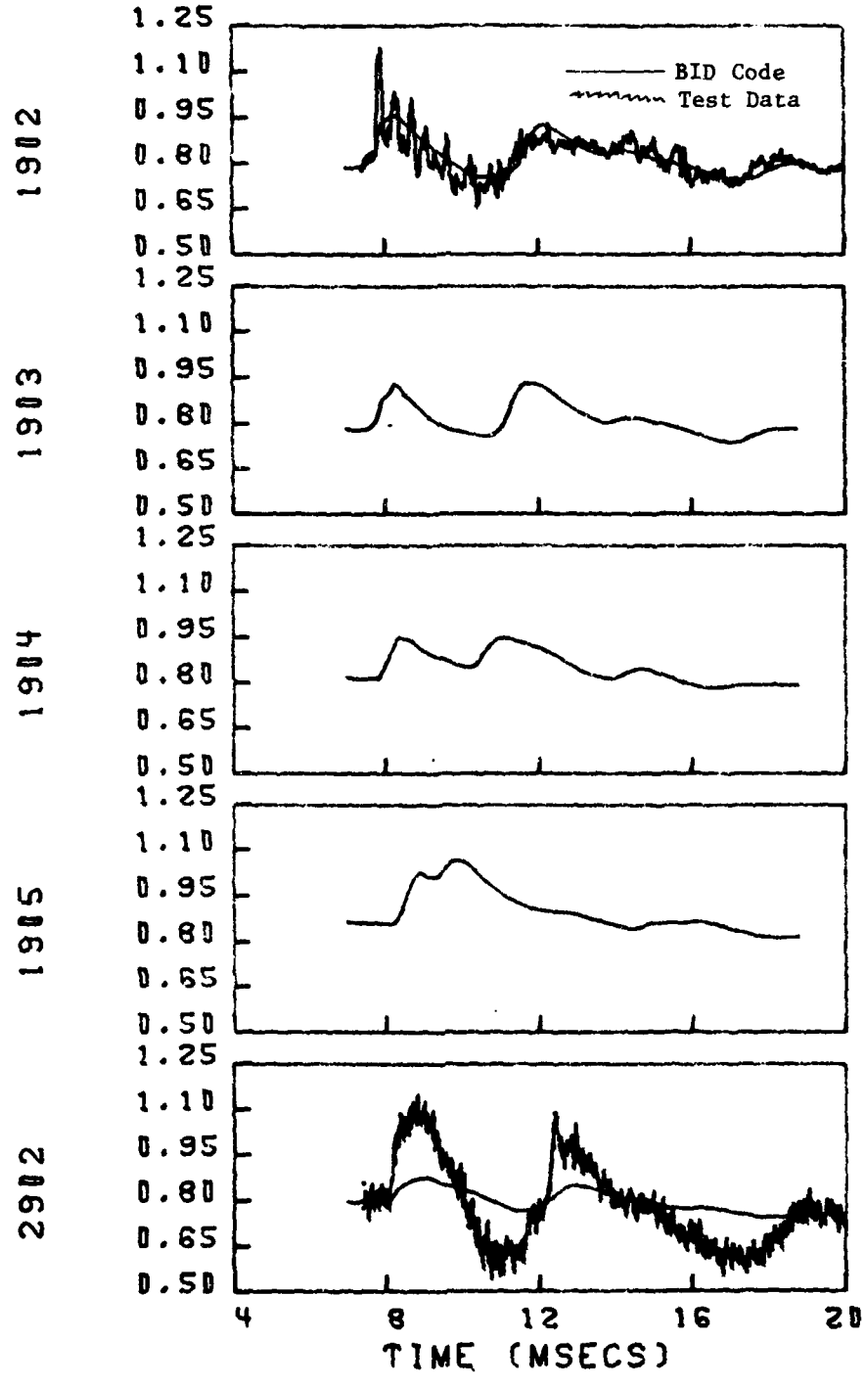

Figure 5.5. Comparison of theoretical and experimental time histories of cowl pressures for Run 39 (Part 544).

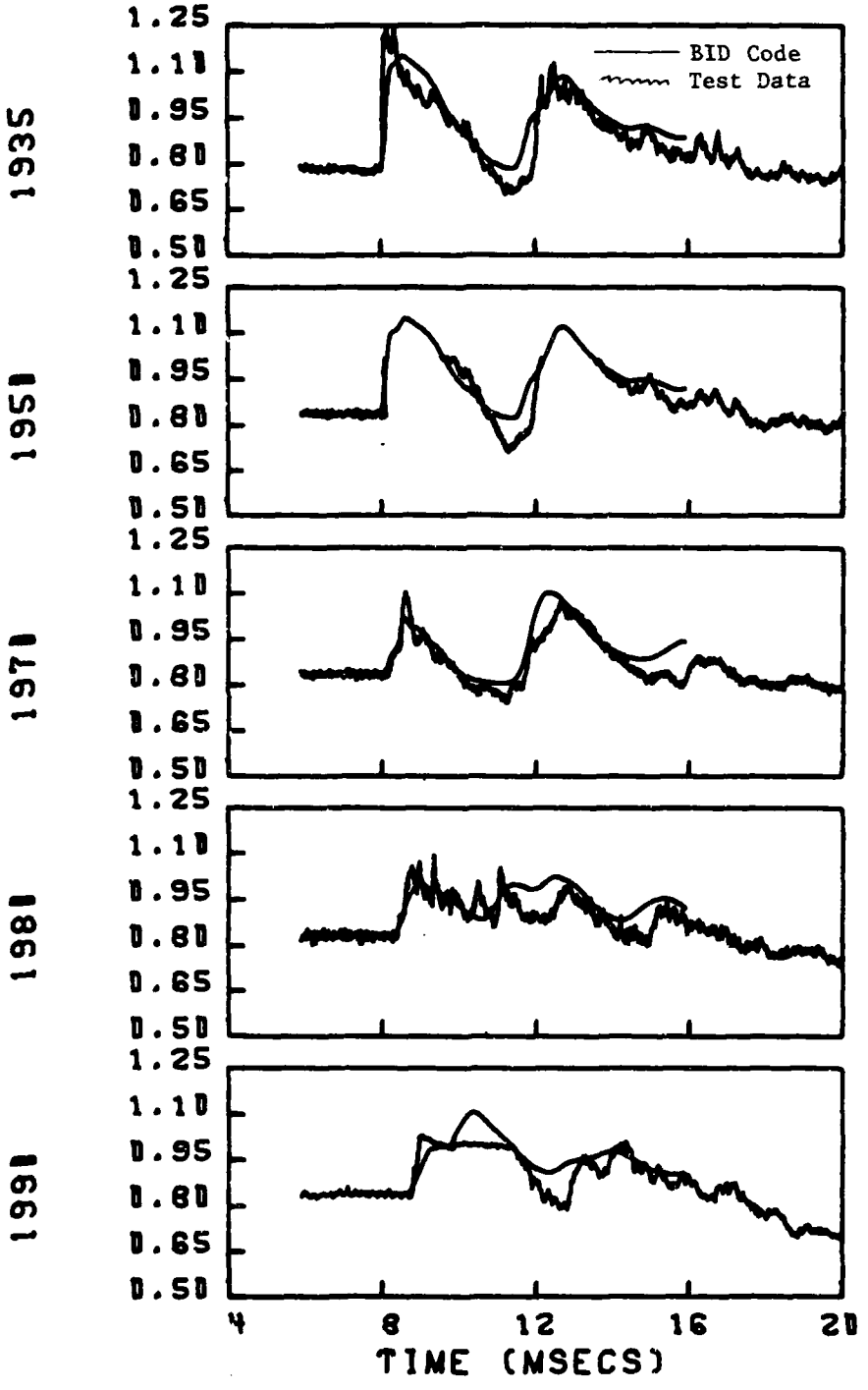

Figure 5.6. Comparison of theoretical and experimental time histories of ramp pressures for Run 40 (Part 619).

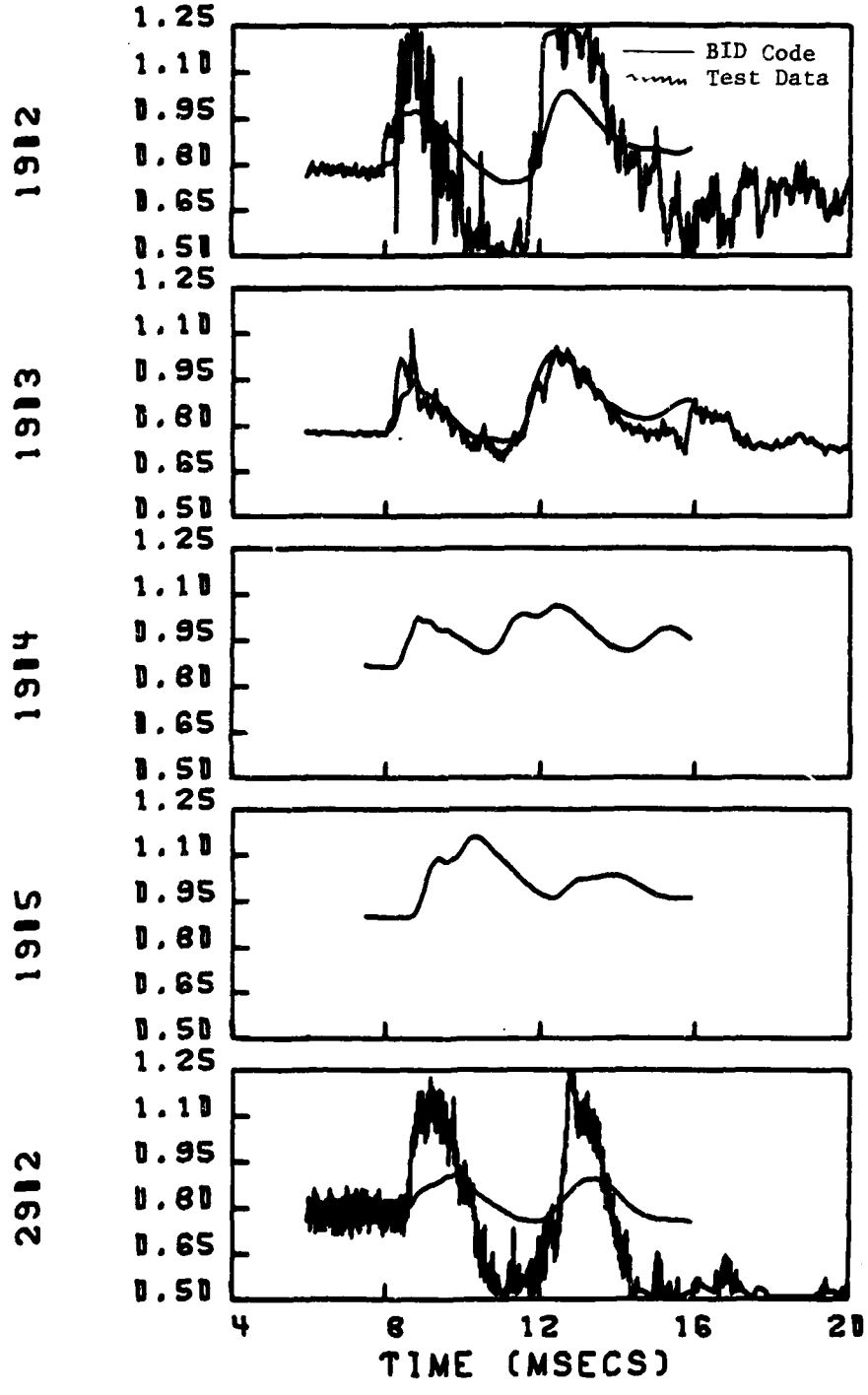

Figure 5.7. Comparison of theoretical and experimental time histories of cowl pressures for Run 40 (Part 619).

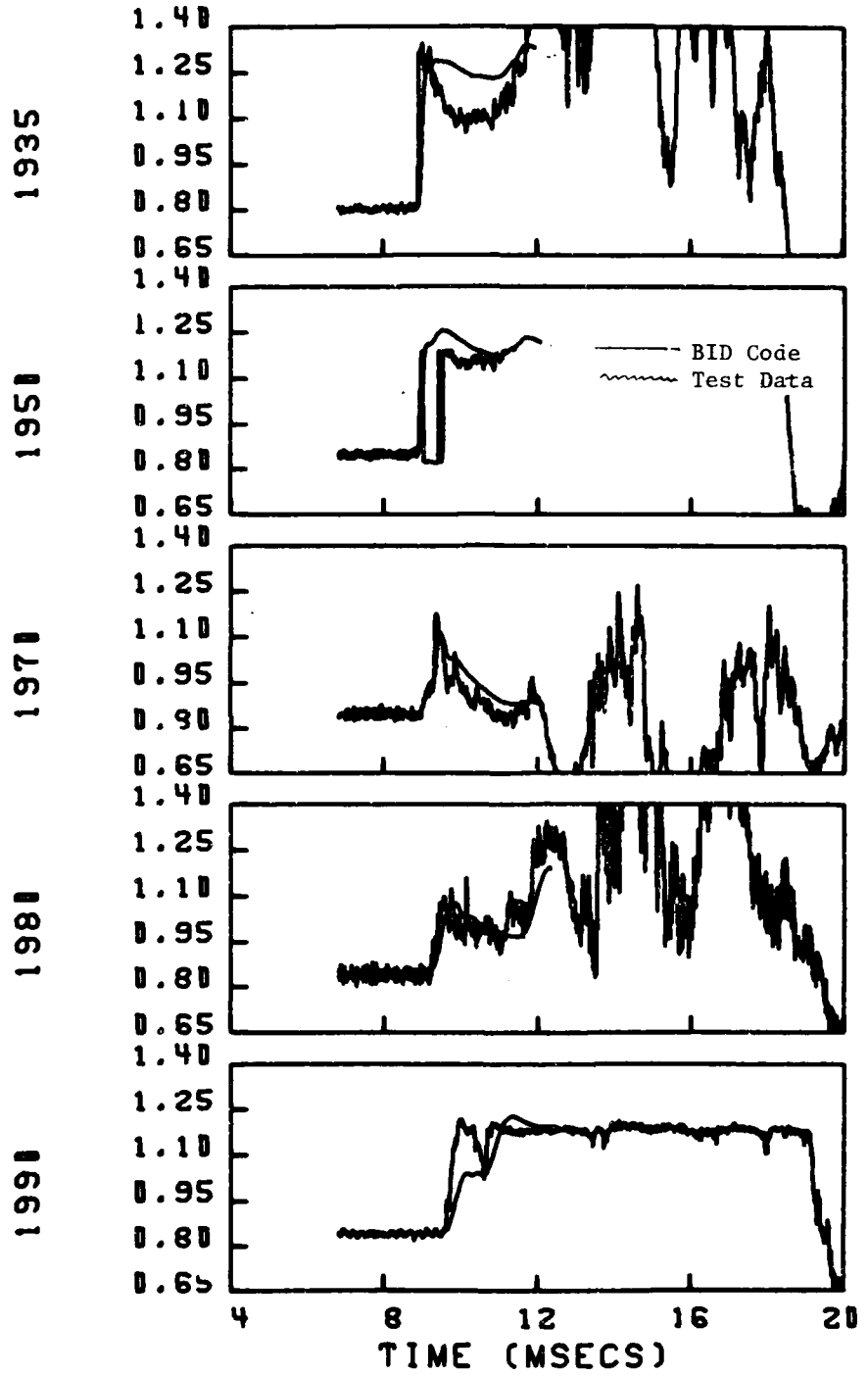

Figure 5.8. Comparison of theoretical and experimental time histories of ramp pressures for Run 18 (Part 624).

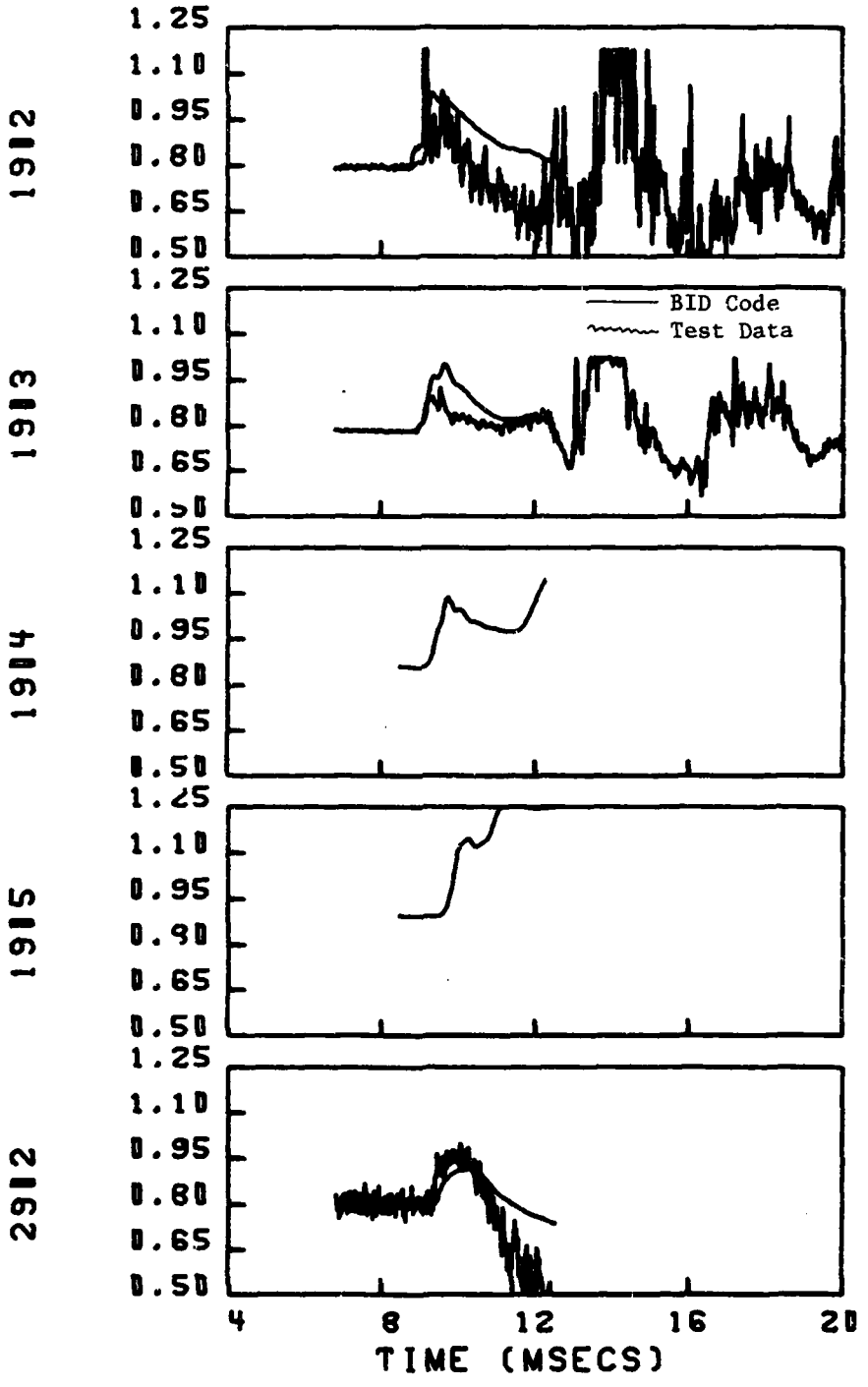

Figure 5.9. Comparison of theoretical and experimental time histories of cowl pressures for Run 18 (Part 624).

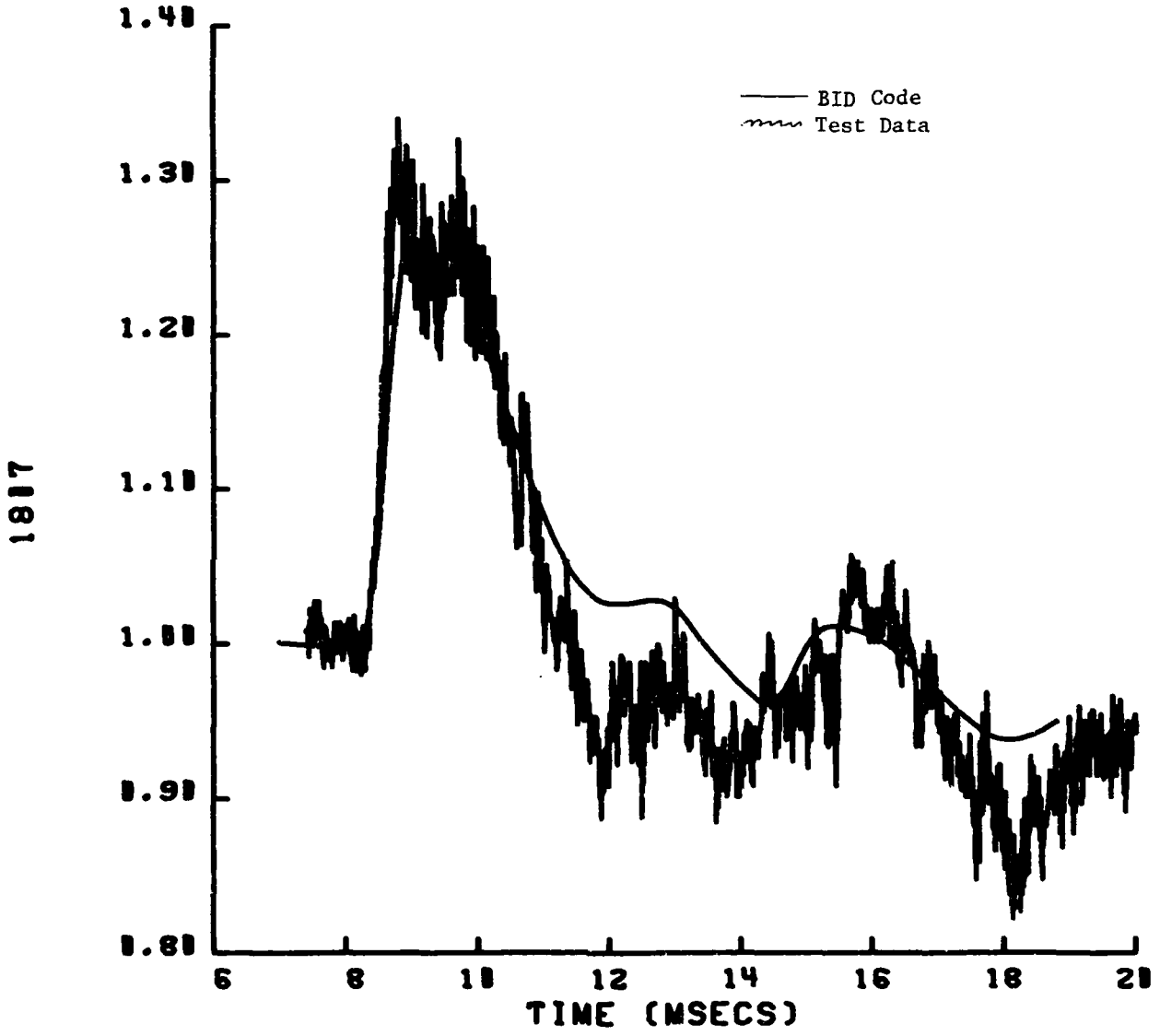

Figure 5.10a. Transducer 1807.

Figure 5.10. Comparison of theoretical and experimental time histories of engine face total pressures for Run 39 (Part 544), blastward (outboard) inlet.

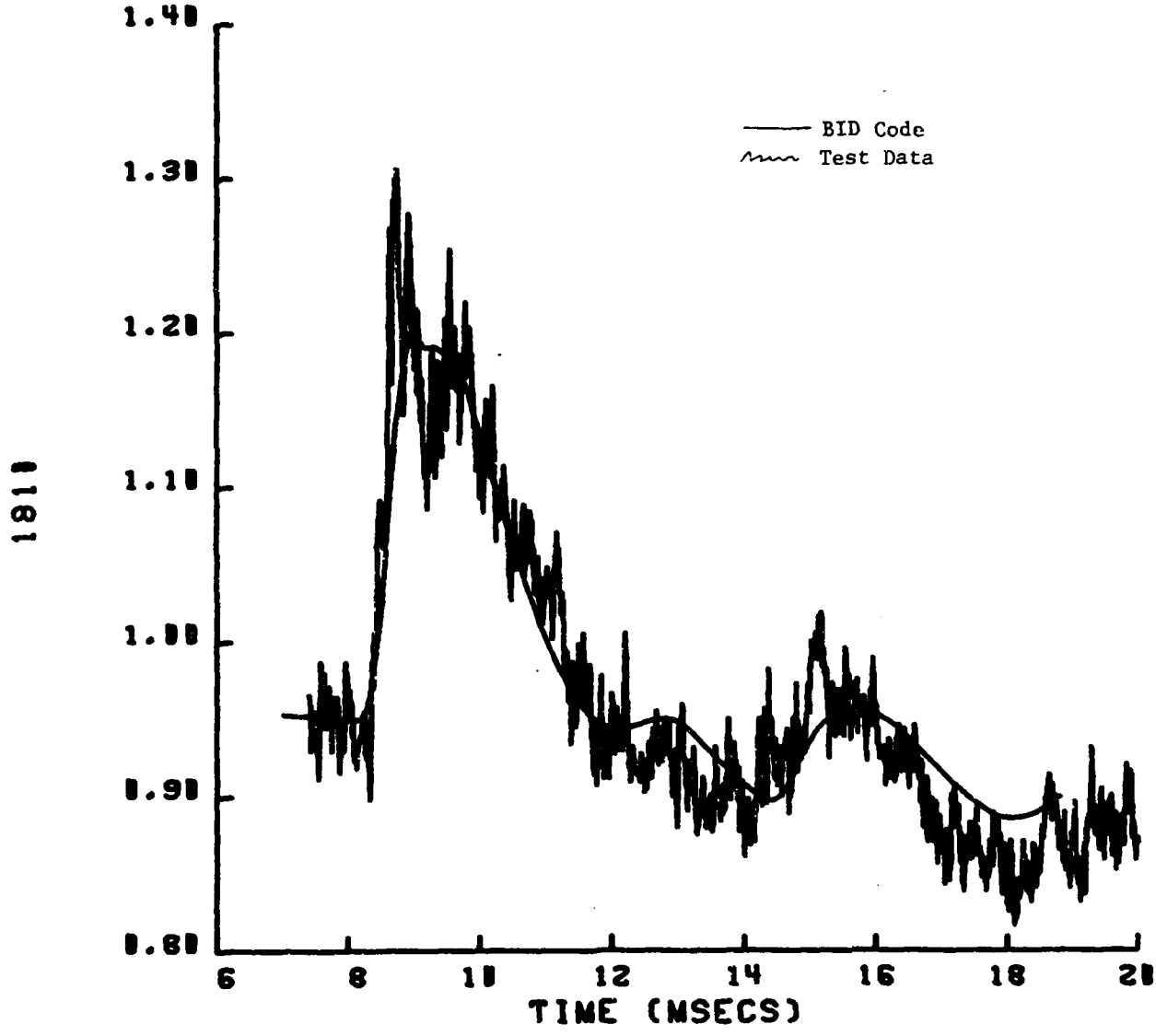

Figure 5.10b. Transducer 1810.

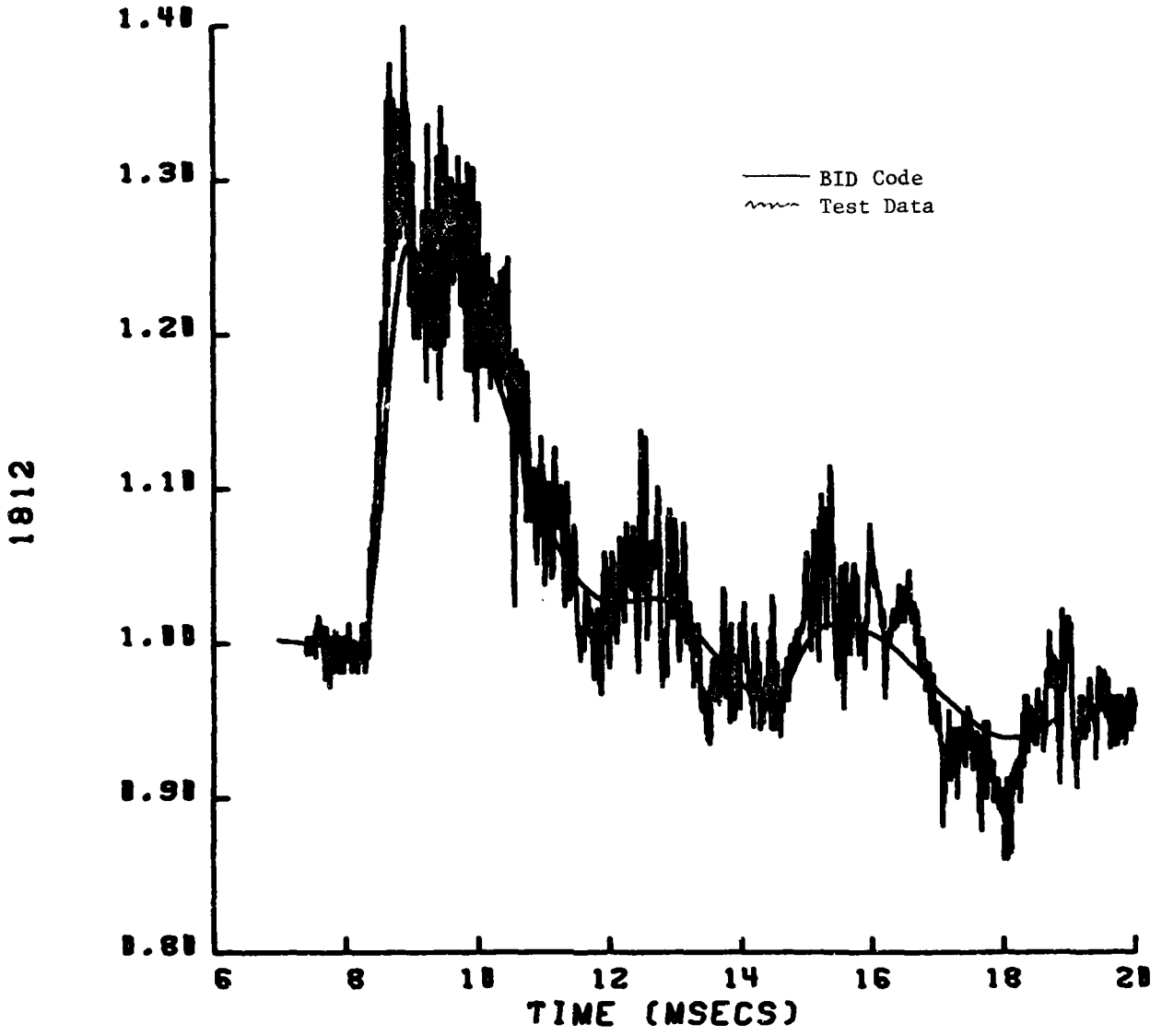

Figure 5.10c. Transducer 1812.

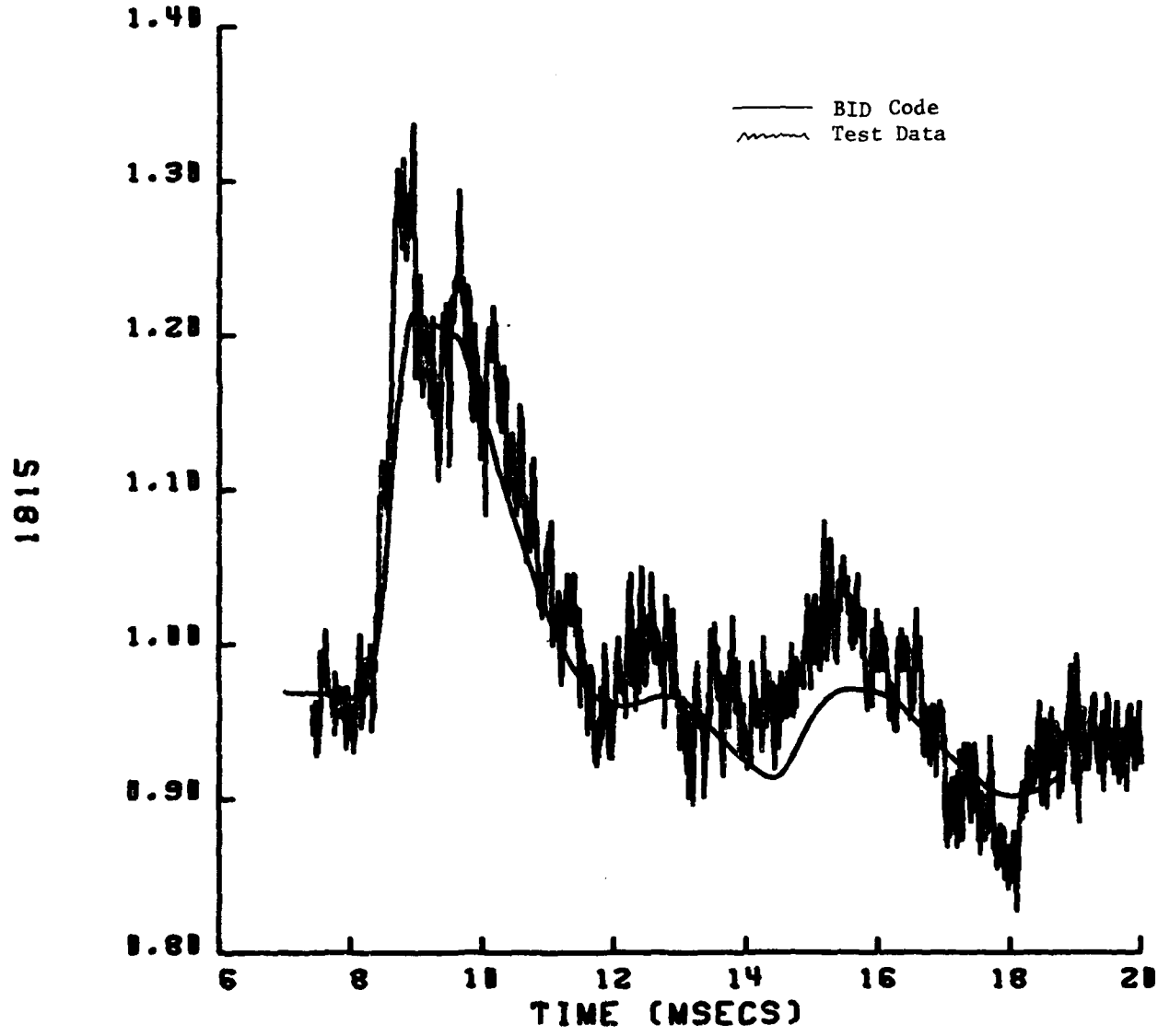

Figure 5.10d. Transducer 1815.

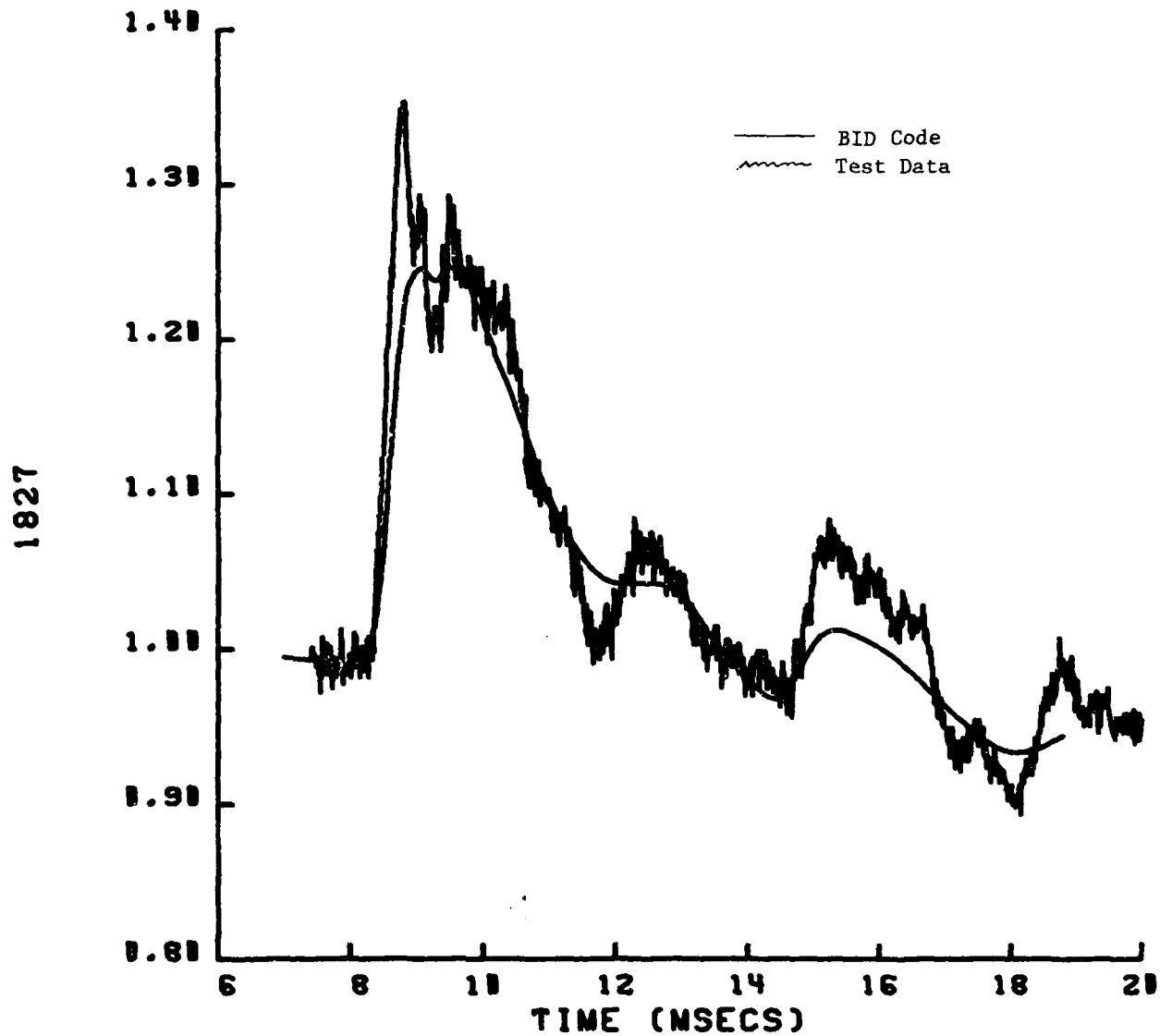

Figure 5.10e. Transducer 1827.

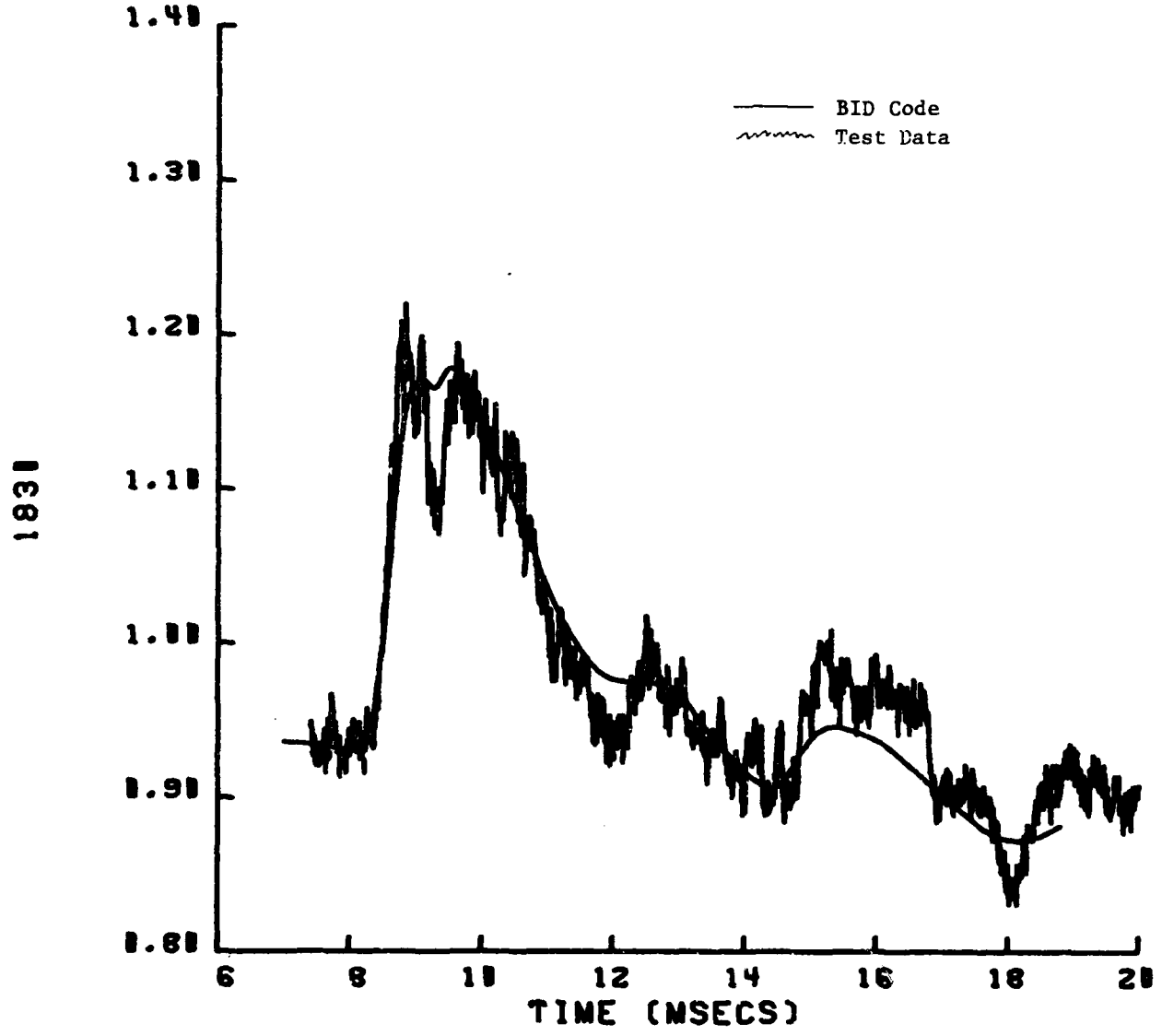

Figure 5.10f. Transducer 1830.

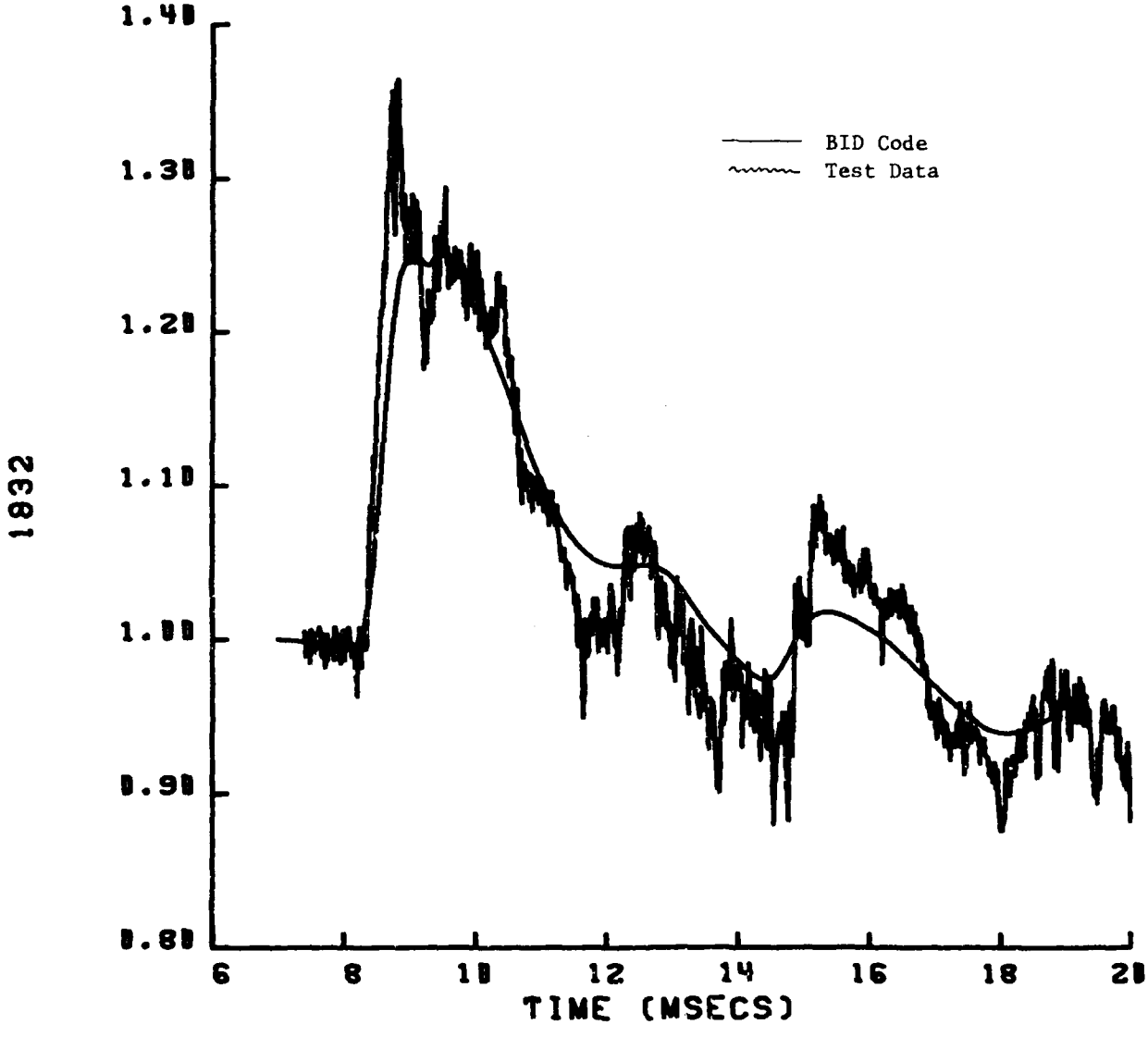

Figure 5.10g. Transducer 1832.

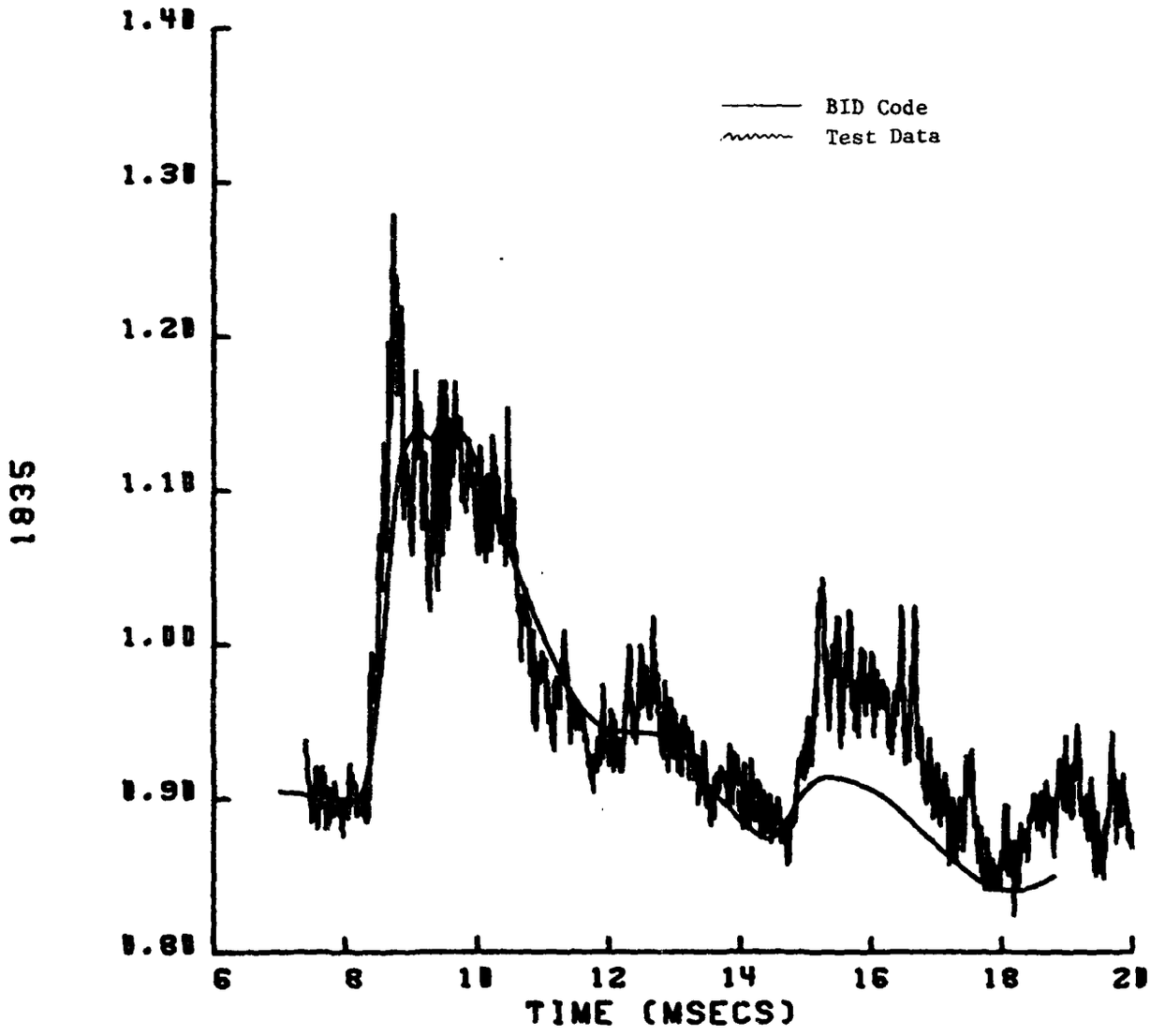

Figure 5.10h. Transducer 1835.

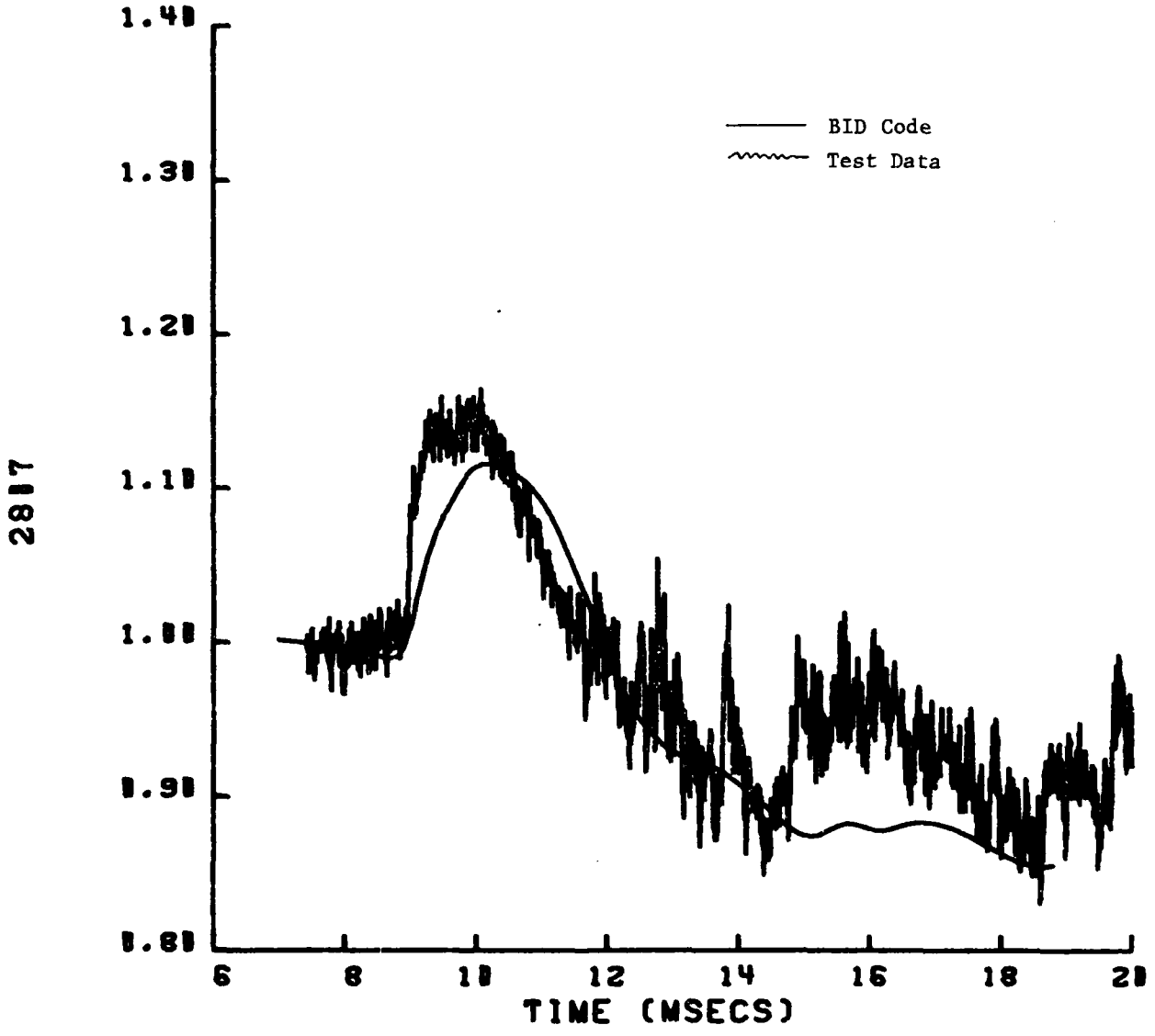

Figure 5.11a. Transducer 2807.

Figure 5.11. Comparison of theoretical and experimental time histories of engine face total pressures for Run 39 (Part 544), leeward (inboard) inlet.

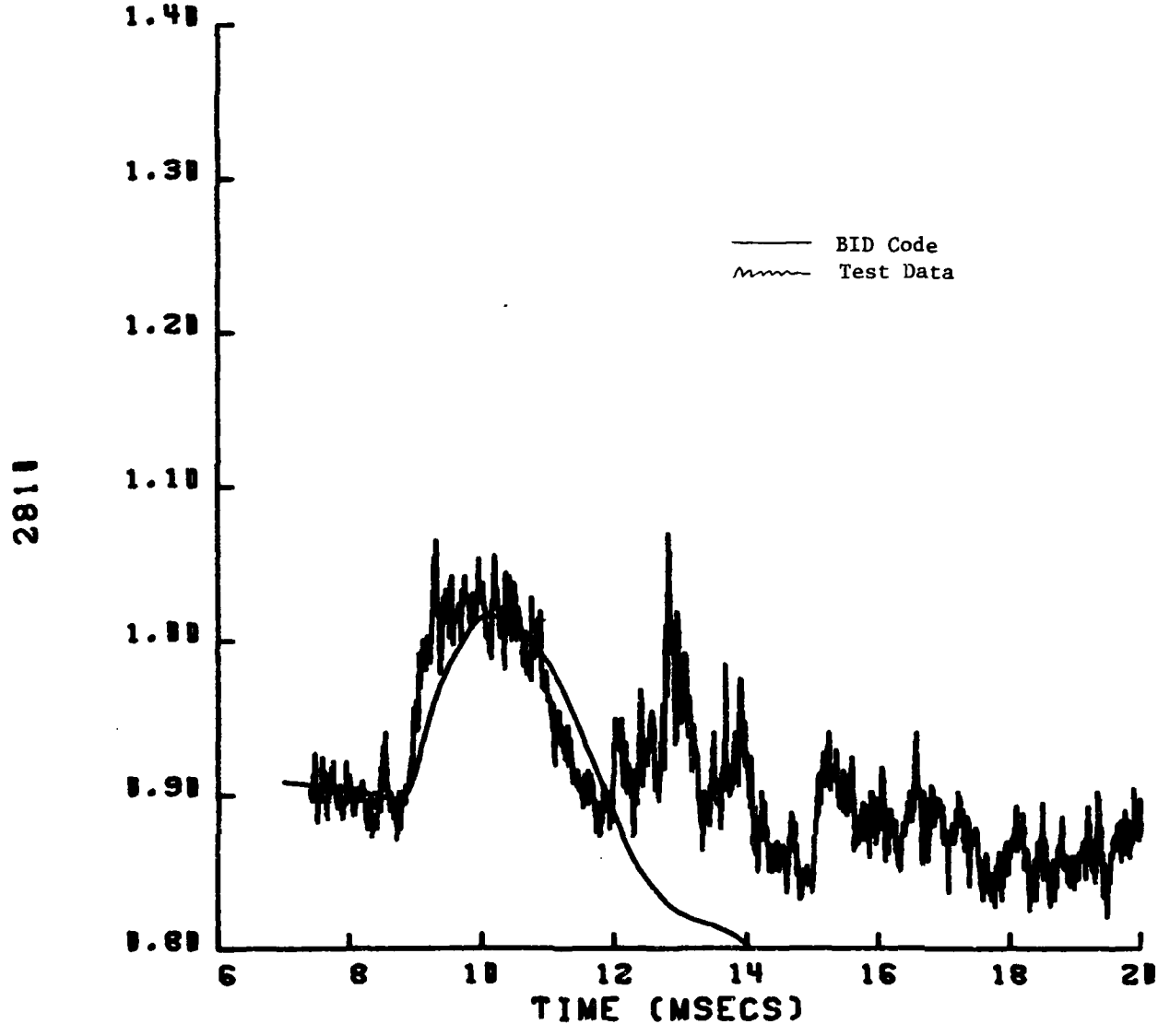

Figure 5.11b. Transducer 2810.

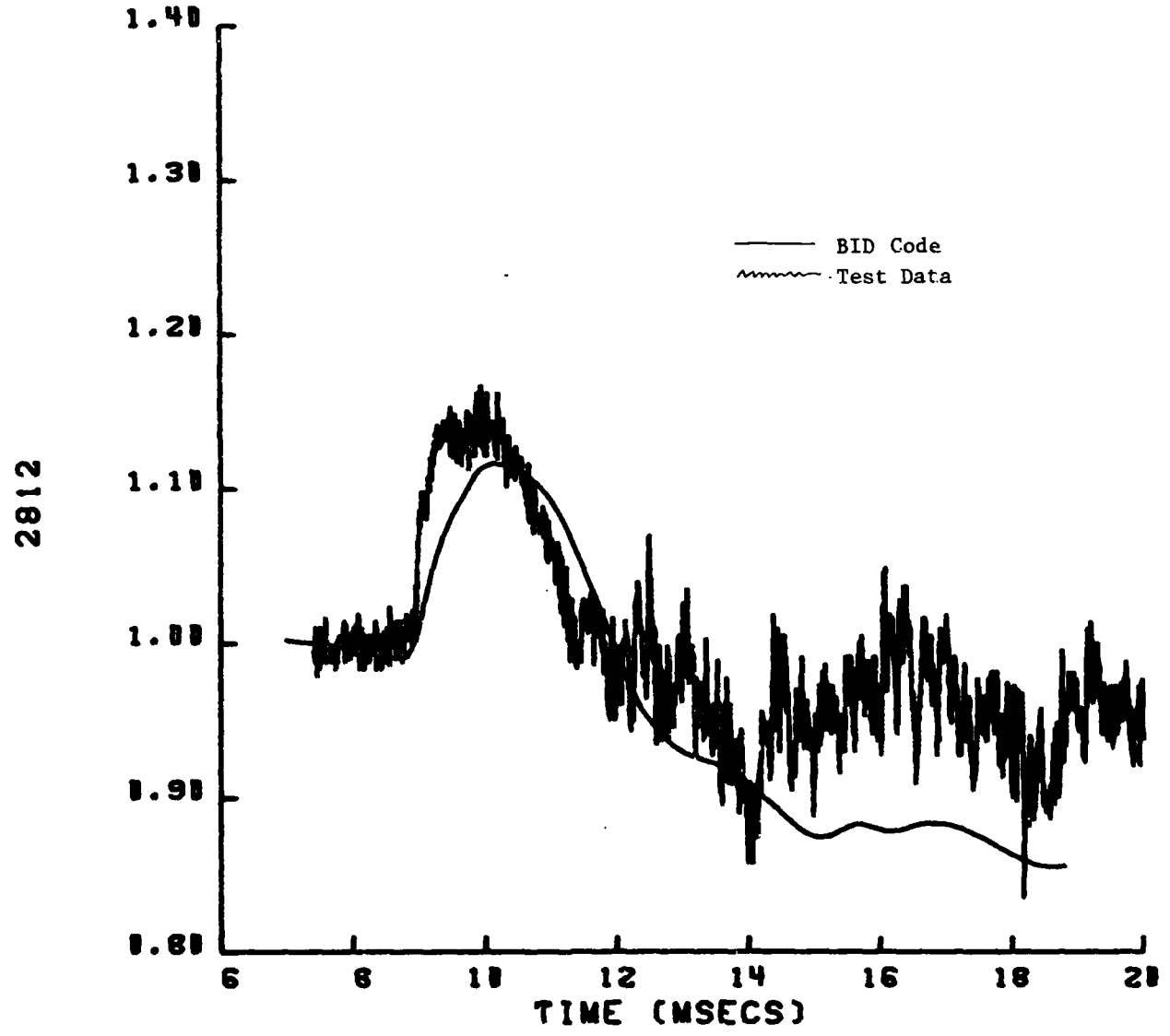

Figure 5.11c. Transducer 2812.

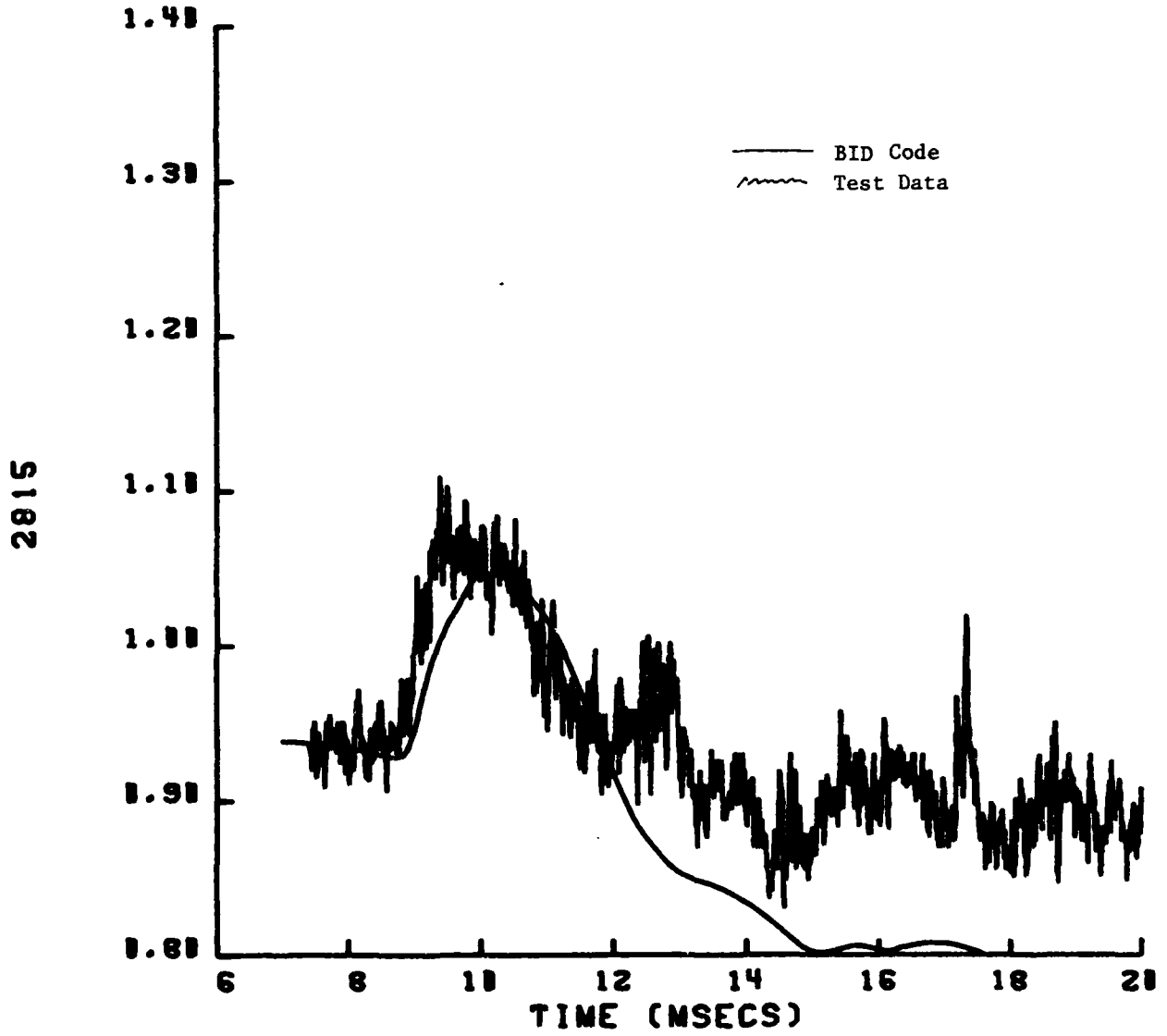

Figure 5.11d. Transducer 2815.

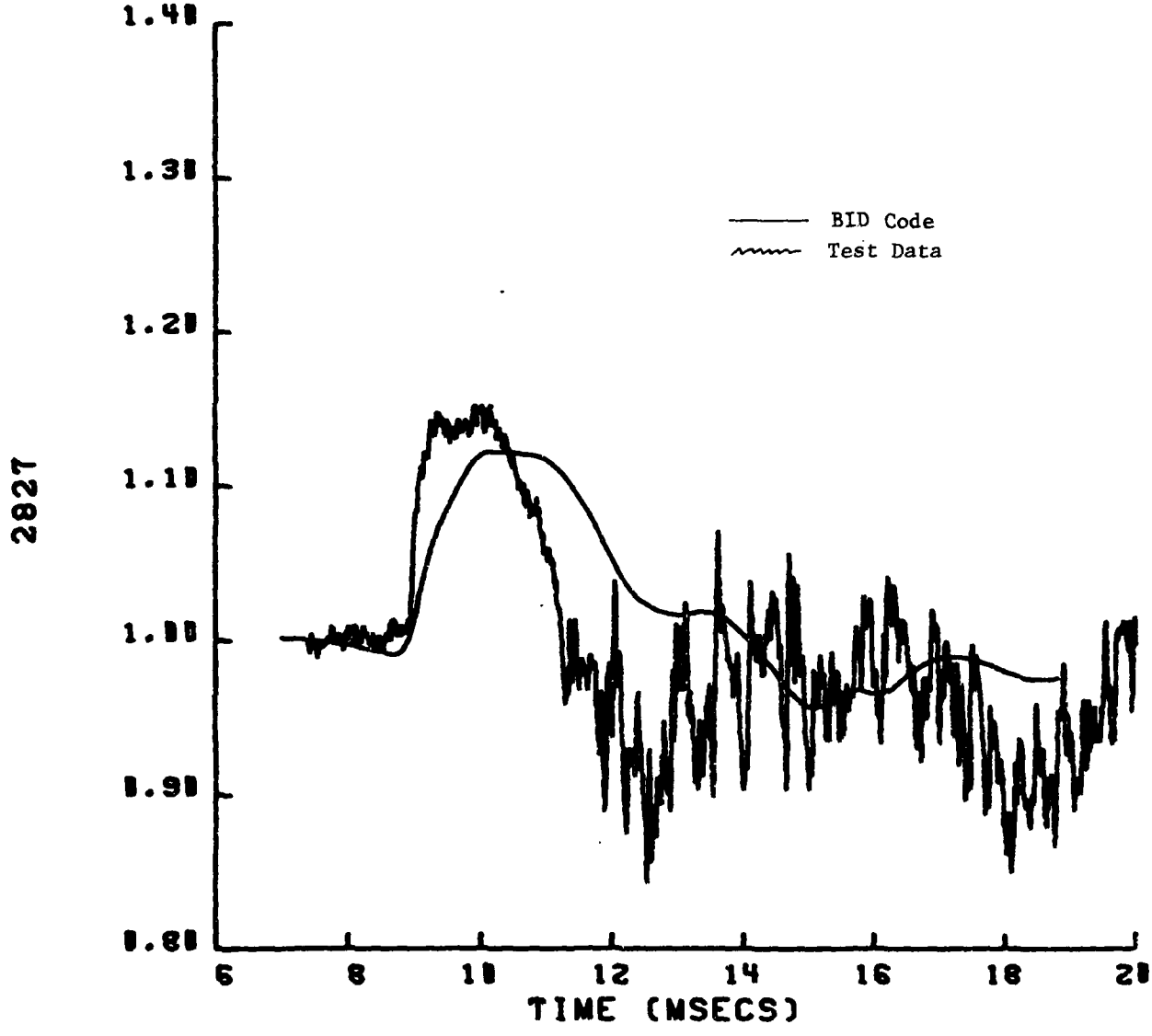

Figure 5.11e. Transducer 2827.

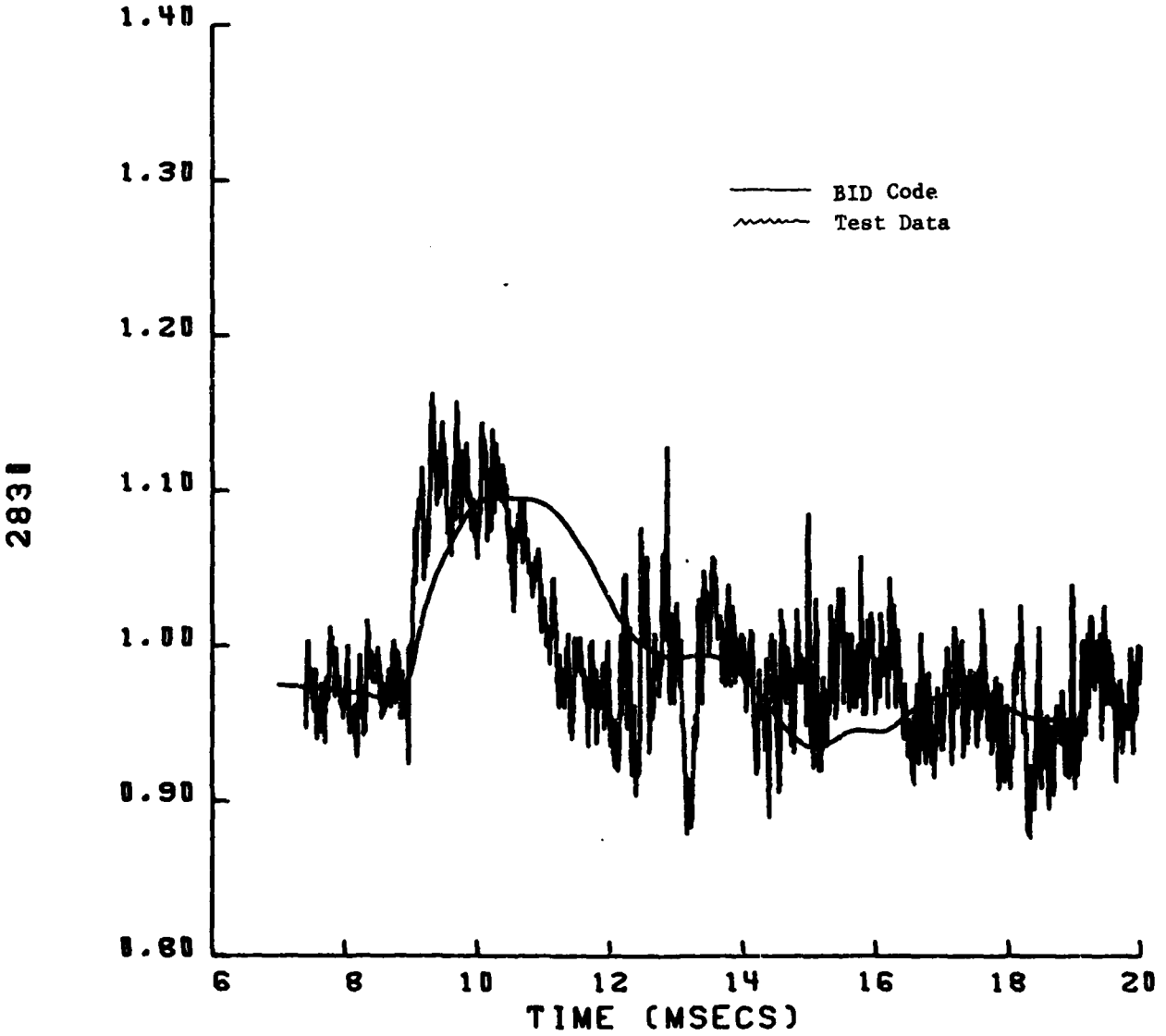

Figure 5.11f. Transducer 2830.

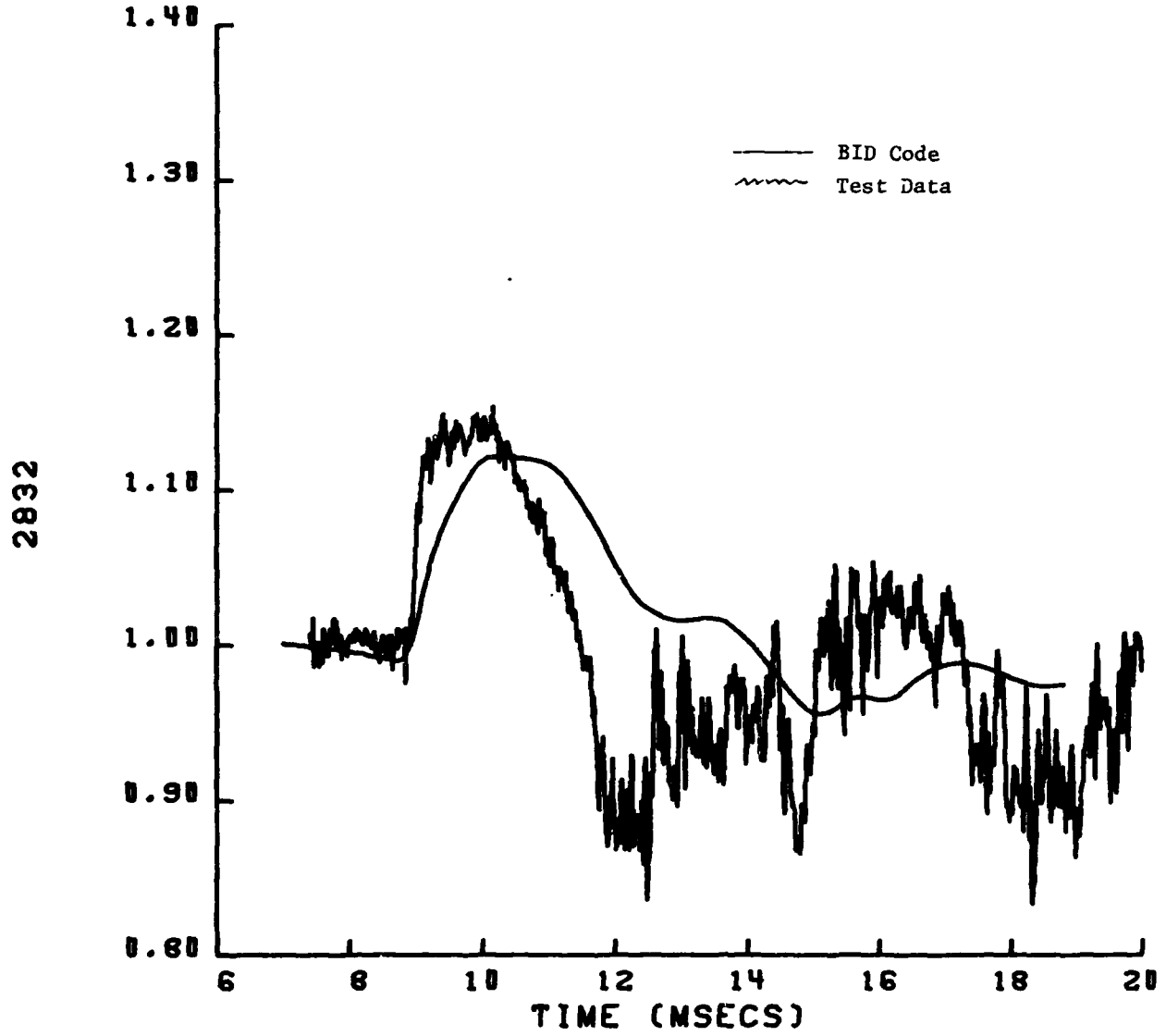

Figure 5.11g. Transducer 2832.

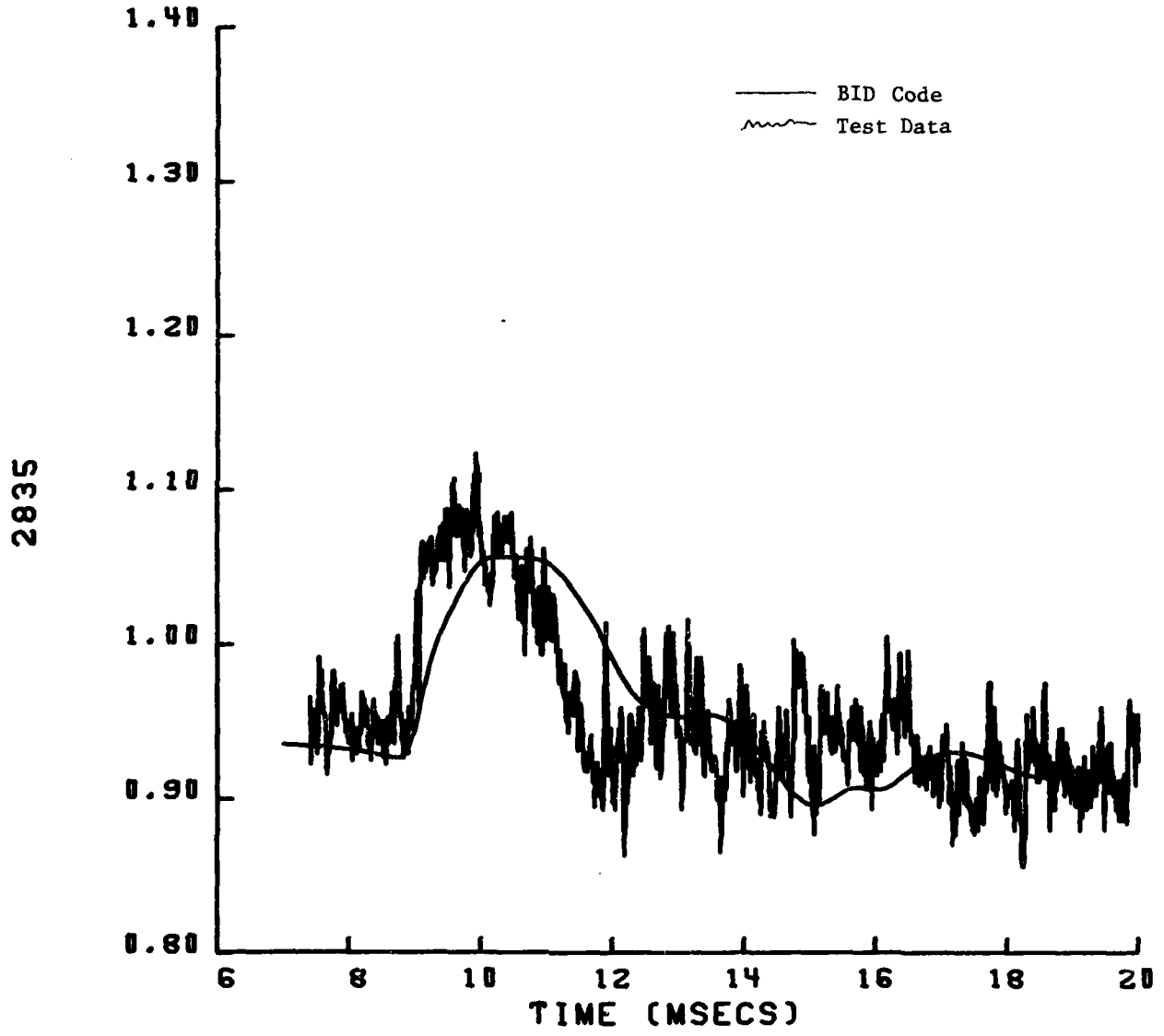

Figure 5.11h. Transducer 2835.

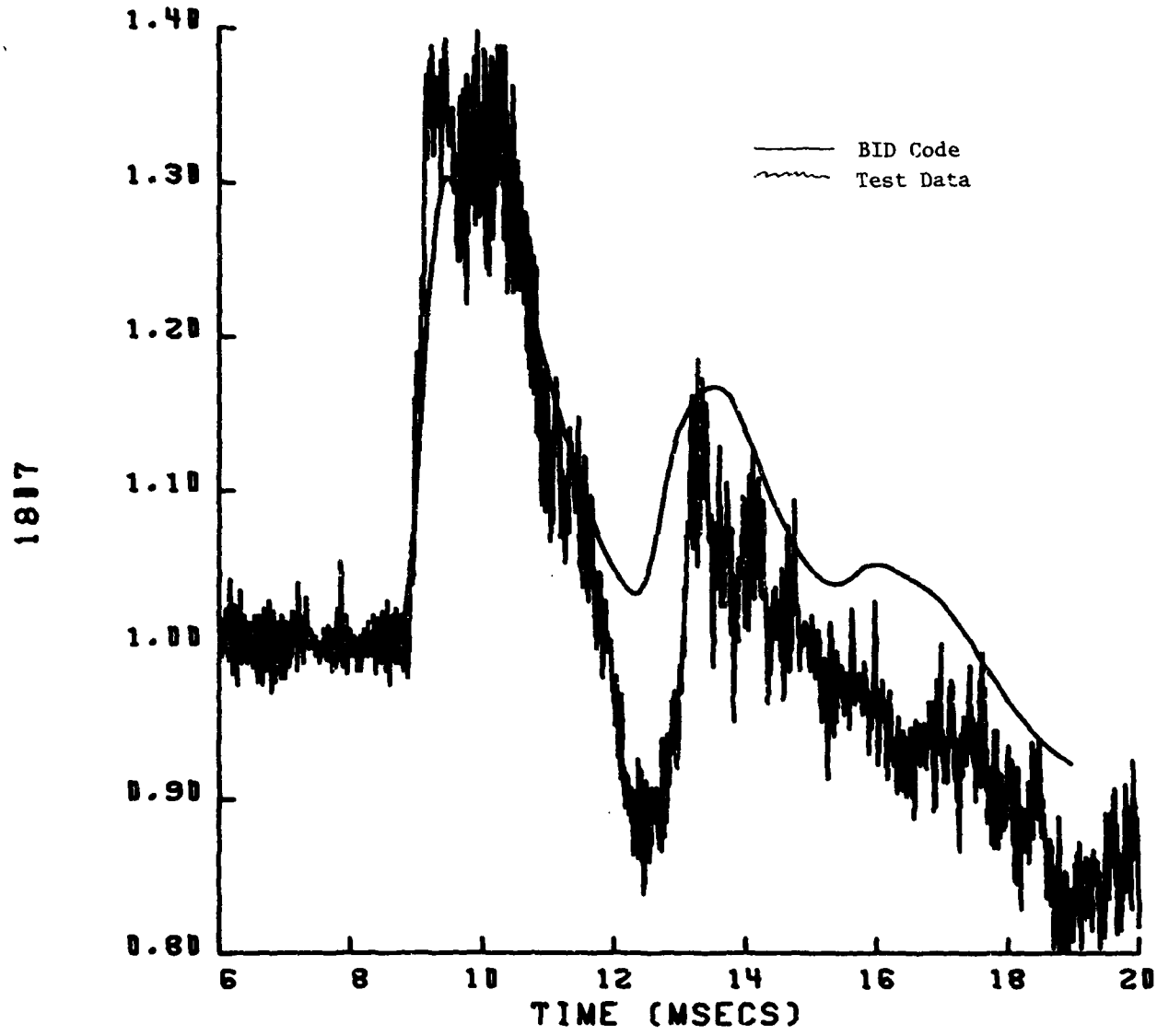

Figure 5.12a. Transducer 1807.

Figure 5.12. Comparison of theoretical and experimental time histories of engine face total pressures for Run 40 (Part 619), blastward (outboard) inlet.

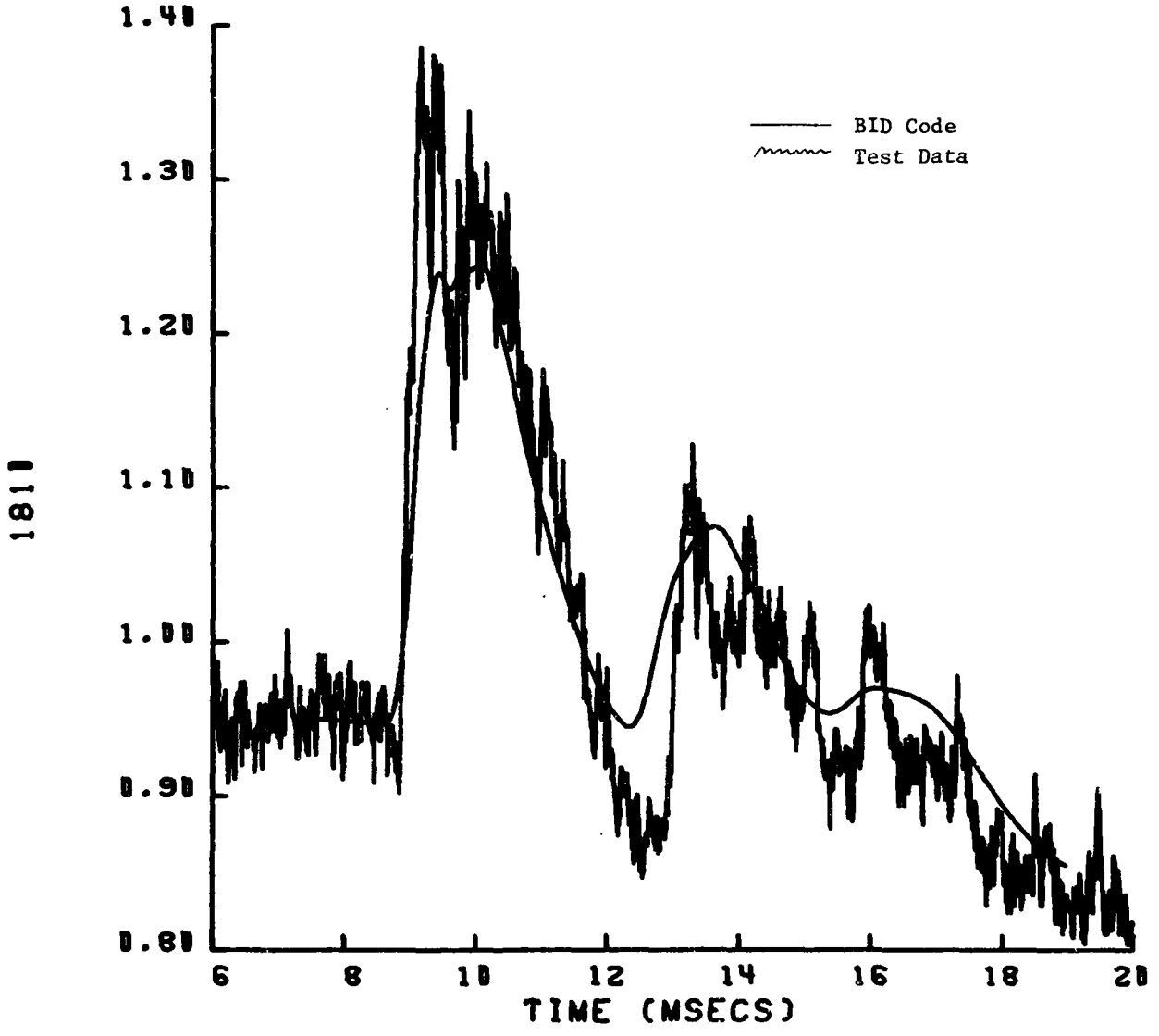

Figure 5.12b. Transducer 1810.

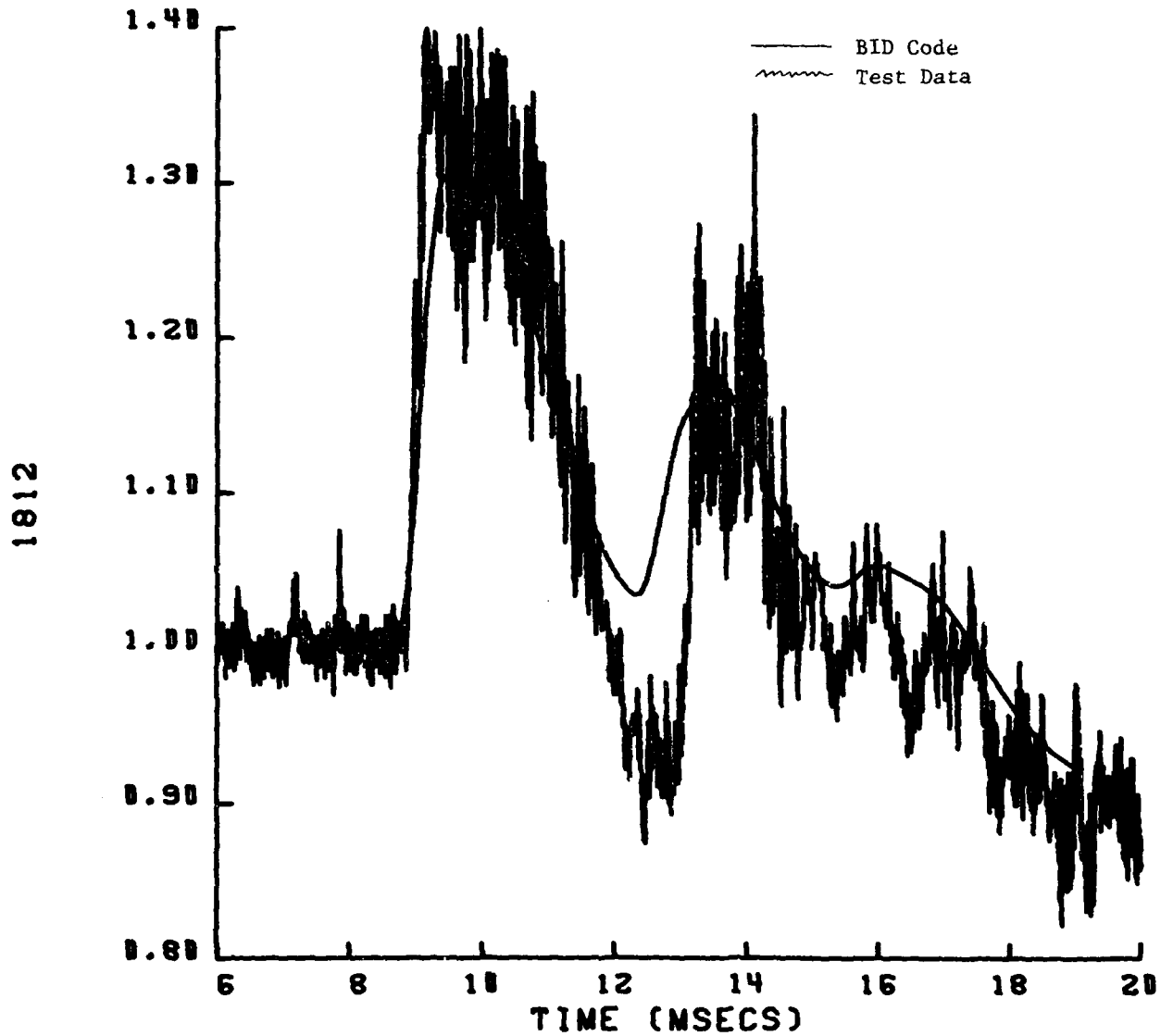

Figure 5.12c. Transducer 1812.

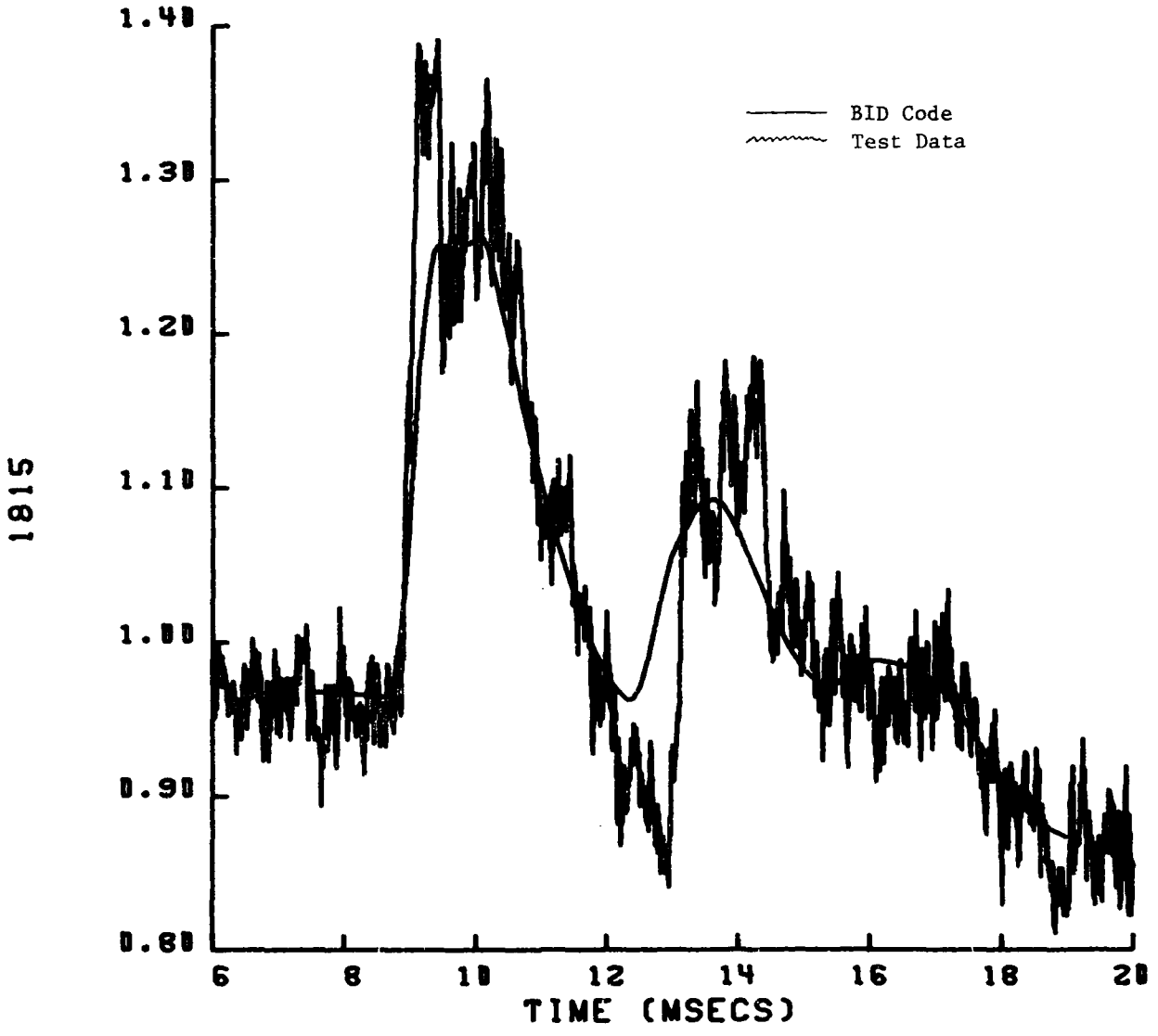

Figure 5.12d. Transducer 1815.

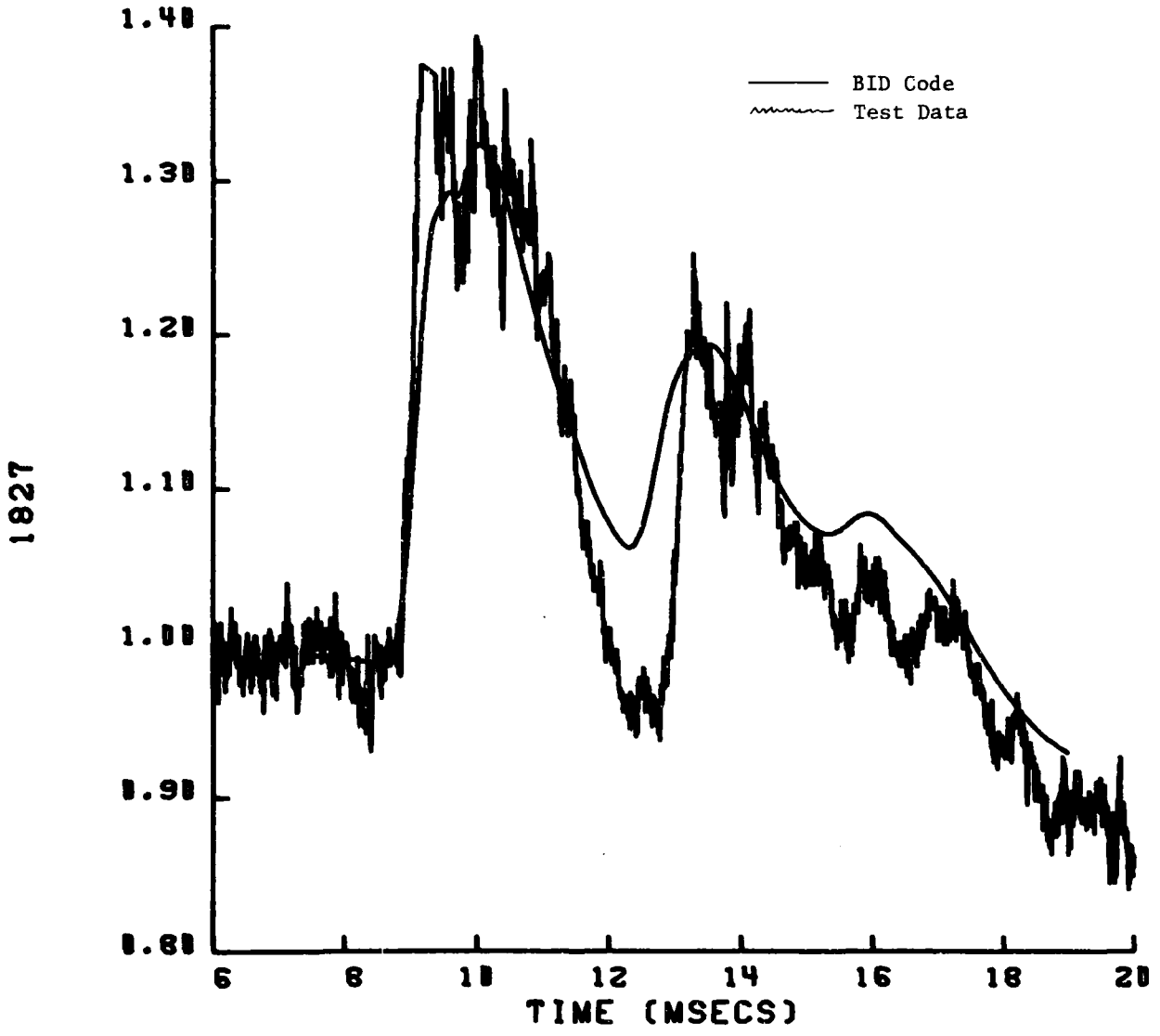

Figure 5.12e. Transducer 1827.

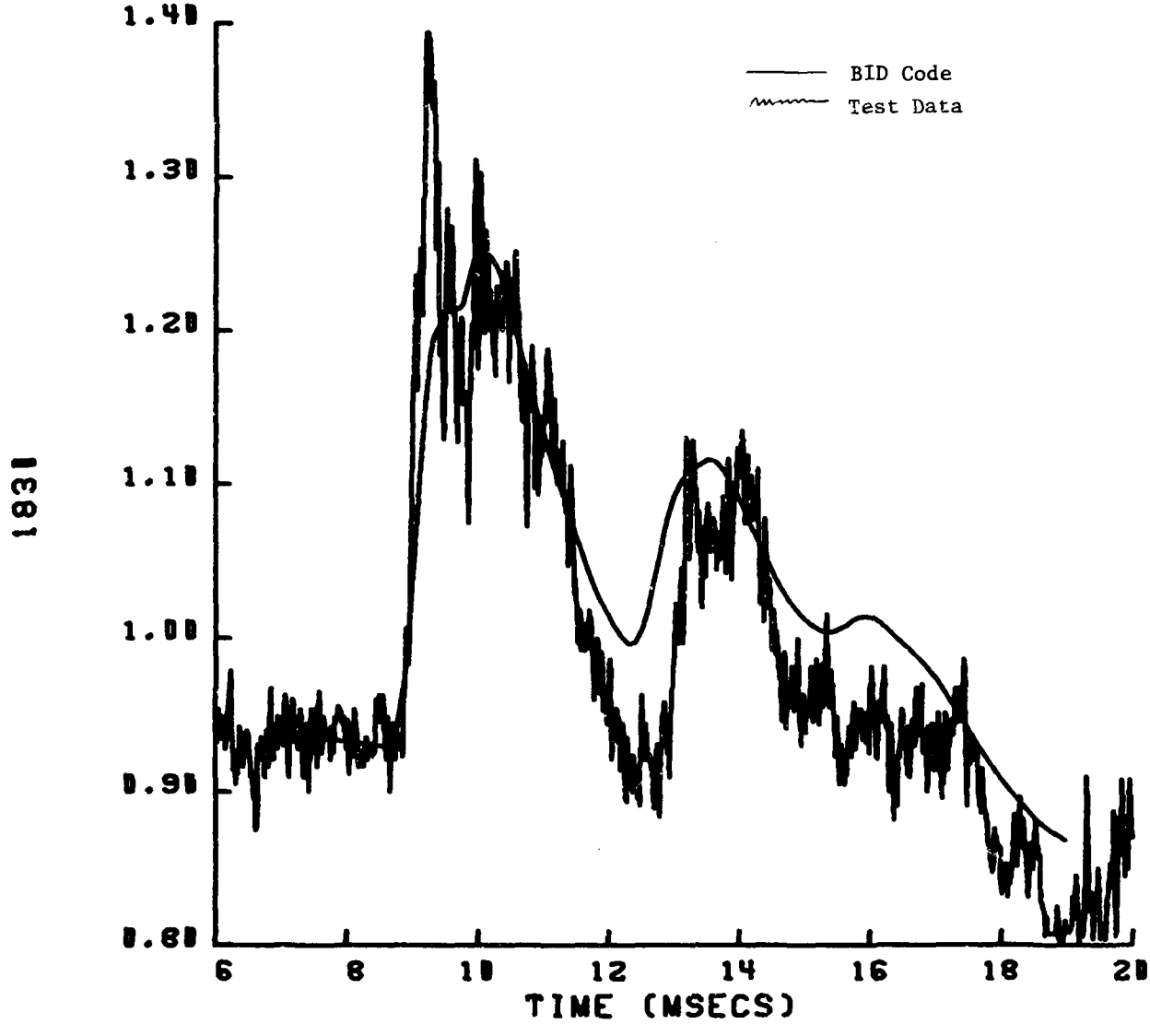

Figure 5.12f. Transducer 1830.

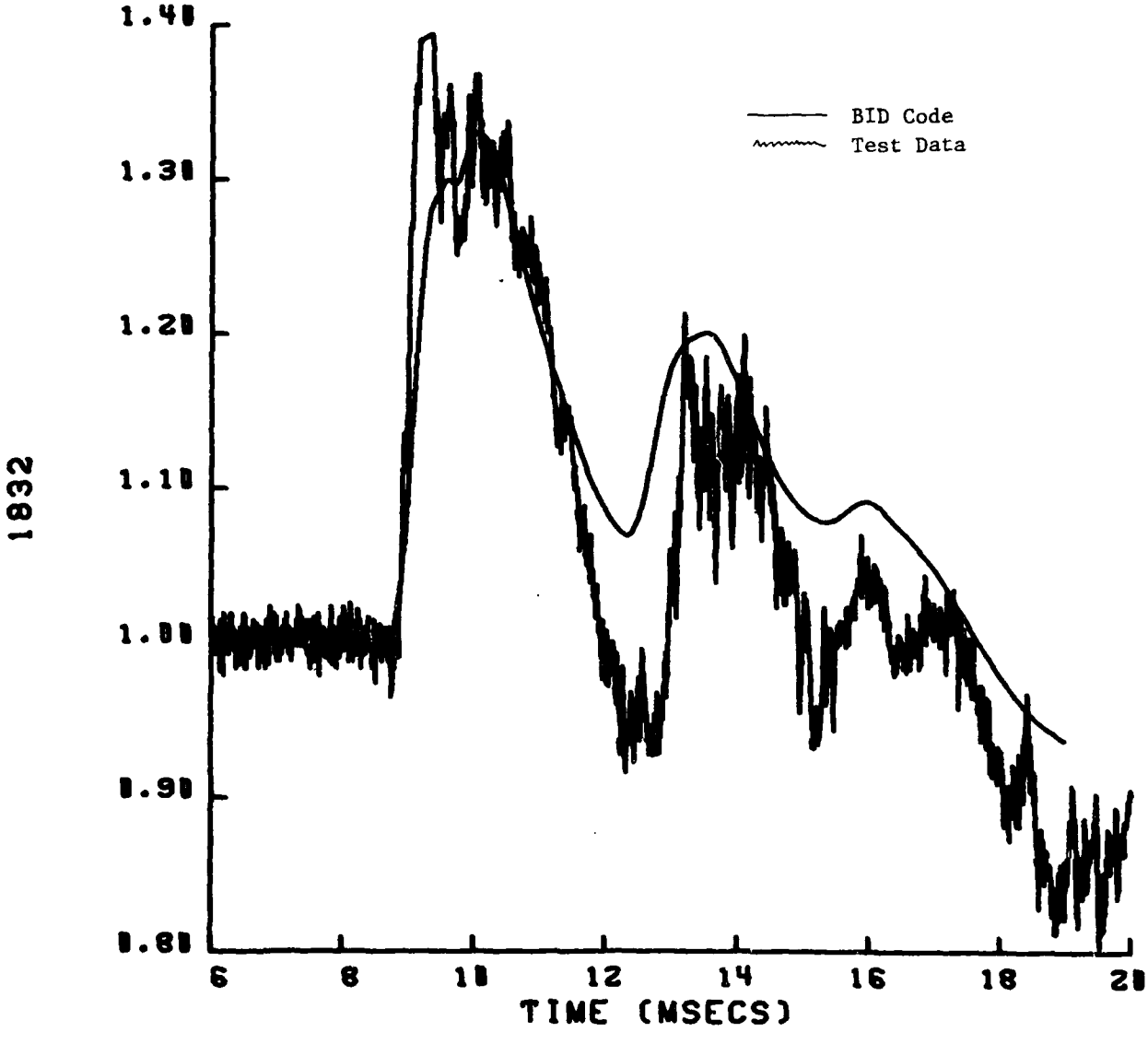

Figure 5.12g. Transducer 1832.

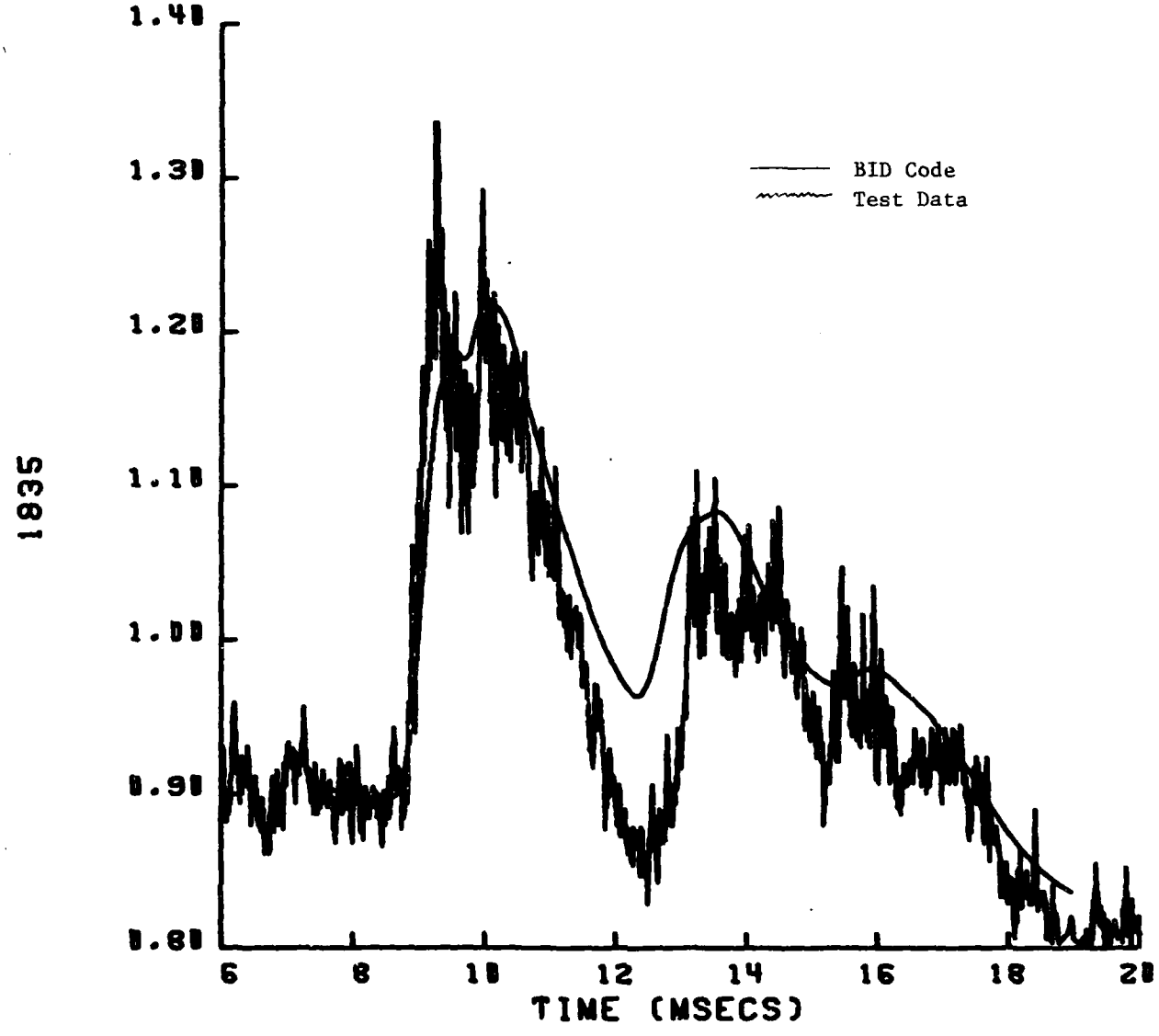

Figure 5.12h. Transducer 1835.

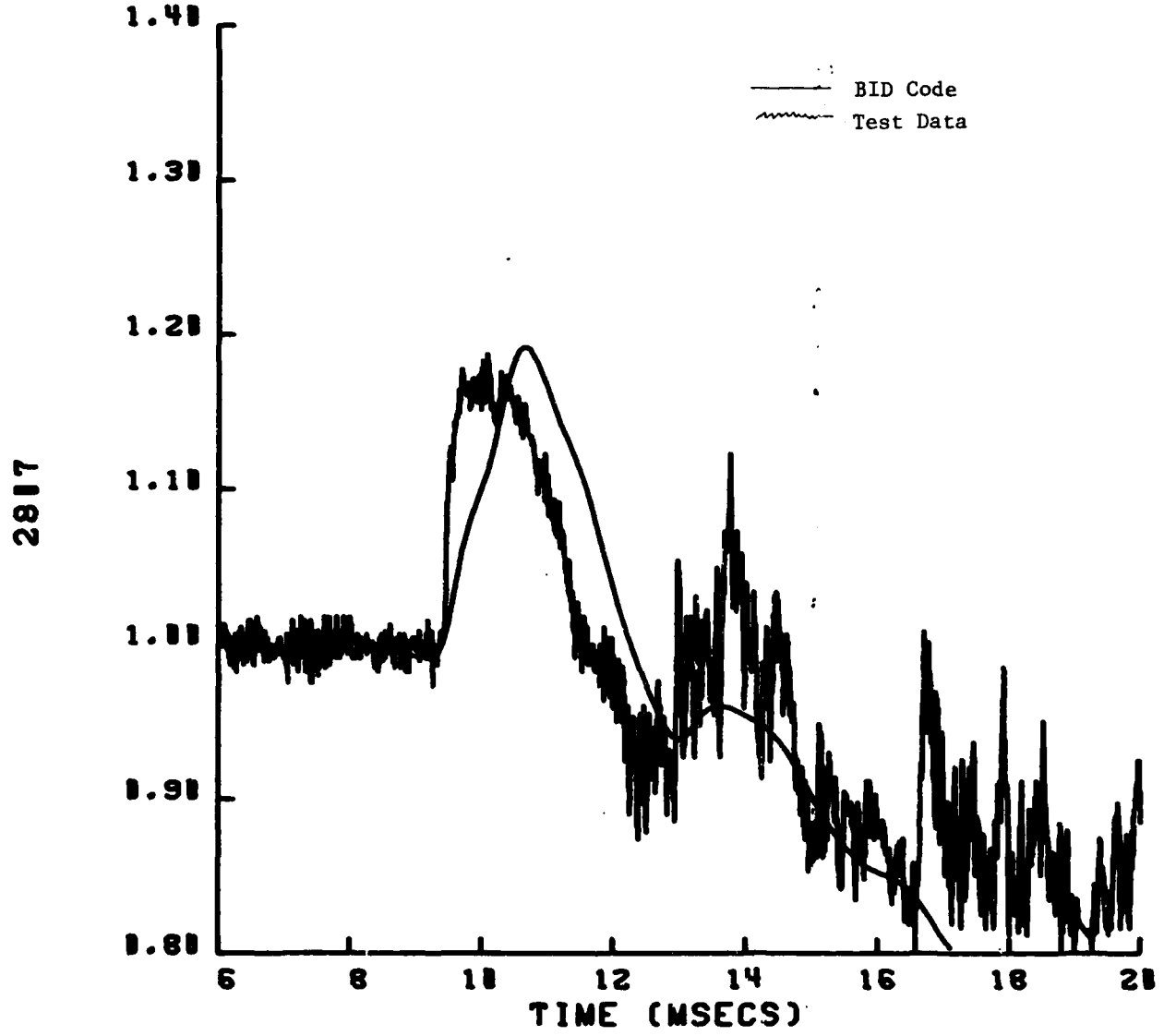

Figure 5.13a. Transducer 2807.

Figure 5.13. Comparison of theoretical and experimental time histories of engine face total pressures for Run 40 (Part 619), leeward (inboard) inlet.

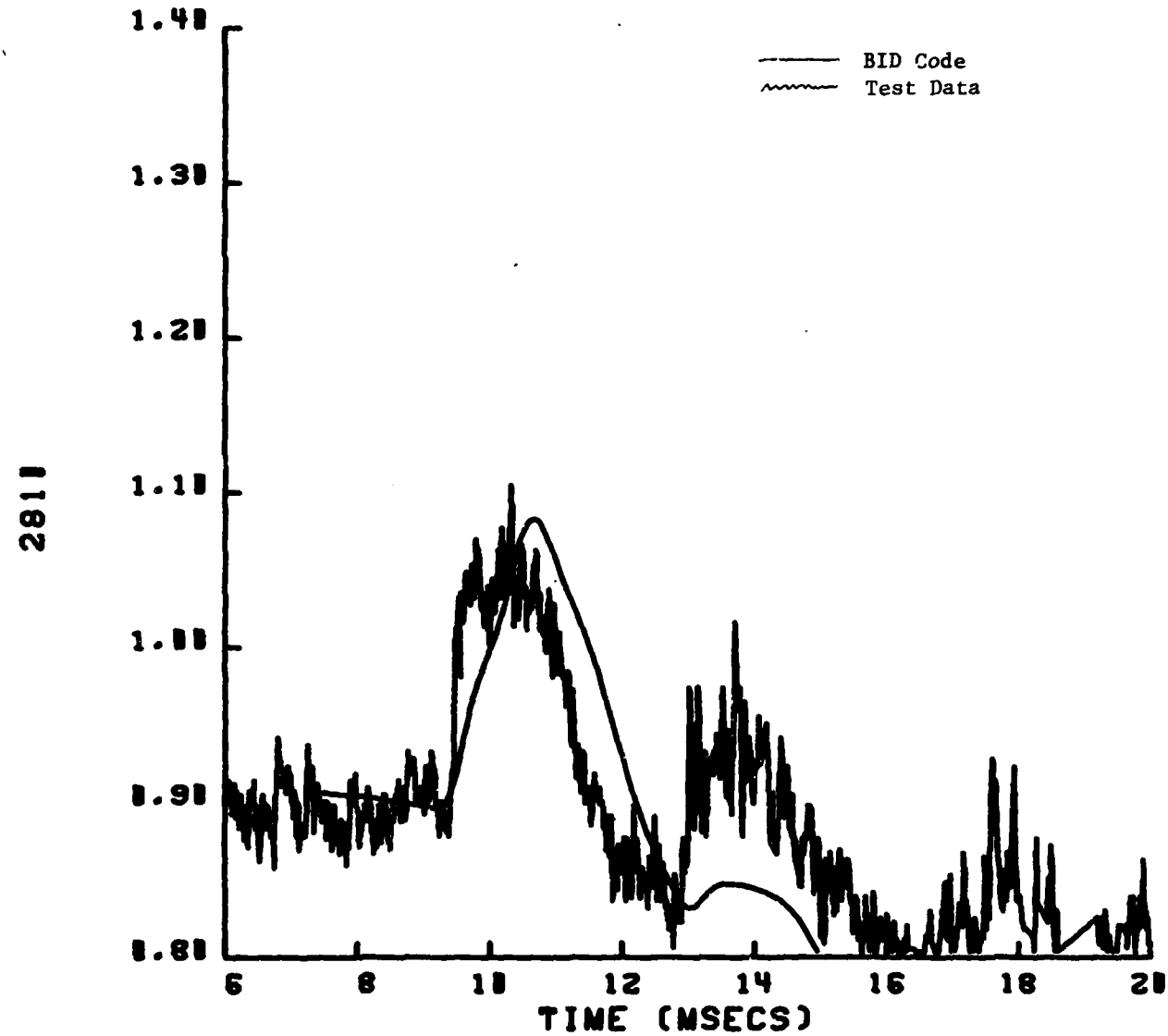

Figure 5.13b. Transducer 2810.

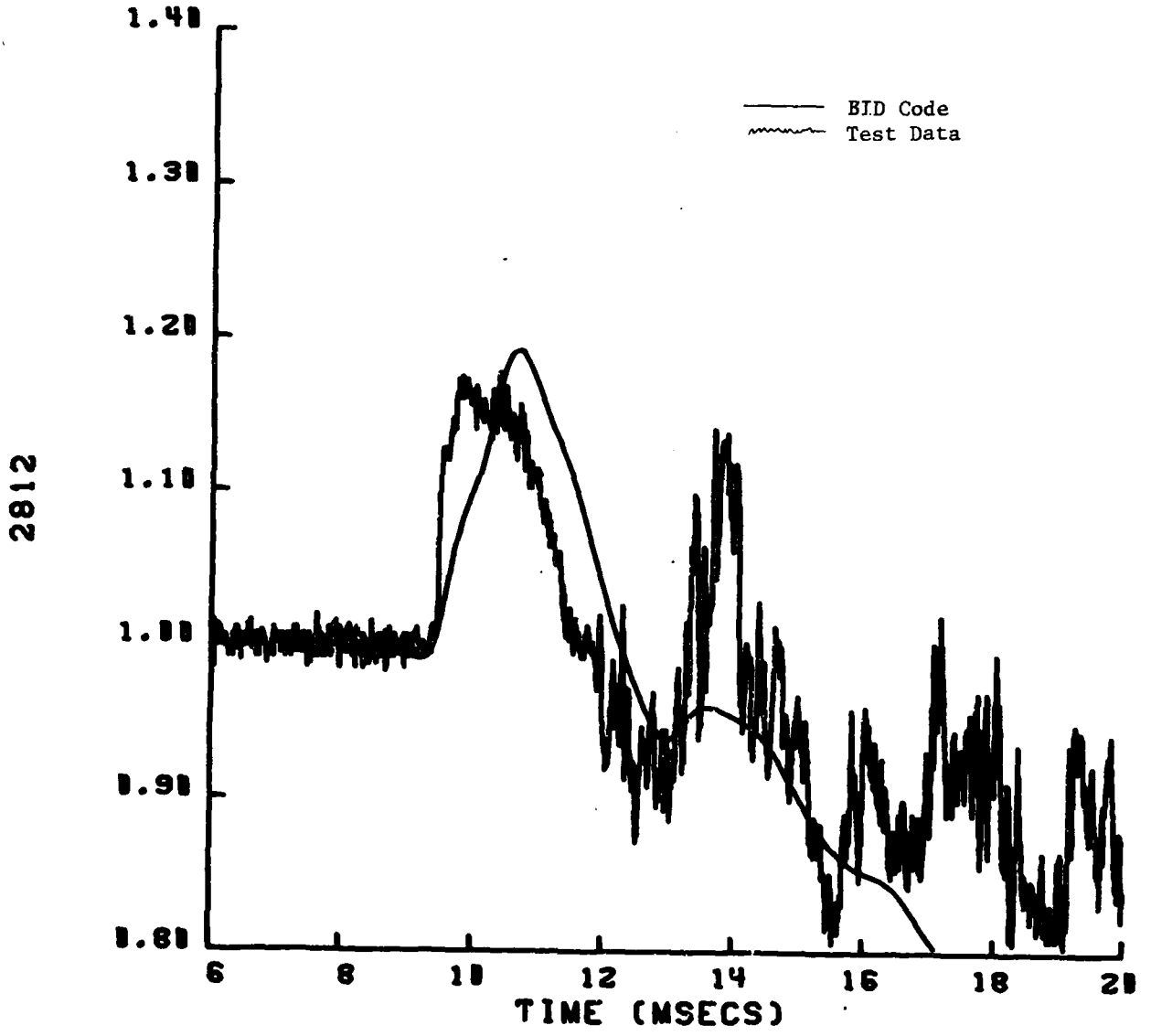

Figure 5.13c. Transducer 2812.

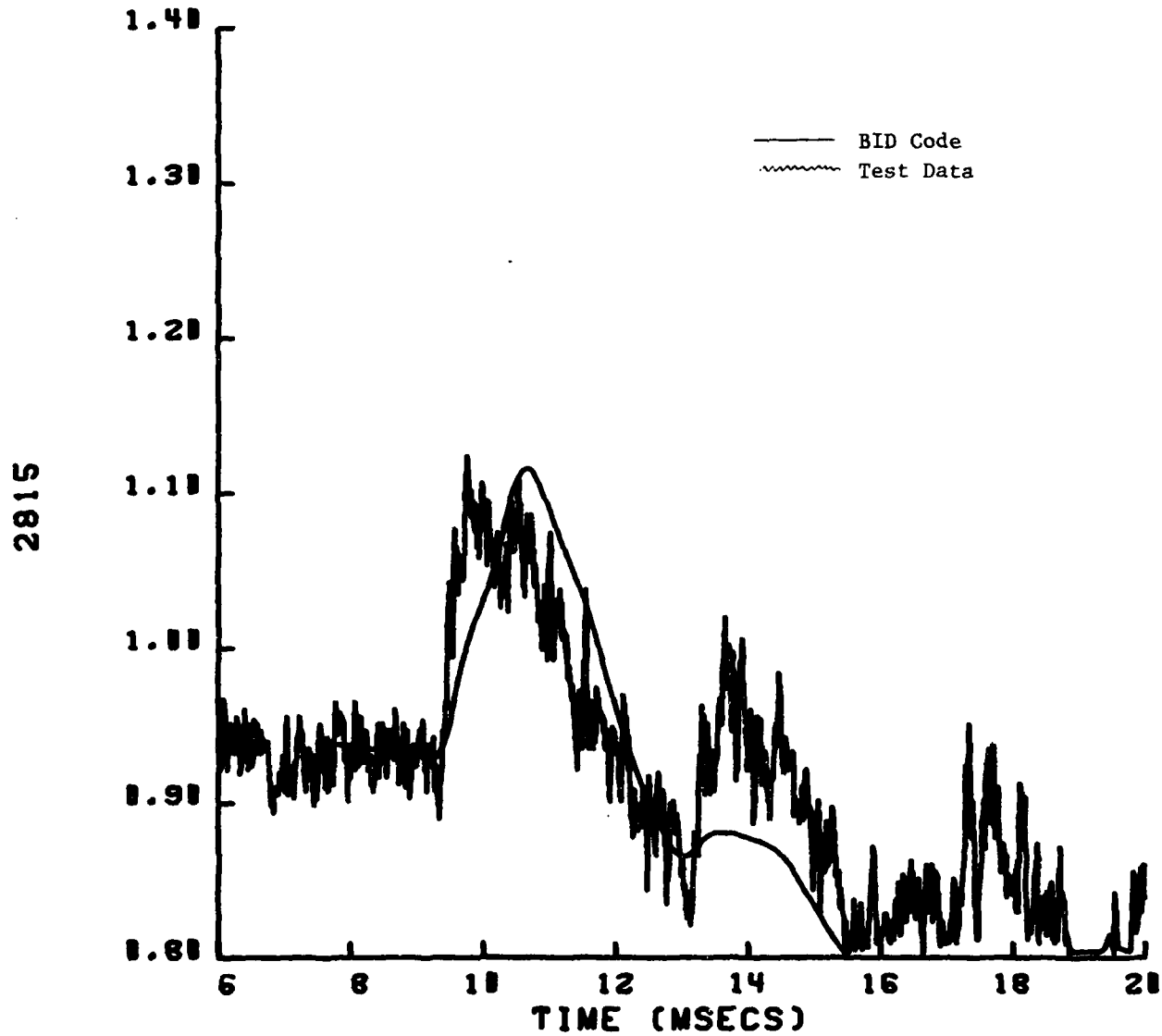

Figure 5.13d. Transducer 2815.

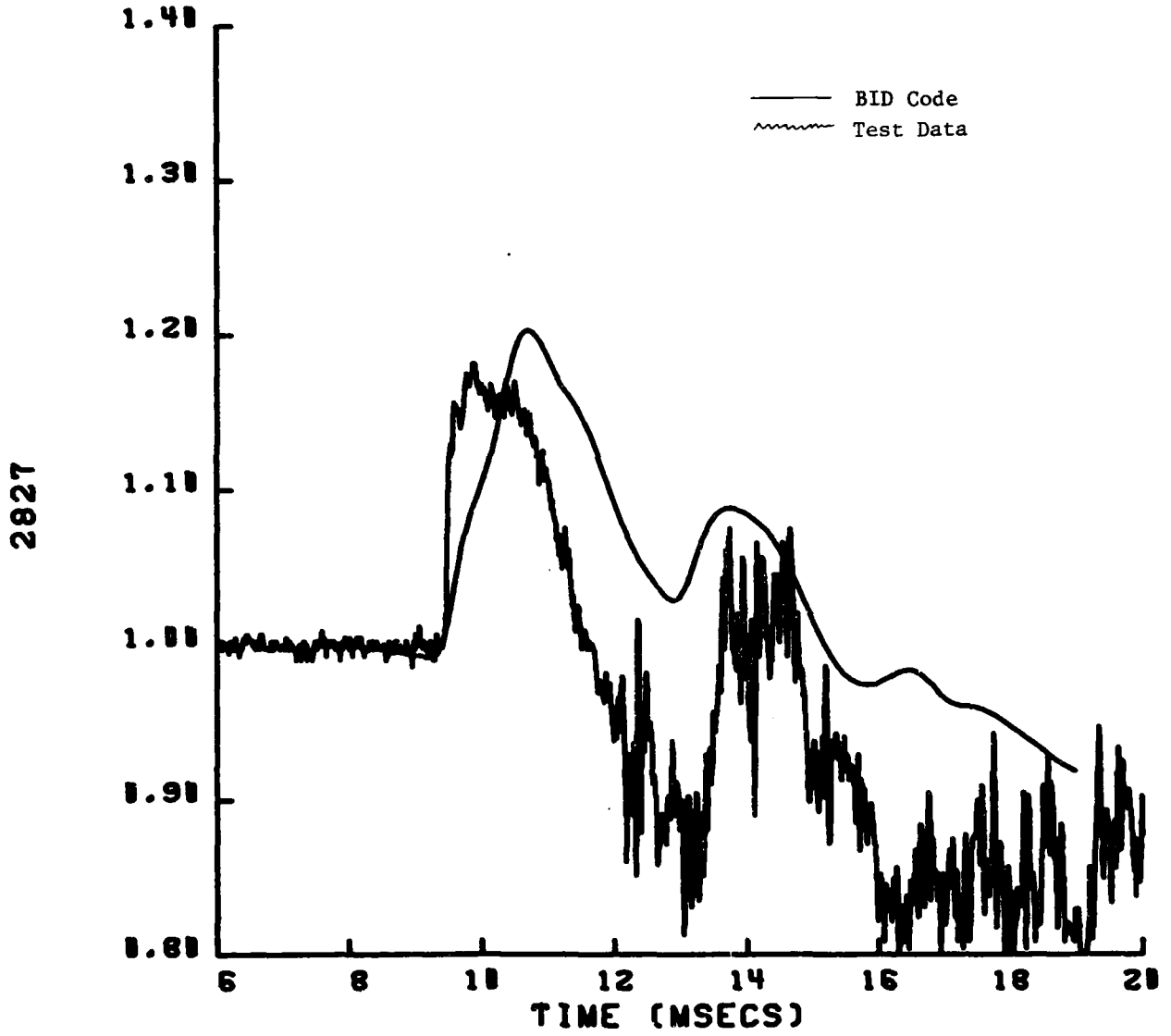

Figure 5.13e. Transducer 2827.

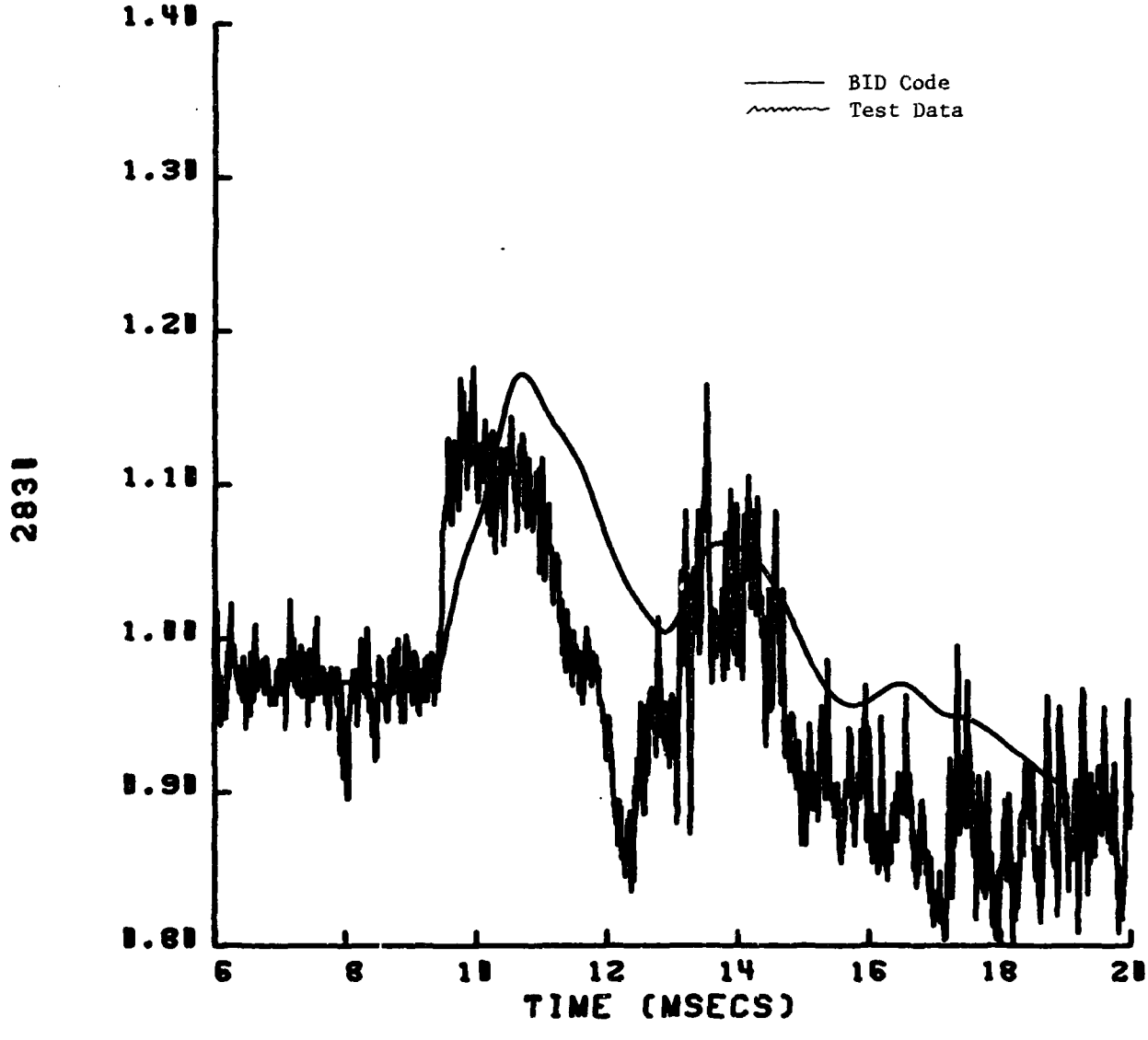

Figure 5.13f. Transducer 2830.

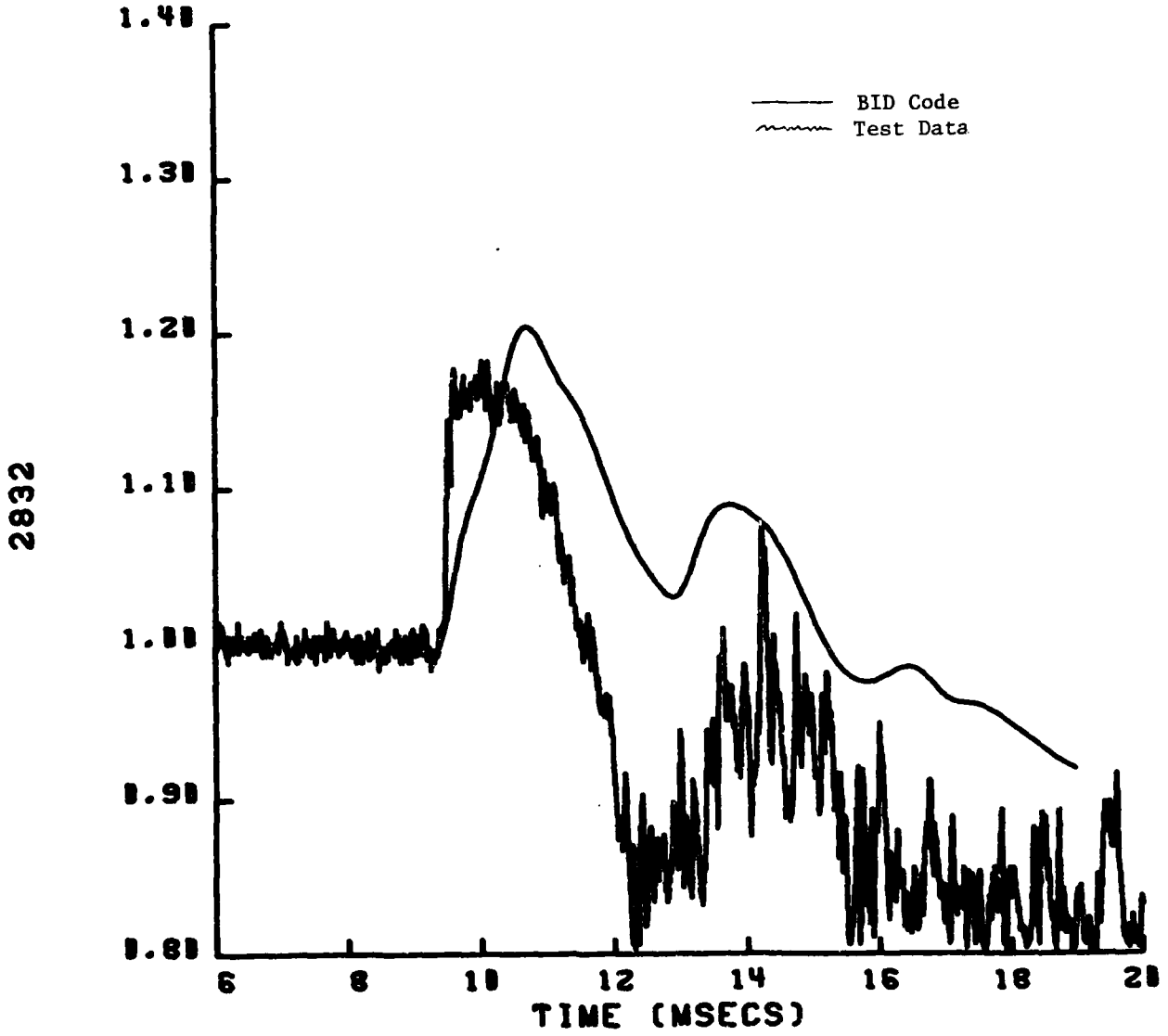

Figure 5.13g. Transducer 2832.

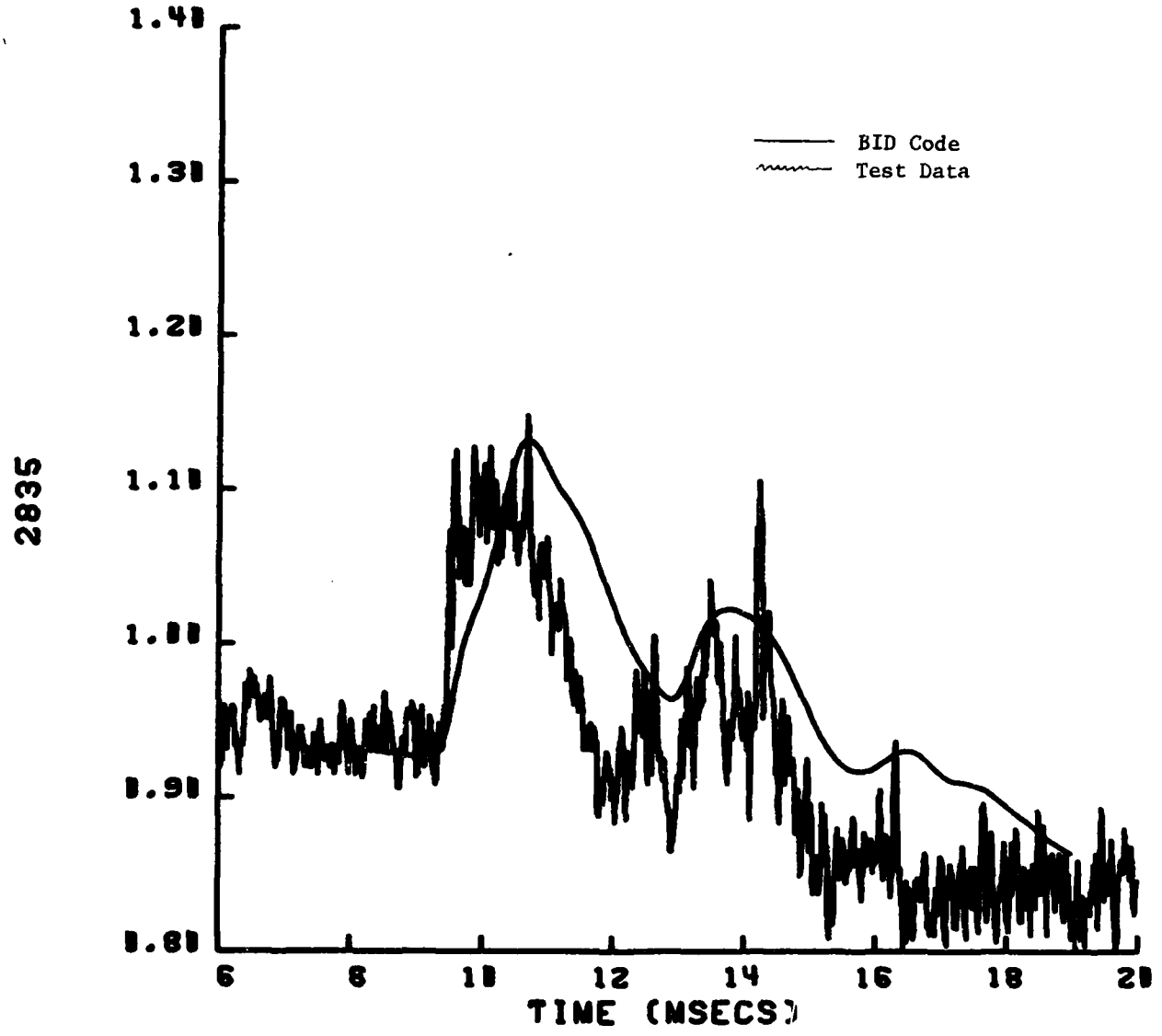

Figure 5.13h. Transducer 2835.

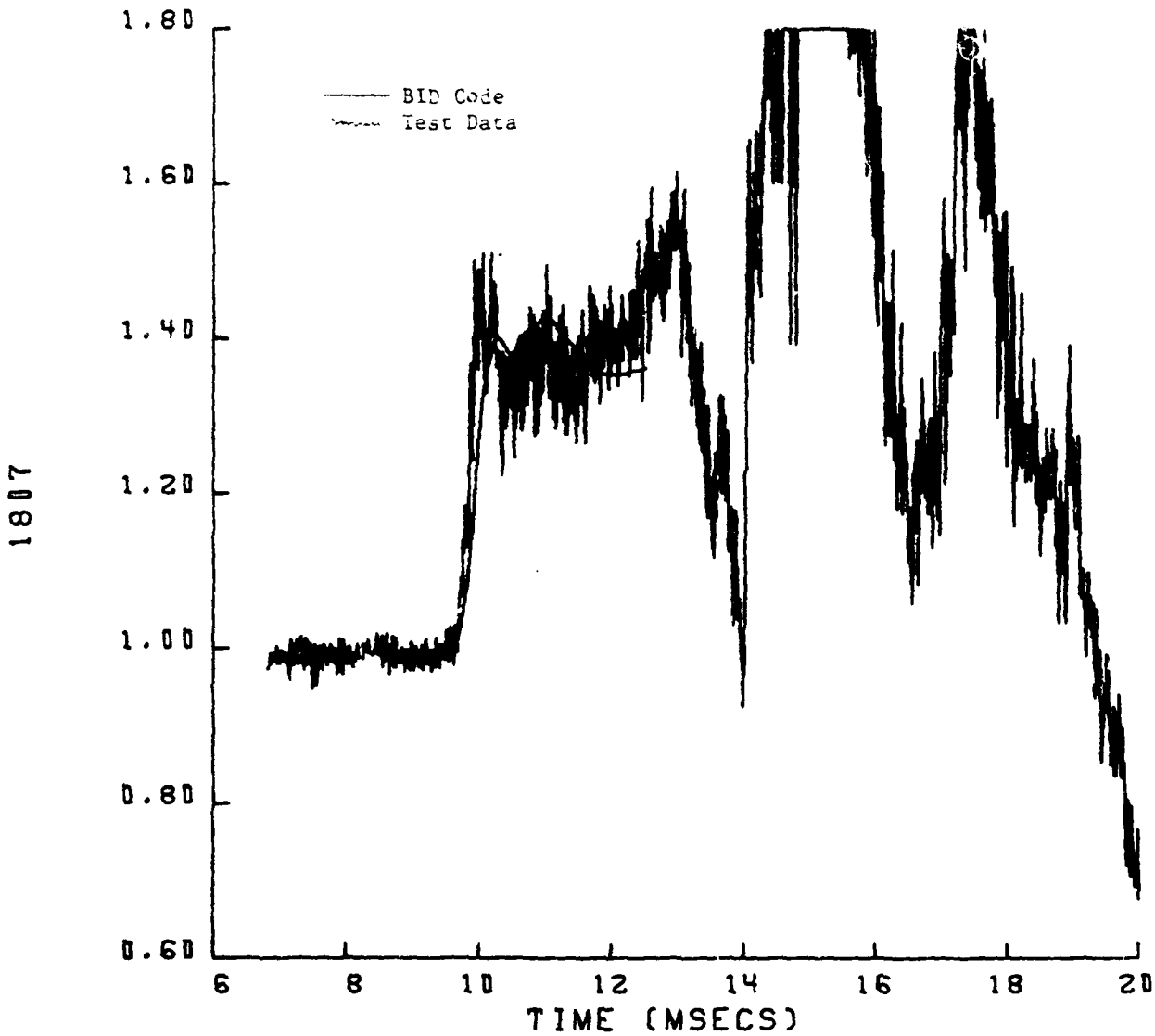

Figure 5.14a. Transducer 1810.

Figure 5.14. Comparison of theoretical and experimental time histories of engine face total pressures for Run 18 (Part 624), blastward (outboard) inlet.

AD-A088 511 KAMAN AVIDYNE BURLINGTON MA F/G 21/5
FURTHER EVALUATION OF BLAST TESTS OF AN ENGINE INLET.(U)
MAR 79 J R RUETENIK, R F SMILEY, M A TOMAYKO DNA001-78-C-0239
UNCLASSIFIED KA-TR-165 DNA-4994F NL

3 OF 3
AD A 088511

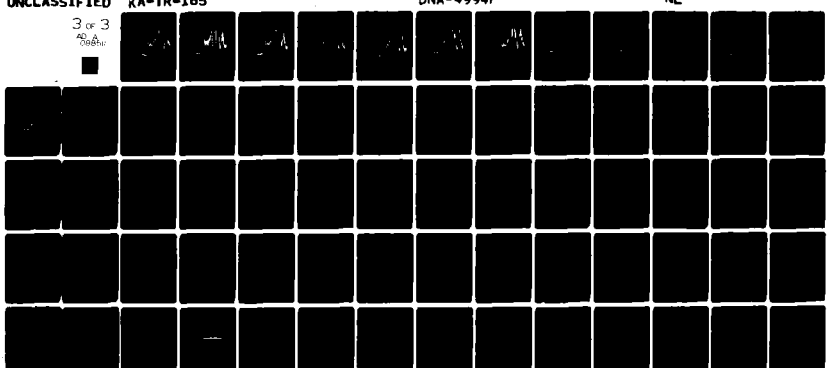

END
DATE FILMED
9-80
DTIC

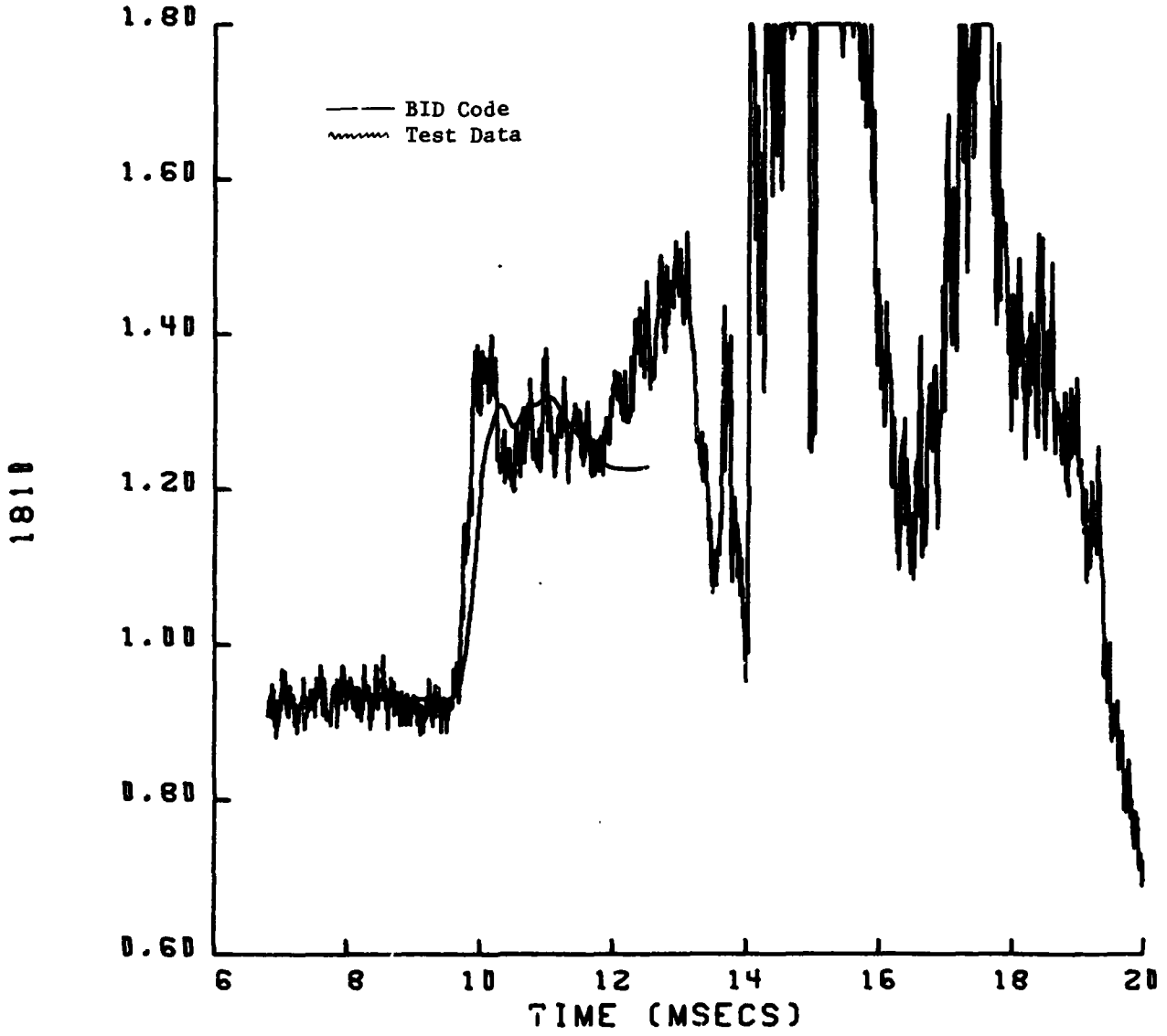

Figure 5.14b. Transducer 1310.

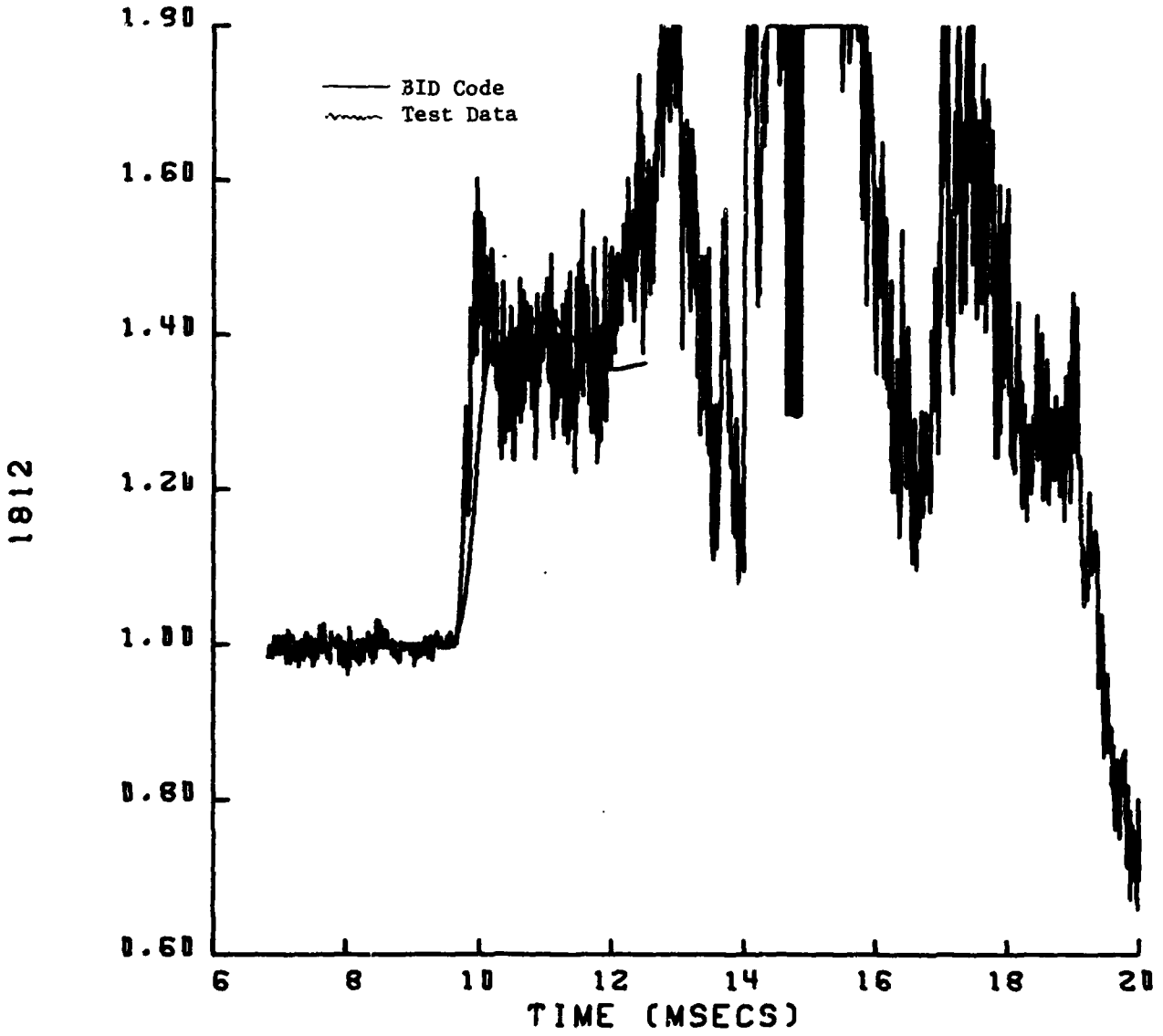

Figure 5.14c. Transducer 1812.

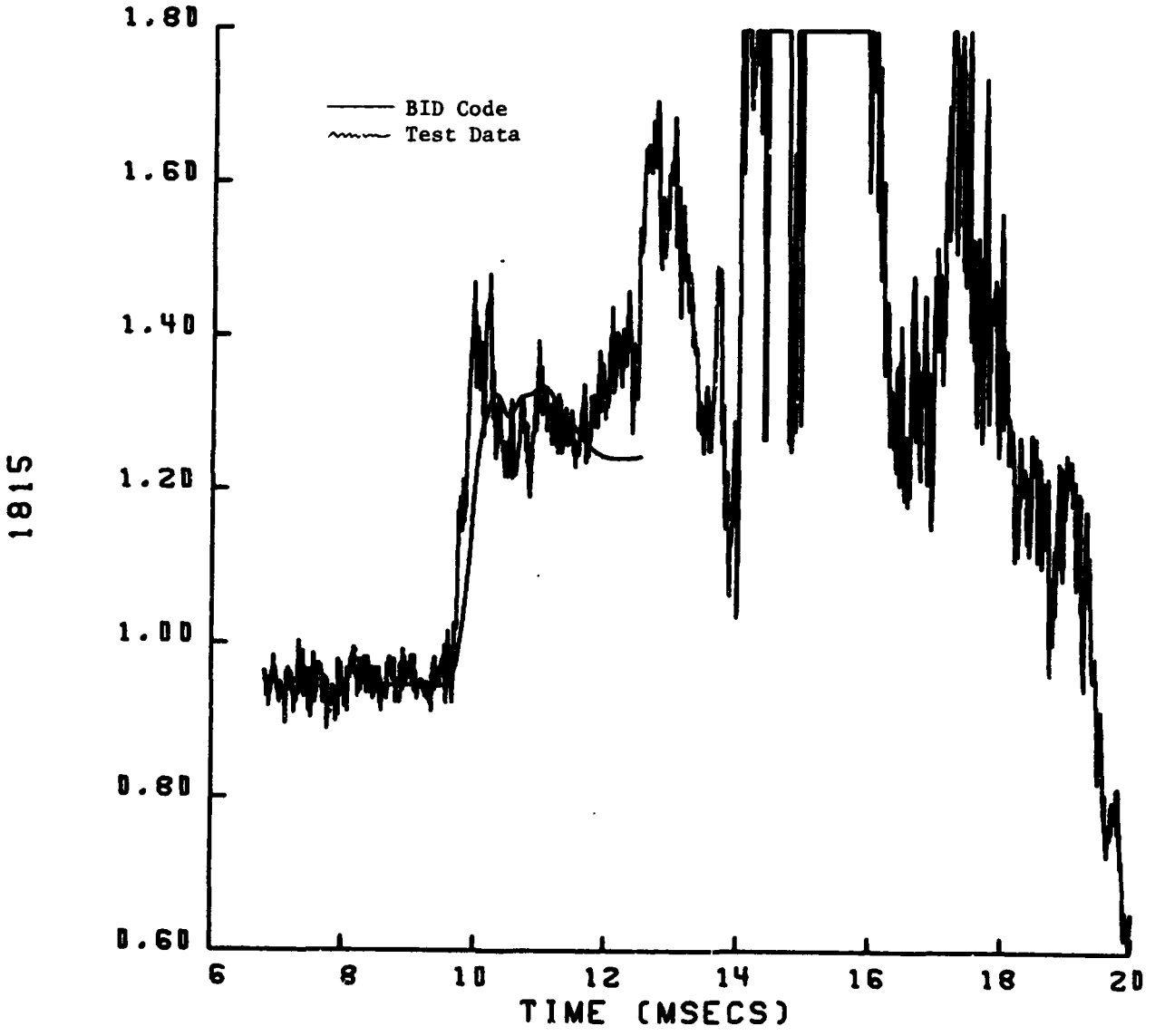

Figure 5.14d. Transducer 1815.

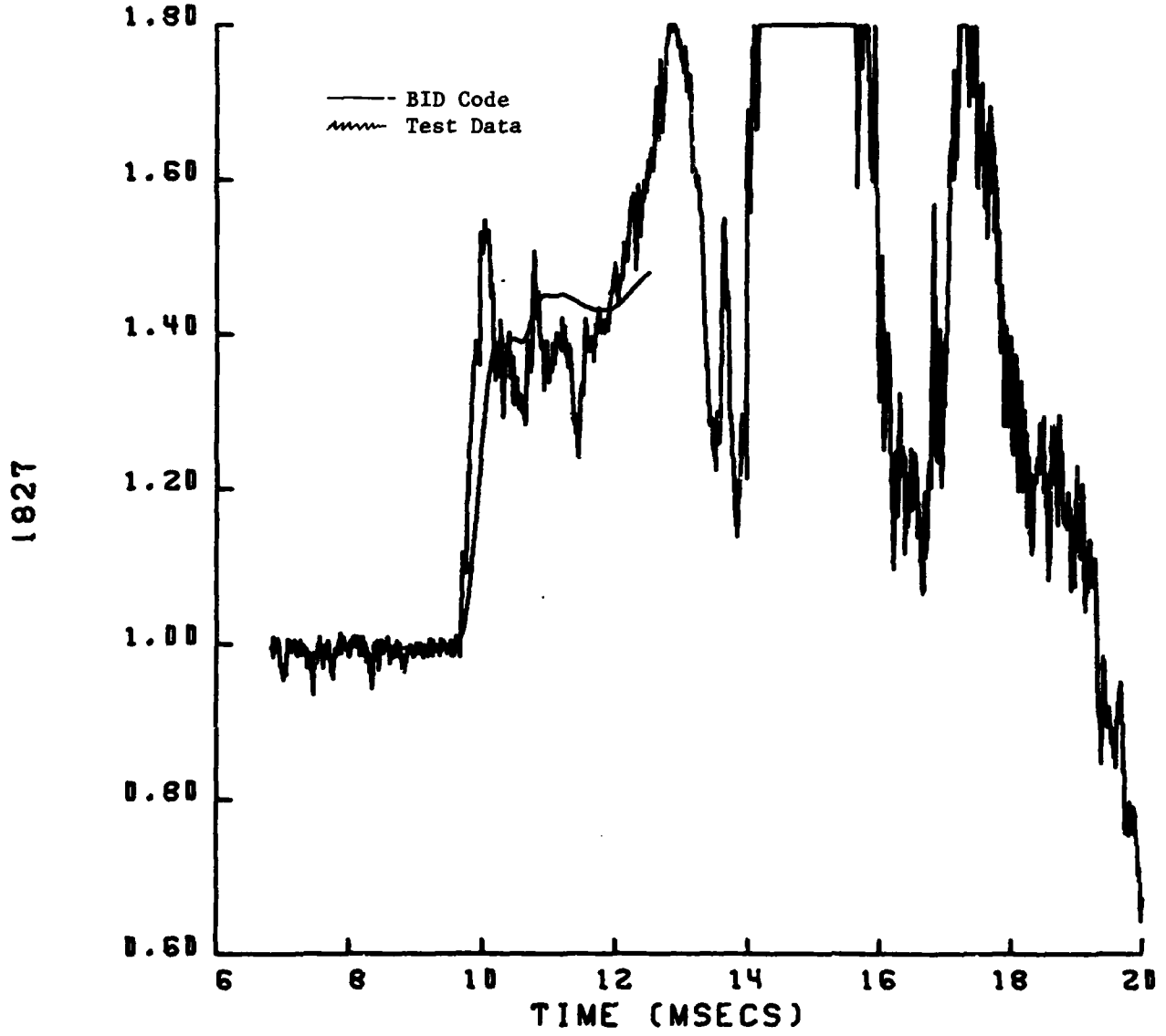

Figure 5.14e. Transducer 1827.

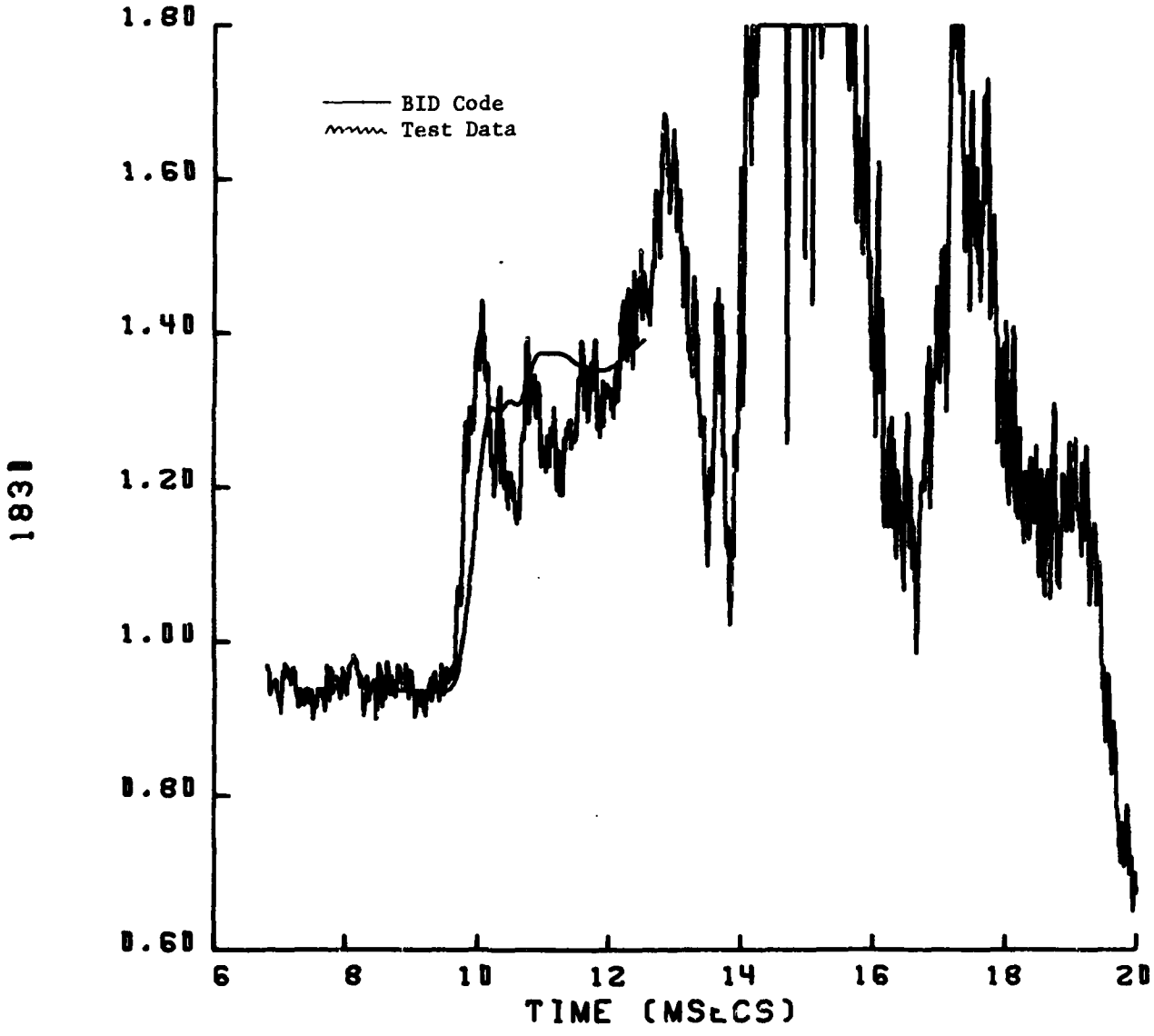

Figure 5.14f. Transducer 1830.

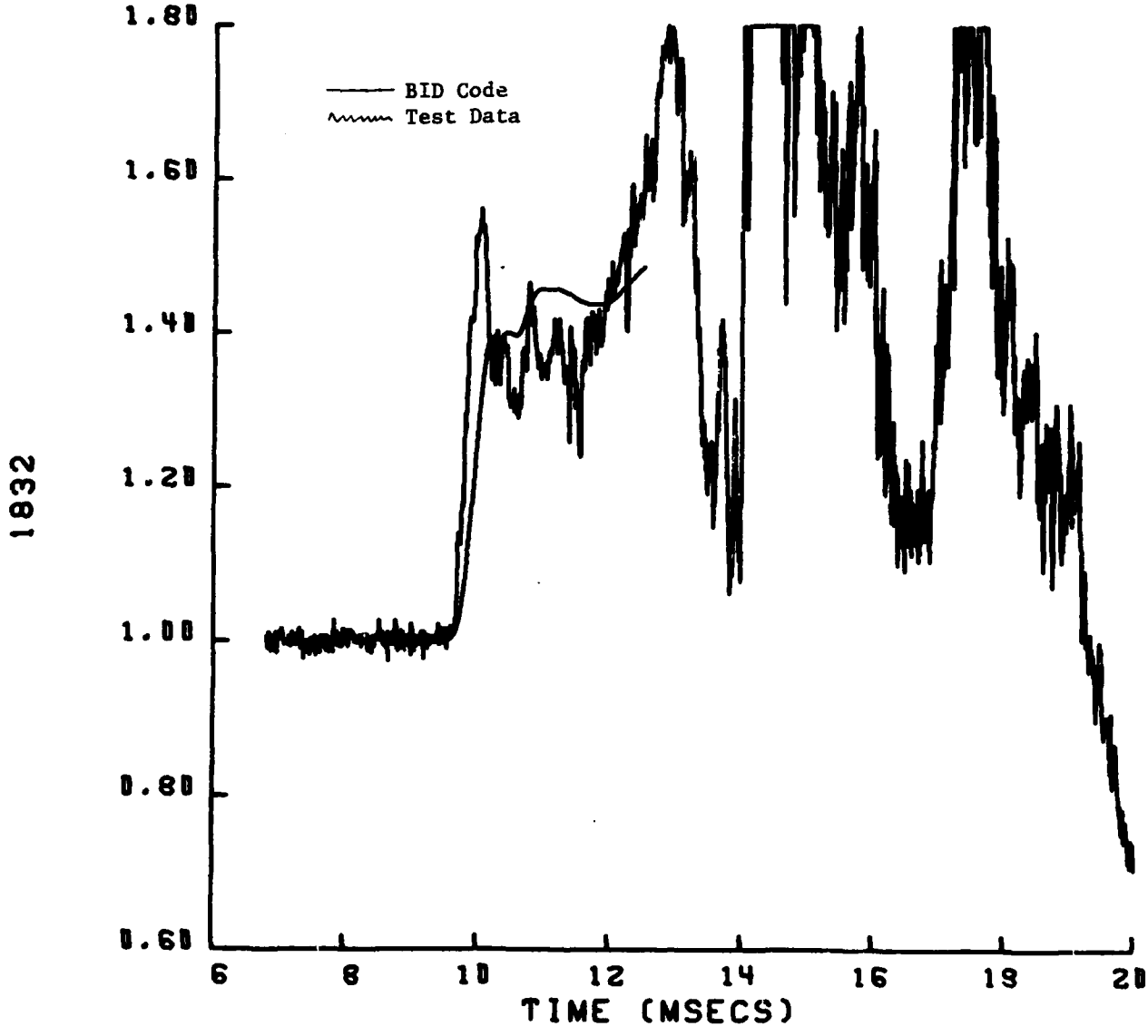

Figure 5.14g. Transducer 1832.

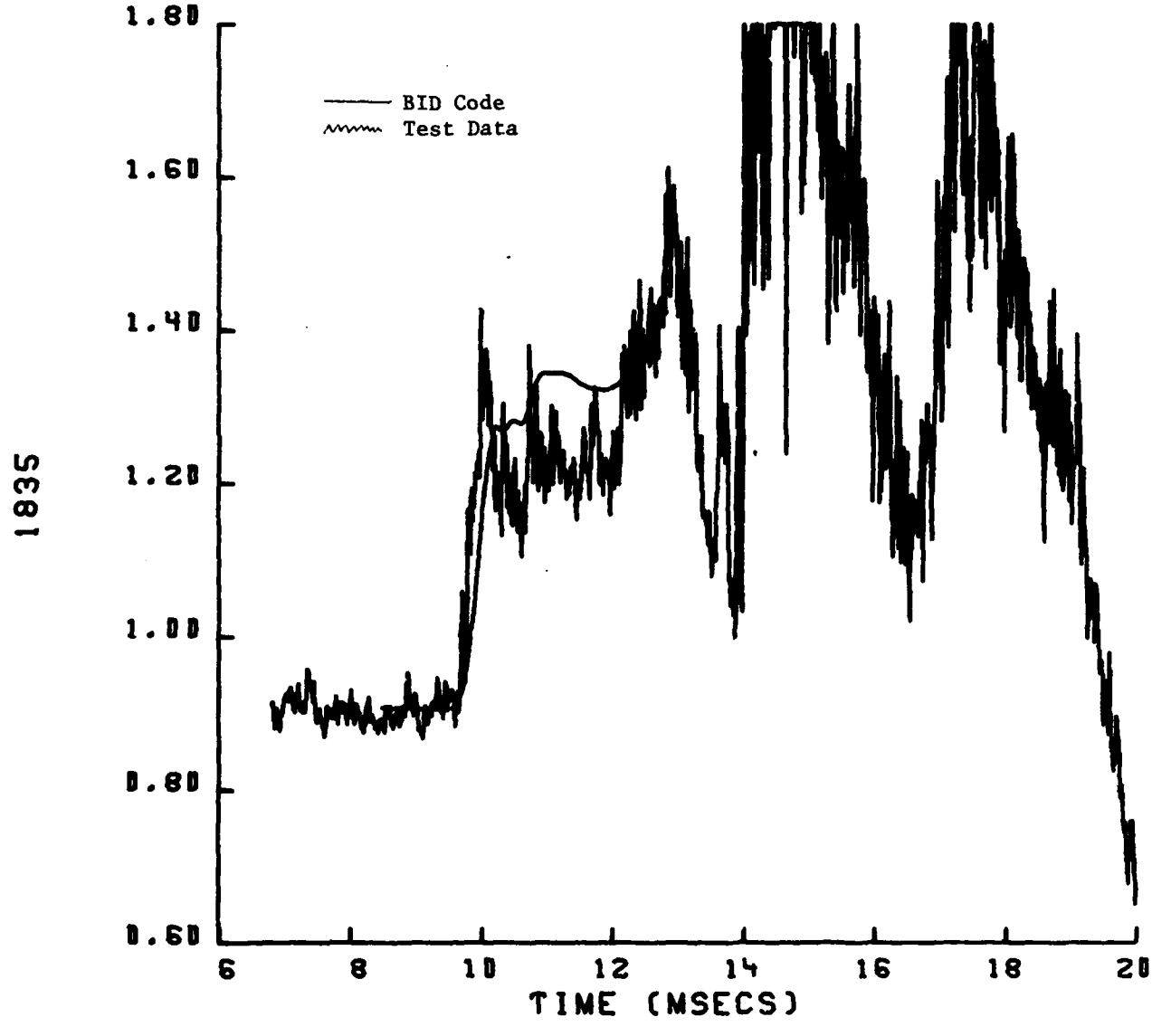

Figure 5.14h. Transducer 1835.

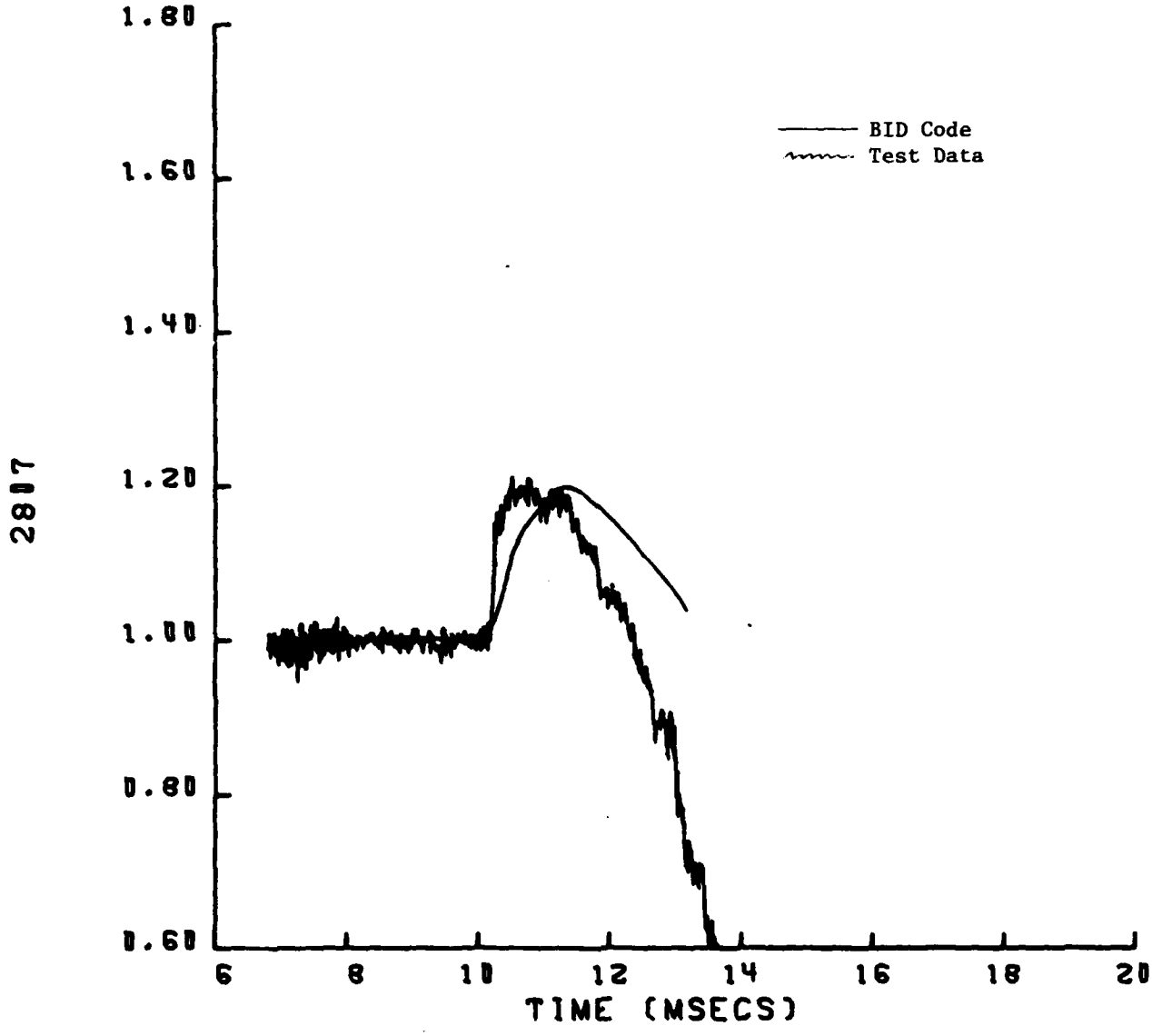

Figure 5.15a. Transducer 2807.

Figure 5.15. Comparison of theoretical and experimental time histories of engine face total pressures for Run 18 (Part 624), leeward (inboard) inlet.

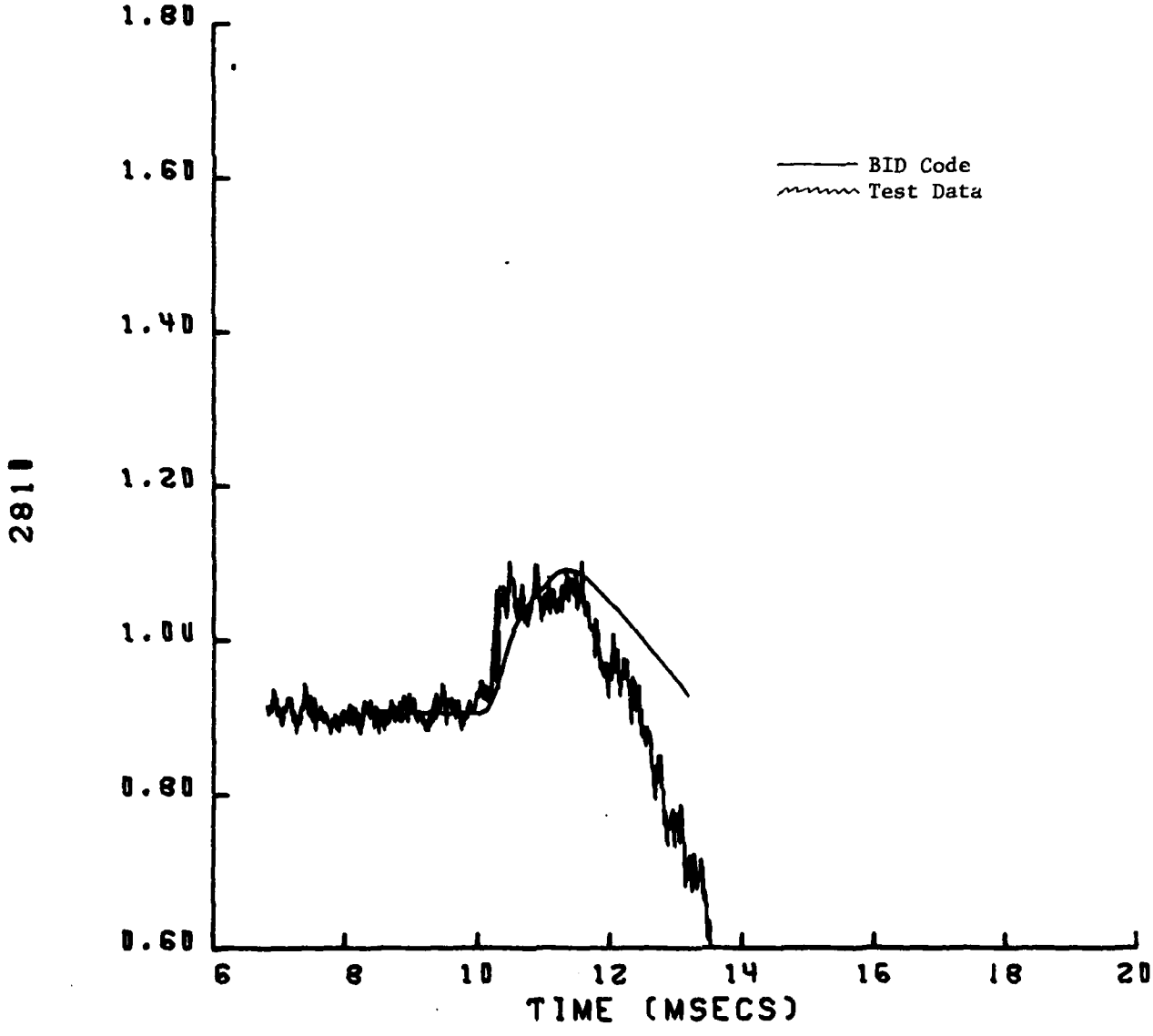

Figure 5.15b. Transducer 2810.

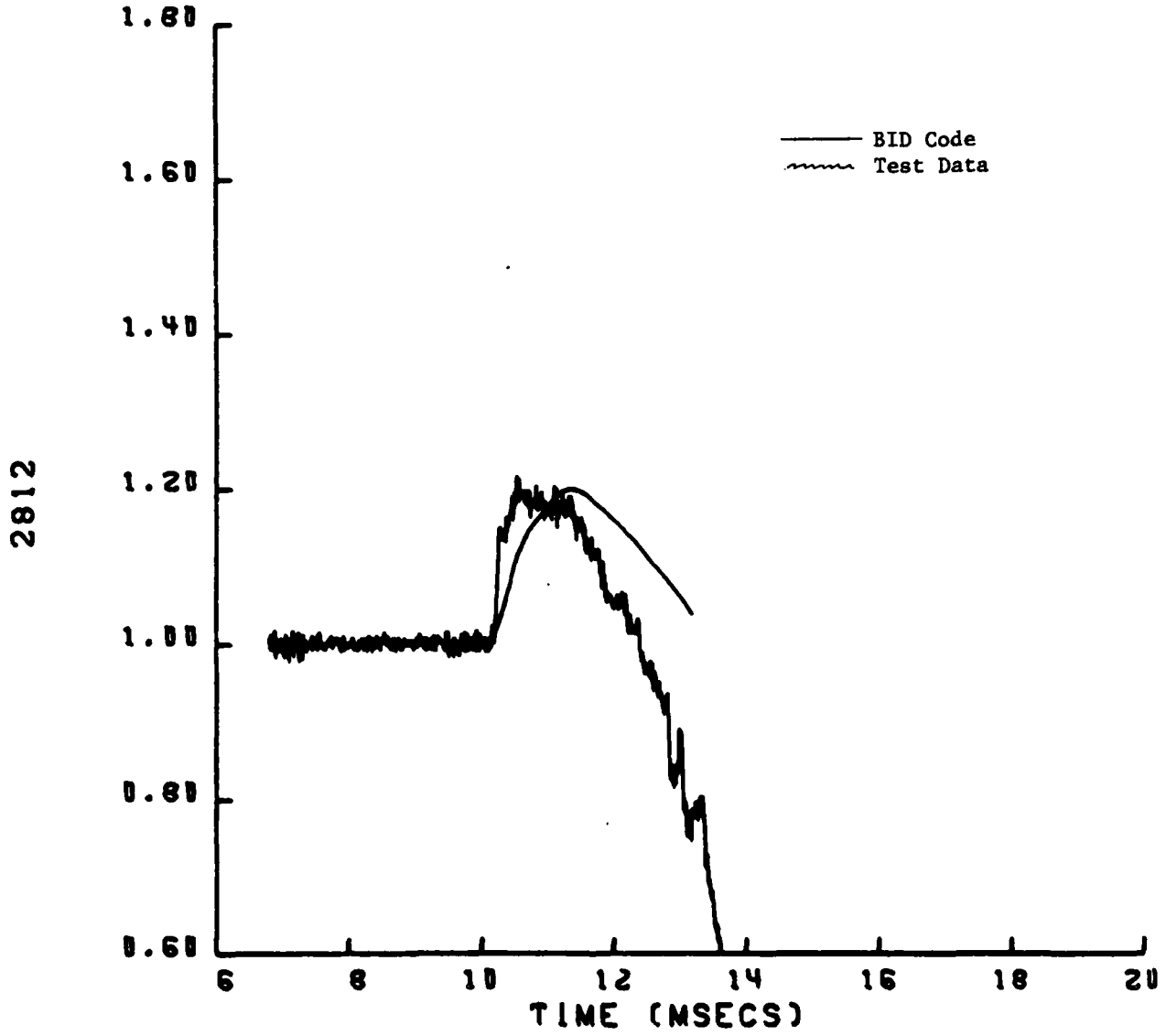

Figure 5.15c. Transducer 2812.

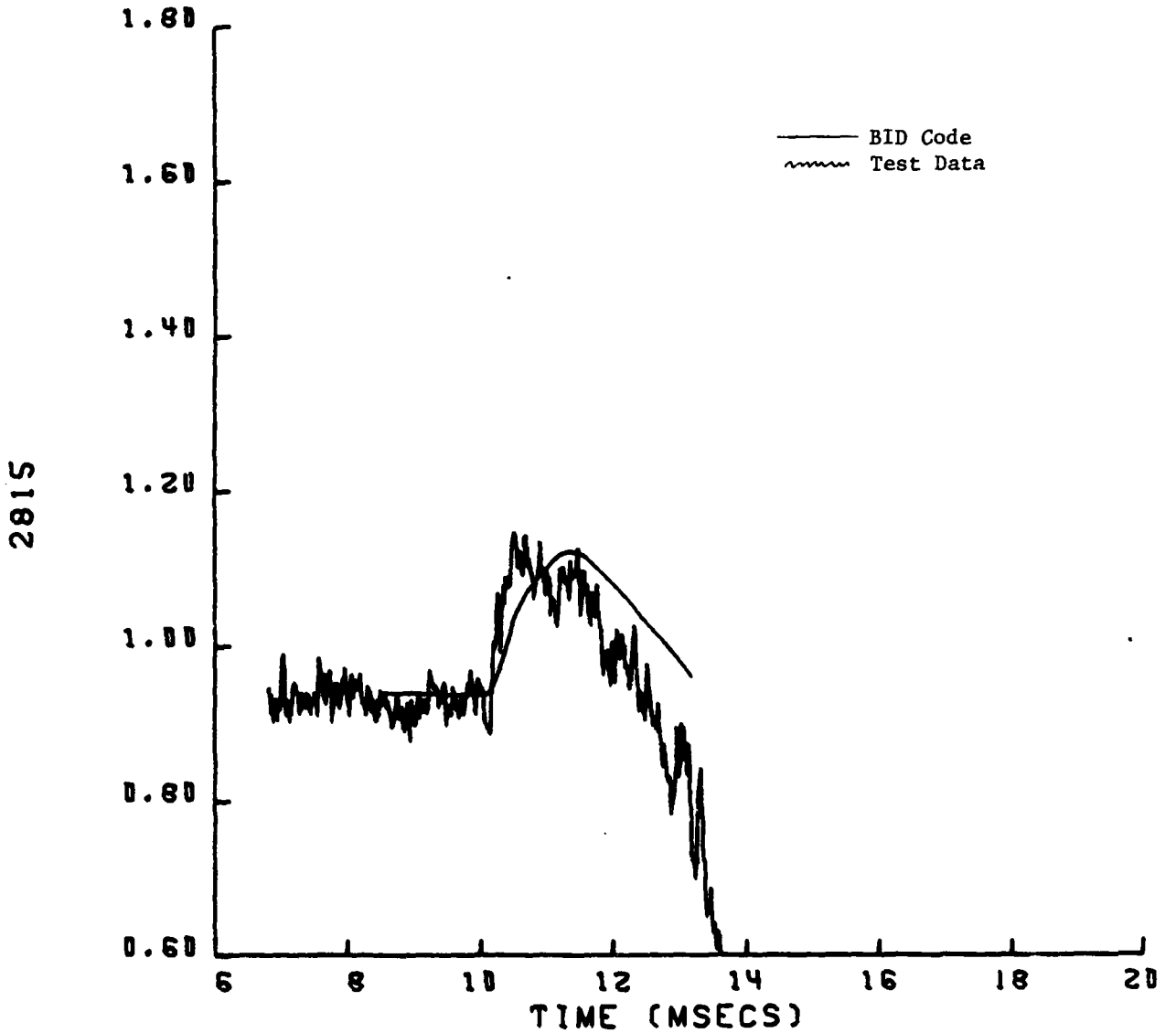

Figure 5.15d. Transducer 2815.

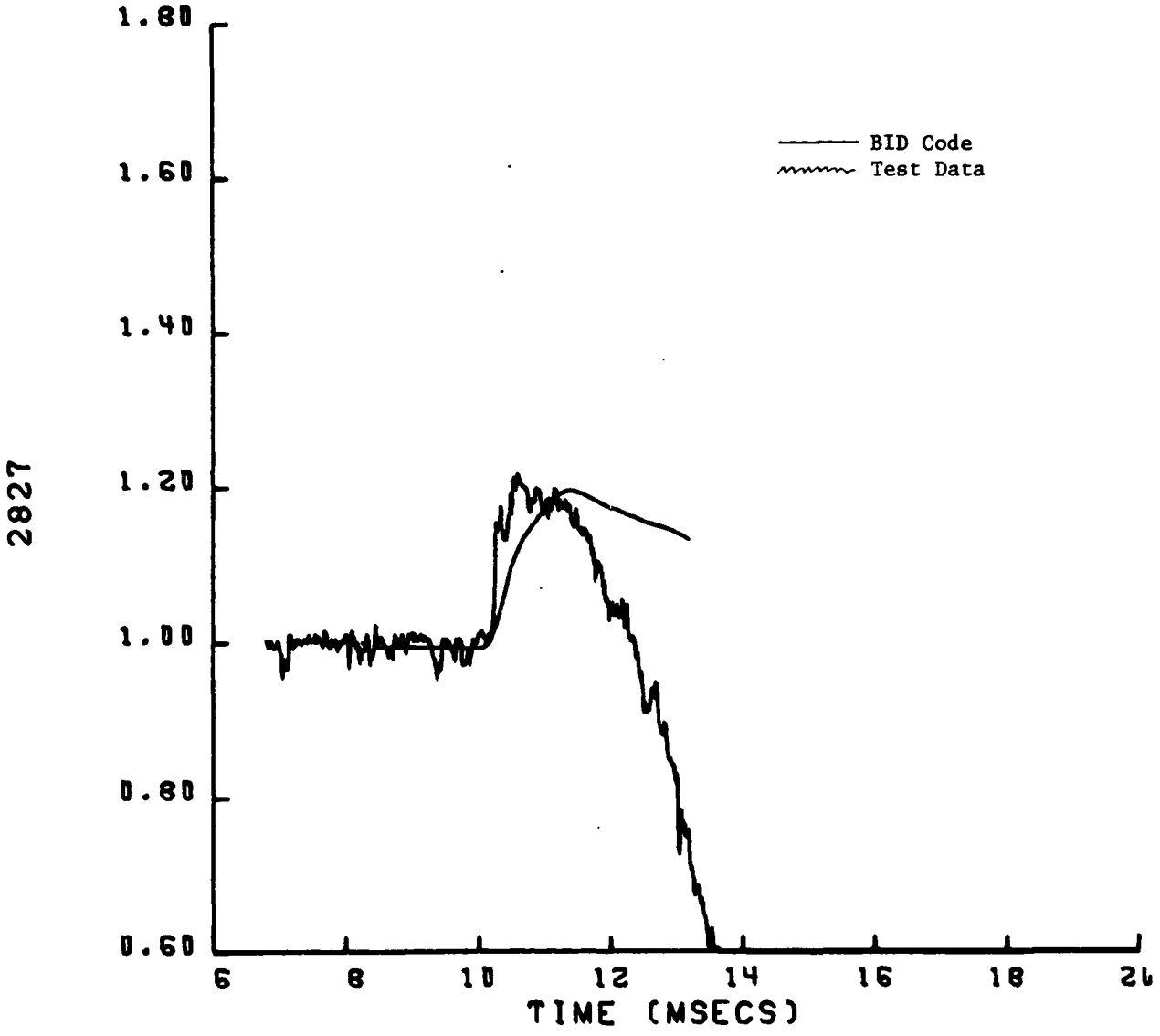

Figure 5.15e. Transducer 2827.

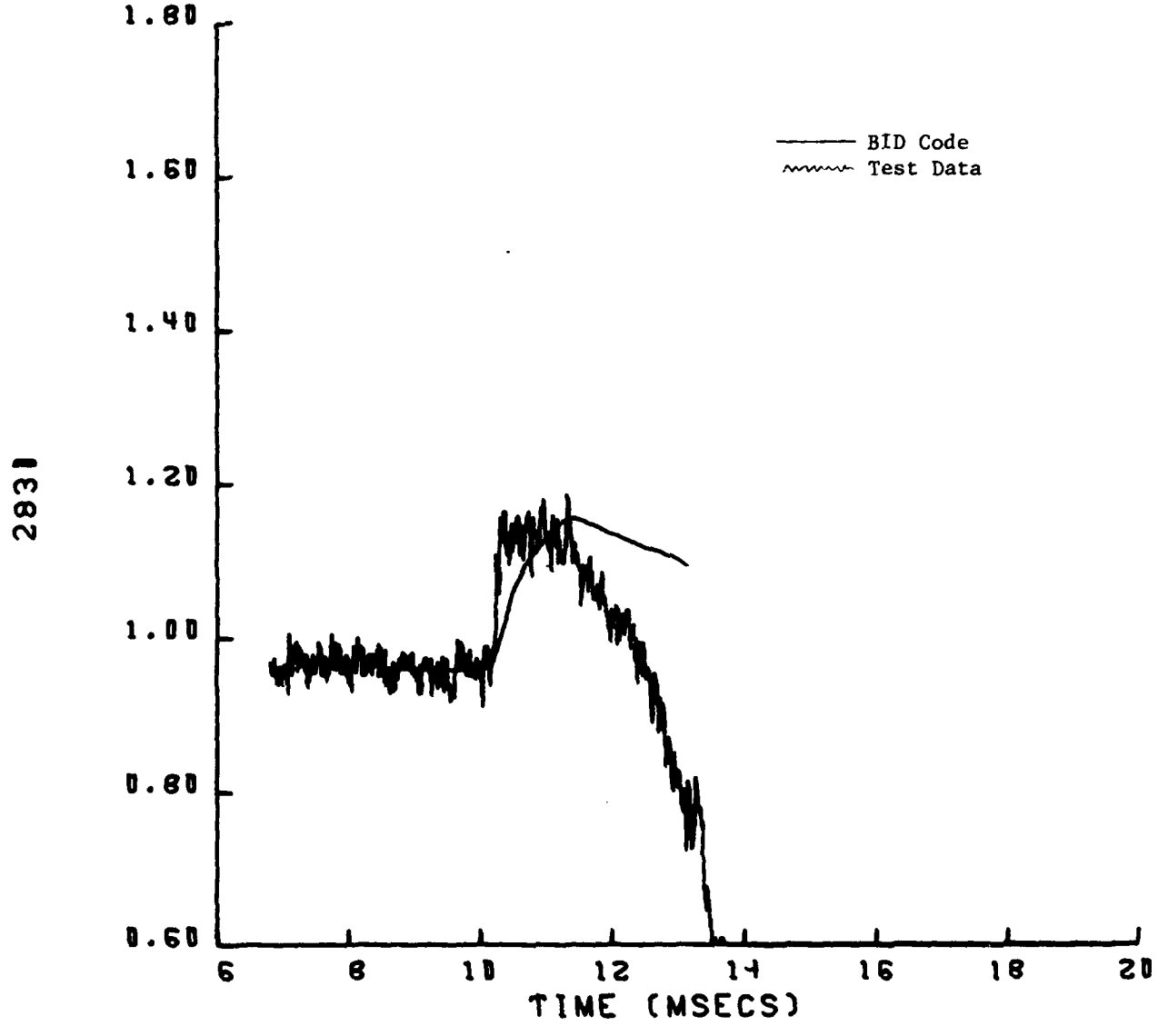

Figure 5.15f. Transducer 2830.

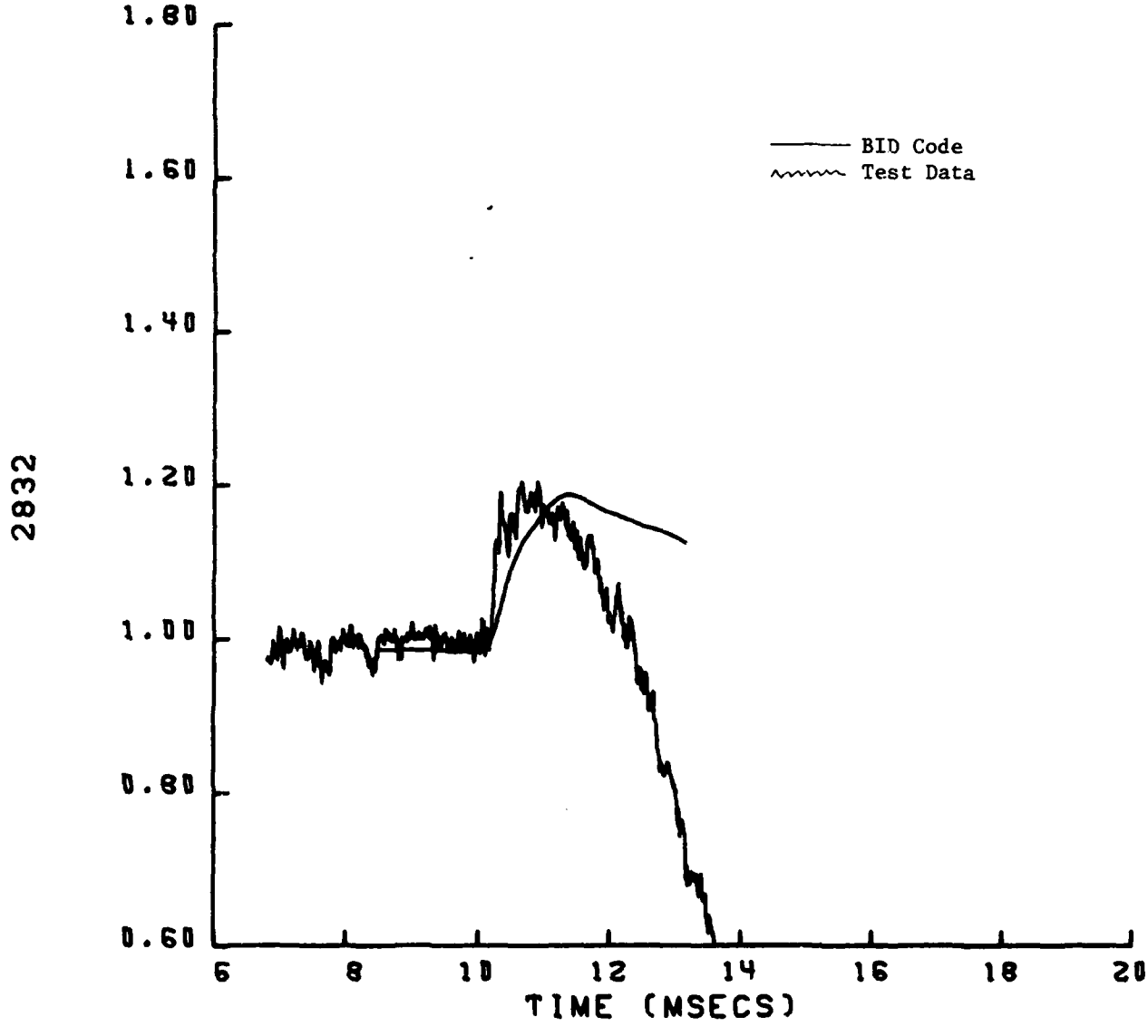

Figure 5.15g. Transducer 2832.

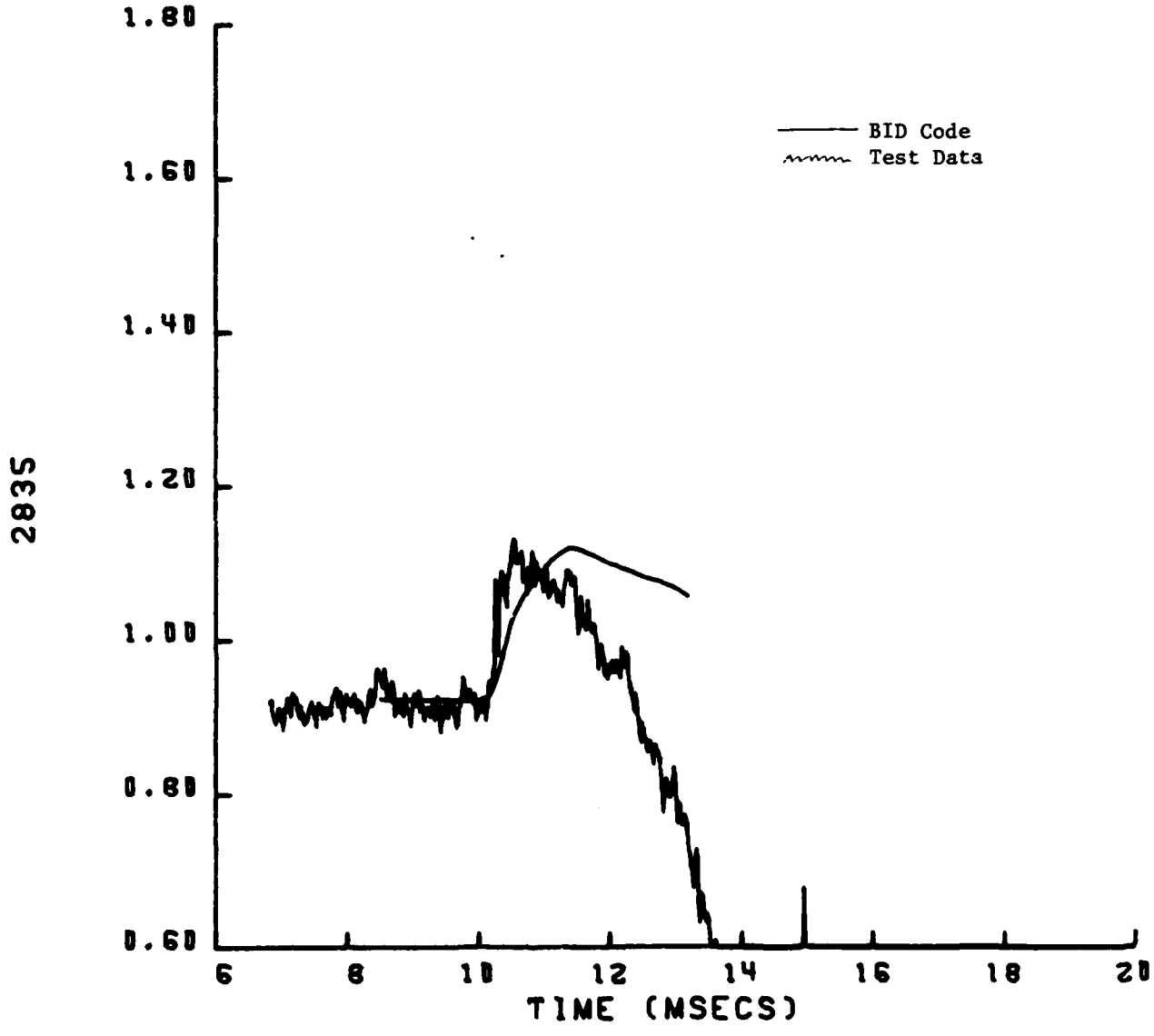

Figure 5.15h. Transducer 2835.

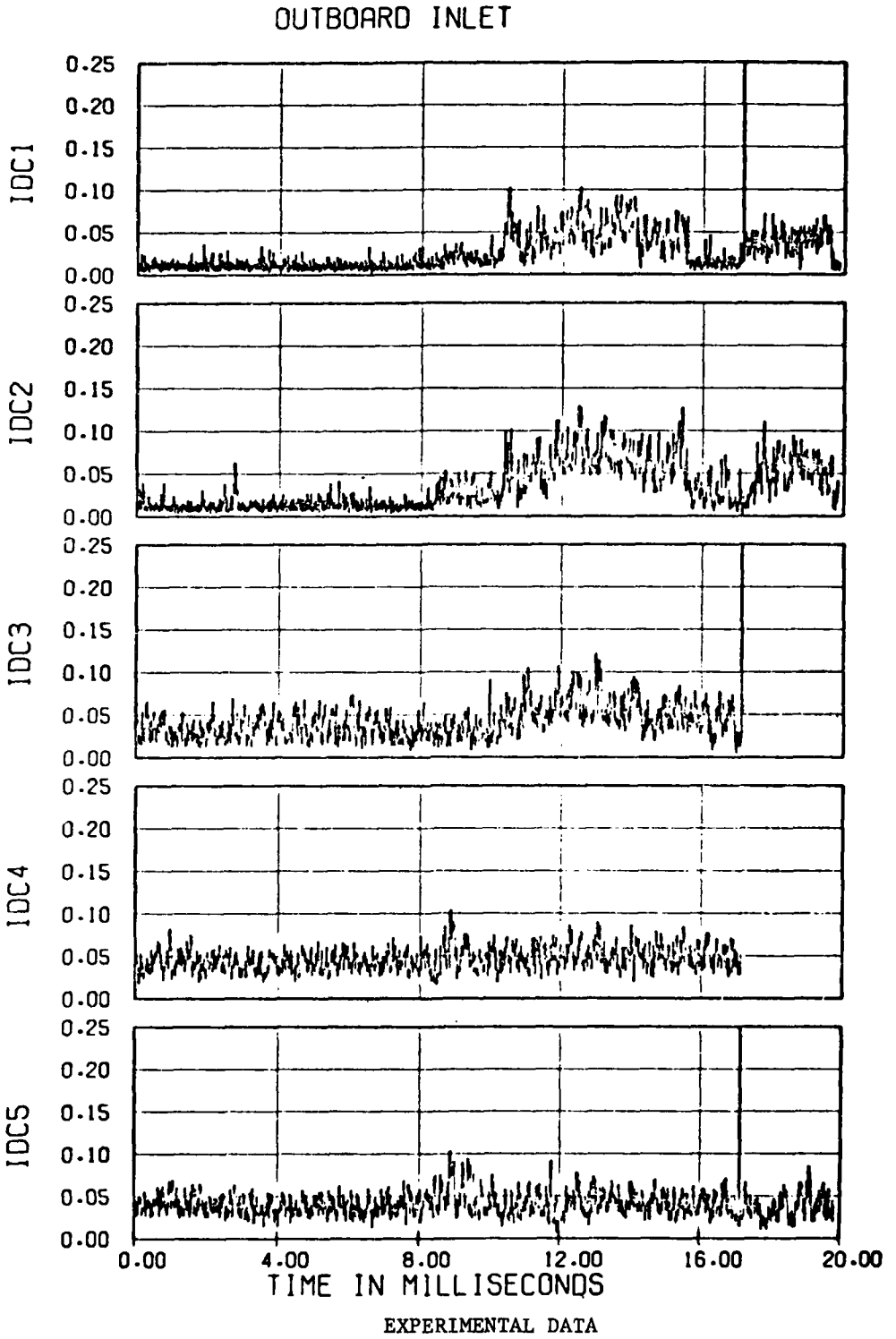

Figure 5.16a. Circumferential distortion.

Figure 5.16. Comparison of theoretical and experimental time histories of engine face distortion for Run 39 (Part 544), blastward (outboard) inlet.

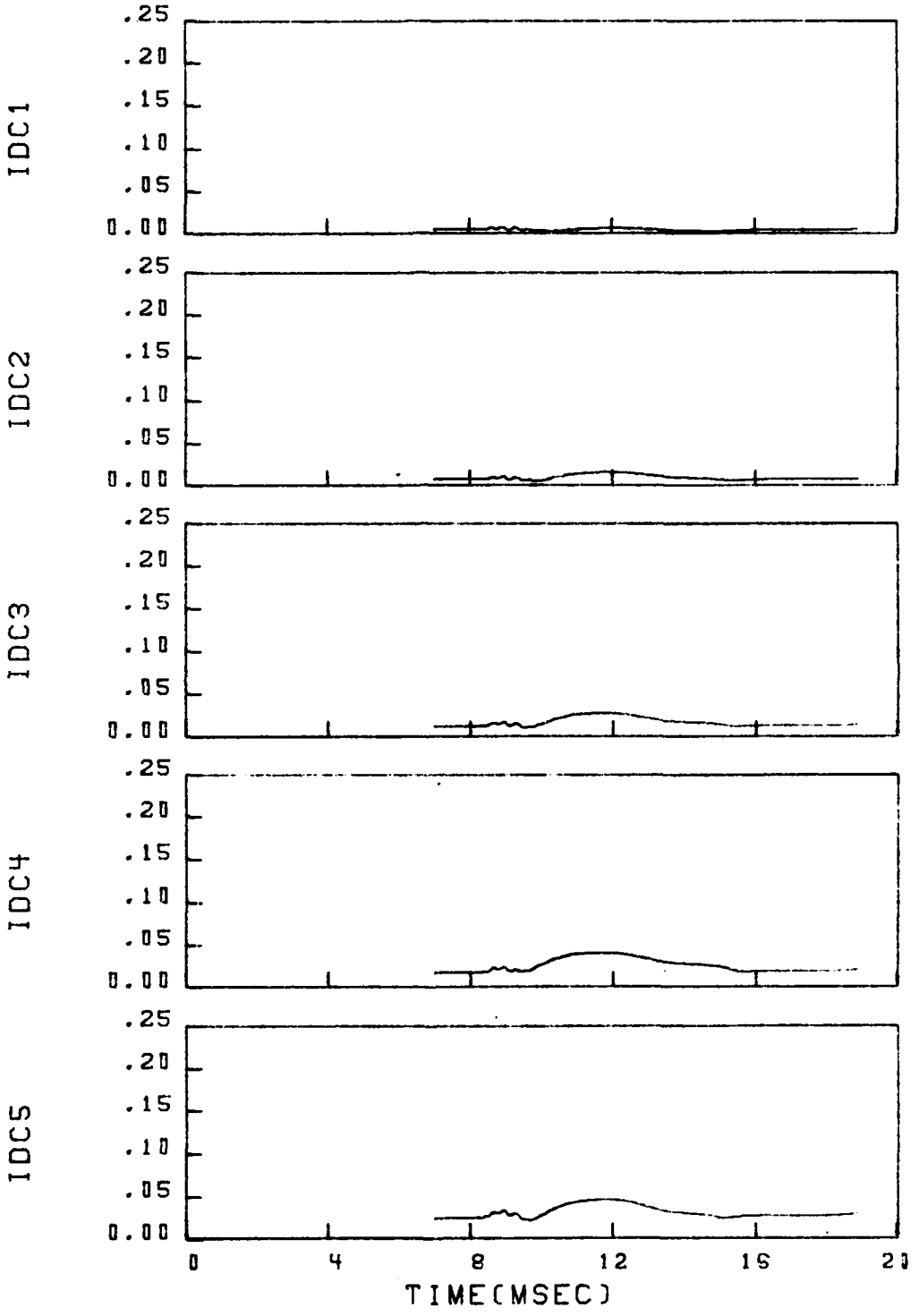

BID CODE

Figure 5.16a. Concluded.

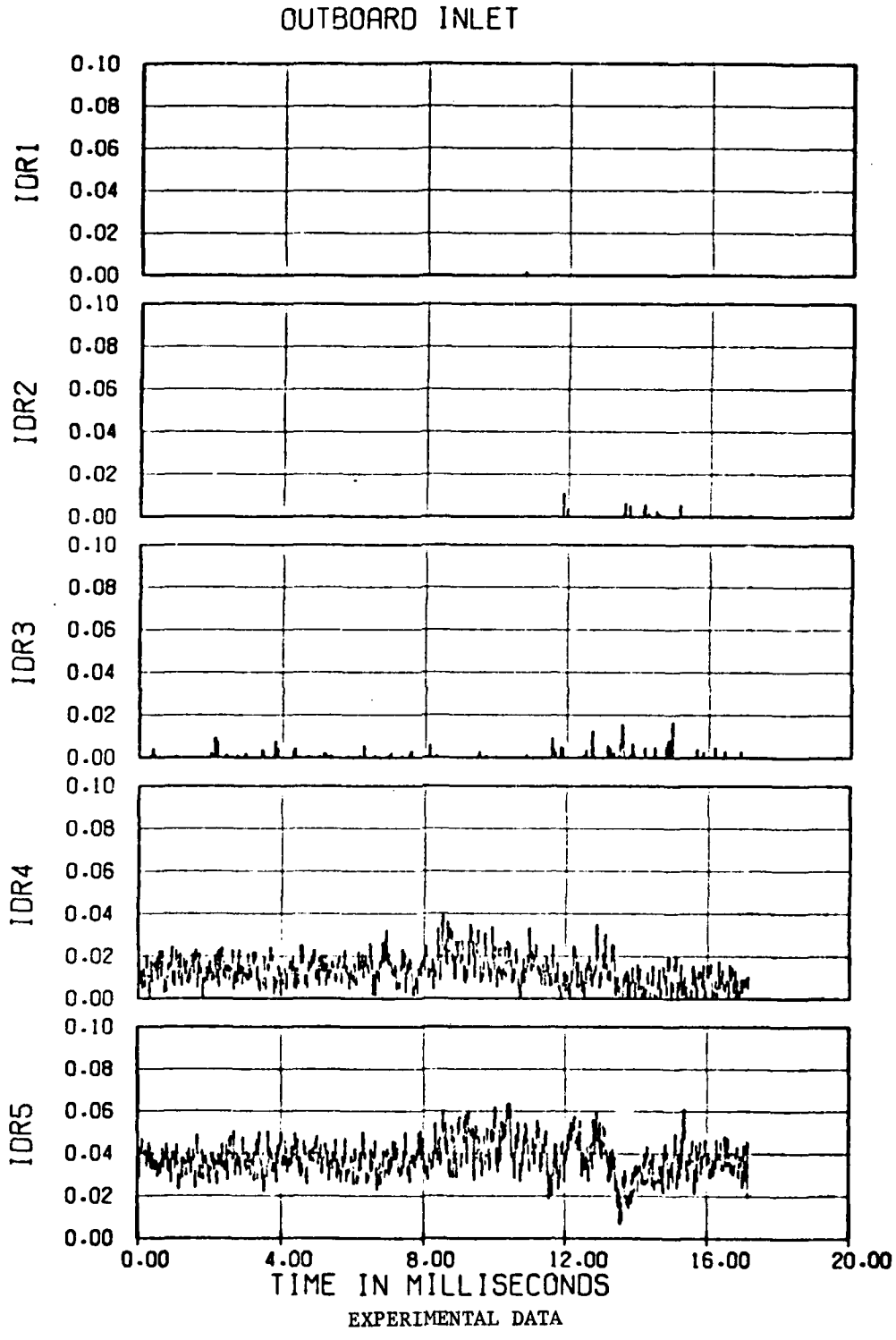

Figure 5.16b. Radial distortion.

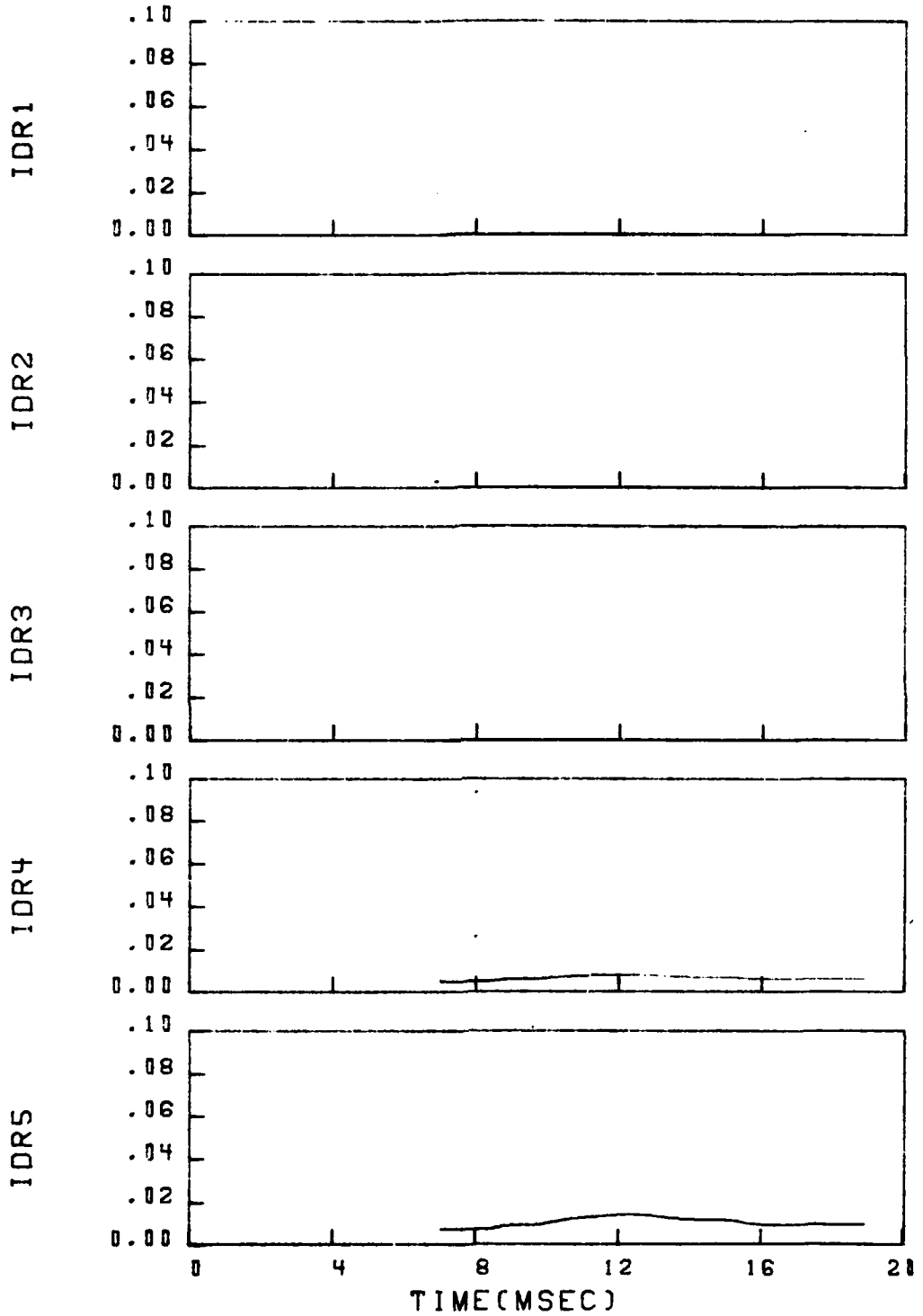

BID CODE

Figure 5.16b. Concluded.

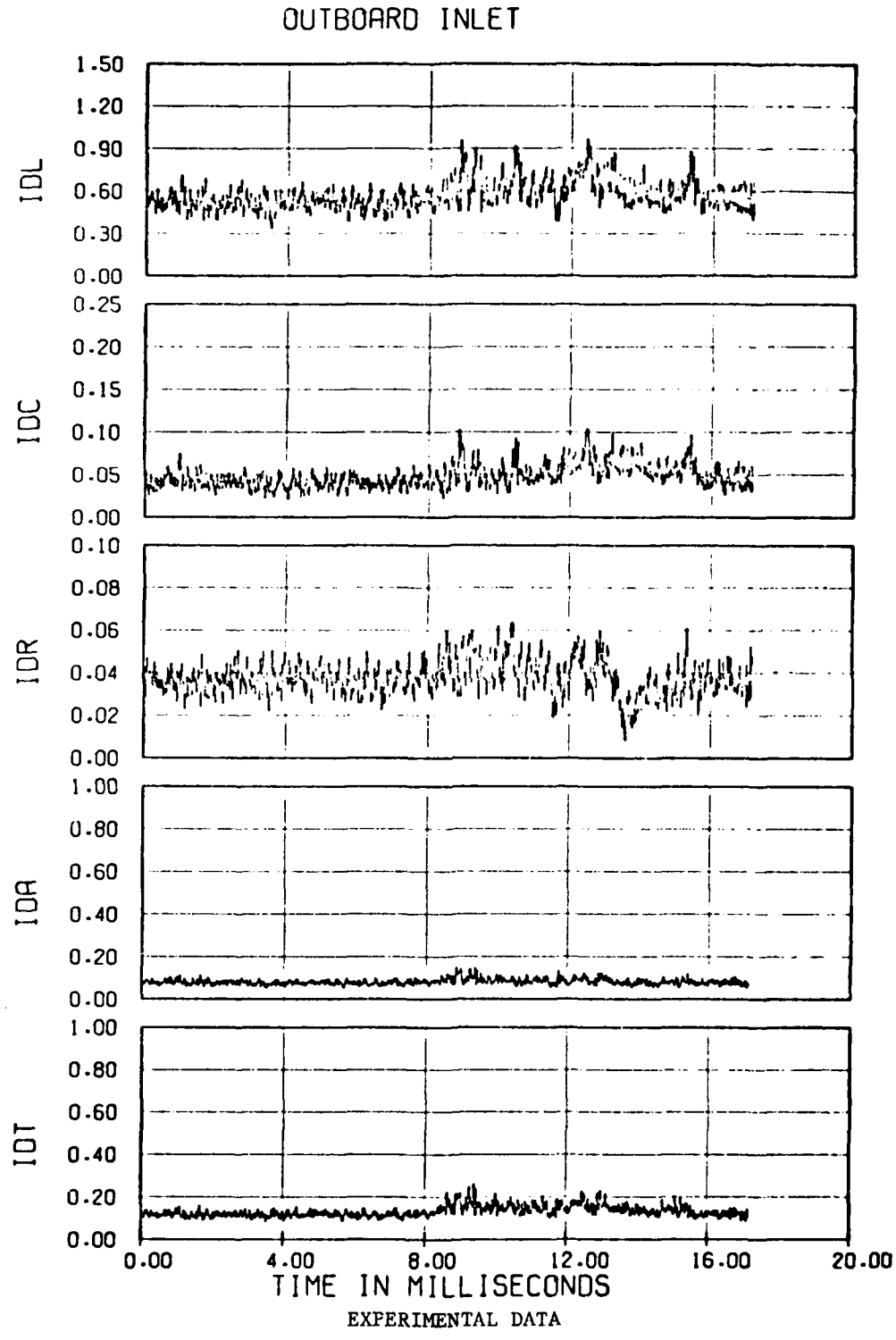

Figure 5.16c. Overall distortion.

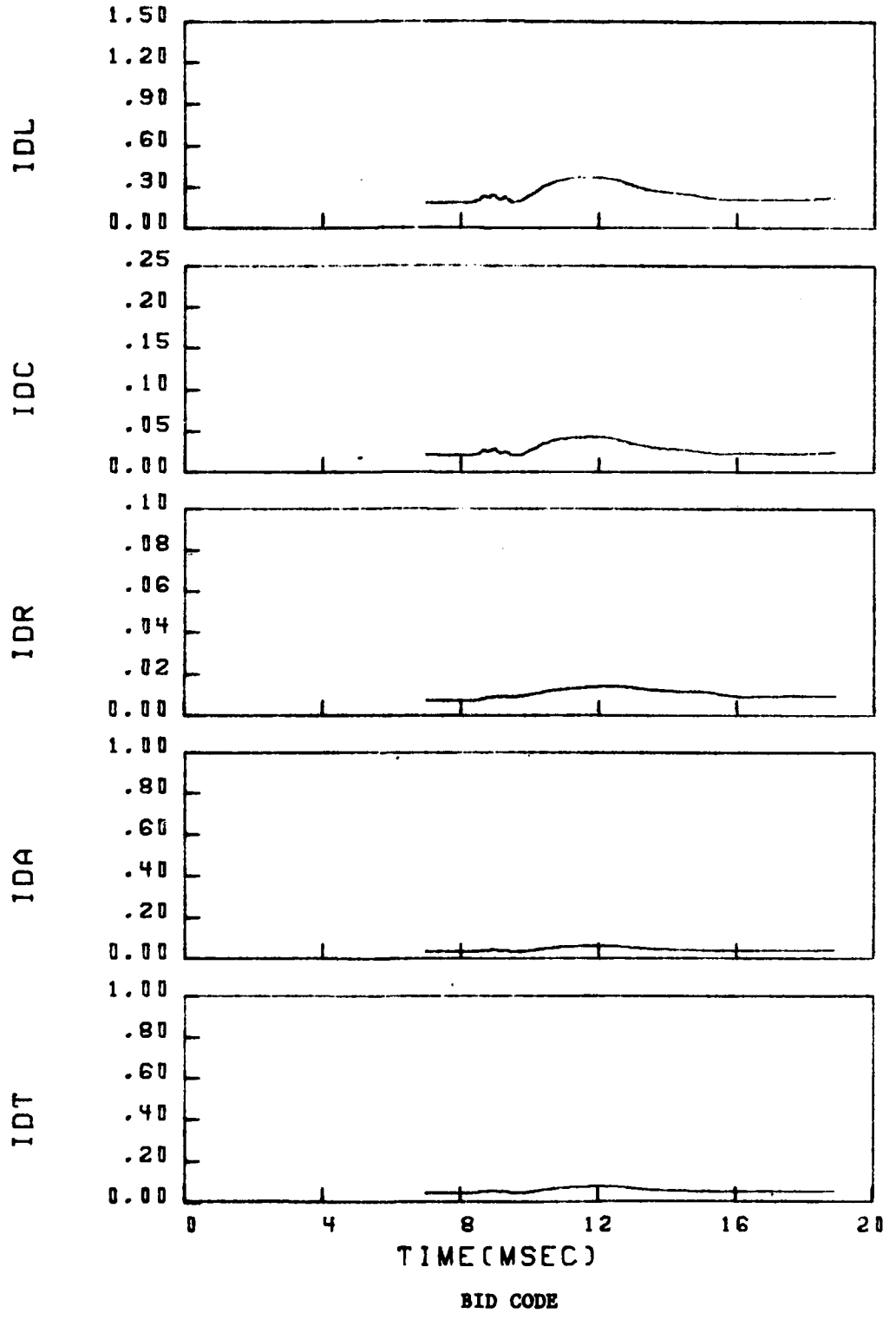

Figure 5.16c. Concluded.

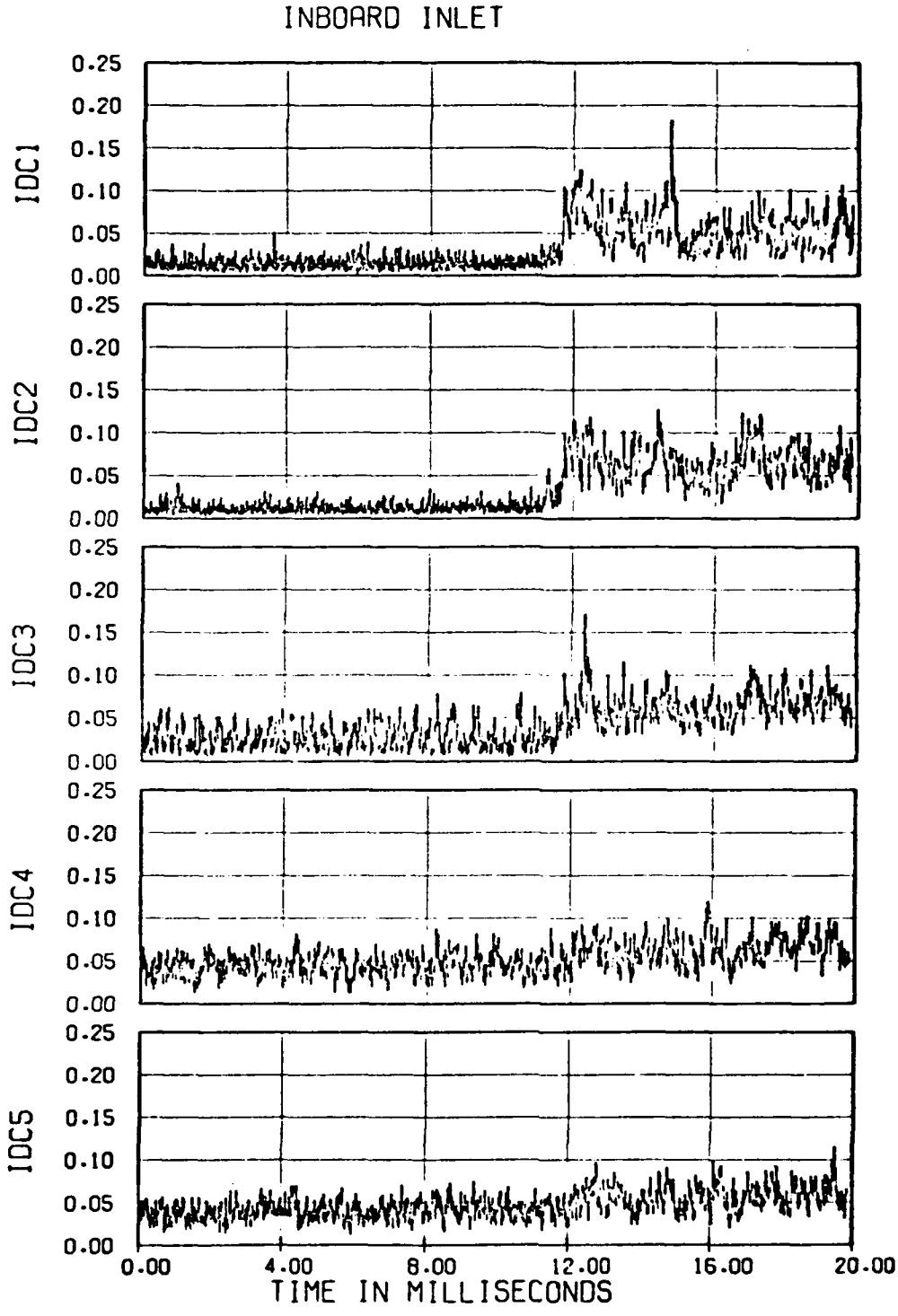

EXPERIMENTAL DATA

Figure 5.17a. Circumferential distortion.

Figure 5.17. Comparison of theoretical and experimental time histories of engine face distortion for Run 39 (Part 544), leeward (inboard) inlet.

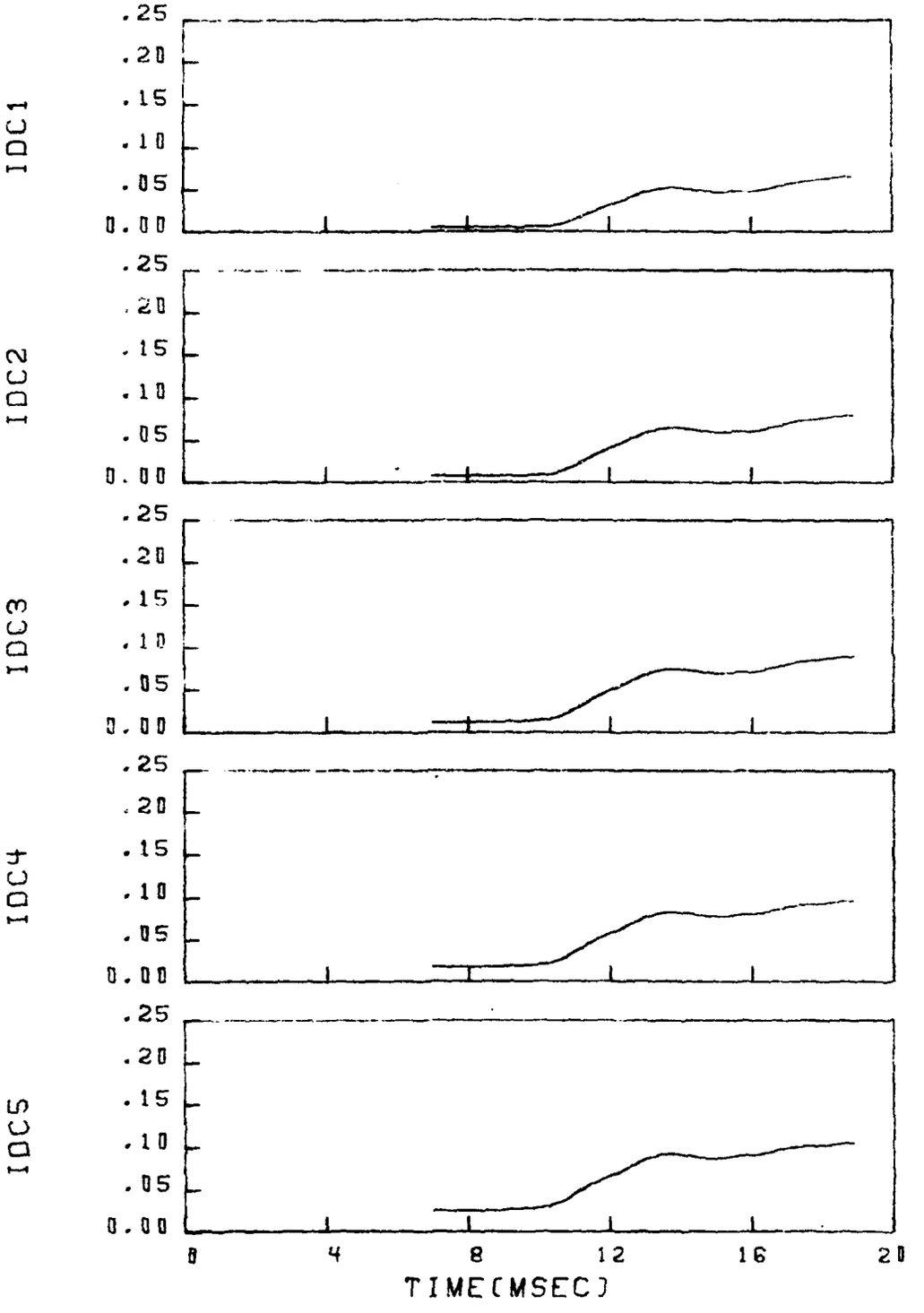

BID CODE

Figure 5.17a. Concluded.

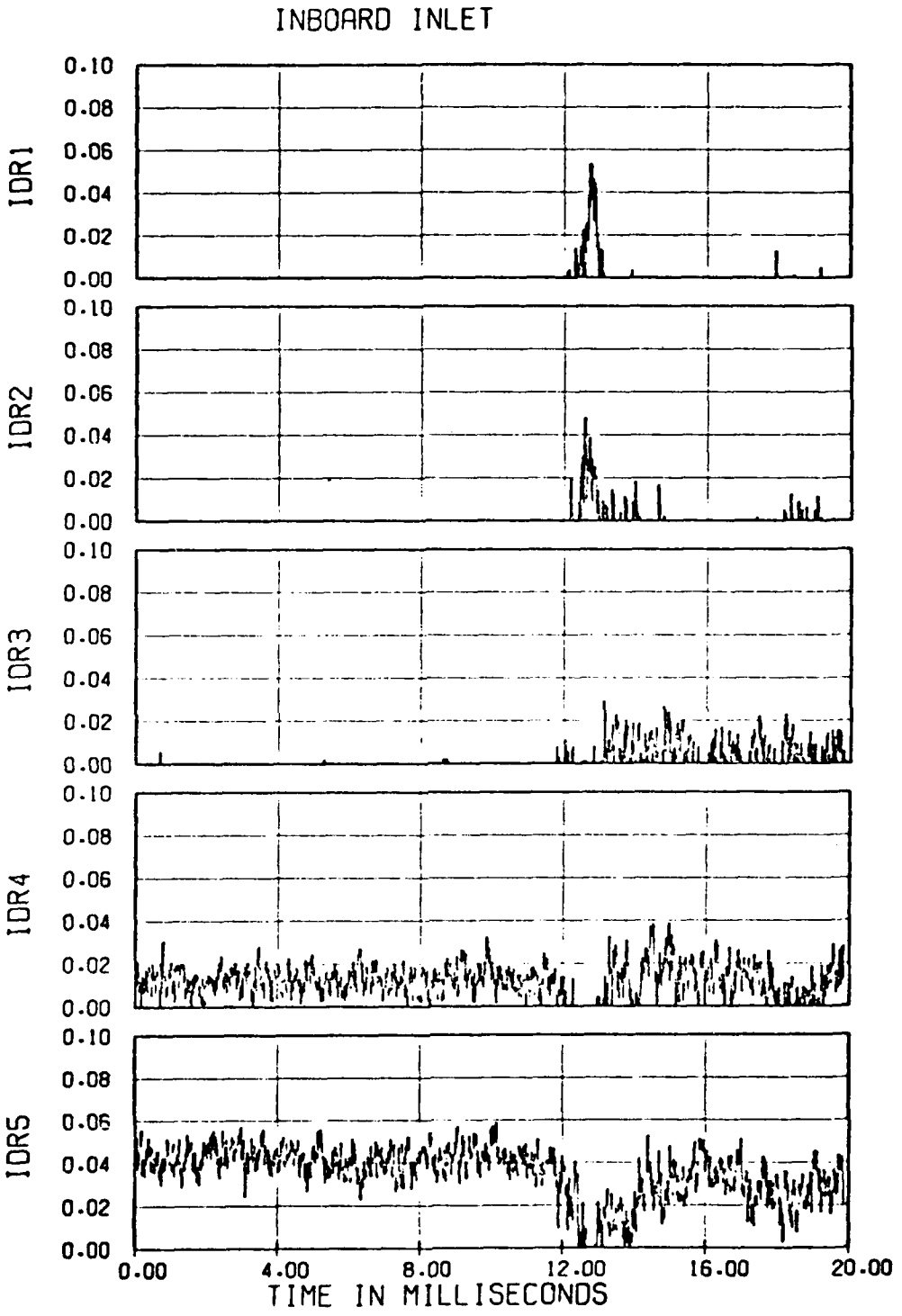

Figure 5.17b. Radial distortion.

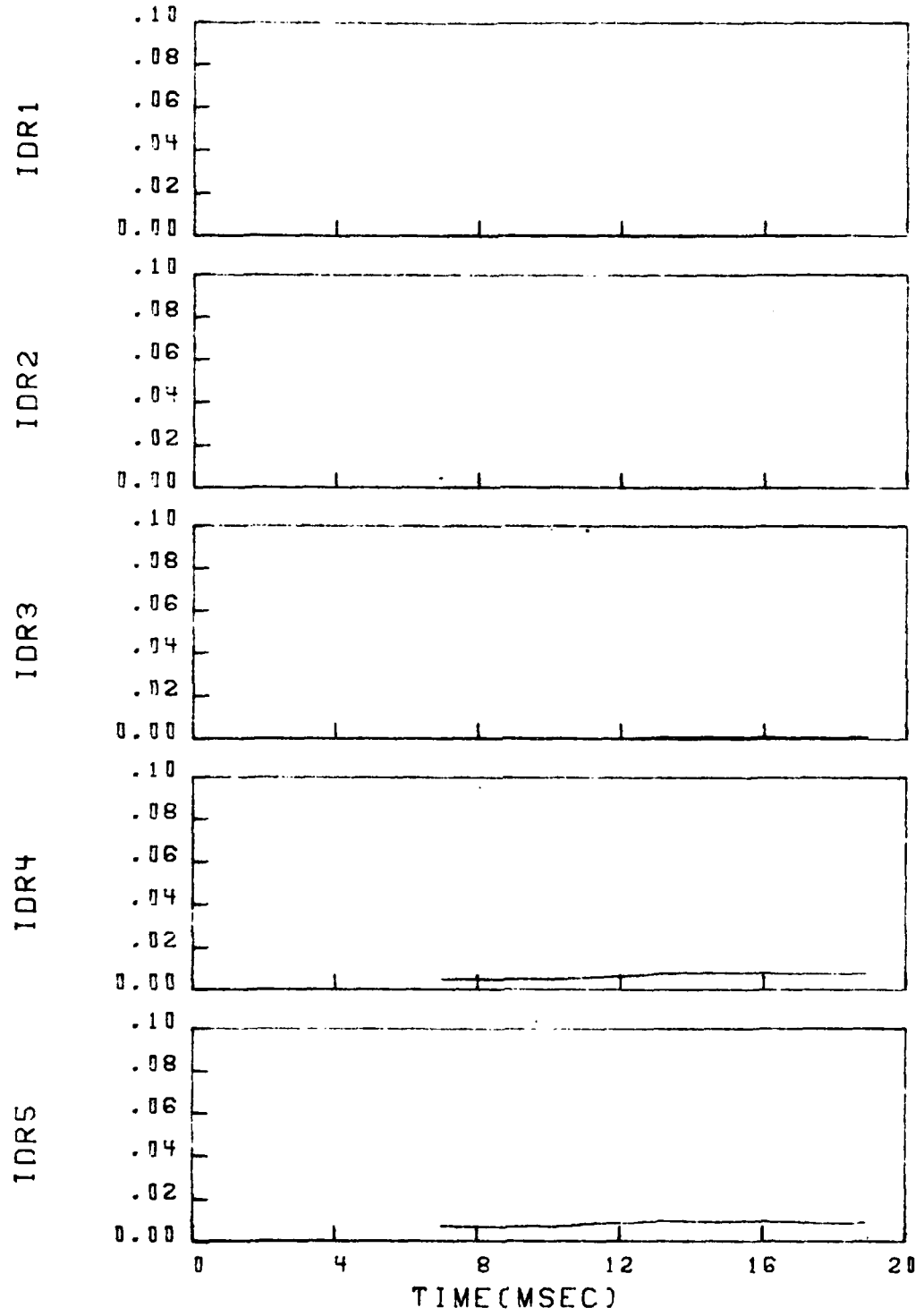

Figure 5.17b. Concluded.

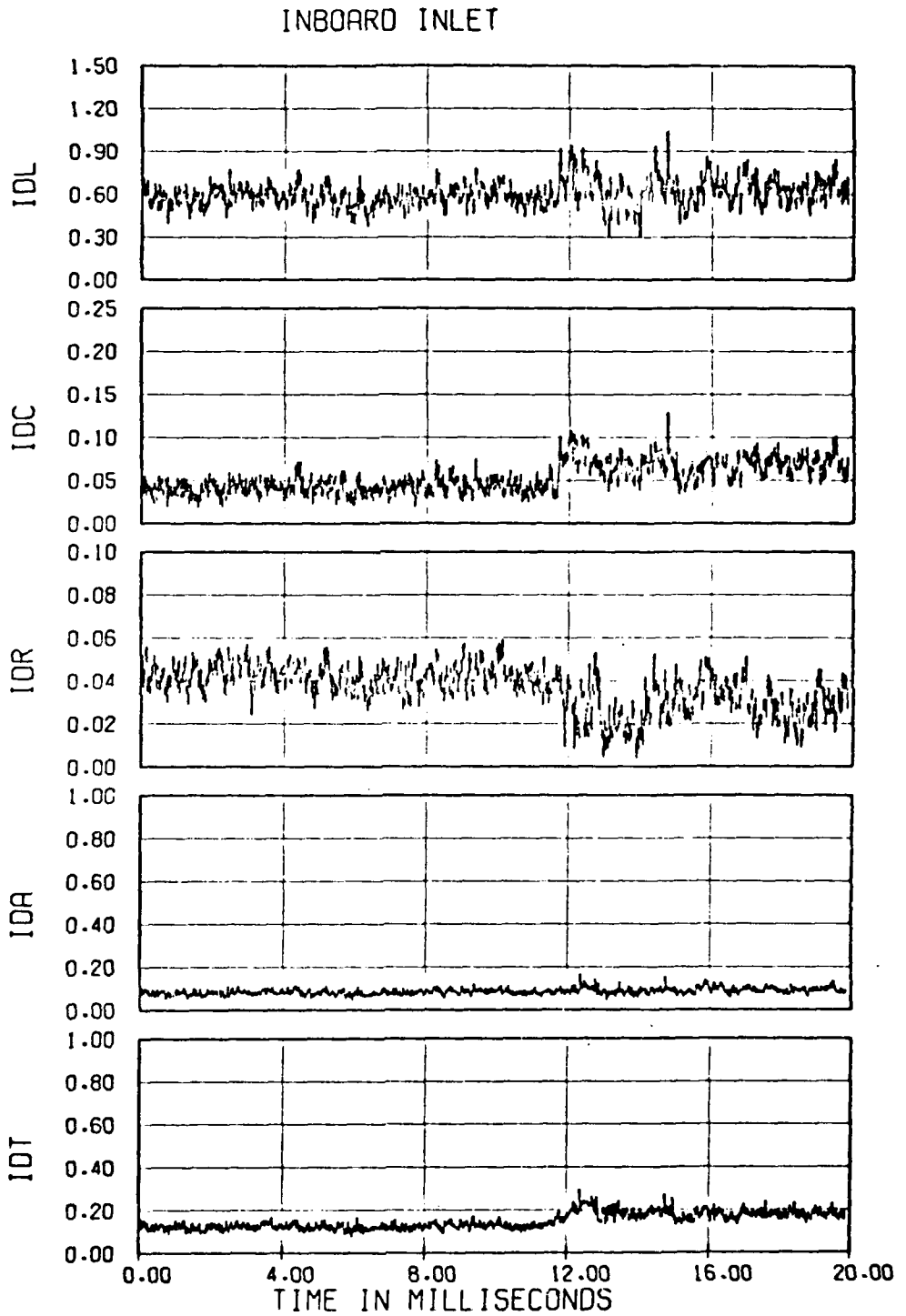

EXPERIMENTAL DATA

Figure 5.17c. Overall distortion.

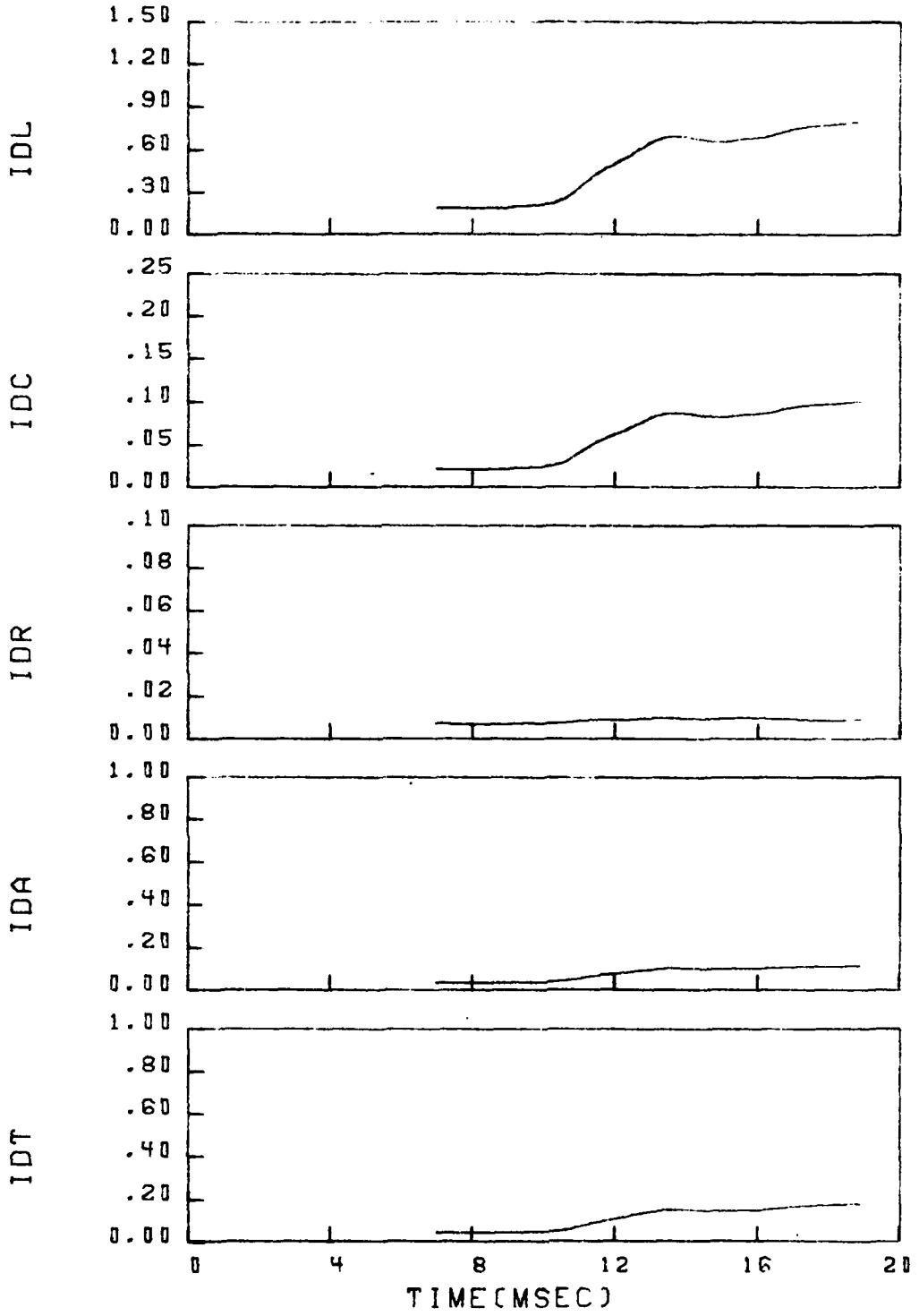

BID CODE

Figure 5.17c. Concluded.

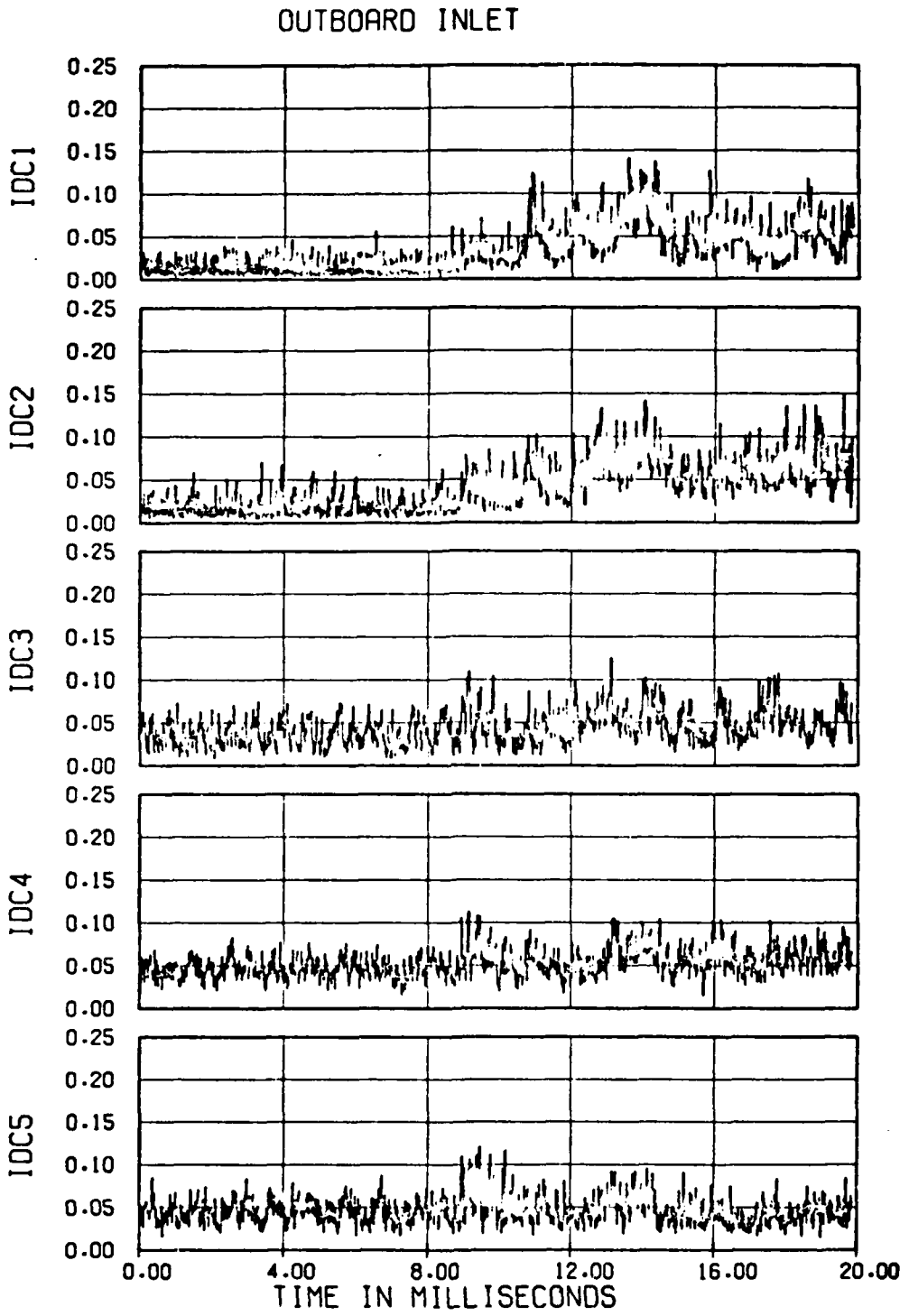

EXPERIMENTAL DATA

Figure 5.18a. Circumferential distortion.

Figure 5.18. Comparison of theoretical and experimental time histories of engine face distortion for Run 40 (Part 619), blastward (outboard) inlet.

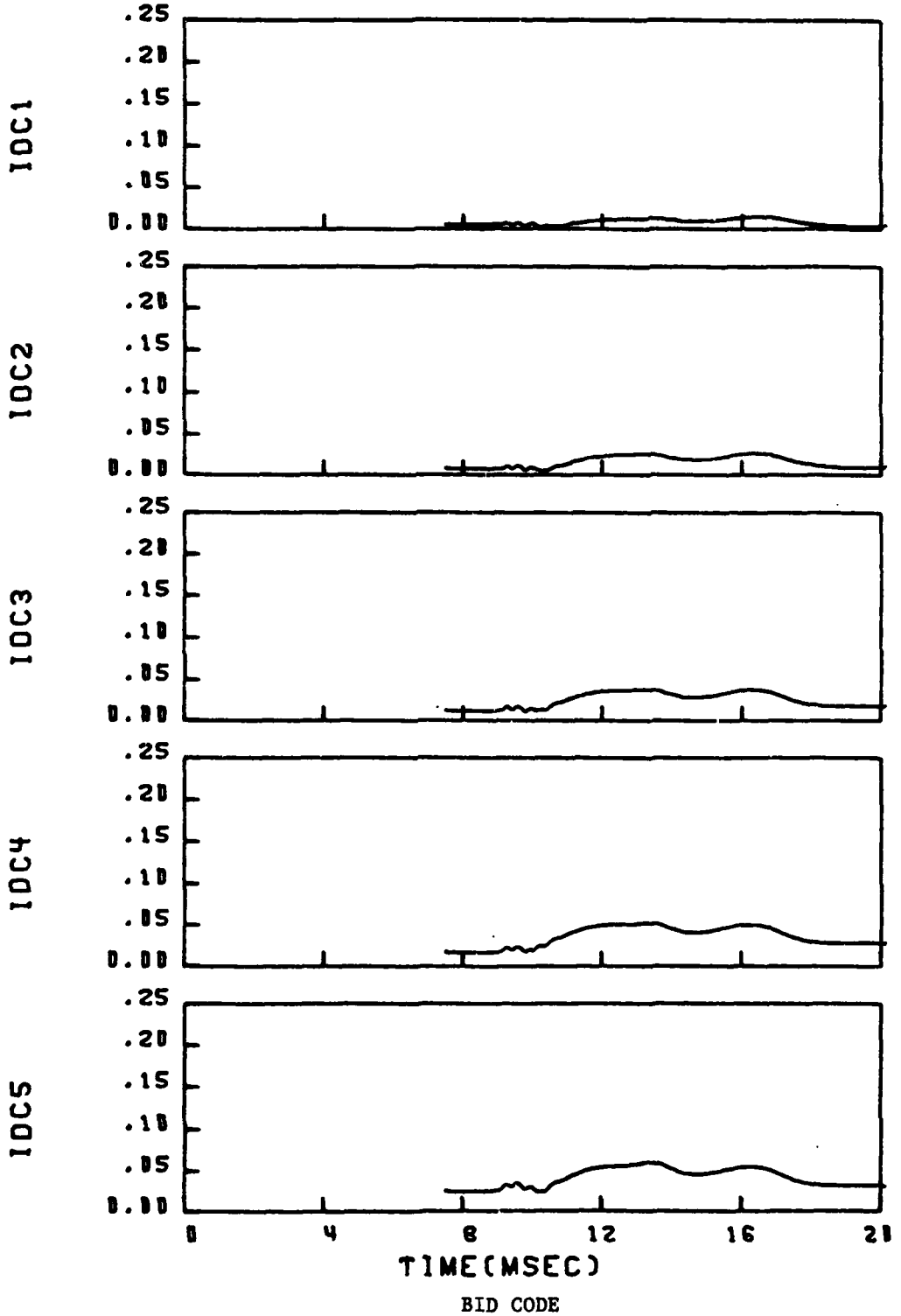

Figure 5.18a. Concluded.

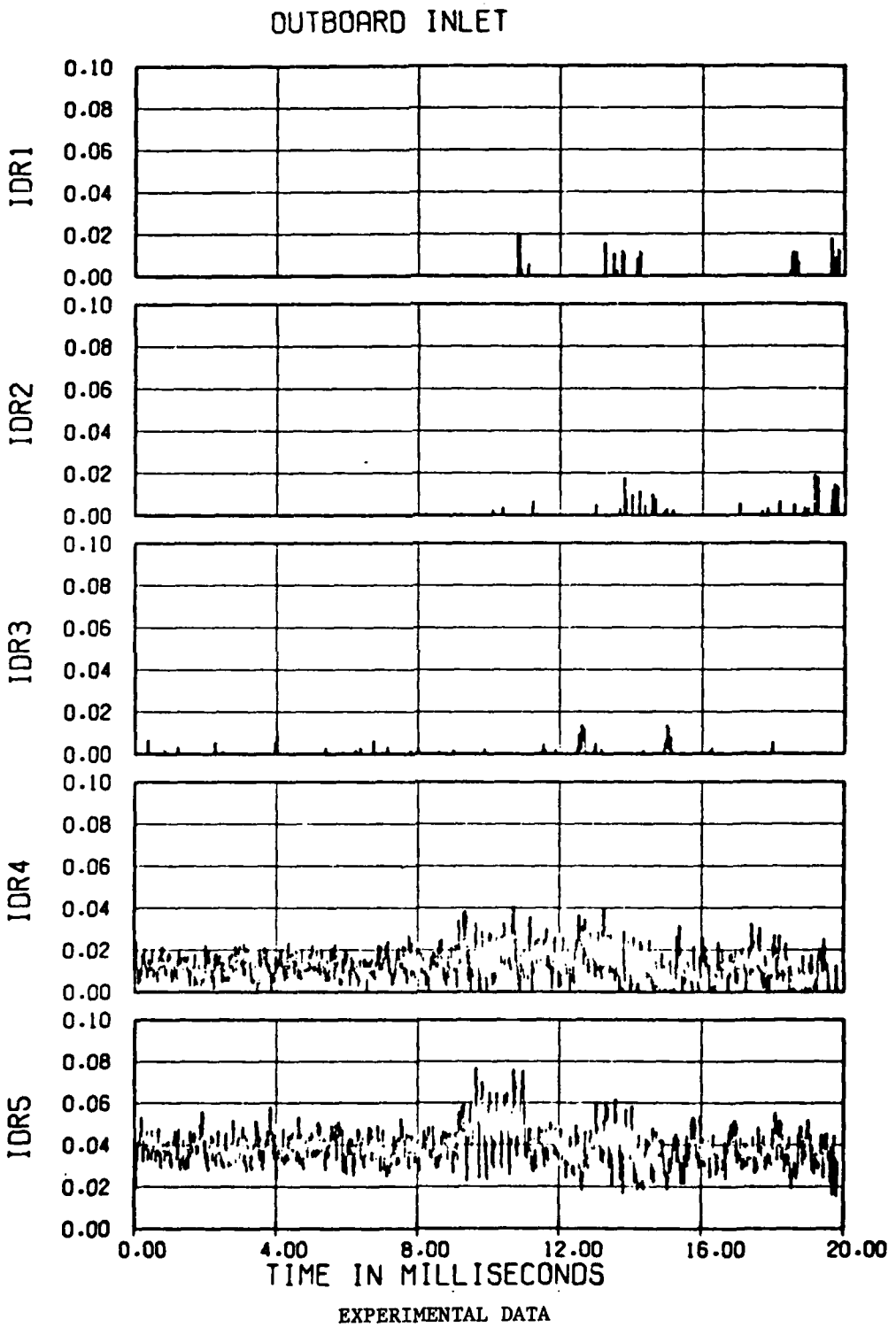

Figure 5.18b. Radial distortion.

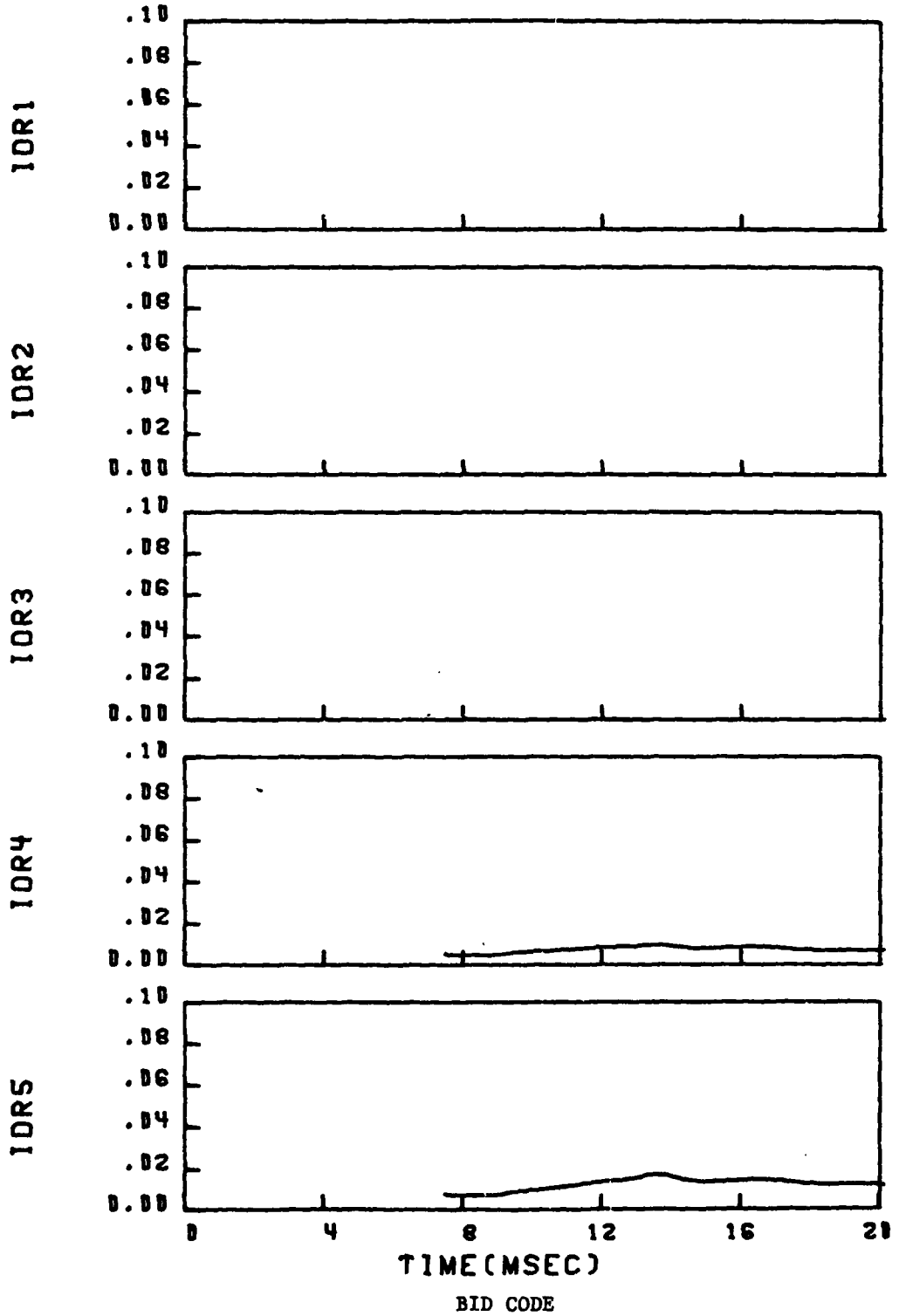

Figure 5.18b. Concluded.

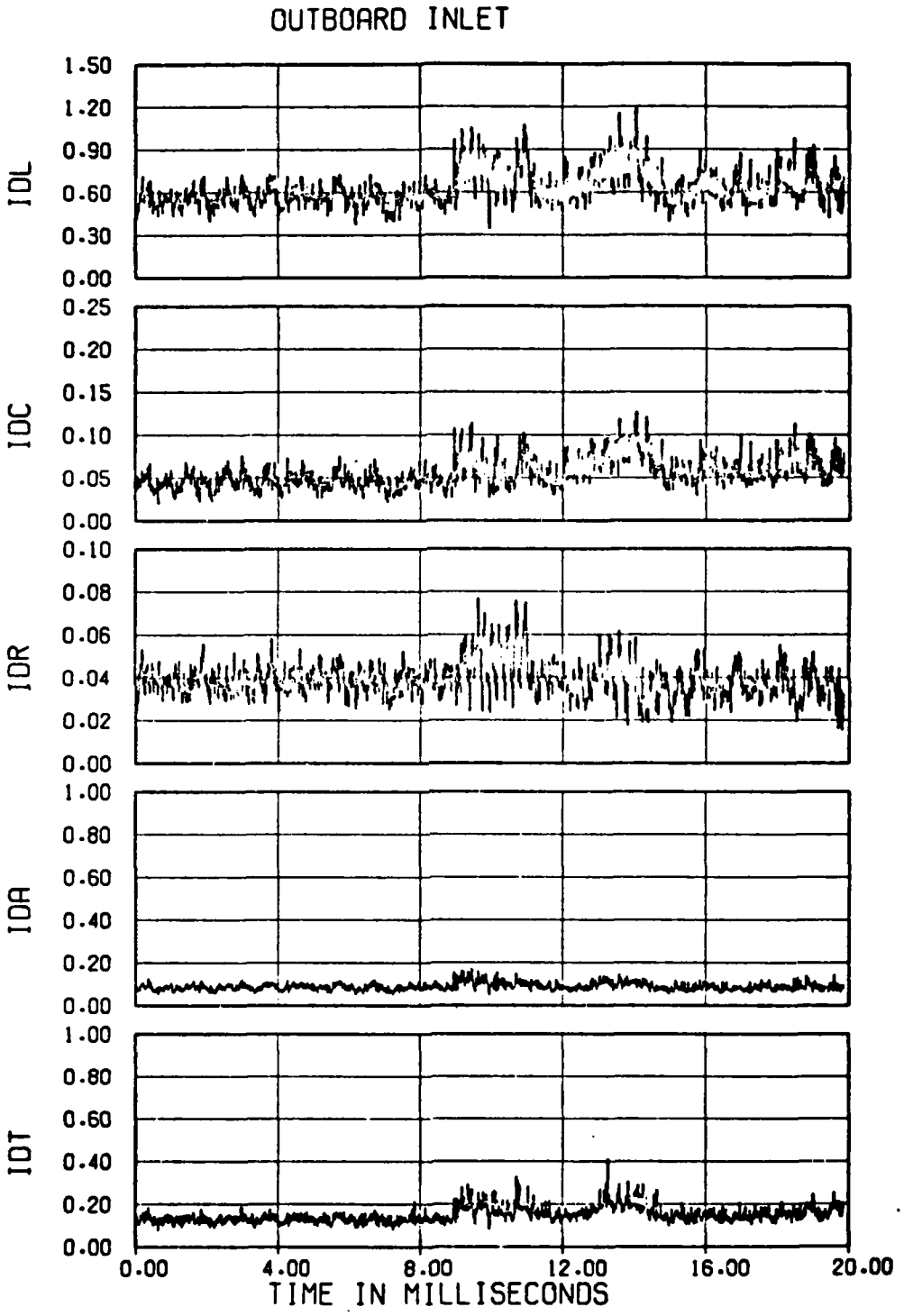

EXPERIMENTAL DATA

Figure 5.18c. Overall distortion.

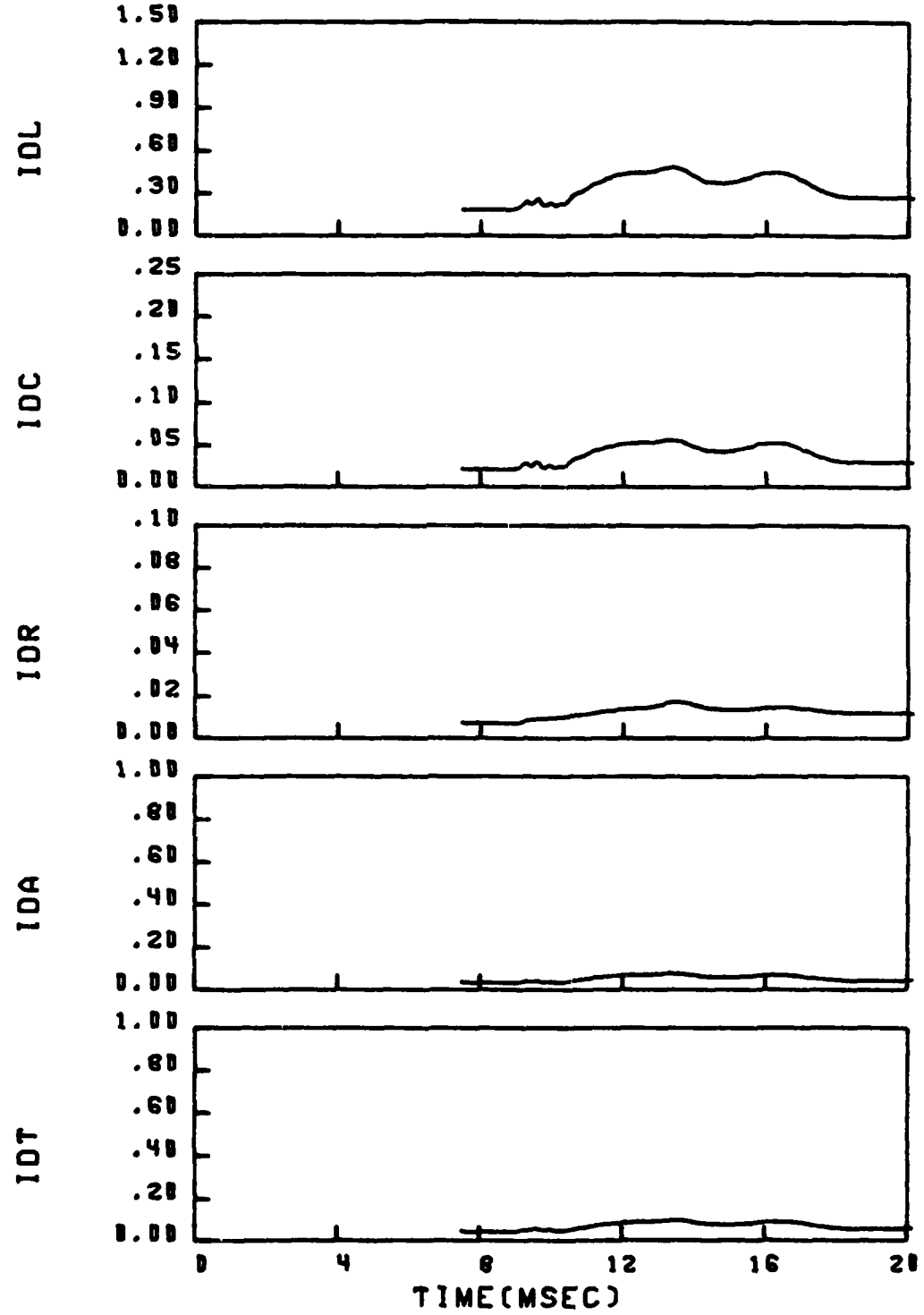

BID CODE

Figure 5.18c. Concluded.

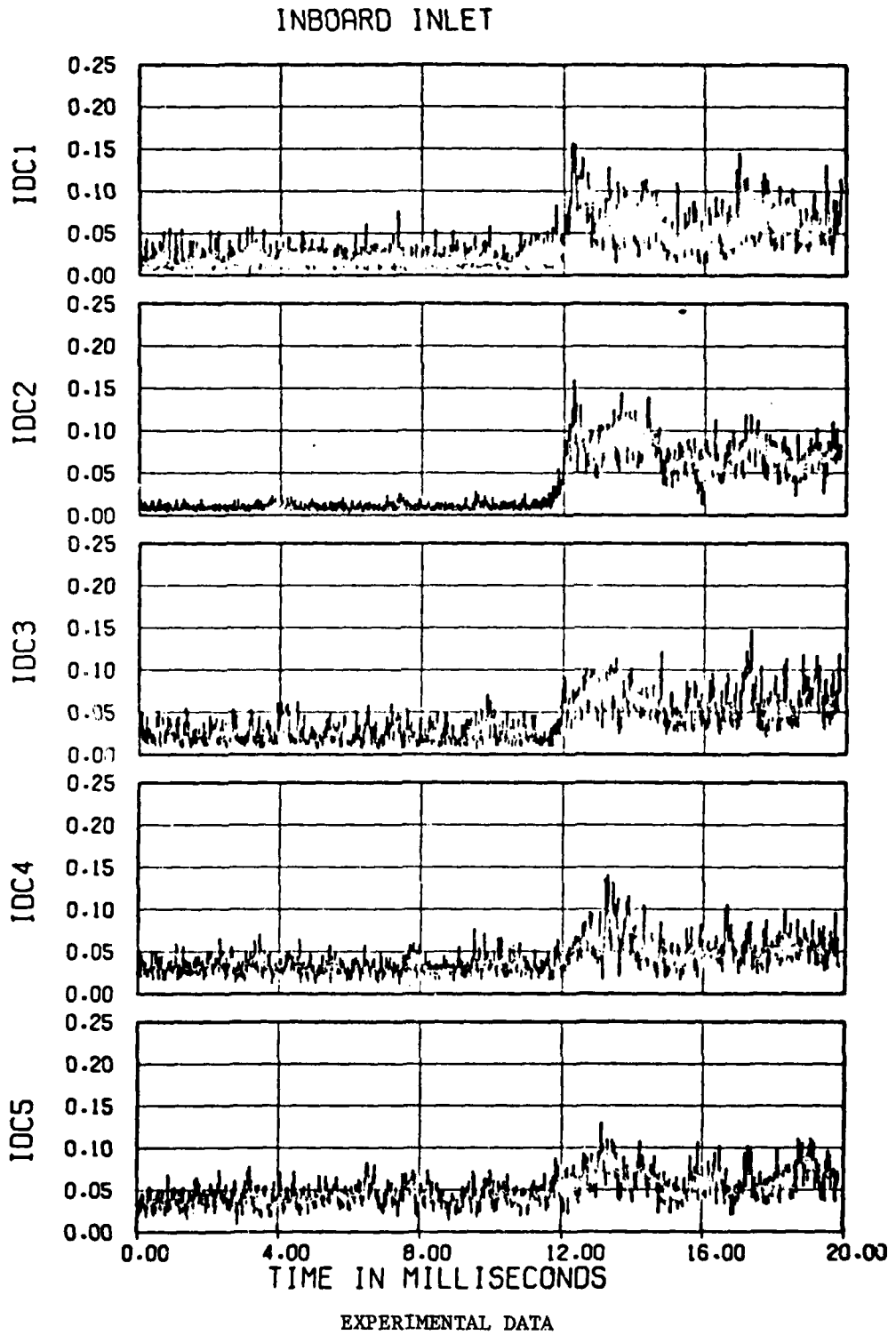

Figure 5.19a. Circumferential distortion.

Figure 5.19. Comparison of theoretical and experimental time histories of engine face distortion for Run 40 (Part 619), leeward (inboard) inlet.

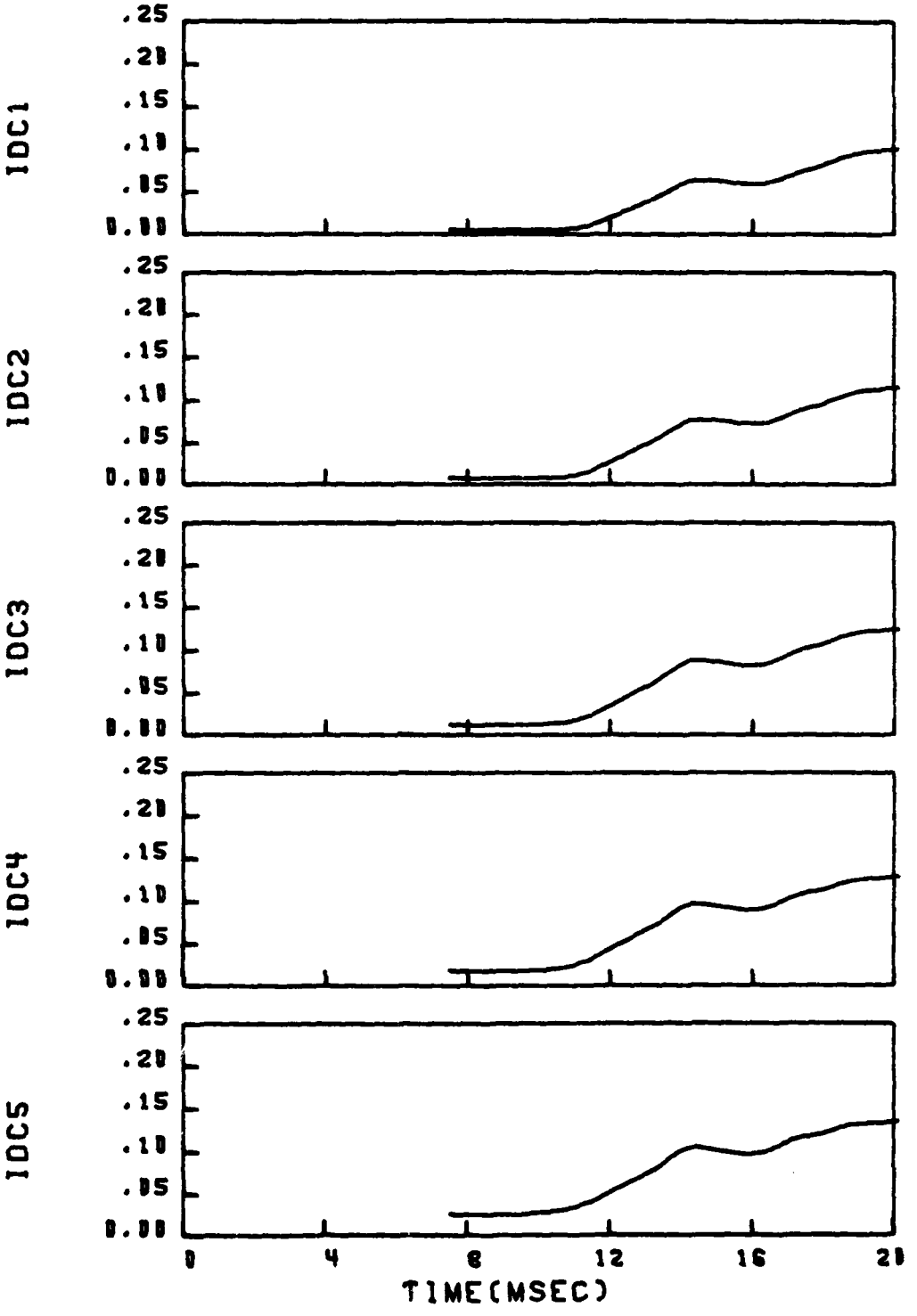

BID CODE

Figure 5.19a. Concluded.

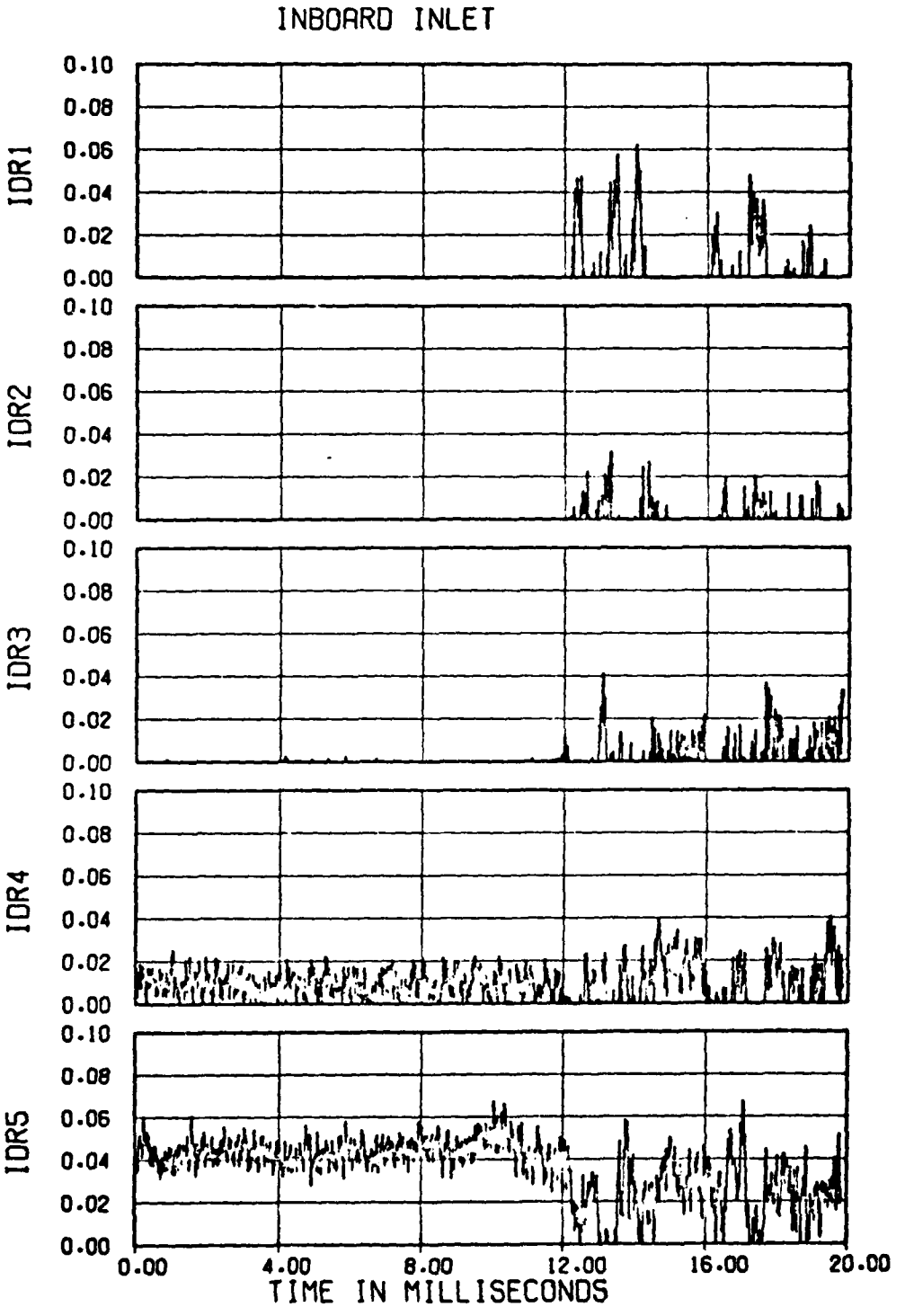

Figure 5.19b. Radial distortion.

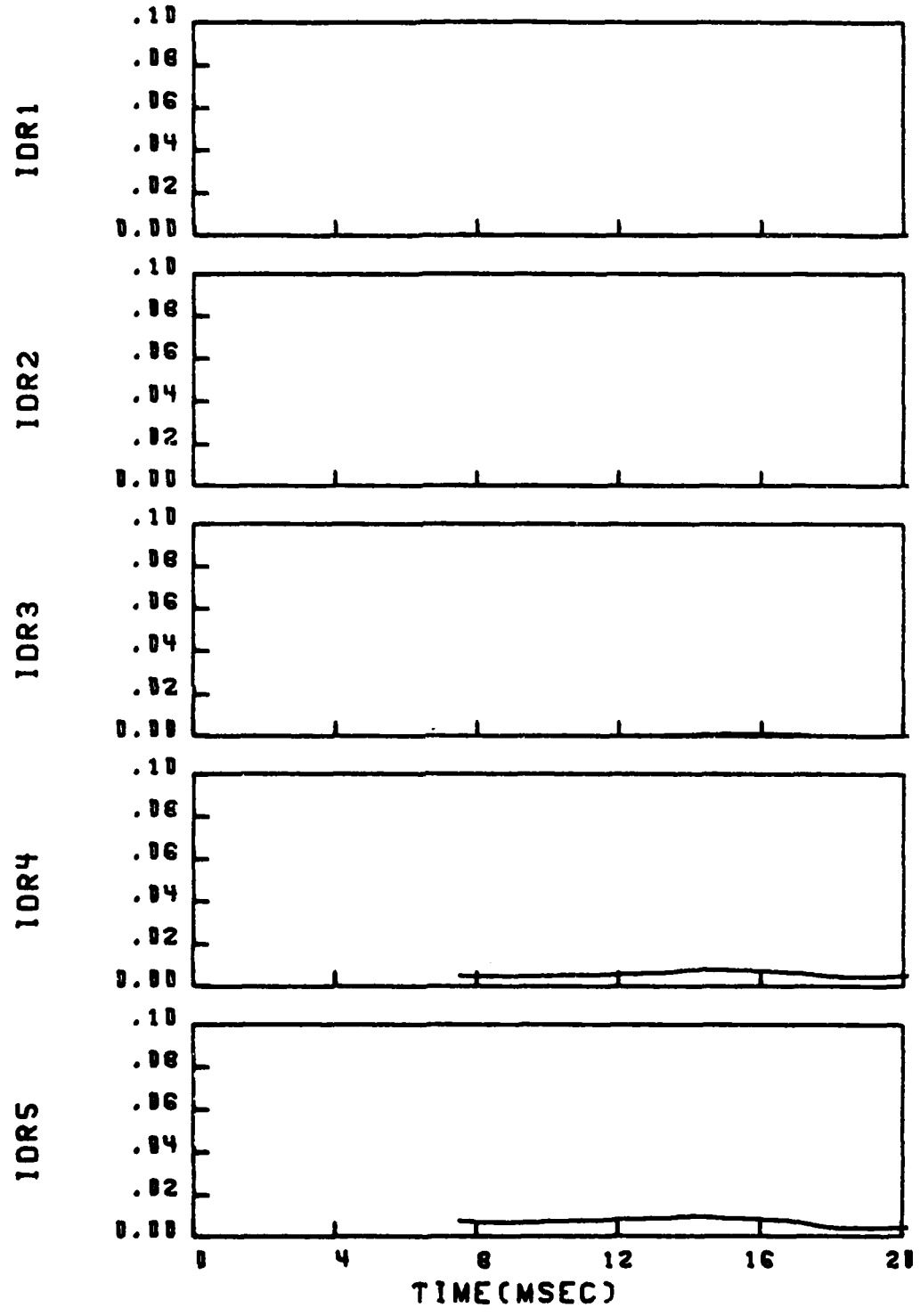

BID CODE

Figure 5.19b. Concluded.

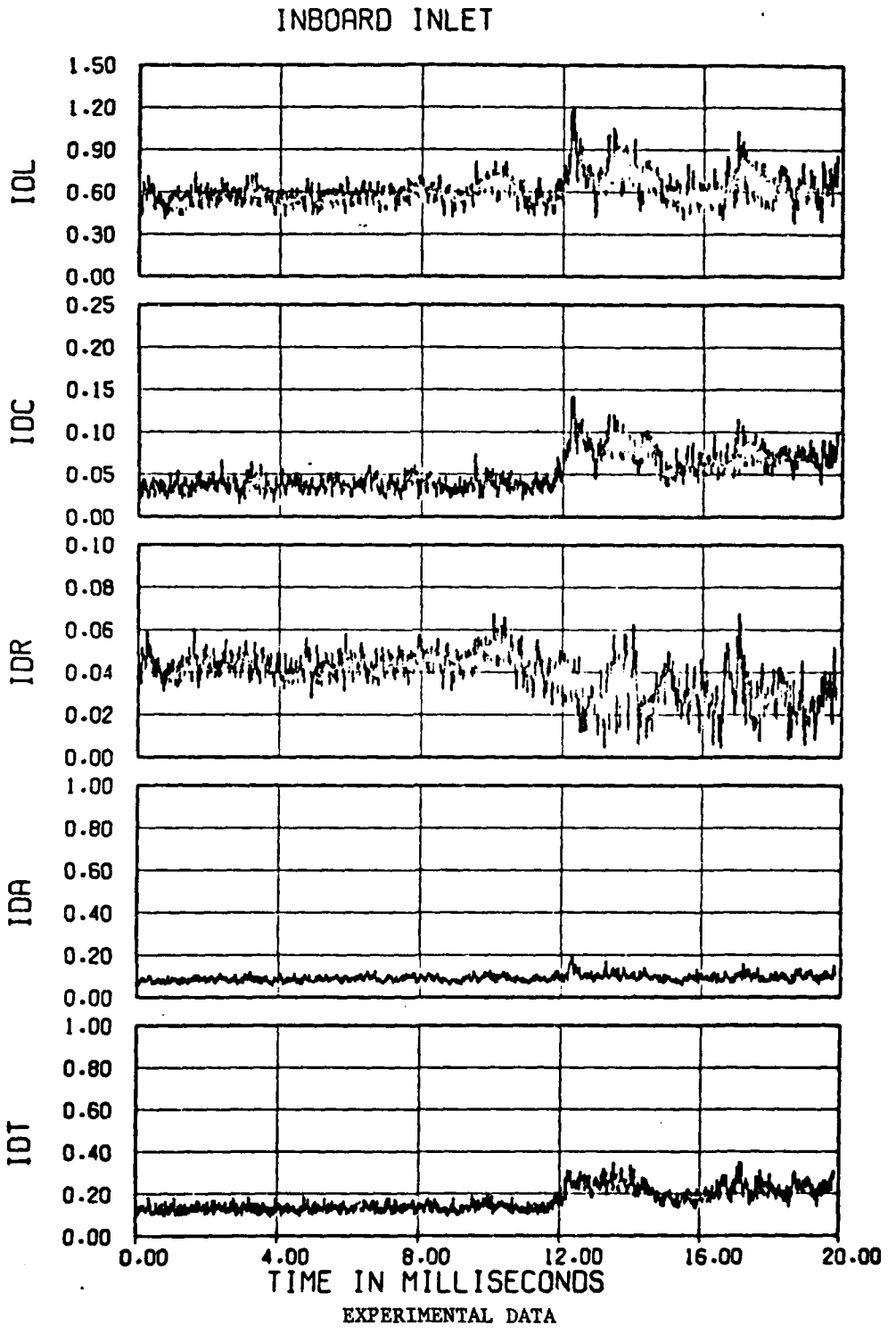

Figure 5.19c. Overall distortion.

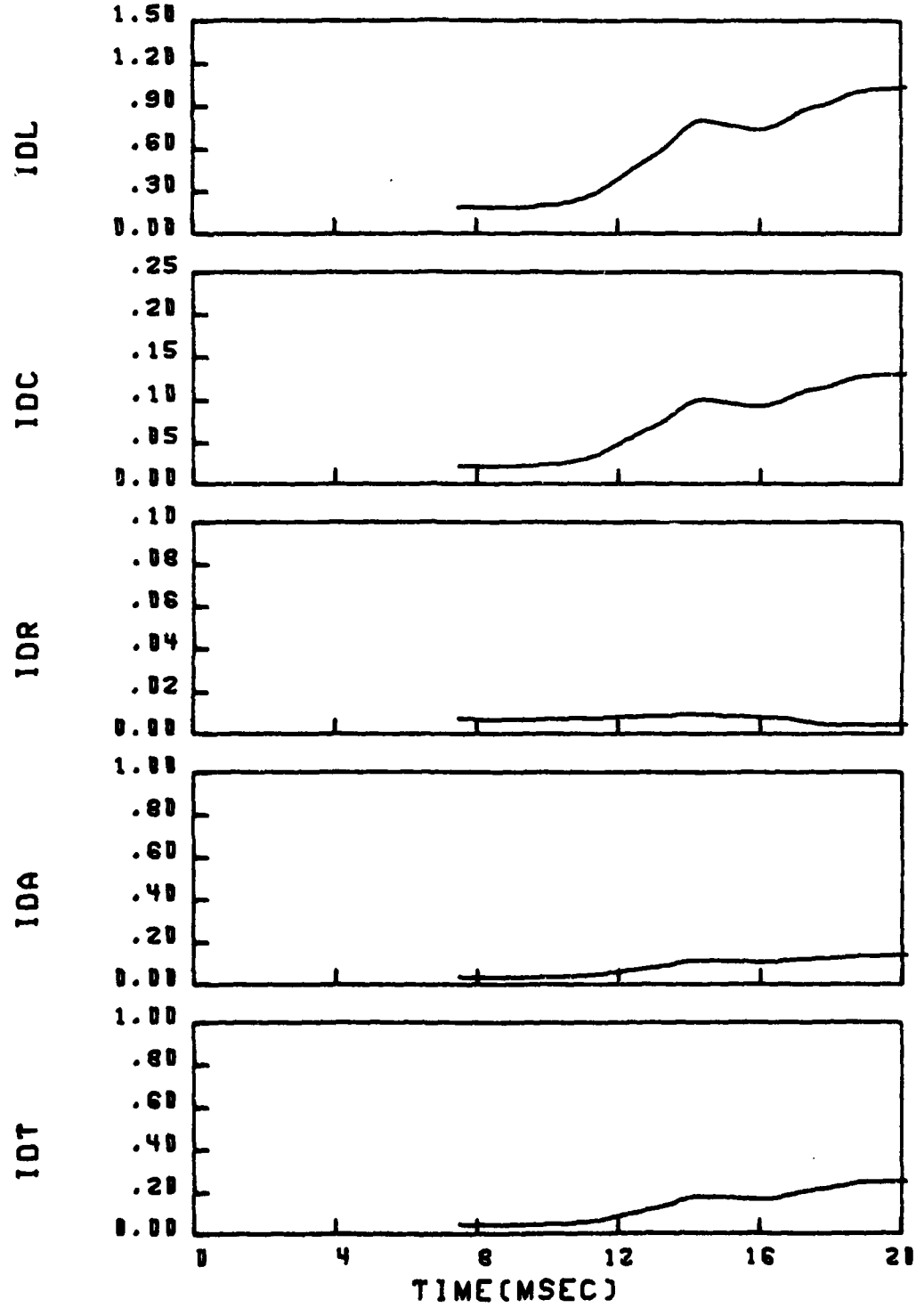

BID CODE

Figure 5.19c. Concluded.

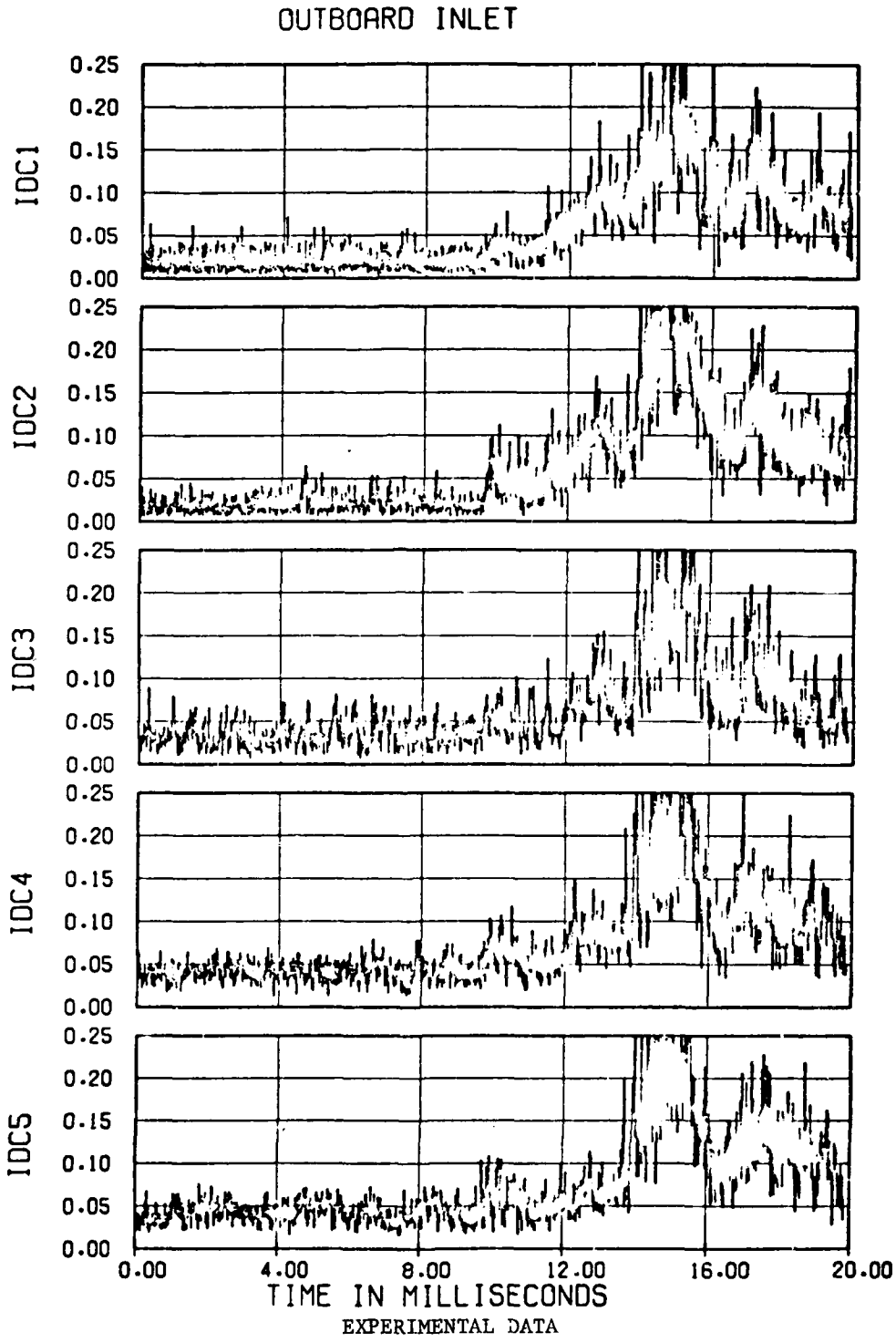

Figure 5.20a. Circumferential distortion.

Figure 5.20. Comparison of theoretical and experimental time histories of engine face distortion for Run 18 (Part 624), blastward (outboard) inlet.

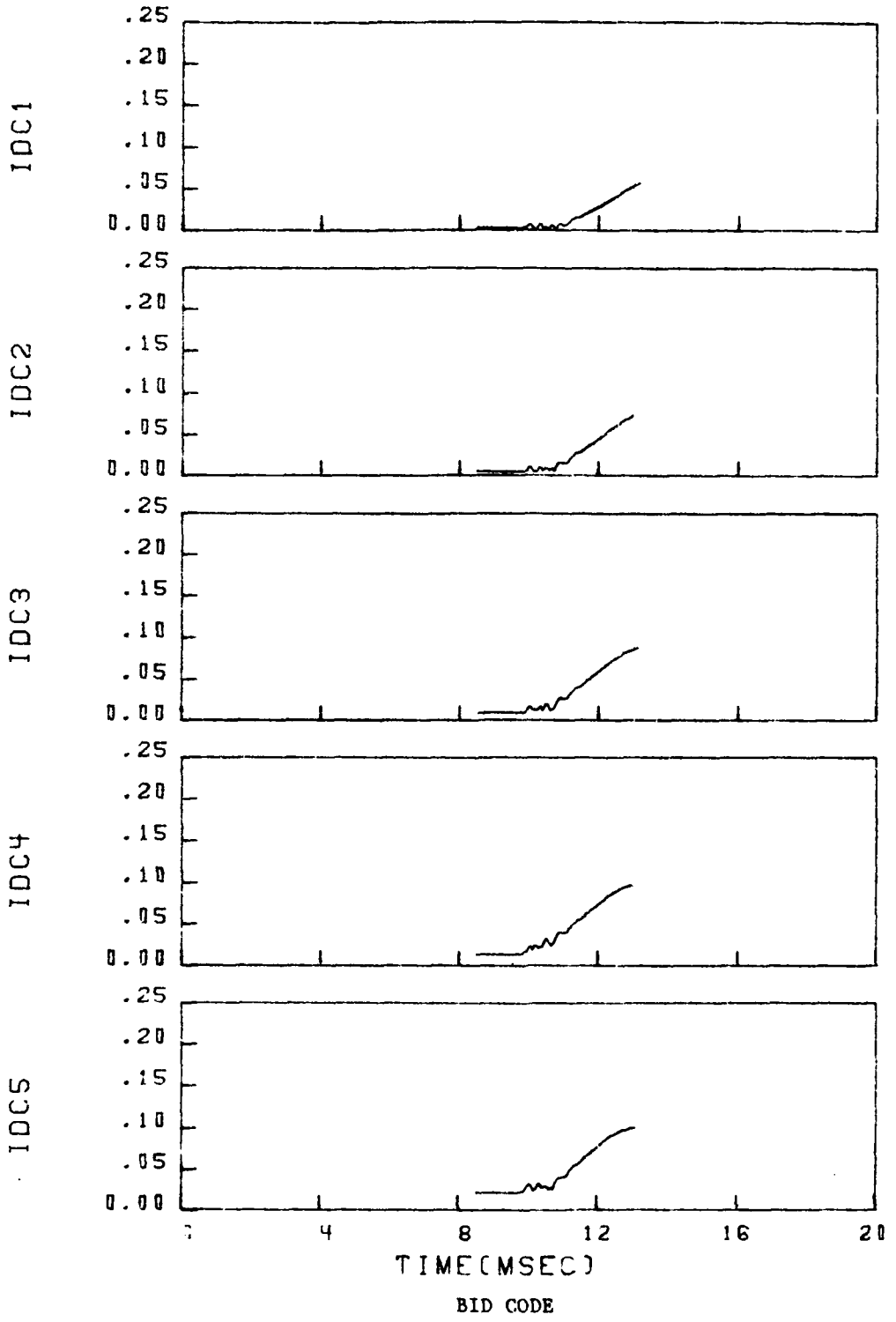

Figure 5.20a. Concluded.

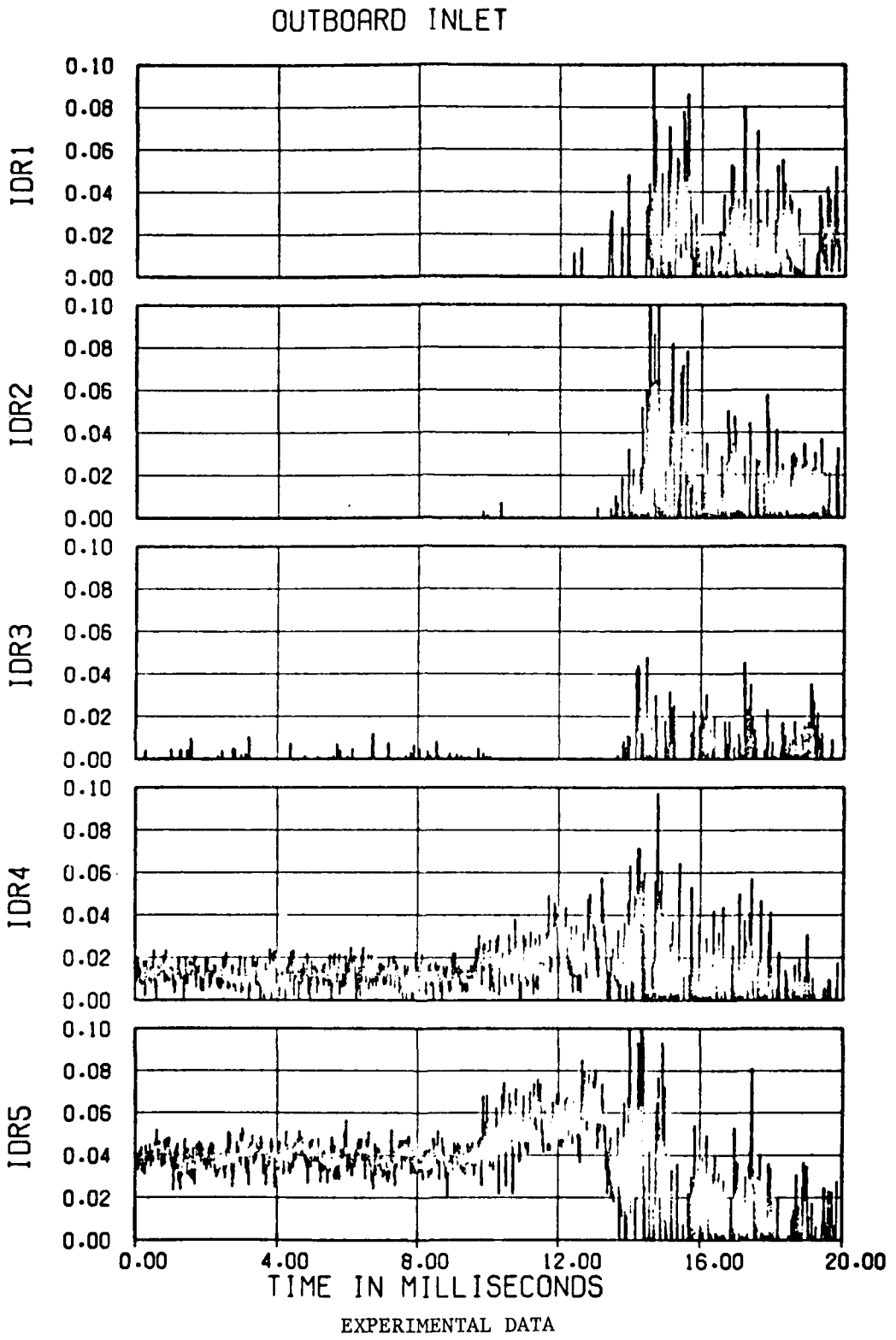

Figure 5.20b. Radial distortion.

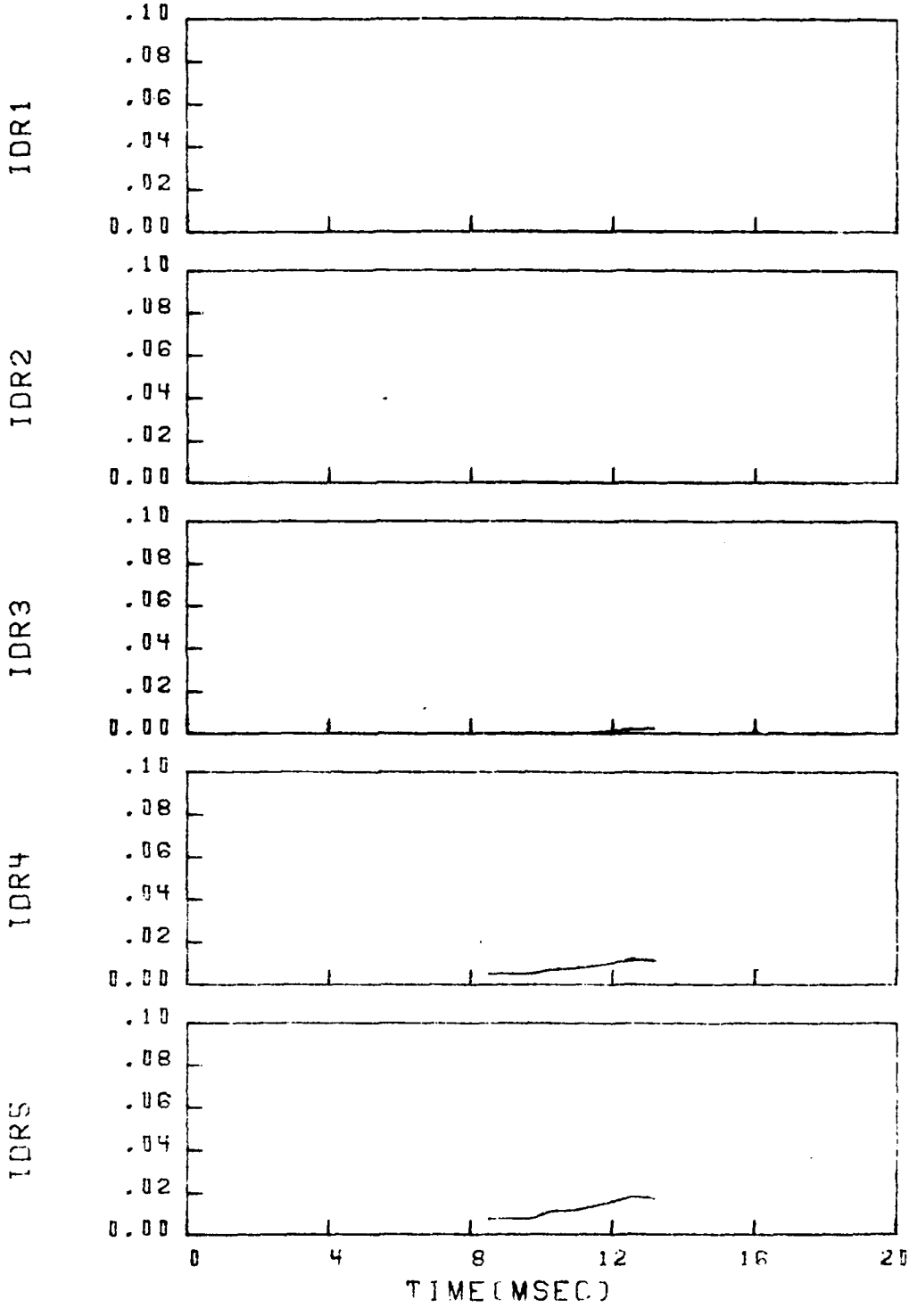

Figure 5.20b. Concluded.

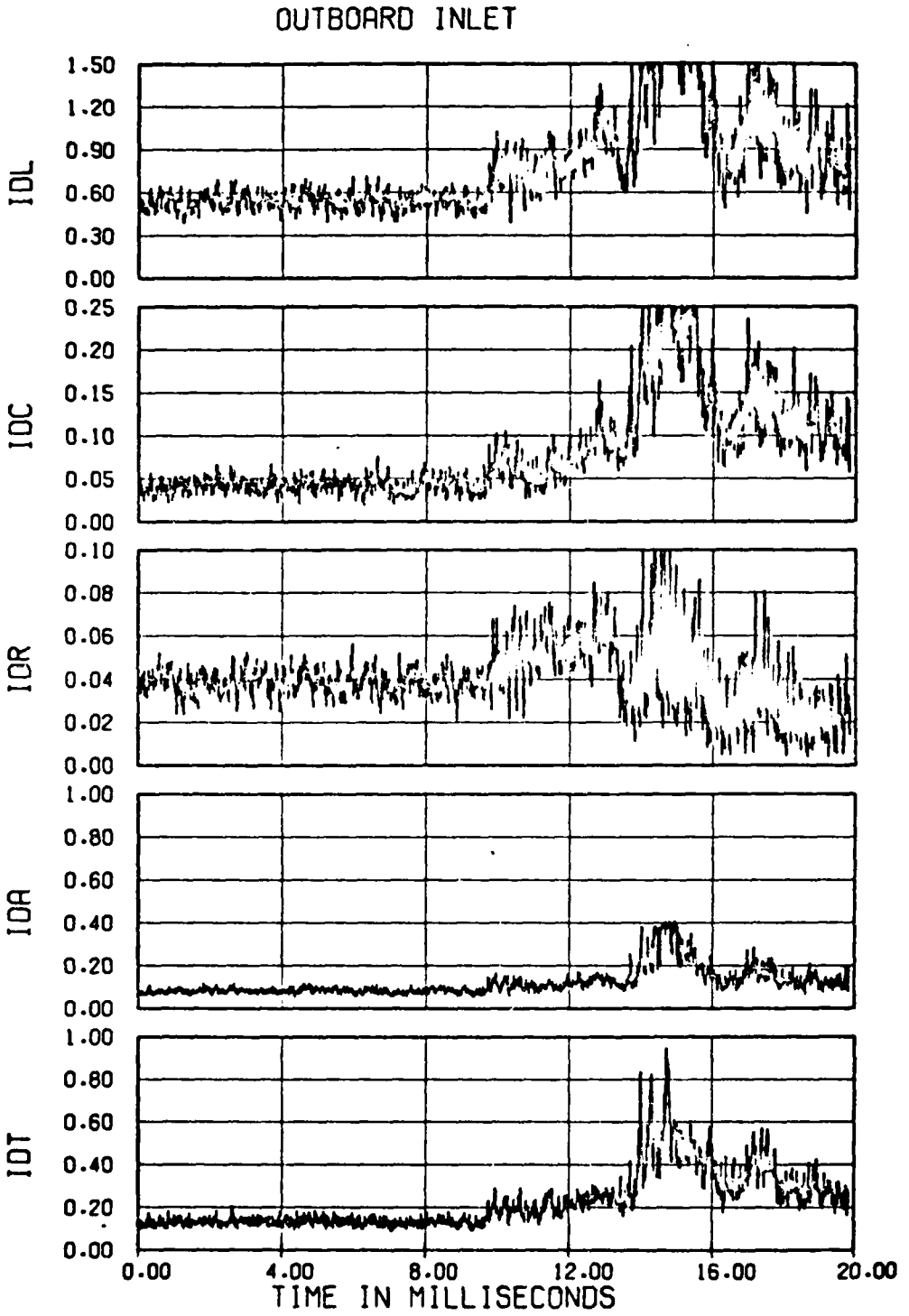

EXPERIMENTAL DATA

Figure 5.20c. Overall distortion.

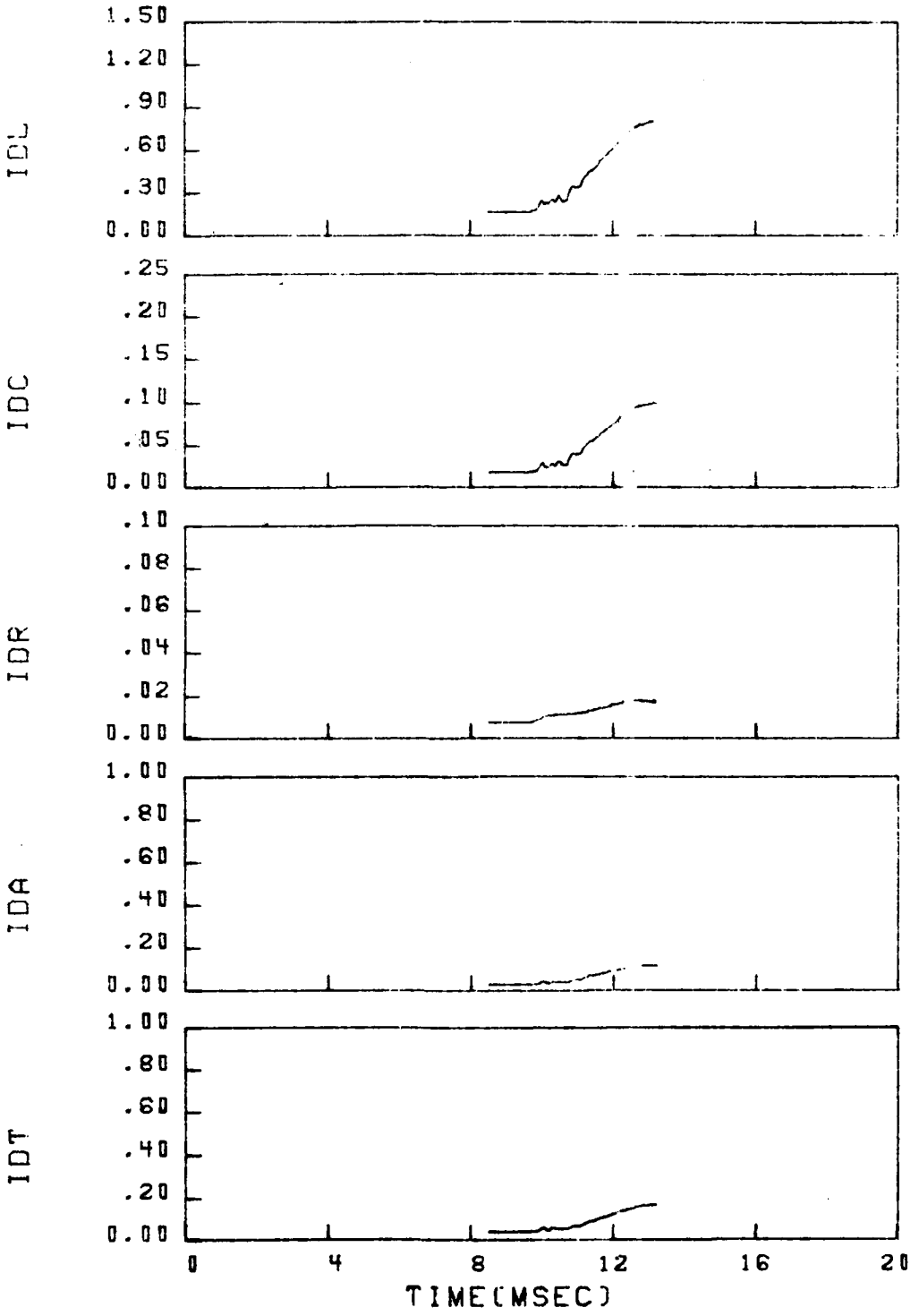

BID CODE

Figure 5.20c. Concluded.

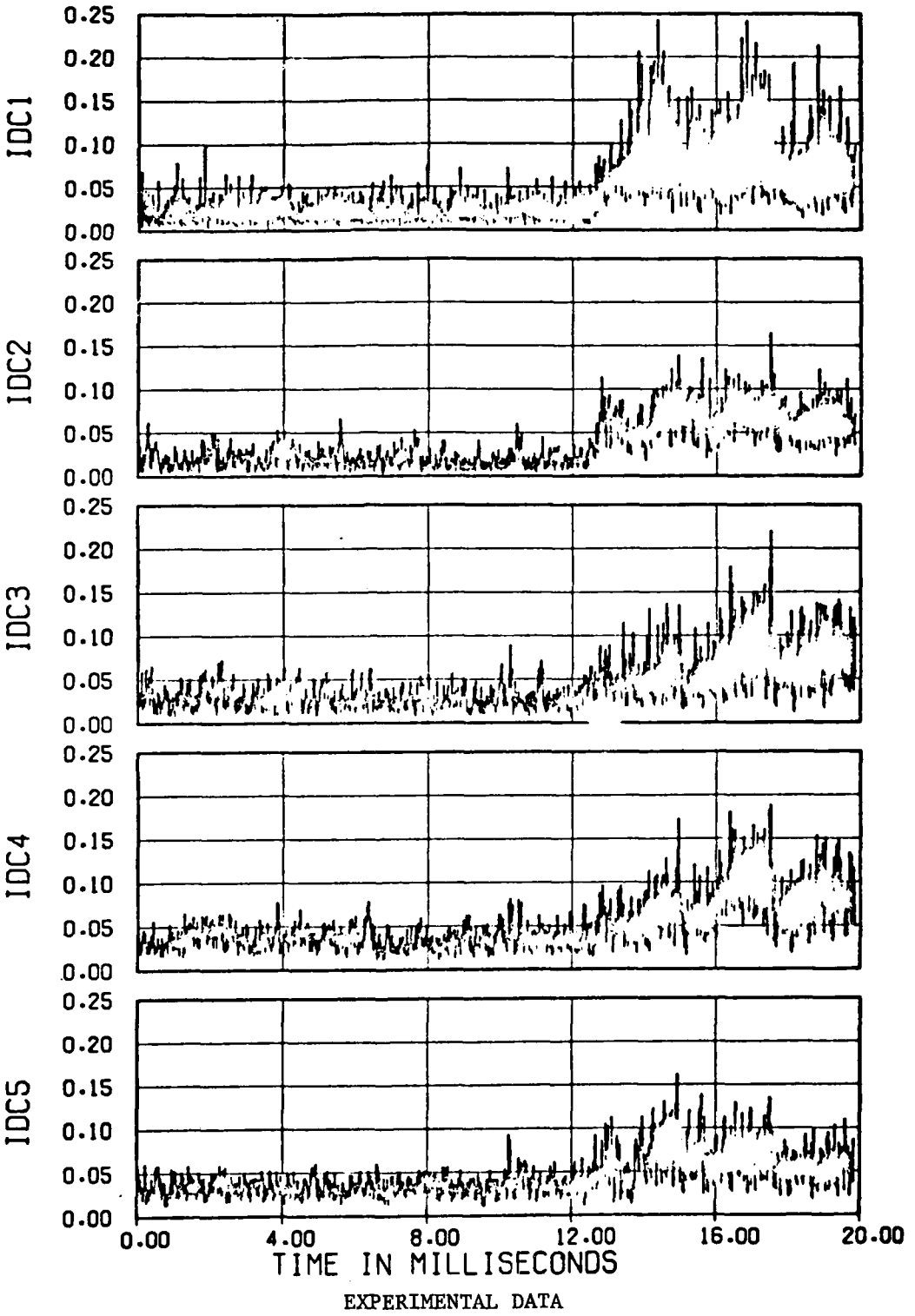

Figure 5.21a. Circumferential distortion.

Figure 5.21. Comparison of theoretical and experimental time histories of engine face distortion for Run 18 (Part 624), leeward (inboard) inlet.

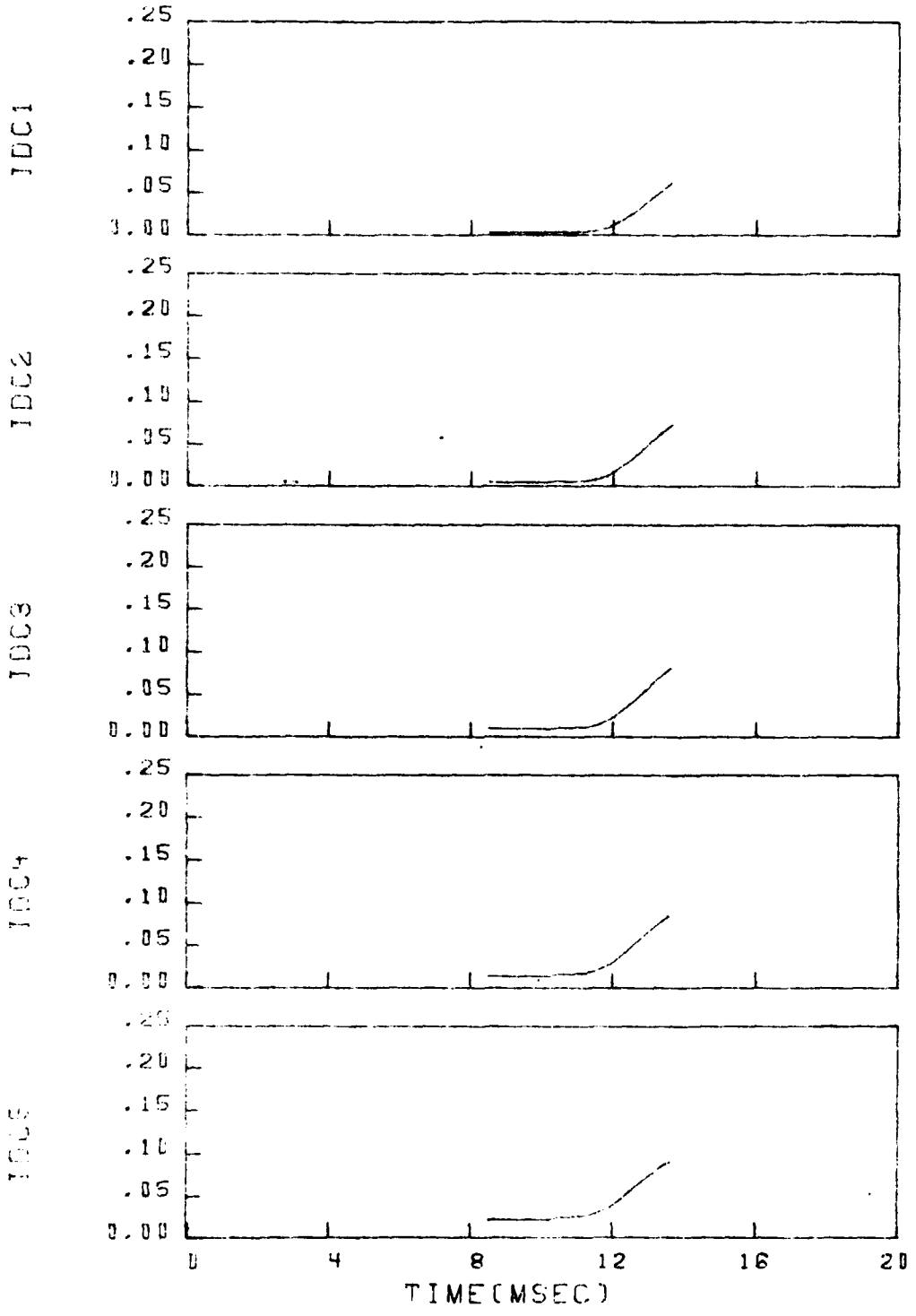

Figure 5.21a. Concluded.

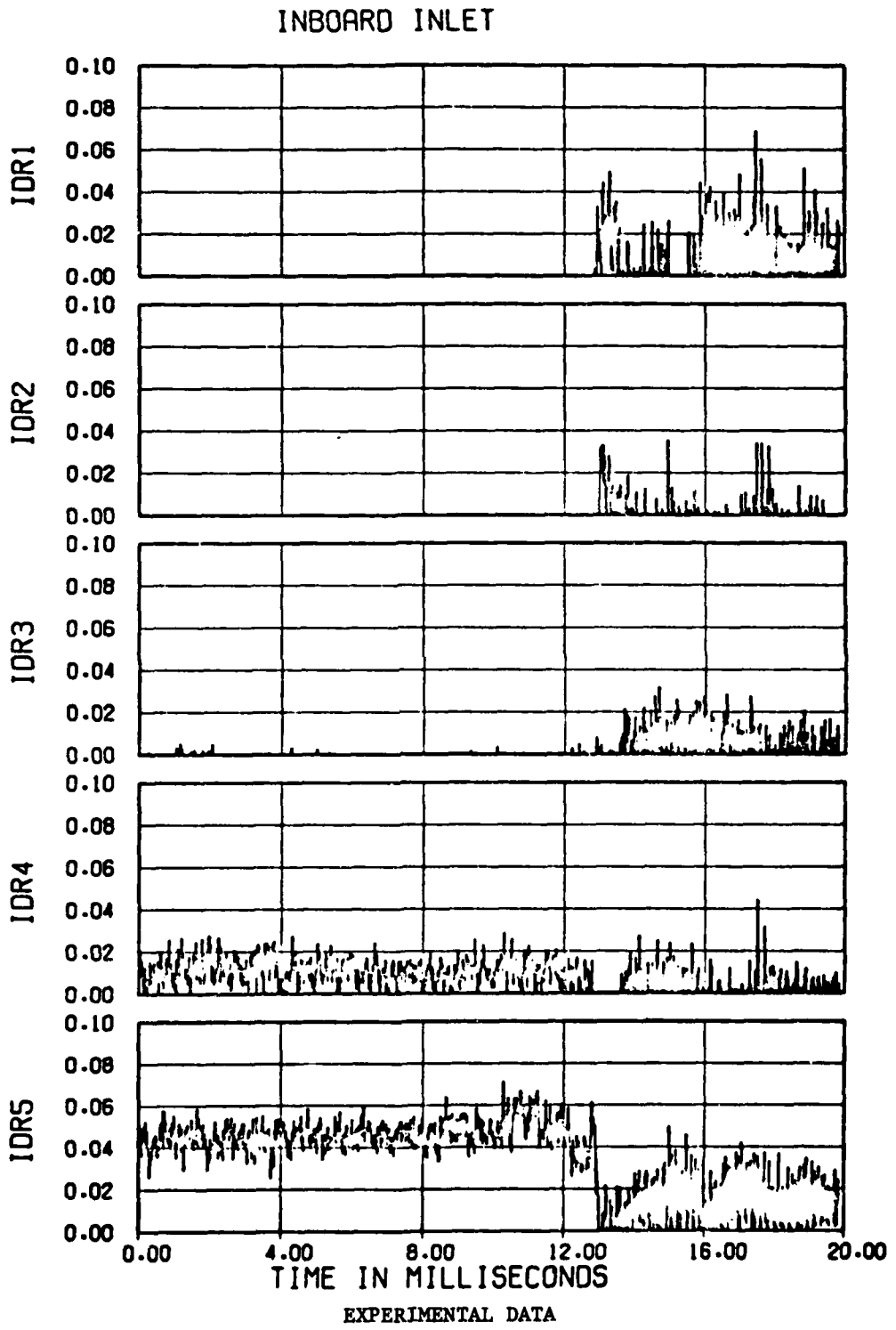

Figure 5.21b. Radial distortion.

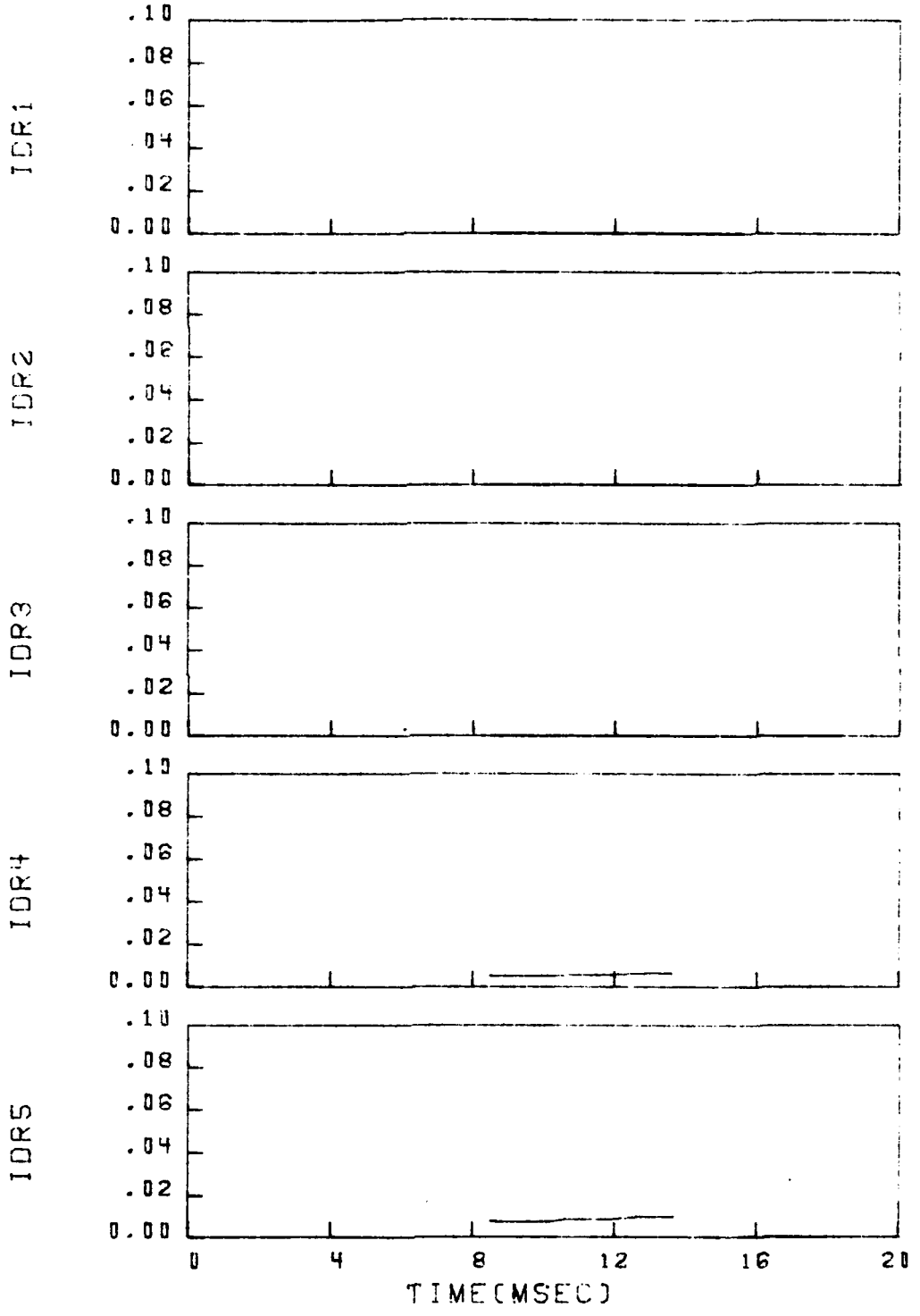

Figure 5.21b. Concluded.

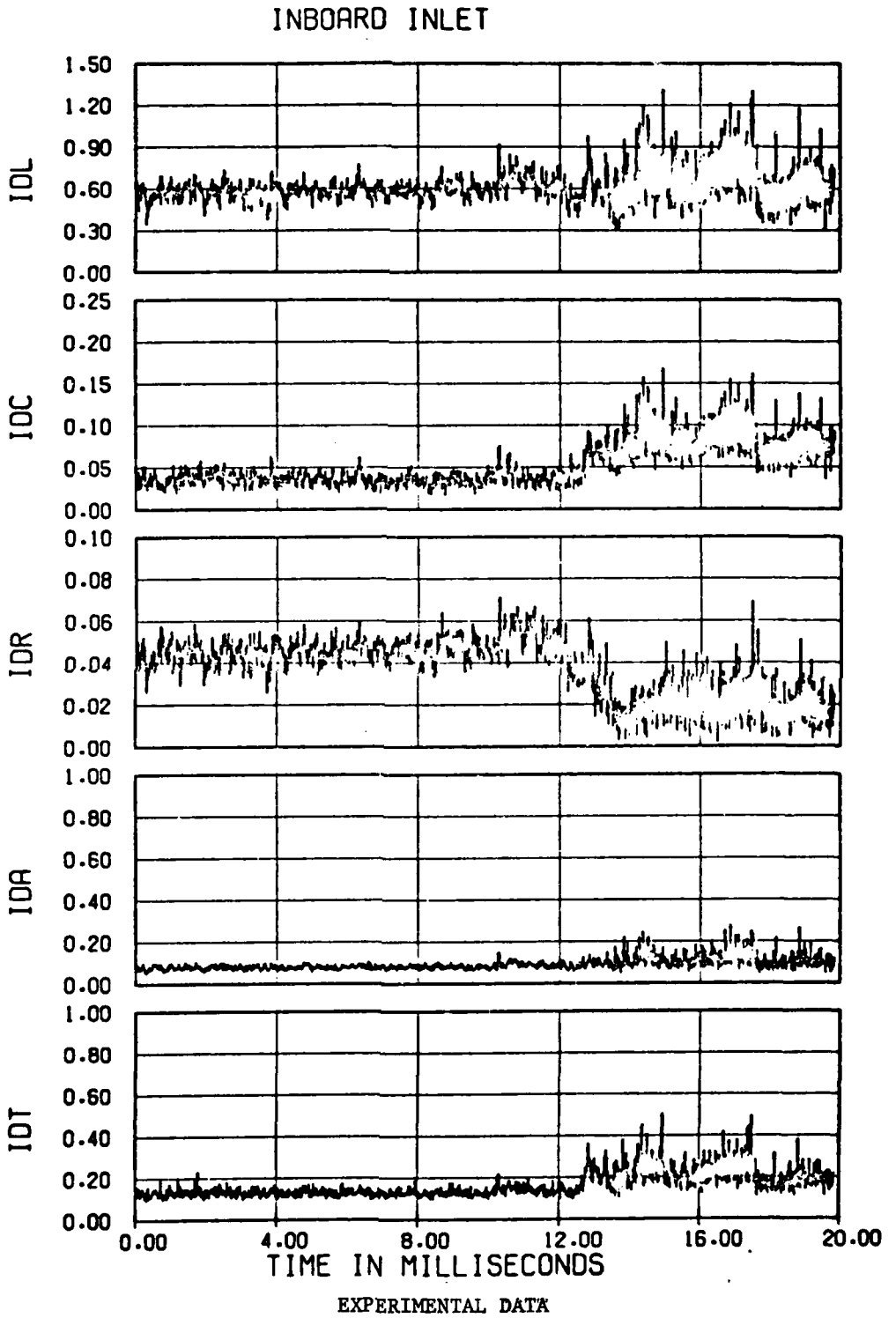

Figure 5.21c. Overall distortion.

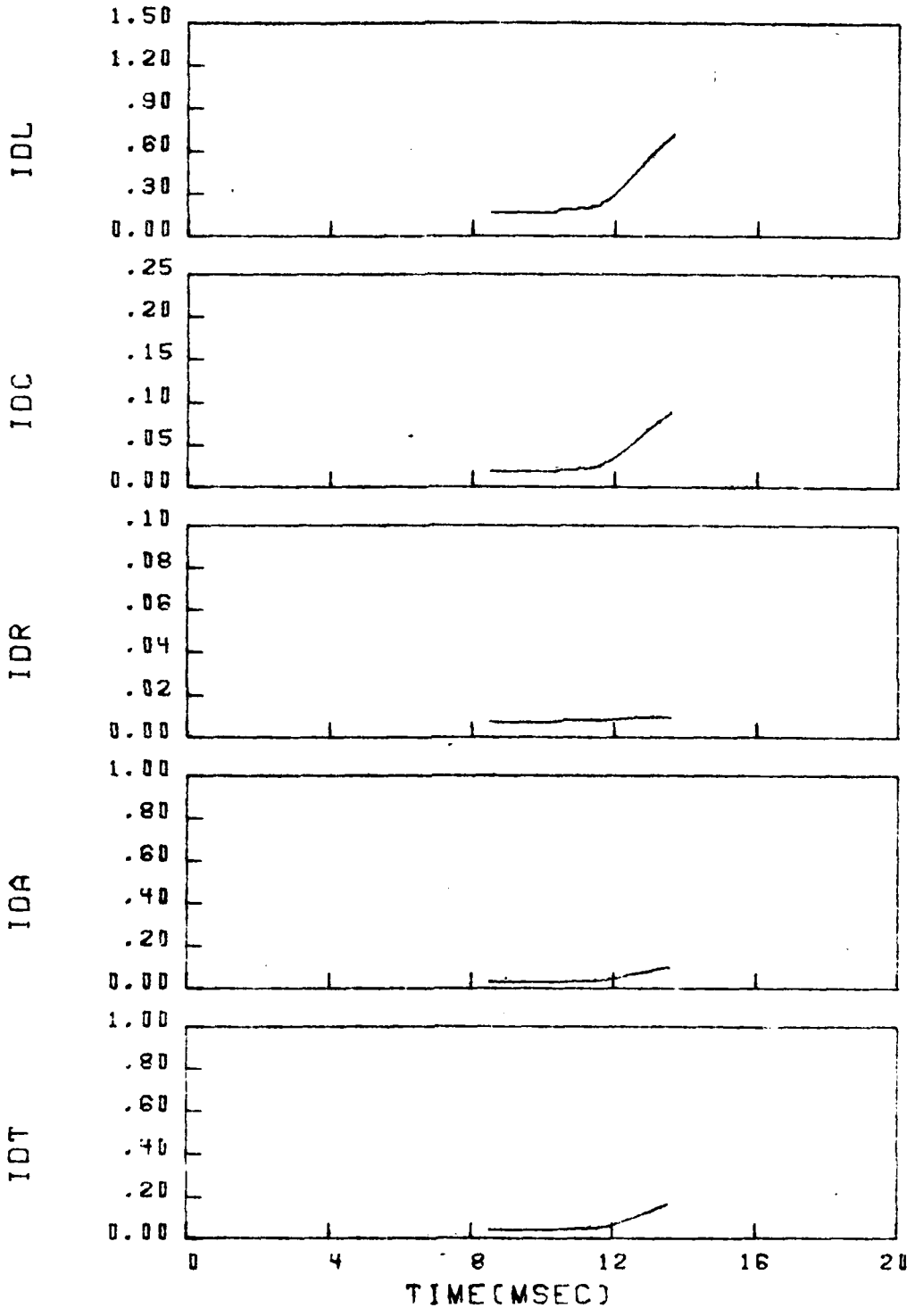

BID CODE

Figure 5.21c. Concluded.

SECTION 6
EVALUATION OF LATE TIME LARGE DISTORTION VALUES

It was found in the inlet-blast tests of Reference 1 that generally very few large distortion values were obtained during the early-time, definitely blast-type, flow periods of the tests. However, there were some observed large distortion values at times after the fairly definite blast type flow duration of about 3.3 ms, which appeared to deserve more detailed study.

As part of the present study, a detailed re-evaluation was made of the 16T inlet blast test results to determine whether the large distortion values observed at late times (after the nominal blast event) on some firings could be attributed to inlet response behavior or to other effects. An initial appraisal identified 26 firings with significant late time distortions which appeared worthy of consideration. For these runs it was found that the large observed IDL values could be correlated with one or more of the following circumstances.

1. Some IDL peaks correlated closely to significant rises in total pressure, indicating that these peaks were produced by the effects of the cold jet from the shock tube passing directly into the inlet.

2. Some IDL peaks corresponded closely to rapid changes in input pressures measured by the claw probes, indicating that the distortion values were caused primarily by input variations rather than inlet response effects.

3. For some runs, there were significant differences in the input pressures measured by the different claw and static probes, indicating a considerable distortion of the flow entering the inlet. Hence, for these runs the engine face distortion could have resulted from the input distortion rather than from inlet response effects.

4. For several runs, large apparent distortion peaks were caused by the readings of one pressure transducer (1802), whose readings were somewhat erratic and were inconsistent with the measurements of two adjacent transducers (1801 and 1804).

5. For at least one run, large apparent distortion values were attributed to erratic behavior of a group of 4 pressure transducers which were recorded on the same oscillograph track. These transducers gave pressures inconsistent with adjacent transducers.

6. In some cases transducers bottomed, producing false indications of large distortion values.

In summary, no cases were found where large late time distortion values (IDL > 1) were obtained which could be definitely attributed to inlet response behavior. In all cases there was evidence to suggest that the large distortion values could be attributed at least in part to either cold gas jet impact on the inlet, large input distortions or transducer malfunctions.

The above observations do not completely resolve the question as to whether any of the large late time distortions observed in the tests can be attributed to inlet blast response effects. It can only be said that the factors pointed out above would appear to make any such determination from the late time test data a difficult matter and any results of such a determination could be suspect.

SECTION 7
REFLECTED SHOCK-BOUNDARY LAYER INTERACTION

The reflected wave from the engine, as it moves upstream through the inlet, makes an adverse pressure gradient for the flow within the inlet. The adverse pressure gradient produces some distortion of the flow. If the gradient is large enough, boundary-layer separation takes place and large distortion of the flow would result, as pointed out in Section 3 and 4 and in Reference 1.

A sketch illustrating the effect of the reflected waves on the boundary layers in the two inlets is shown in Figure 7.1. The waves, shown here as two shocks, produce an adverse pressure gradient within the boundary layers on the walls of the inlets. The pressure gradients produce more rapid thickening of the boundary layers and retardation of the flow within the layers. If the gradients are sufficiently large, separation of the flow from the walls would take place resulting in large distortion.

There were indications that separation by the reflected shock may have taken place in some of these tests. The problem is that distortion at the engine face would have resulted after the end of the test period, about 3 ms, so effect of separation could not be verified.

Calculations are presented in Reference 1 using the NASA BLAYER code of Reference 4. As pointed out there, the BLAYER calculations are limited by the assumption of a constant total pressure and total temperature in the free stream, whereas the variations produced by blast interaction can be large (Reference 1).

NASA has generalized the BLAYER code, subsequent to the work published in Reference 4, to include variations of the total pressure and total temperature in the free stream. A copy of the generalized BLAYER code was provided to Kaman AviDyne (Reference 5), and it has been employed for the calculations reported below.

7-1 SHOCK-BOUNDARY LAYER CALCULATION.

Calculations of the boundary layers on the inlet cowls and ramps were made using pressure, temperature and velocity data from BID code results for the free-stream conditions. BID results for properties in the cells contiguous to the respective wall were employed. The BID data used were the same as for the calculations reported in Reference 1: BID Run 10/26/77, M=0.85, W2R=350 lb/s, ϕ=90 deg and Δp_s=5 psi. The data selected were for a fixed time of 33.6 ms (full scale) after blast arrival, when the reflected waves were well into both inlets.

The generalized BLAYER code assumes a steady-state boundary layer, i.e. the conditions do not vary with time. Therefore the BID data distributions for the free-stream properties were assumed to be frozen, i.e. non-varying with time. In actuality the reflected waves move upstream with time, so the properties are time varying. The assumption of a steady state flow is believed to be conservative, because the pressure gradients experienced by the boundary layers with the moving wave would be greater than for the assumed frozen conditions.

The results of the calculations are expressed in terms of a parameter called the boundary-layer factor H_i, essentially representing the velocity distribution across the boundary layer (normal to the wall). If the velocity distribution is more uniform, the parameter approaches unity. A value of 1.2 to 1.4 is typical for a turbulent boundary layer on a flat plate in the absence of a pressure gradient. In an adverse pressure gradient (increasing pressure in the direction of flow) the velocity decreases towards the wall so H_i increases. When the velocity gradient normal to the wall goes to zero, the flow can separate from the wall. Experience shows that separation may occur for H_i values as low as 2.0 and definitely by 2.8.

The generalized-BLAYER calculations were carried out for three cases: the boundary layers on the two cowls and on the blastward splitter ramp. The boundary layers were assumed to be turbulent from the leading edges.

Calculations were not made for the leeward splitter ramp, because of undefined starting conditions. The data indicate a possible separation bubble near the leading edge with probable reattachment. The boundary-layer conditions are not believed to be well enough defined at this point for meaningful boundary-layer calculations.

The results of these calculations are presented in Figures 7.2 to 7.4. The input data (p_1, p_t, T_t) and output (H_i) are presented as functions of the station along each inlet, measured from the leading edge of the splitter ramps.

Within the blastward inlet the primary part of the reflected wave at 33.6 ms extends between ramp Stations 12 and 17 (ft), as indicated by the rise in total pressure. On the blastward cowl there is an adverse (positive) pressure (static) gradient between Stations 8 and about 13 due to recovery within the inlet. The pressure-gradient decreases somewhat between about Stations 12 and 13.6, where the pressure gradient of the reflected wave is picked up. The form factor H_i increases to a peak value of 1.57 at station 11.7, which would be well below the minimum separation value of 2.0. H_i then decreases to 1.38 at Station 14.8 where the adverse pressure gradient of the reflected wave causes it to increase rapidly, reaching the separation value of 2.8 at Station 16.8.

At the ramp the adverse pressure gradient begins at about Station 10. H_i is fairly constant to about Station 16 where the gradient increases markedly. The separation value of 2.8 is reached at Station 18.3.

In the leeward inlet the reflected wave has not had a significant impact on the flow at this time (33.6 ms). There is some effect over about the downstream half of the inlet but the effect is to reduce somewhat the large negative gradient in total pressure produced by the incident blast wave. The static pressure gradient produced by the blast wave is large, so H_i rises all along the cowl, and the boundary-layer separation value of 2.8 is reached by Station 20.6. The pressure essentially levels off beyond that point, so the determination of separation is not as definite as for the leeward cowl.

It is concluded that separation caused by the reflected waves would have occurred in the blastward inlet and possibly in the leeward inlet. There are several factors that are believed to make the calculation conservative (under-predict separation). First, a fan stage is expected to reflect a stronger wave than the choked throttle that was employed in the BID calculation. Seccnd, the BID code is dissipative, so adverse pressure gradients are expected to be somewhat under-predicted. Third, the generalized BLAYER code applies for a steady-state boundary layer, and the unsteady effect is expected to increase the tendency toward separation.

Tests are needed having blast durations that are sufficiently long to observe the separation and resultant distortion at the engine face. The test period for these test conditions should be roughly doubled.

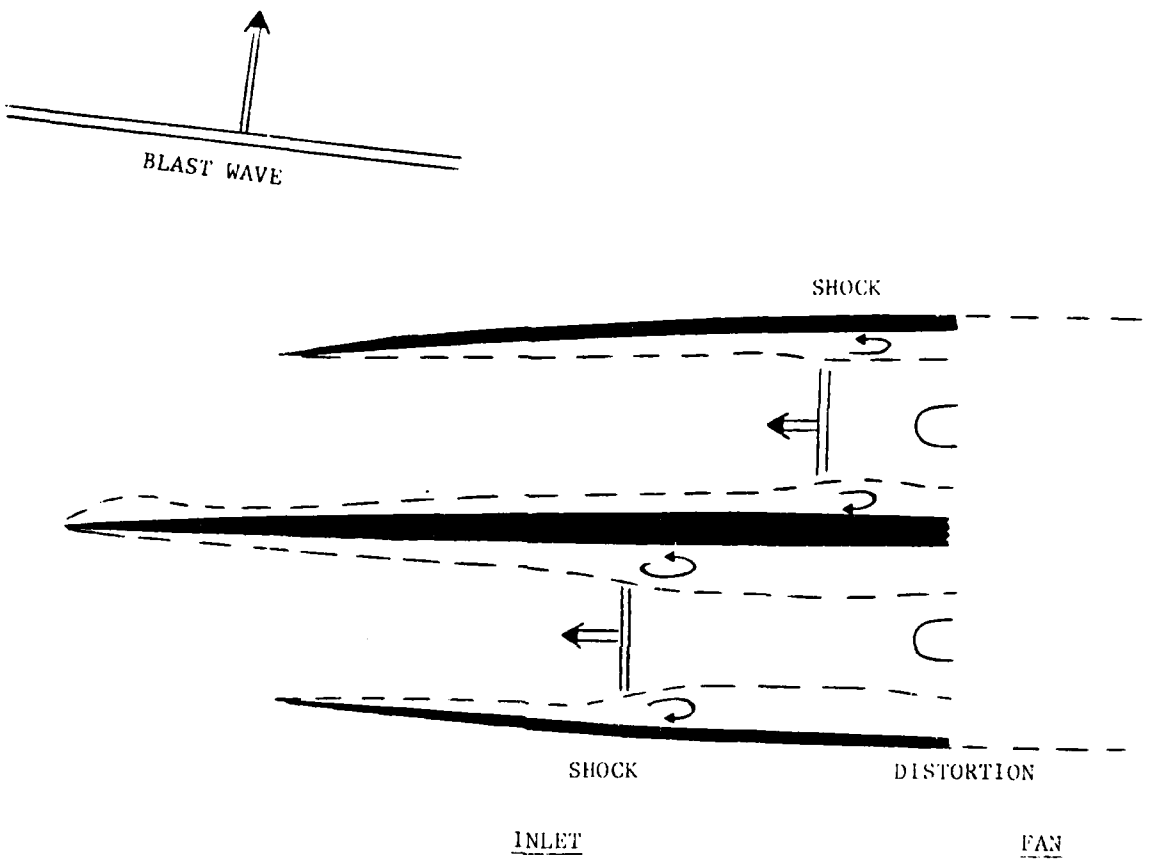

Figure 7.1. Boundary layer separation and distortion from fan reflected shock wave.

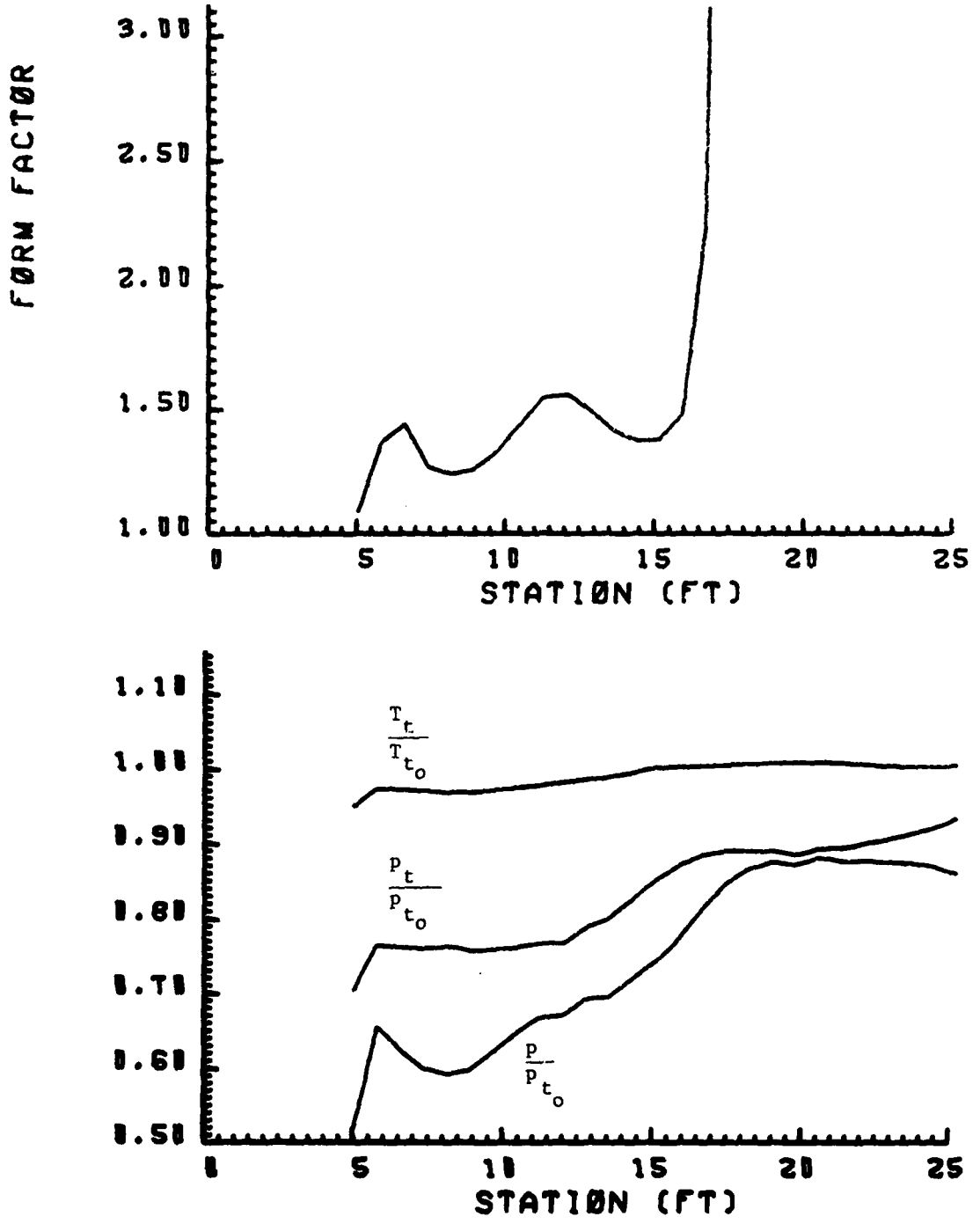

Figure 7.2 - Predicted free-stream properties and form factor H_i of boundary layer on cowl of blastward inlet. After reflected wave enters inlet.

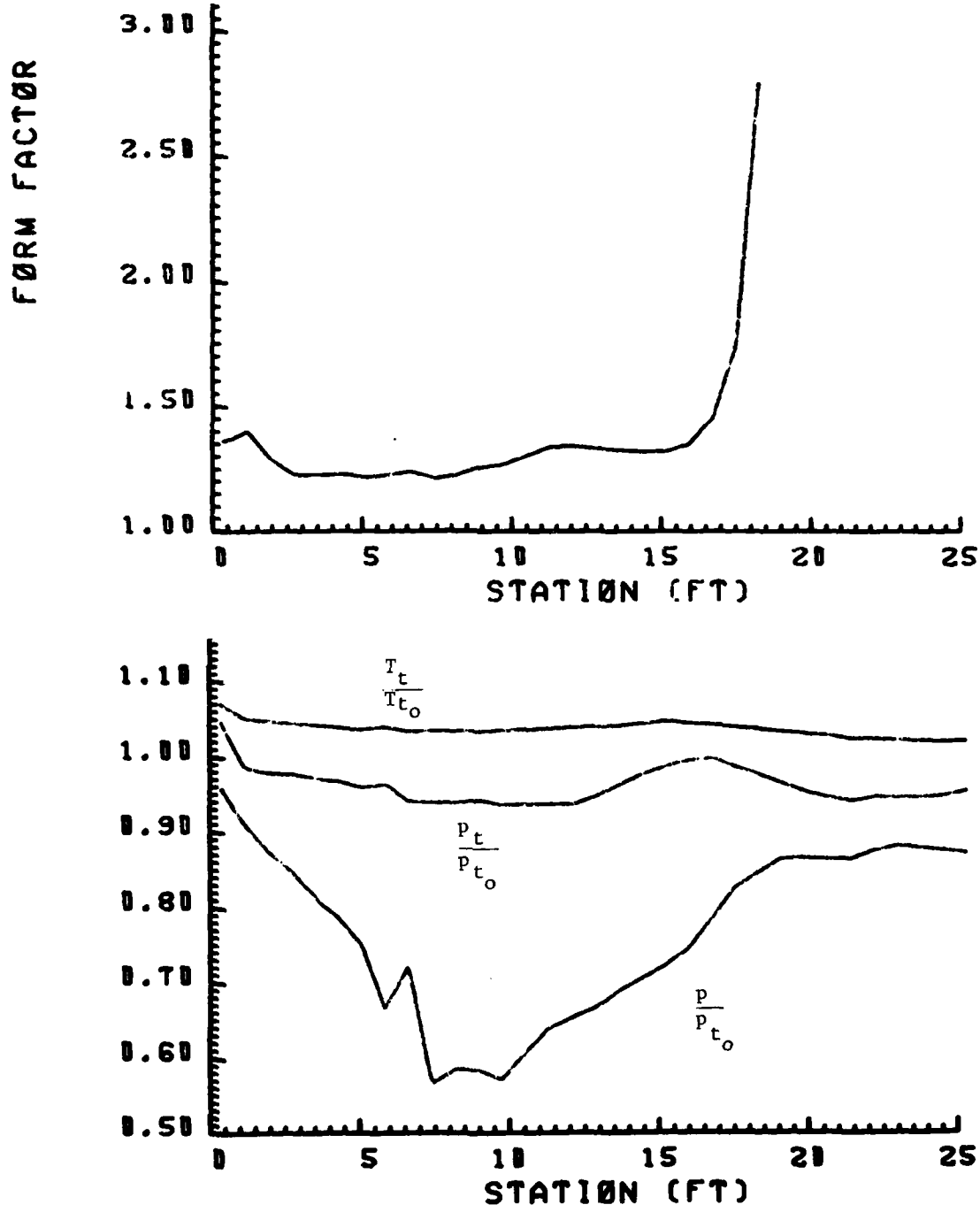

Figure 7.3 - Predicted free-stream properties and form factor H_1 of boundary layer on ramp of blastward inlet. After reflected wave enters inlet.

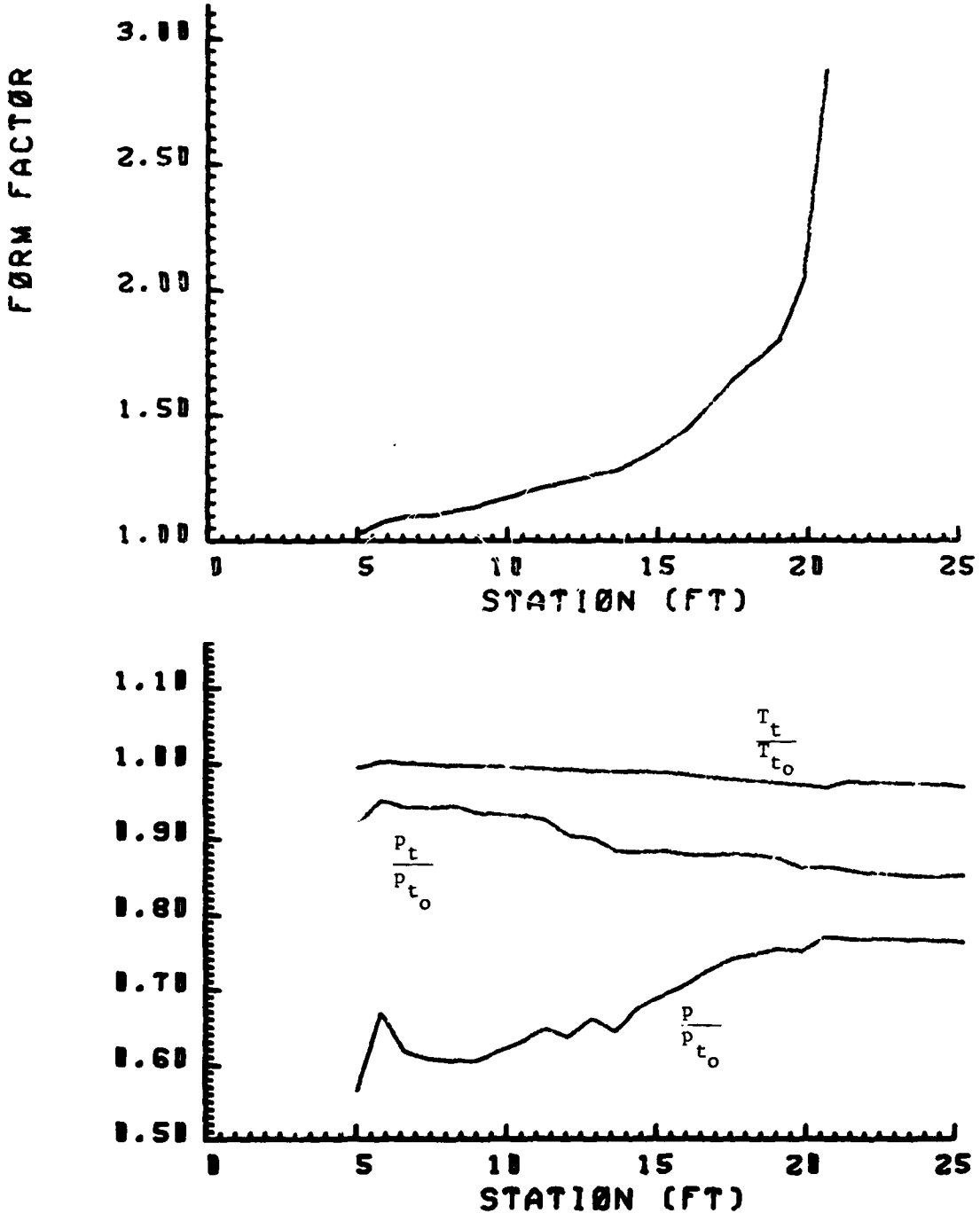

Figure 7.4 - Predicted free-stream properties and form factor H_i of boundary layer on cowl of leeward inlet. After reflected wave enters inlet.

SECTION 8
CONCLUSIONS

From evaluating the results of blast-wave engine-inlet interaction tests with a B-1 type engine inlet, the following conclusions are reached.

1. The blast interaction with the windward inlet produced a rise in the mean total pressure at the engine face followed by a decay. A second rise occurred due to reflection from the choked control vanes simulating the engine. The magnitude of the first peak is found to be nearly 1.41 times as large ($\pm$11 percent) as the increment in total pressure across the incident blast shock. This ratio varies some with inlet weight flow and Mach number but it is unaffected by changes in shock overpressure and intercept angle, over the range tested (76 to 110 deg).

2. The reflection of the blast wave from the engine is expected to be a potential cause of distortion through boundary-layer retardation. The rise rate approaching the second peak in engine face total pressure increased with shock overpressure. The magnitude of the rise to the second peak increased with lower intercept angles (more head-on) and lower weight flows (low engine thrust conditions) and was essentially unaffected by Mach number.

3. The mean total pressure at the engine face rose more slowly in the leeward inlet than the blastward inlet, following blast intercept, and by a smaller amount. In many of the tests the rise in total pressure was followed within a millisecond or so by a rapid fall-off, attributed to possible separation of the flow from the walls of the inlet.

4. The two-dimensional BID code provides a good representation of those features of the blast-induced inlet flow which can be reasonably represented by a two-dimensional inviscid approach, particularly the inlet ramp and cowl pressures and engine face pressures for the blastward inlet. For flow characteristics which may be appreciably affected by three-dimensional effects, such as the leeward inlet and engine face pressures, agreement is not as good but still fair. For flow distortion characteristics, which may be affected both by three-dimensional effects and by viscosity effects (not included in BID), agreement is less satisfactory. To improve this situation, extension of the BID code to the three-dimensional case appears feasible.

5. A study of large apparent distortion values observed at late times during the AEDC tests, after the limited test period of about 3 ms, indicated no cases where these large distortion values could be definitely attributed to inlet response behavior. The limited test period was too short to permit observation of possible large late time distortion effects not masked by extraneous factors. It is recommended that the test duration for future tests be increased, by a factor of two or more.

6. Calculations of the effect of the engine-reflected blast wave on the boundary layers in the inlets, made using the generalized NASA-Lewis BLAYER code, agree with the previous results (DNA 4590F) that indicated boundary-layer separation would occur on the cowl and splitter of the blastward inlet and possibly on the cowl of the leeward inlet. The blast shock overpressure was 5 psi and the intercept angle 90 degrees.

REFERENCES

1. Ruetenik, J.R., and Smiley, R.F., Wind-Tunnel Shock-Tube Simulation and Evaluation of Blast Effects on an Engine Inlet, Kaman AviDyne Report TR-147, DNA 4590F, 1978.

2. AEDC Reports, Data Tabulations, Plots and Tapes on the DNA B-1 Blast Effects Test, AEDC Project P41T-D2A, Test TF-419, 1976-1977.

3. Thompson, J.H., Tomayko, M.A., and Ruetenik, J.R., BID Code for Computing Aircraft Engine-Inlet Response to Blast Disturbances, Kaman AviDyne. Unpublished.

4. McNally, W.D., FORTRAN Program for Calculating Compressible Laminar and Turbulent Boundary Layers in Arbitrary Pressure Gradients, NASA Technical Note D-5681, May 1970.

5. McNally, W.D., NASA Lewis Research Center, Correspondence to Dr. Ruetenik, 28 April 1978.

APPENDIX
TRANSDUCER CALIBRATION EVALUATION

The experimental ramp and cowl pressures measured inside the subject model inlet during the tests of References 1 and 2 are of interest both for assessing blast-induced inlet loadings and for providing a basis for evaluation of the BID code for predicting inlet pressures and velocities. However, in using these data for such purposes it is important for the data user to appreciate that some of these data appear unreliable to some extent because of experimental difficulties experienced during the tests. This appendix points out briefly the principal problems encountered and indicates the degree of reliability of different parts of the data.

The primary problem experienced with the ramp/cowl pressure transducers was an inability to calibrate the transducers accurately during the test period due primarily to unanticipated constrictions in some of the tubes connecting the transducers to the calibration pressure source. This problem could not be resolved in the very limited time that was available for the model tests. The resulting data as presented in References 1 and 2, therefore, had to be reduced on the basis of sometimes nominal or questionable calibration results.

To clarify this calibration problem, KA examined the test data for all ramp/cowl transducers with the aim of identifying questionable data and providing correction factors if possible. Data calibration errors were identified by such means as comparing transducer pressures for the same transducer for similar runs, and/or by comparing transducer pressures for adjacent transducers which should have about the same pressure on the average. E.g., transducers 1970 and 1903 face each other at the same axial location inside the outboard inlet, and normally have quite similar late-time blast-response pressure time histories, both according to many test runs and to the BID code. Consequently, since transducer 1970 had no apparent calibration problem, any strong

difference between the indicated pressures for these two transducers can be reasonably interpreted as an indication that the calibration factor used for transducer 1903 is unreliable.

Using comparisons of this type, Table A.1 was prepared, which indicates the KA estimate of the degree of reliability of the calibration factors used to reduce the data presented in References 1 and 2. In this table, questionable data are identified as either H or L, depending on whether the pressure values presented in References 1 and 2 appeared conclusively to be too high (H) or too low (L). Data for some other runs also appears questionable to a lesser extent (not indicated in the table), but the evidence for such cases is less conclusive.

Some attempts were made to obtain correction factors for some of the questionable data, but it appeared that additional information (not available for this study) would be required from AEDC to effectively accomplish this purpose.

TABLE A.1

RAMP/COWL TRANSDUCER EVALUATION

AEDC Part No.	Ramp/Cowl Transducer Number*						
	1903	1905	1935	1950	1970	1990	2902
512	X	X	H	X	X	H	H
513	X	X	H	X	X	H	H
517	X	H	H	X	X	H	H
518	X	H	H	X	X	H	H
519	X	X	H	X	X	H	H
525	X	X	H	X	X	H	H
526	X	H	H	X	X	H	H
527	X	H	H	X	X	H	H
544	X	X			L		H
545	X	X			L		H
546	X				L		H
550	X	X			L		H
551	X	X			L		H
553	X	X			L		H
558	X	X					H
559	X	X					H
568	X	X					H
569	X						H
570	X						H
573	X						H
574	X						H
582	L						H
583	L						H
584	L	X		X			H
589		H					H
590		H					H
591		H					H
596	L	X		X		X	H
597	L	X				X	H
598	L	X		X		X	H
600	L			X		X	H
601	L					X	H
602	L	X		X		X	H
607		X					H
608		X		X			H
615		X					H
619		X		X			H
620		X					H
621		X					H
624	L	X		X			
625	L						
626	L	X					

*Transducers 1902 and 1980 appeared generally reliable; transducer 1904 provided no useful data.

X Designates no useful data obtained.
H Indicates pressure values in Reference 2 appear to be too high.
L Indicates pressure values in Reference 2 appear to be too low.

DISTRIBUTION LIST

DEPARTMENT OF DEFENSE

Assistant to the Secretary of Defense
Atomic Energy
ATTN: Executive Assistant

Defense Intelligence Agency
ATTN: DB-4C, V. Fratzke

Defense Nuclear Agency
ATTN: SPAS
ATTN: STSP
4 cy ATTN: TITL

Defense Technical Information Center
12 cy ATTN: DD

Field Command
Defense Nuclear Agency
ATTN: FCPR
ATTN: FCT, W. Tyler

Field Command
Defense Nuclear Agency
Livermore Division
ATTN: FCPRL

NATO School (SHAPE)
ATTN: U.S. Documents Officer

Undersecretary of Defense for Rsch. & Engrg.
ATTN: Strategic & Space Systems (OS)

DEPARTMENT OF THE ARMY

Harry Diamond Laboratories
Department of the Army
ATTN: DELHD-N-P, J. Gwaltney

U.S. Army Ballistic Research Labs.
ATTN: DRDAR-BLT, W. Taylor
ATTN: DRDAR-BLT, J. Keefer

U.S. Army Materiel Dev. & Readiness Cmd.
ATTN: DRCDE-D, L. Flynn

U.S. Army Nuclear & Chemical Agency
ATTN: Library

DEPARTMENT OF THE NAVY

Naval Material Command
ATTN: MAT 08T-22

Naval Research Laboratory
ATTN: Code 2627

Naval Surface Weapons Center
ATTN: Code F31, K. Caudle

Naval Weapons Evaluation Facility
ATTN: L. Oliver

Office of Naval Research
ATTN: Code 465

DEPARTMENT OF THE NAVY (Continued)

Strategic Systems Project Office
Department of the Navy
ATTN: NSP-272

DEPARTMENT OF THE AIR FORCE

Aeronautical Systems Division
Air Force Systems Command
ATTN: ASD/ENFT, R. Bachman
4 cy ATTN: ASD/ENFTV, D. Ward

Air Force Aero-Propulsion Laboratory
ATTN: TBC, M. Stibich

Air Force Materials Laboratory
ATTN: MBE, G. Schmitt

Air Force Weapons Laboratory
Air Force Systems Command
ATTN: DYV, A. Sharp
ATTN: SUL
ATTN: DYV, G. Campbell

Assistant Chief of Staff
Studies & Analyses
Department of the Air Force
ATTN: AF/SASC, R. Mathis
ATTN: AF/SASB, R. Mathis

Deputy Chief of Staff
Research, Development, & Acq.
Department of the Air Force
ATTN: AFRD-P, N. Alexandrov

Foreign Technology Division
Air Force Systems Command
ATTN: SDBF, S. Spring

Secretary of the Air Force
ATTN: SAFAL, H. Cooper

Strategic Air Command
Department of the Air Force
ATTN: XPFS, B. Stephan
ATTN: XPFS, F. Tedesco

DEPARTMENT OF ENERGY CONTRACTOR

Sandia National Laboratories
ATTN: A. Lieber

DEPARTMENT OF DEFENSE CONTRACTORS

AVCO Research & Systems Group
ATTN: P. Grady
ATTN: J. Patrick

BDM Corp.
ATTN: C. Somers

Boeing Co.
ATTN: M/S 85/20, E. York

DEPARTMENT OF DEFENSE CONTRACTORS (Continued)

Boeing Wichita Co.
ATTN: R. Syring

Calspan Corp.
ATTN: M. Dunn

University of Dayton
ATTN: B. Wilt

Effects Technology, Inc.
ATTN: R. Wengler
ATTN: R. Globus
ATTN: E. Bick

General Electric Company—TEMPO
ATTN: DASIAC
ATTN: J. Moulton

General Research Corp.
ATTN: T. Stathacopoulos
ATTN: J. Cunningham

Kaman AviDyne
ATTN: R. Ruetenik
ATTN: E. Criscione
ATTN: N. Hobbs
ATTN: B. Lee

DEPARTMENT OF DEFENSE CONTRACTORS (Continued)

Kaman Sciences Corp.
ATTN: D. Sachs

Los Alamos Technical Associates, Inc.
ATTN: P. Hughes
ATTN: C. Sparling

McDonnell Douglas Corp.
ATTN: M. Potter
ATTN: J. McGrew

Prototype Development Associates, Inc.
ATTN: J. McDonald
ATTN: H. Moody
ATTN: C. Thacker

R & D Associates
ATTN: F. Field
ATTN: A. Kuhl
ATTN: P. Haas